Aus dem Physiologischen Institut,
Lehrstuhl für Zelluläre Physiologie der
Ludwig-Maximilians-Universität München

Vorstand: Prof. Dr. Claudia Veigel

Functional Characterization of *Leishmania donovani* Myosin-XXI in Transfection and Lipid Binding Studies

Dissertation
zum Erwerb des Doktorgrades der Naturwissenschaften
an der Medizinischen Fakultät der
Ludwig-Maximilians-Universität München

vorgelegt von

Constanze Helbig

aus
Hoyerswerda

2016

Mit Genehmigung der Medizinischen Fakultät der Ludwig-Maximilians-Universität München.

Betreuerin: Priv.-Doz. Dr. rer. nat. Beate Averbeck

Zweitgutachter: Prof. Dr. Axel Imhof

Dekan: Prof. Dr. med. dent. Reinhard Hickel

Tag der mündlichen Prüfung: 28.07.2017

When the storms are raging round you, stay right where you are.

(Queen, “Don´t try so hard”)

Abstract

Myosins establish a superfamily of cytoskeleton-associated motor proteins, which are encoded in the genome of virtually all eukaryotic organisms. As molecular motors powered by the hydrolysis of ATP, myosins are capable of translocating along filamentous actin. The transduction of chemical into mechanical energy enables myosins to fulfill a plethora of different functions, as for example muscle contraction, cell-cell adhesion, protein transport, or membrane trafficking.

In this context, myosin-XXI plays an extraordinary role. The motor protein, which has recently been described in the literature, is the only myosin the expression of which could thus far be verified in the parasite *Leishmania donovani*. For the parasite, myosin-XXI is a vital motor protein mediating the important cellular processes of endocytosis, exocytosis, vesicular trafficking, and flagellum formation.

In the present work, the molecular bases underlying the function of this essential multifunctional motor protein were aimed to be further elucidated.

For this purpose, the full-length myosin as well as individual myosin-XXI domains were characterized using *in vivo* and *in vitro* methods. In mammalian cell transfection experiments, functionality and cellular distribution of myosin-XXI were examined in a physiological environment devoid of endogenously expressed myosin-XXI. With the help of gliding filament assays and lipid bilayer binding experiments, directionality of myosin-XXI translocation along F-actin was determined and membrane attachment of the molecular motor was investigated.

The transfection studies indicated that myosin-XXI is capable of performing processive movement in mammalian cells, and that the motor protein most probably promotes actin polymerization within the filopodia of transfected cells. These processes depended on the presence of the N-terminal portion of myosin-XXI (aa 1 to 800) comprising an SH3-like domain, the complete motor domain, and part of the adjacent neck and tail region. Gliding filament assays verified for the first time that myosin-XXI, like the vast majority of myosins known to date, is a plus end-directed molecular motor. The analysis of myosin-XXI´s association with membranes demonstrated that the motor protein´s attachment to lipid bilayers requires positive bilayer curvature. In addition, it was shown that myosin-XXI exhibits at least two separate curvature sensitive lipid binding sites.

The results obtained in the present study give evidence that the N-terminal domains of myosin-XXI are of great importance for the motor protein´s functionality, though they are known not to be involved in the localization of myosin-XXI within *Leishmania donovani*. A potential function of the N-terminal parts of myosin-XXI might include the regulation of actin polymerization in membrane protrusions, a process that could possibly play a role in the myosin-XXI-mediated formation of the *Leishmania donovani* flagellum. From the results of the membrane binding studies, it can be concluded that membrane curvature has a regulatory effect on the spatial distribution of myosin-XXI.

Abstract

Accordingly, myosin-XXI is the first myosin described to bind to membranes depending on membrane geometry. The existence of several separate curvature sensitive lipid binding motifs within the motor protein might in fact guarantee maintenance of the myosin-XXI-membrane association during the conformational changes occurring when myosin-XXI passes through its catalytic cycle.

Kurzfassung

Myosine bilden eine Superfamilie Cytoskelett-assoziierter Motorproteine, die im Genom nahezu aller eukaryotischen Organismen kodiert sind. Angetrieben durch die Hydrolyse von ATP können sich Myosine als molekulare Motoren entlang von filamentösem Aktin fortbewegen. Die Umwandlung chemischer in mechanische Energie ermöglicht es Myosinen, eine Vielzahl verschiedener Funktionen, wie zum Beispiel Muskelkontraktion, Zell-Zell-Adhäsion, Proteintransport oder membranverlagernden Transport zu erfüllen.

Myosin-XXI nimmt hierbei eine besondere Stellung ein. Dieses in der Literatur beschriebene Motorprotein ist das bislang einzige Myosin, dessen Expression in dem Parasiten *Leishmania donovani* nachgewiesen werden konnte. Für den Parasiten stellt Myosin-XXI ein lebensnotwendiges Motorprotein dar, welches die wichtigen zellulären Prozesse Endozytose, Exozytose, Vesikeltransport und Flagellenbildung vermittelt.

Ziel der vorliegenden Arbeit war es, die molekularen Grundlagen der Funktion dieses essenziellen multifunktionalen Motorproteins weiter aufzuklären.

Hierzu wurden sowohl das vollständige Myosin als auch einzelne seiner Domänen mit Hilfe von *in-vivo*- und *in-vitro*-Methoden charakterisiert. In Transfektionsexperimenten an Säugetierzellen wurden die Funktionalität und die zelluläre Verteilung von Myosin-XXI in einer physiologischen Umgebung untersucht, in der kein endogen exprimiertes Myosin-XXI vorhanden war. Mittels Gleitfilamentversuchen und Experimenten zur Bindung an Lipiddoppelschichten wurde die Richtung der Myosinbewegung entlang von F-Aktin bestimmt sowie das Membranbindeverhalten des molekularen Motors genauer erforscht.

Die Transfektionsversuche zeigten, dass Myosin-XXI in Säugetierzellen in der Lage ist, sich prozessiv zu bewegen und dass es sehr wahrscheinlich die Aktinpolymerisation in den Filopodien der transfizierten Zellen verstärkt. Für diese Prozesse ist der N-terminale Abschnitt des Myosin-XXI-Moleküls (Aminosäuren 1 bis 800) erforderlich, welcher eine SH3-ähnliche Domäne, die vollständige Motordomäne und einen Teil der anschließenden Hals- und Schwanz-Region umfasst. In Gleitfilamentversuchen wurde erstmalig nachgewiesen, dass sich Myosin-XXI wie die überwiegende Mehrheit der bisher bekannten Myosine in Richtung des Plus-Endes von F-Aktin bewegt. Die Untersuchungen zum Membranbindeverhalten von Myosin-XXI verdeutlichten, dass die Anlagerung des Motorproteins an Lipiddoppelschichten eine positive Oberflächenkrümmung der Doppelschichten voraussetzt. Ferner konnte gezeigt werden, dass das Motorprotein mindestens zwei eigenständige krümmungssensitive Lipidbindungsstellen aufweist.

Die Ergebnisse der vorliegenden Arbeit belegen, dass die N-terminalen Domänen von Myosin-XXI von hoher Wichtigkeit für die Funktionalität des Motorproteins sind, auch wenn sie bekanntermaßen bei der Lokalisation von Myosin-XXI in *Leishmania donovani* keine Rolle spielen. Eine mögliche Funktion

des N-terminalen Abschnitts von Myosin-XXI könnte die Regulation der Aktinpolymerisation in Membranausstülpungen sein, ein Prozess, der möglicherweise bei der Myosin-XXI-vermittelten Bildung des *Leishmania-donovani*-Flagellums von Bedeutung ist. Aus den Ergebnissen der Membranbindungsstudien lässt sich schlussfolgern, dass die Oberflächenkrümmung von Membranen regulatorisch auf die räumliche Verteilung von Myosin-XXI wirkt. Hierbei ist Myosin-XXI das erste Myosin, für das eine Abhängigkeit der Membranbindung von der Membrangeometrie beschrieben wird. Das Vorhandensein mehrerer eigenständiger krümmungssensitiver Lipidbindemotive innerhalb des Motorproteins könnte dabei gewährleisten, dass die Membranbindung von Myosin-XXI aufrechterhalten werden kann, während das Motorprotein seinen katalytischen Zyklus und die damit einhergehenden Konformationsänderungen durchläuft.

Contents

Figures and Tables

List of Figures

List of Tables

Abbreviations

aa	amino acid
AB^-	ATP-free Assay Buffer
AB^+	ATP-supplemented Assay Buffer
ACEX Buffer	Actin Extraction Buffer
ADP	adenosine diphosphate
ATP	adenosine triphosphate
BHB	basic-hydrophobic-basic
BAR domain	Bin-amphiphysin-Rvs domain
Biotin DHPE	N-(biotinoyl)-1,2-dihexadecanoyl-sn-glycero-3-phosphoethanolamine
BSA	bovine serum albumin
COS-7	*Cercopithecus aethiops* kidney fibroblasts
DiO	3,3'-dihexadecyloxacarbocyanine perchlorate
DOPC	1,2-dioleoyl-*sn*-glycero-3-phosphocholine
DsRed2	*Discosoma* species red fluorescent protein 2
E. coli	*Escherichia coli*
EDC	1-ethyl-3-(3-dimethylaminopropyl)carbodiimide hydrochloride
eGFP	enhanced green fluorescent protein
eNBAR	endophilin A1 N-BAR domain
F-actin	filamentous actin
FERM domain	4.1/ezrin/radixin/moesin domain
FITC	fluorescein isothiocyanate
FRAP	Fluorescence Recovery after Photobleaching
G-actin	globular actin
GF 150 Buffer	Gel Filtration 150 Buffer
H_2O	water
HEK-293	human embryonic kidney epithelial cells
HeLa	human cervix epithelial carcinoma cells
HMM	heavy meromyosin
L. donovani	*Leishmania donovani*
Lipo-PEG	1,2-distearoyl-*sn*-glycero-3-phosphoethanolamine-N-[amino(polyethylene glycol)-2000]
LMM	light meromyosin
MCS	membrane curvature sensitivity
N-BAR domain	functional unit of N-terminal amphipathic helix and BAR domain
NHS	N-hydroxysuccinimide

NIH-3T3	*Mus musculus* embryonic fibroblasts
OCT	octenyltrichlorosilane
PBS	Phosphate-Buffered Saline
PC	phosphatidylcholine
PCR	polymerase chain reaction
PE	L-α-phosphatidylethanolamine
PEG	polyethylene glycol
PH domain	pleckstrin homology domain
P_i	inorganic phosphate
PI	phosphatidylinositol
PI(3,5)P_2	phosphatidylinositol 3,5-bisphosphate
PI(3)P	phosphatidylinositol 3-phosphate
PI(4,5)P_2	phosphatidylinositol 4,5-bisphosphate
PI(4)P	L-α-phosphatidylinositol-4-phosphate
POPC	1-palmitoyl-2-oleoyl-*sn*-glycero-3-phosphocholine
PS	phosphatidylserine
PX domain	phox homology domain
RFP	red fluorescent protein
Rhodamine DHPE	Lissamine™ Rhodamine B 1,2-dihexadecanoyl-sn-glycero-3-phosphoethanolamine
ROI	region of interest
RT	room temperature
s.d.	standard deviation
SDS-PAGE	sodium dodecyl sulfate-polyacrylamide gel electrophoresis
Sf21 cells	*Spodoptera frugiperda* ovary cells
SH3 domain	SRC homology 3 domain
SLB	supported lipid bilayer
SLiC assay	Single Liposome Curvature assay
STORM	Stochastic Optical Reconstruction Microscopy
TBE Buffer	Tris/borate/EDTA Buffer
TBS	Tris-Buffered Saline
TG Buffer	Tris Glycine Buffer
TIRF	total internal reflection fluorescence
TRITC	tetramethylrhodamine B isothiocyanate
UBA domain	ubiquitin-associated domain
ZsGreen1	*Zoanthus* species green fluorescent protein 1

1 Introduction

1.1 The Eukaryotic Cytoskeleton

The cytoskeleton of eukaryotic cells is composed of a filamentous network of proteins that fulfills a multitude of tasks essential for proper cell function and thus survival. Not only does the cytoskeleton define and stabilize cellular shape, it is also involved in the interaction of the cell with its environment, and is the fundamental structure in the internal spatial organization of eukaryotic cells (Alberts *et al.*, 2007).

To adapt to the plethora of different functions of the cytoskeleton, different types of cytoskeletal filaments evolved. These filament types comprise actin filaments, microtubules, and intermediate filaments. As the present study is concerned with the actin-based motor protein myosin-XXI, actin filaments will be described in greater detail.

1.1.1 Actin Filaments

In eukaryotes, spatial structures formed by actin play important roles in various processes including muscle contraction, cell division, cell motility, and vesicle transport. Further, actin filaments define cell shape of animal cells (Pollard and Cooper, 2009). In conjunction with cell motility and changes in cell shape, actin forms and stabilizes membrane protrusions (Nambiar *et al.*, 2010). A prominent example of actin-based membrane protrusions are filopodia, which will be described in subsection 1.5.7. Actin is highly abundant in eukaryotes accounting for 1 % to 10 % of a cell´s total protein content depending on the cell type.

In its monomeric form, called globular actin or G-actin, it is a protein of a molecular weight of 42 kDa, a length of 5.5 nm and a width of 3.5 nm. Each actin monomer consists of two subunits and exhibits an ATP/ADP (ADP: adenosine diphosphate) binding pocket between these subunits (Figure 1; Kabsch *et al.*, 1990; Graeve and Müller, 2014).

Actin monomers bind to each other by forming non-covalent bonds resulting in the formation of double-stranded filaments called filamentous actin or F-actin. Actin filaments are flexible helices composed of two so-called protofilaments, linear strings of end-to-end associated monomers. Helices exhibit a diameter of 5 to 9 nm and a 36 nm helical repeat. One twist of an F-actin helix consists of 13 G-actin units (Figure 1; Holmes *et al.*, 1990; Alberts *et al.*, 2007). The formation of actin polymers starts with a nucleation process of slow kinetics, which is the rate limiting step of the polymerization reaction and causes a lag phase prior to the beginning of filament assembly. Nuclei of actin are expected to be trimeric (Sept and McCammon, 2001). At a constant G-actin concentration, the lag phase is followed by a phase of elongation until the rates of monomer attachment and

detachment are equal. At this point, an equilibrium or steady state is reached, at which filament length remains constant (Figure 2). The concentration of free G-actin in solution in the steady state is called critical concentration (c_c). As actin monomers always attach to F-actin in the same head-to-tail orientation, actin filaments display a polar architecture. This polarity is associated with divergent rates of polymerization and depolymerization at the distinct ends of a filament. The end exhibiting higher assembly and disassembly rates is called the plus end, whilst the filament end showing slower monomer attachment and detachment is referred to as the minus end. Originating from the appearance of myosin-decorated actin filaments in electron microscopy images, plus ends are also termed barbed ends and minus ends are called pointed ends (Alberts *et al.*, 2007). Within eukaryotic cells, actin filaments are arranged with their barbed ends facing the cell periphery (Mooseker and Tilney, 1975; Tilney *et al.*, 1981).

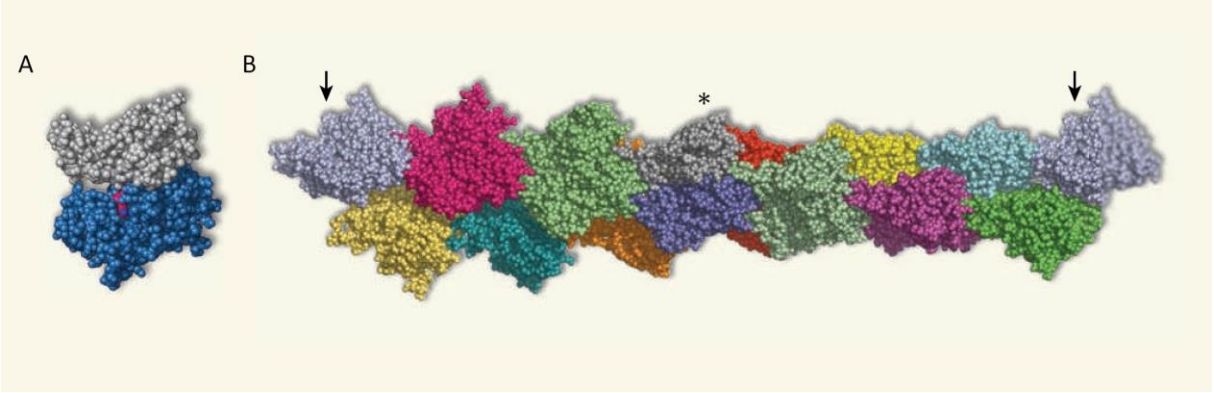

Figure 1 Atomic models of G-actin and F-actin. (A) G-actin consists of two subdomains (blue, grey) enclosing an ATP/ADP binding pocket. Here, conformation of an ADP-bound (red) actin monomer is shown. (B) F-actin is a polar helical polymer resulting from the assembly of actin monomers in a head-to-tail fashion. One twist of the helix (indicated by arrows) contains 13 monomers and is 36 nm long. Here, the middle G-actin (∗) is two-colored for comparison with (A), all other monomers are single-colored. Figure taken from Holmes (2009).

The occurrence of polymerization and depolymerization at the plus and minus ends is determined by the concentration of free actin monomers in solution. Above the critical concentration c_c G-actin binds to the filament ends, while filaments disassemble as soon as the monomer concentration drops below c_c. In a simple association reaction, c_c would be determined by the rate k_{on} of monomer association and k_{off} of monomer dissociation

$$c_c = \frac{k_{off}}{k_{on}} \tag{1}$$

and would be equal for both filament ends. However, actin hydrolyzes ATP resulting in the release of energy. Soon after actin monomers get incorporated into a filament, ATPase activity is induced and the released energy is stored within the polymer lattice. As a consequence, detachment of an ADP-bound monomer is energetically more favorable than dissociation of an ATP-bound monomer. Hence, the rate of monomer addition to the filament end determines whether this end is formed by

ADP-bound or ATP-bound monomers. Accordingly, the slowly growing minus end is more likely occupied by ADP-bound G-actin and hence the average dissociation rate at the minus end is higher than the one at the plus end of a filament. Thus, as c_c can still be approximated by equation (1), the critical concentration $c_{c(-)}$ of the minus end is higher than $c_{c(+)}$ of the plus end. In consequence, a concentration regime exists in between $c_{c(-)}$ and $c_{c(+)}$ where filament growth proceeds at the plus end while G-actin detaches from the minus end:

$$c_{c(-)} > c > c_{c(+)}. \tag{2}$$

At a defined concentration c_{TM} within this regime, monomer association and dissociation balance and actin filaments exhibit a behavior called treadmilling characterized by a constant filament length (Figure 2; Hill and Kirschner, 1982; Mitchison, 1995).

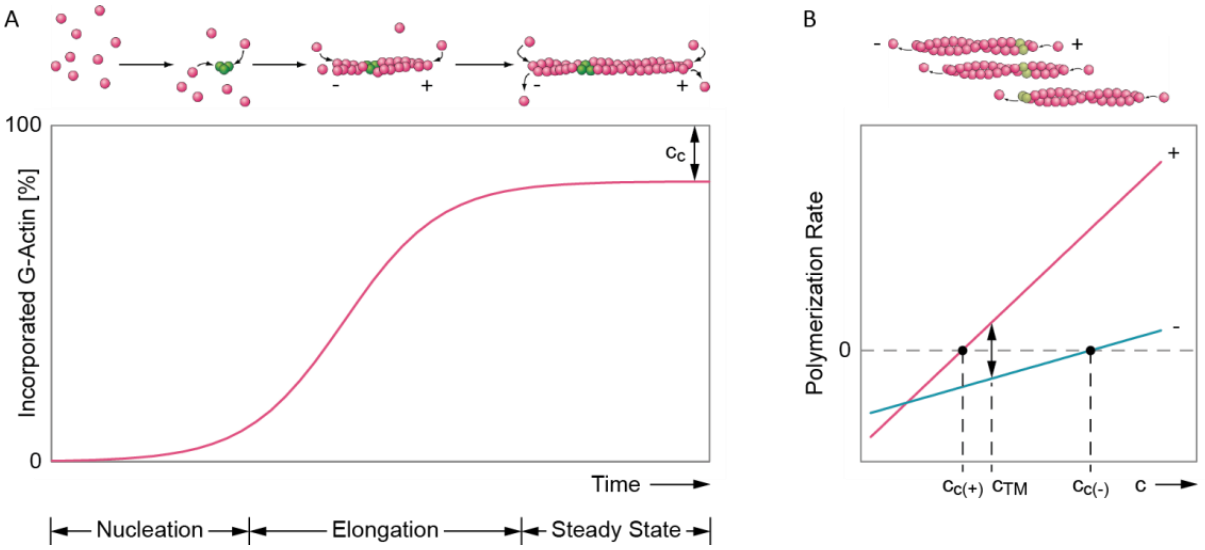

Figure 2 Kinetics of actin polymerization. (A) Time course of the polymerization reaction. The vertical axis depicts the percentage of monomeric actin which is incorporated into the filament, i.e. removed from solution. Assembly of G-actin (pink) into filaments is initiated by the formation of a trimeric nucleus (green). This first step is of slow kinetics thus causing a lag time in the polymerization process. Once a trimer has formed, monomers associate with this nucleus resulting in the formation of a filament and subsequent elongation. However, G-actin association proceeds faster at the so-called plus end, while the minus end grows more slowly. As soon as the concentration of free monomeric actin left in solution reaches the critical concentration (c_c), the polymerization process reaches a steady state, at which G-actin attachment and detachment rates are equal. Importantly, *in vivo* kinetics of filament assembly are modified by the action of various accessory proteins. (B) Polymerization rates at the plus (+) and minus (-) ends of filamentous actin as functions of free G-actin concentration (c). At a negative polymerization rate a filament end disassembles, at a positive rate a filament end elongates. Resulting from G-actin´s capability to hydrolyze ATP, the plus ends and minus ends of filamentous actin exhibit differing critical concentrations, denoted as $c_{c(+)}$ (for plus ends) and $c_{c(-)}$ (for minus ends) here. At a G-actin concentration $\boldsymbol{c < c_{c(+)} < c_{c(-)}}$, filaments cannot be formed. As c exceeds $c_{c(+)}$, filament growth at the plus end begins. Initially, merely unstable filaments form as depolymerization rate at the minus end is higher than polymerization rate at the plus end. At a defined concentration $\boldsymbol{c_{c(+)} < c_{TM} < c_{c(-)}}$, assembly and disassembly rates at the two ends are equal and treadmilling occurs, which is characterized by the constancy of filament length. The treadmilling process is depicted in the cartoon above the diagram. As soon as c increases beyond c_{TM}, the overall filament length grows until finally, when c exceeds $c_{c(-)}$, filament elongation advances at both the plus and the minus end. Cartoons taken from Graeve and Müller (2014).

In vivo, formation of actin polymers is additionally regulated by further proteins, e.g. capping proteins, which bind to the barbed ends of filaments thus inhibiting attachment of G-actin. One of these capping proteins is gelsolin, which in addition exhibits an actin filament severing activity. The

actin-depolymerizing factor ADF/cofilin represents another important regulator of filament assembly as it depolymerizes F-actin (Weber *et al.*, 1991; Carlier, 1998; Pantaloni *et al.*, 2001). Arrangement of filamentous actin into higher structures is mediated by further accessory proteins like fascin, which aggregates F-actin into bundles, or the ARP2/3 complex, which organizes F-actin into branched meshworks (Otto, 1994; Pollard and Cooper, 2009).

1.2 Molecular Motors

Molecular motors are enzymes which convert energy provided by electrochemical gradients or by the hydrolysis of nucleoside triphosphates into mechanical work or chemical energy (von Delius and Leigh, 2011). The cytoskeleton of eukaryotes is associated with molecular motors belonging to the superfamilies of myosins, kinesins, and dyneins. Force generation and transport mediated by cytoskeleton-associated motor proteins play an essential role in many cellular processes ranging from muscle contraction, to movement of cilia and flagella, or transport of organelles, proteins, and RNA (Schliwa and Woehlke, 2003).

Motors of the myosin, kinesin and dynein superfamilies possess a catalytic motor domain, also termed head domain, which binds to a specific type of filament and hydrolyzes ATP into ADP and a free inorganic phosphate (P_i). This chemical cycle of ATP cleavage is coupled to a mechanical cycle in which small conformational changes in the head domain are amplified and translated into movement (von Delius and Leigh, 2011). Throughout the resulting chemo-mechanical cycle, strength of the interaction between the head domain and the filament changes enabling the motor to detach and reattach thus allowing the molecule to move along its filament track (Alberts *et al.*, 2007). During this movement, loss of track is guaranteed by different mechanisms: processive molecular motors stay attached to the filament at all times, as for example in the case of dimeric processive motors, where one head stays attached to the track while the second motor domain is translocated. Non-processive motors, which completely detach from the filament, can for instance perform processive movement by forming motor ensembles such as thick filaments formed by skeletal muscle myosin-II. The translocation of cytoskeletal motor proteins along polar filaments proceeds with a defined directionality.

Protein domains outside the head regulate the enzymatic activity of cytoskeletal motors, and mediate oligomerization and the interaction with cargo (Schliwa and Woehlke, 2003; von Delius and Leigh, 2011).

1.3 Myosins

Molecular motors of the myosin superfamily are involved in a broad range of processes, including contractile processes like muscle contraction and cell motility, establishment of cell-cell and cell-substrate adhesion, membrane trafficking processes (i.e. organelle transport, exocytosis, endocytosis), and protein and RNA transport (Krendel and Mooseker, 2005). Due to their important functional role, myosins are expressed in most eukaryotic cells, and thus far, only three unicellular eukaryotes have been reported not to possess any myosin gene (Odronitz and Kollmar, 2007; Bloemink and Geeves, 2011).

Myosins are characterized by their capability to translocate along filamentous actin thus either moving along F-actin or powering gliding of actin filaments. This actin-based movement is directed toward the barbed end of actin filaments for nearly all myosins. To date, only one full-length myosin, namely myosin-VI, and a tail-less myosin-IX construct have been shown to perform pointed end-directed movement (Sellers, 1999; Wells *et al.*, 1999; Inoue *et al*, 2002).

Myosins are multimeric proteins consisting of one or two heavy and several light polypeptide chains (Figure 3). Their heavy chains consist of at least three structurally and hence functionally different domains, namely the head, neck, and tail domain (Sellers, 1999; Lodish *et al.*, 2000). The head exhibits a molecular weight of approximately 80 kDa and its basic structural motifs like the ATP/ADP binding pocket, the actin binding site, switch I, switch II, and the relay loop are highly conserved. Switch I and II are flexible loop regions which regulate the conformational state of the motor domain thereby modulating its catalytic activity and its interaction with actin filaments (Cheney *et al.*, 1993; Cope *et al.*, 1996; Geeves and Holmes, 1999). The relay loop is located C-terminal of the nucleotide binding site and translates conformational changes in the ATP/ADP binding pocket into a repositioning of the so-called converter domain, which in turn results in the movement of the myosin neck (Sasaki *et al.*, 2003; Fischer *et al.*, 2005). A detailed description of the myosin chemo-mechanical cycle is given in section 1.4. Occasionally, additional motifs precede the head domain at the myosin N-terminus. For instance, N-terminal SH3 (SRC homology 3) or SH3-like domains, which could mediate interactions with other proteins or interact with the motor domain itself, have been identified in several myosins including myosin-XXI (Foth *et al.*, 2006; Mooseker and Foth, 2008; Batters *et al.*, 2014). At its C-terminus, the motor domain is followed by a neck domain primarily composed of α-helices. The neck functions as a lever arm amplifying the amplitude of the movement generated by the head and is mechanically stabilized by the binding of myosin light chains. The number and type of light chains associated with the heavy chain varies between different myosins (Sellers, 1999; Mooseker and Foth, 2008). Association of light chains is mediated by IQ motifs, which are composed of approximately 24 amino acids (aa) and display a core sequence of IQxxxRGxxR (I: isoleucine, Q: glutamine, x: arbitrary aa, R: arginine, G: glycine). The maximum number of IQ

motifs has thus far been discovered in the neck of a *Phytophthora ramorum* myosin, which contains 17 such motifs. Myosin light chains comprise calmodulin and calmodulin-related proteins (Cheney and Mooseker, 1992; Mooseker and Foth, 2008). Calmodulin, which is activated upon the binding of Ca^{2+}, has been shown to be capable of modulating the function of several myosins, for example by increasing the stiffness of the neck region, by regulating the molecular conformation of myosin, or by controlling dimerization (Lin *et al.*, 2005; Alberts *et al.*, 2007; Batters *et al.*, 2014, 2016).

The far C-terminal part of myosins is formed by the tail domain, which is the most variable part of the molecule concerning primary sequence, structure and function. However, within a given class of myosins, apart from the head the combined neck and tail domain is generally conserved as well indicating a coevolution of head, neck, and tail. The myosin tail contains binding sites for additional binding partners hence determining myosin cargo and localization. Furthermore, the tails of several myosins form coiled coil domains mediating dimerization, i.e. the formation of two-headed motors. In class II myosins, the tail actually enables self-association into filaments. Together with the biochemical kinetic properties defined by the motor domain, the tail specifies myosin function (Sellers, 1999; Korn, 2000; Krendel and Mooseker, 2005).

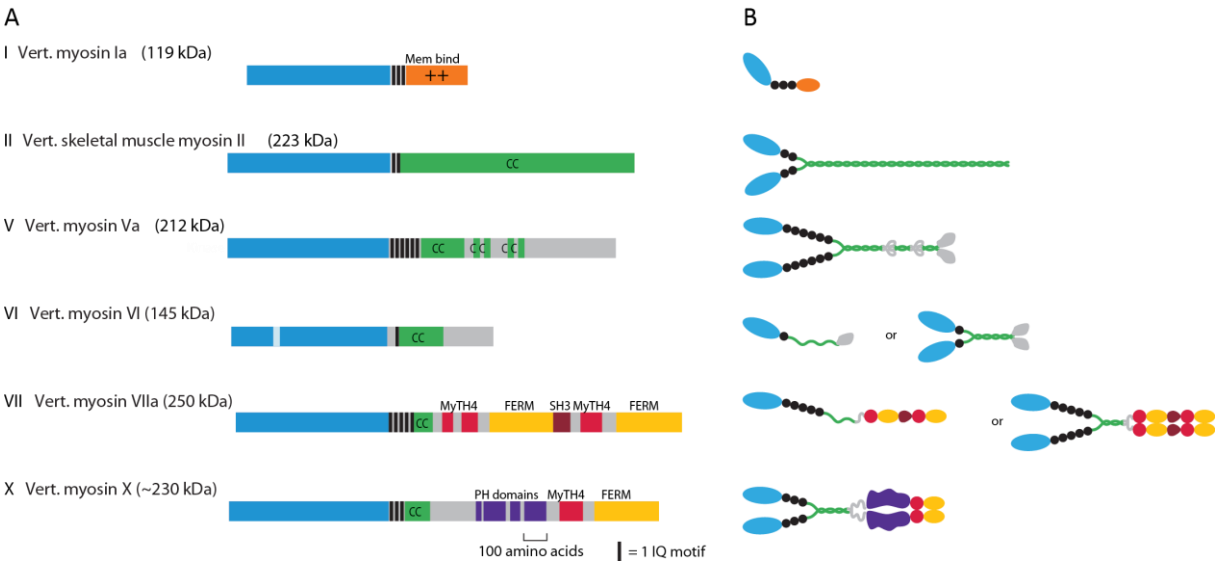

Figure 3 Structure of selected members of the myosin superfamily. Myosins are molecular motors consisting of one or two heavy polypeptide chains. Each heavy chain consists of at least three distinct structural domains: the head, also called motor domain, the neck, and the tail. The highly conserved motor domain (blue) binds to F-actin und hydrolyzes ATP. Within the neck domain, light chain binding IQ motifs (black) are located. The tail region is the most variable part, which in different myosins contains different structural motifs, e.g. coiled coil regions (green), which can mediate dimerization, membrane binding domains (orange), or other cargo binding domains like FERM (4.1/ezrin/radixin/moesin, yellow), MyTH4 (myosin tail homology 4, red), or PH (pleckstrin homology, purple) domains. The SH3 domain (brown) in myosin-VII is proposed to regulate the orientation of the tail (Wang *et al.*, 2007). Class VI and class VII myosins might exist in both a monomeric or dimeric form. (A) Scheme of the domain sequences of selected vertebrate myosins. (B) Respective illustration of the protein structure. Figure taken from Krendel and Mooseker (2005).

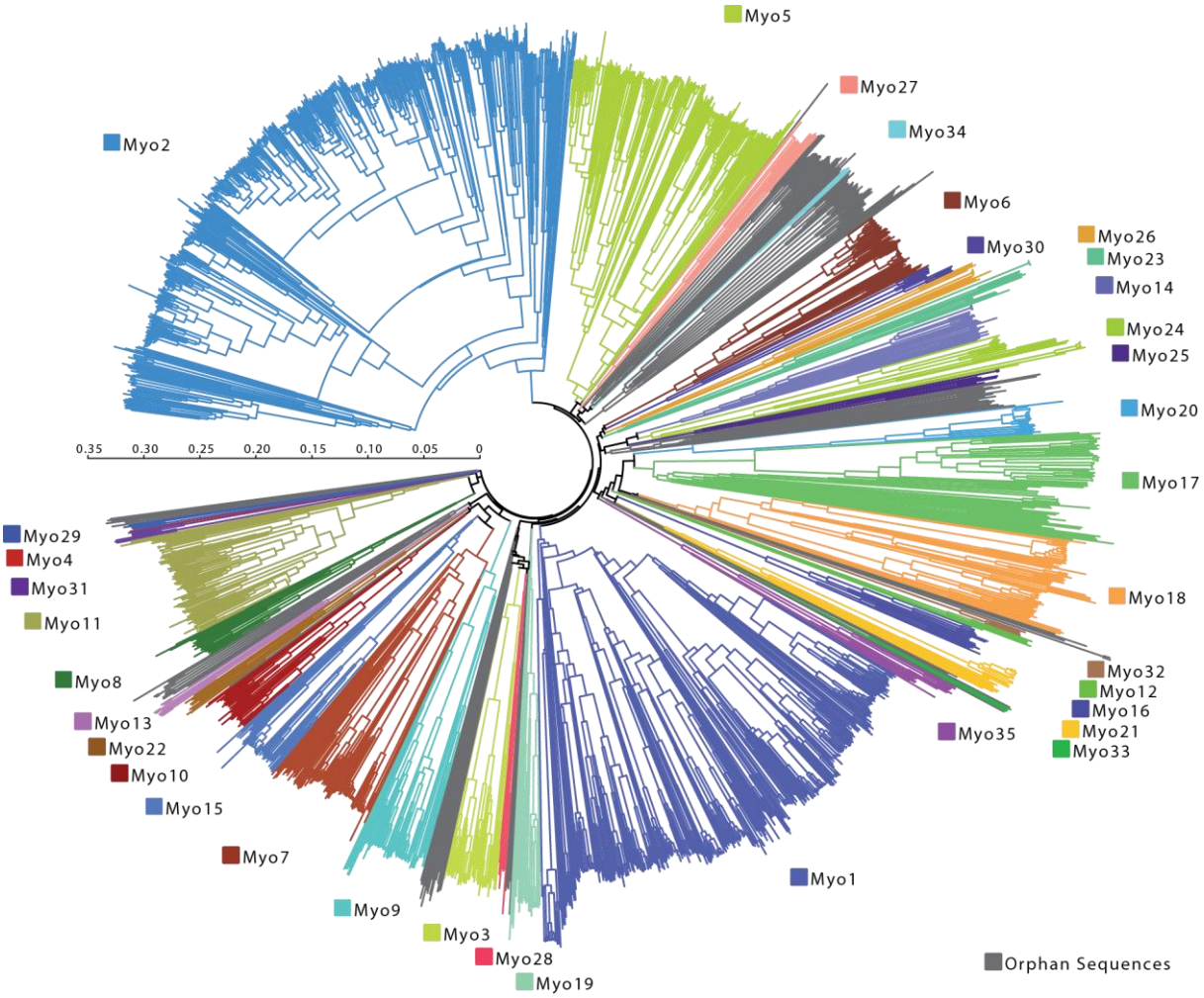

Figure 4 Unrooted phylogenetic tree of the myosin superfamily. Based on the genetic sequence of their motor domains, Odronitz and Kollmar (2007) grouped myosins into 35 distinct classes. In the above illustration, branches demonstrate the evolution of myosins within each class. Time scale indicates 10^3 years. Orphan sequences are sequences of myosins which could not be assigned to one of the defined classes. Figure taken from Odronitz and Kollmar (2007).

The subfamily of myosins is divided into classes according to the homology of their motor domain nucleic acid sequences or aa sequences respectively (Figure 4). As more and more myosins are identified, the number of established classes has been continuously growing throughout the past years: while in 1993, merely 7 myosin classes were defined (Cheney *et al.*, 1993), in 2000, 17 classes were described (Hodge and Cope, 2000). In 2007, a phylogenetic analysis by Odronitz and Kollmar grouped myosins into 35 distinct classes. In humans, genome analysis revealed the existence of 39 genes encoding myosins from 12 distinct classes (Berg *et al.*, 2001).

The first myosins to be described were skeletal muscle myosins of class II (see subsection 1.3.1), thus class II myosins are also referred to as conventional myosins. The first so-called unconventional myosin was isolated from *Acanthamoeba*. As this myosin turned out to be a single-headed motor, it was named myosin-I, while double-headed conventional myosins were now called myosin-II. Subsequently identified myosins were assigned a Roman numeral according to the chronology of their discovery (Alberts *et al.*, 2007; Mooseker and Foth, 2008).

1.3.1 Skeletal Muscle Myosin-II

Class II skeletal muscle myosins were the first myosins to be discovered. As they have been intensely studied throughout the past decades, a profound knowledge of their structure and function exists. In the present work, a proteolytic fragment of rabbit skeletal muscle myosin-II was used as control in experiments investigating the directionality of the actin-based movement of myosin-XXI (see section 4.4). For these reasons, a brief introduction on skeletal muscle myosins-II is given here.

Class II skeletal muscle myosins are dimeric motor proteins composed of two heavy chains and four light chains (Figure 5). Each heavy chain contains two IQ motifs mediating the association of the heavy chain with one regulatory (also termed phosphorylatable) light chain and one essential (also called alkali) light chain. Light chains belong to the calmodulin/troponin-C superfamily. The tail of skeletal muscle myosin-II is an extended α-helical domain acting as dimerization site by forming a coiled coil structure. In addition to dimer formation, the tail mediates the self-assembly of dimeric myosin-II into thick filaments at low ionic strength, and serves as binding site for proteins which stabilize filament structure and interlink filaments (Sellers, 1999; Reggiani and Bottinelli, 2008).

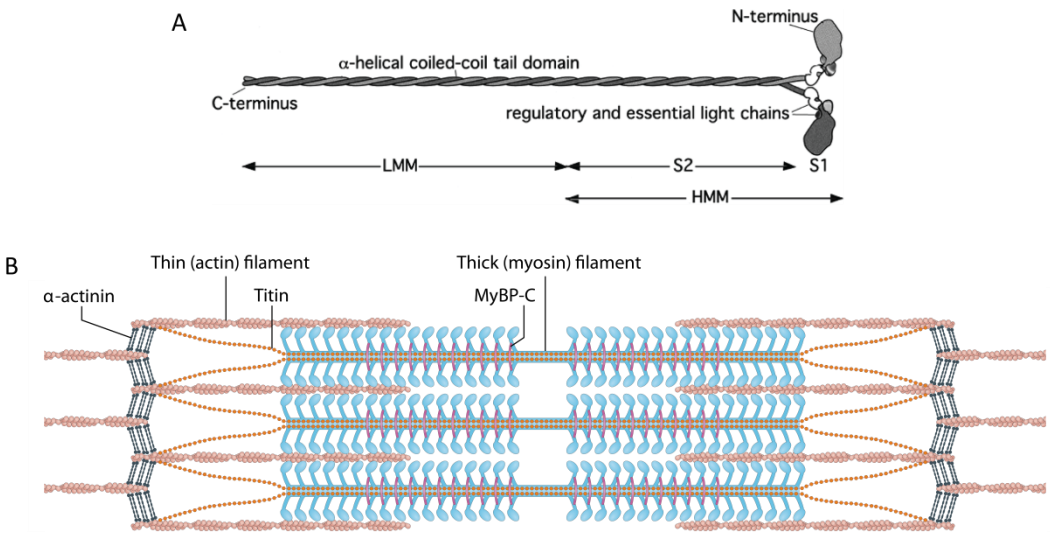

Figure 5 Structural properties of skeletal muscle myosin-II. (A) Dimeric skeletal muscle myosin-II. The myosin dimer is formed by two heavy and four light polypeptide chains. Dimerization of heavy chains is mediated by coiled coil formation along the alpha-helical tail domains. With the help of controlled tryptic digestion, myosin-II dimers can be separated into distinct functional fragments: HMM contains both motor domains, the neck region, and approximately one third of the dimeric tail, and is capable of translocating along filamentous actin. This fragment can be further digested into subfragments S1, i.e. two monomeric fragments each containing a motor and neck domain, and subfragment S2, i.e. the respective tail segment. LMM is composed of the C-terminal part of the myosin-II tail, and unlike HMM, it aggregates into paracrystalline-like structures at low ionic strength. Figure taken from Holmes (2008). (B) Structure of the sarcomere, the basic structural unit of skeletal muscles. Under conditions of low ionic strength, the tail-mediated assembly of myosin-II molecules results in the formation of bipolar thick filaments with a head-free central zone. Together with actin-based thin filaments, thick filaments form the basic structural unit of skeletal muscles. The sliding of myosin-II heads along surrounding oppositely oriented thin filaments causes a contraction of the sarcomere. Importantly, sarcomere formation also requires the presence of accessory proteins like α-actinin, which crosslinks thin filaments, or myosin binding proteins, e.g. titin and MYBP-C (myosin binding protein-C), which stabilize and interlink thick filaments. Figure taken from Hwang and Sykes (2015).

Within thick filaments, myosin tails position parallel to the filament axis. The staggered arrangement of myosin molecules in the filaments results in the periodic emergence of myosin-II heads at the surface. Importantly, thick filaments, which contain several hundreds of myosin heads, exhibit a bipolar architecture characterized by a central head-free zone, referred to as bare zone. The bipolarity of skeletal muscle myosin-II filaments enables them to slide surrounding actin-based thin filaments past each other thus driving muscle contraction (Figure 5; Cooke, 1986; Reggiani and Bottinelli, 2008).

Noteworthily, skeletal muscle myosin-II can be cleaved into separate functional fragments by controlled proteolysis (Figure 5). Digestion with trypsin produces two fragments called heavy meromyosin (HMM) and light meromyosin (LMM). HMM contains the catalytic motor domains and a segment of the myosin tail sufficiently long for dimerization. It is capable of translocating F-actin but does not aggregate into filaments. HMM can be further tryptically digested into two single-headed subfragments S1, each consisting of head and neck, and a dimeric subfragment S2, merely comprising the remaining tail segment. LMM, which consists of the C-terminal approximate two thirds of the myosin-II tail, dimerizes and assembles into paracrystalline-like aggregates at low ionic strength (Cooke, 1986; Sellers, 1999).

1.4 Chemo-Mechanical Transduction in Myosins

The catalytic cycle of myosins, in which chemical energy released during ATP hydrolysis is converted into mechanical force, seems to be a highly conserved process occurring in all myosins characterized so far (De La Cruz and Ostap, 2004; El-Mezgueldi and Bagshaw, 2008).

This process is composed of a defined sequence of biochemical reactions involving the attachment to and detachment from F-actin, nucleotide binding, and release of hydrolysis products (Lymn and Taylor, 1971; Eisenberg and Greene, 1980). However, significant variations in the rates of transition between different states of myosin in the ATPase cycle allow for an efficient adjustment of myosin kinetic properties to specific physiological tasks. In accordance with differing myosin functions, these variations even exist within a given class of myosins (De La Cruz and Ostap, 2004; Sweeney and Houdusse, 2010).

The initially proposed model of chemo-mechanical energy transduction, the swinging crossbridge model, was originally postulated by Huxley (1957) and later further developed by Huxley and Simmons (1971). In this model, force generation by myosins was hypothesized to solely result from conformational changes within the myosin motor domain. Today, the swinging lever arm hypothesis is widely accepted, which states that the performance of mechanical work is a consequence of small conformational changes in the ATP binding pocket being translated into a large swinging motion of the lever arm, i.e. the myosin neck (Spudich, 1994; Holmes, 1997; Sweeney and Houdusse, 2010).

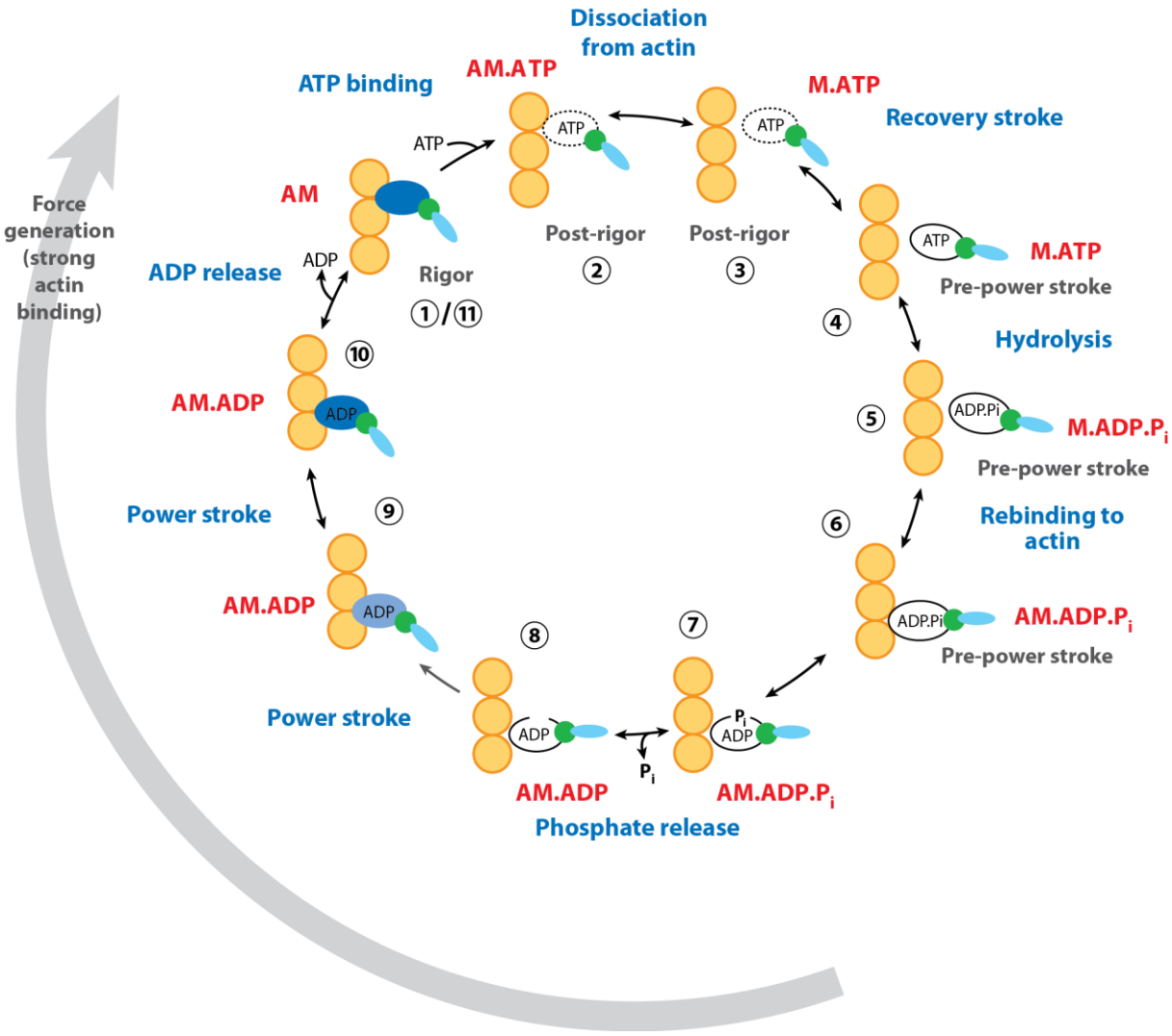

Figure 6 The myosin ATPase cycle. In a conserved cycle of biochemical reactions, myosin (three-part multicolored symbol) converts chemical energy provided by the hydrolysis of ATP into mechanical force. Force is transmitted to F-actin (yellow spheres) via a swinging motion of the lever arm (light blue), the so-called power stroke. In short, nucleotide-free actin-associated myosin (1) binds ATP (2), and subsequently detaches from the actin filament (3). The lever arm position required for force transmission is then restored in the recovery stroke (4), followed by the hydrolysis of ATP (5) and the rebinding of myosin to F-actin (6). Once P_i is released from the motor domain (7-8), myosin performs a two-step power stroke, during which small conformational changes in the nucleotide binding pocket are translated into a swinging lever arm motion of significantly larger amplitude (9-10). Concomitant with the power stroke, myosin´s affinity for ADP markedly decreases resulting in the dissociation of ADP and thus in the transition of actomyosin back into the initial rigor conformation (11). For a detailed description of the myosin catalytic cycle see text. Figure taken from Sweeney and Houdusse (2010).

1.4.1 The Myosin ATPase Cycle

In 1971, a cyclic scheme for the ATP-dependent force generation by myosins was introduced by Lymn and Taylor (1971) for the first time. Accordingly, the myosin catalytic cycle is also referred to as Lymn-Taylor cycle.

In the years following the proposal of cyclic force generation, more detailed information on the myosin ATPase cycle was obtained, for example by the determination of myosin and actomyosin crystal structures, single-molecule mechanical studies of myosins, or kinetic studies in aqueous solution (Sweeney and Houdusse, 2010).

A simplified kinetic scheme of the myosin catalytic cycle as summarized by Sweeney and Houdusse (2010) is depicted in Figure 6. In general, intermediate states of the myosin catalytic cycle are categorized according to the affinity of myosin for actin binding. States of low (i.e. micromolar) affinity comprise actin detachment, the recovery stroke i.e. the repositioning of the lever arm, ATP hydrolysis, and reattachment to actin. High (i.e. submicromolar) affinity states are intermediate states involved in the generation of force, including the power stroke, during which the movement of the myosin lever arm transmits force to the actin filament (Geeves and Holmes, 1999).

In the presence of load and under saturating concentrations of actin and ATP, the ATPase cycle proceeds as follows (Sweeney and Houdusse, 2010):

1. At the end of the preceding enzymatic cycle, nucleotide-free myosin is tightly bound to actin in the so-called rigor state. At this stage, the actomyosin complex is also denoted as AM (A…actin, M…myosin).

Transition to low affinity states of myosin:

2. Subsequently, myosin rapidly rebinds ATP resulting in a conformational change transferring myosin into its post-rigor states. This conformational change significantly weakens the association of myosin with actin. Initially, myosin is still weakly attached to actin (AM.ATP conformation).
3. In the following post-rigor state, myosin has dissociated from the actin filament, thus adopting the ATP-bound M.ATP conformation. Detachment from actin enables myosin to execute the recovery stroke, during which the myosin lever arm swings back into the position required for force transmission.
4. By performing the recovery stroke, myosin reaches its pre-power stroke states, the first of which is characterized by the hydrolysis competence of myosin.
5. Upon the hydrolysis of ATP, myosin remains associated with the respective reaction products, ADP and P_i (M.ADP.P_i conformation).
6. In the succeeding transition into AM.ADP.P_i, reattachment of myosin to the actin filament presumably initiates conformational changes of myosin required for later P_i release.

Transition to high affinity (i.e. force-generating) states of myosin:

7. In the next step, myosin actin association tightens thus likely stabilizing further conformational changes which result in the creation of a P_i escape route alternative to the ordinary exit from the nucleotide binding pocket. The structural basis of this escape route, which is commonly called back door, is yet unknown.

8. Following phosphate release, i.e. the transition into the AM.ADP conformation, closure of the presumed back door prevents rebinding of P_i.
9. In conjunction with back door closure, the lever arm carries out the first swing of the power stroke.
10. In a second swinging motion of the lever arm, the myosin power stroke is completed. During the power stroke, small conformational changes in the motor´s nucleotide binding pocket are translated into a lever arm motion of considerably larger amplitude allowing for an effective transmittance of force to the actin filament. Concomitant with the terminal second step of the power stroke, the strength of myosin´s association with ADP is significantly reduced.
11. In the final state transition of the ATPase cycle, ADP is released from the nucleotide binding pocket, transferring myosin back into its rigor state (1.).

1.4.2 Myosin Kinetic Properties

In accordance with the diverse physiological functions of distinct myosins, these cytoskeletal molecular motors exhibit differing kinetic properties.

An important kinetic parameter for the characterization of myosins is the duty ratio, which is defined as the fraction of the ATPase cycle a myosin spends in its high affinity states, i.e. tightly bound to the actin filament track.

Accordingly, high duty ratio motors like myosin-V and myosin-VI remain strongly attached to F-actin throughout a substantial portion of their catalytic cycle. Importantly, a high duty ratio is a prerequisite for processivity, i.e. the capability of a motor protein to translocate along filaments in multiple consecutive interactions without detaching from the filamentous track (De La Cruz and Ostap, 2004; El-Mezgueldi and Bagshaw, 2008). In the case of myosin-V, processivity was demonstrated to enable this motor protein to continuously translocate along actin over distances of up to several µm *in vitro* (Sakamoto *et al.*, 2000). The minimum number of consecutive myosin-V-actin interactions *in vitro* was estimated to range between 40 and 50 steps (Mehta *et al.*, 1999). For high duty ratio myosins, ADP release was identified as the rate-limiting step of the ATPase cycle.

In turn, low duty ratio myosins merely populate the high affinity states throughout a small part of their catalytic cycle (De La Cruz and Ostap, 2004). For instance, skeletal muscle myosin-II remains strongly associated with F-actin for less than 20 % of the duration of its ATPase cycle (Guilford *et al.*, 1997). This enables fast skeletal muscle myosin-II to generate sarcomere contractions of maximum speed and maximum power output (Sweeney and Houdusse, 2010). In consequence of the proportionally short time low duty ratio myosins remain in the strong binding states, these motor proteins dissociate from actin filaments after passing through a single catalytic cycle. Hence, low duty motors are non-processive. However, when non-processive motors form large assemblies or are

spatially constraint by cytoskeletal structures, they too can effectively perform processive movement (El-Mezgueldi and Bagshaw, 2008). Further, certain monomeric non-processive myosins might as well employ a second tail-located actin binding site in order to translocate without detaching from their filament track (Les Erickson *et al.*, 2003). The rate-limiting transition in the catalytic cycle of low duty ratio myosins is the release of P_i (De La Cruz and Ostap, 2004).

1.5 Biomembranes

Similar to the cytoskeleton, the eukaryotic membranous system plays a crucial role in determining cell shape and function (Sackmann, 1995). Moreover, the interplay between membranes, cytoskeletal filaments and filament-associated motor proteins has been shown to drive essential cellular processes like cell movement, endocytosis, or vesicular transport (Schliwa and Woehlke, 2003; Soldati and Schliwa, 2006; Keren, 2011).

As within the current work, membrane association of the motor protein myosin-XXI was one of the aspects elucidated, the molecular constituents and the architecture of biomembranes will be introduced in this section.

1.5.1 Functions of Biomembranes

Biological membranes, also termed biomembranes, constitute the boundaries of cells and intracellular compartments thus spatially separating the molecular contents of cellular organelles, the cytoplasm, and the cell´s environment. This spatial separation reduces the number of molecules accessible for direct interactions within the cytoplasm and the intracellular compartments. Furthermore, it allows for the establishment of compartment-specific conditions regarding protein content, pH, and ionic composition. The resulting gradients give rise to electrochemical potentials and the directed flow of constituents. In addition, ionic composition and pH of the distinct subspaces regulate the activity of specialized proteins thereby enabling the inner compartments of a cell to fulfill specific, well-defined functions (Sackmann, 1995; Goñi, 2014).

Importantly, biomembranes do not only serve the purpose of spatial separation, but also allow for interactions with a cell´s or an organelle´s surroundings, as for instance during the formation of cell-cell contacts or during signal uptake by receptor proteins (Alberts *et al.*, 2007). Moreover, membrane-associated transport processes like endocytosis, exocytosis or transport via membrane proteins enable the exchange of material, e.g. nutrients, metabolic waste, or ions. Additionally, membrane proteins enable biomembranes to fulfil a multitude of further tasks like ATP synthesis, regulatory functions, or tethering of the cytoskeleton (Lodish *et al.*, 2000).

1.5.2 Membrane Lipids

Lipids are organic molecules which share two common characteristics: insolubility in water and high solubility in organic solvents like chloroform or isopropanol (Lottspeich and Engels, 2012). In biomembranes, they are arranged in a 6 nm to 10 nm thick double layer forming the structural basis of membrane architecture (see subsection 1.5.4). Membranes of eukaryotic cells are composed of three major classes of lipids: **phospholipids**, **glycolipids**, and **cholesterol**.

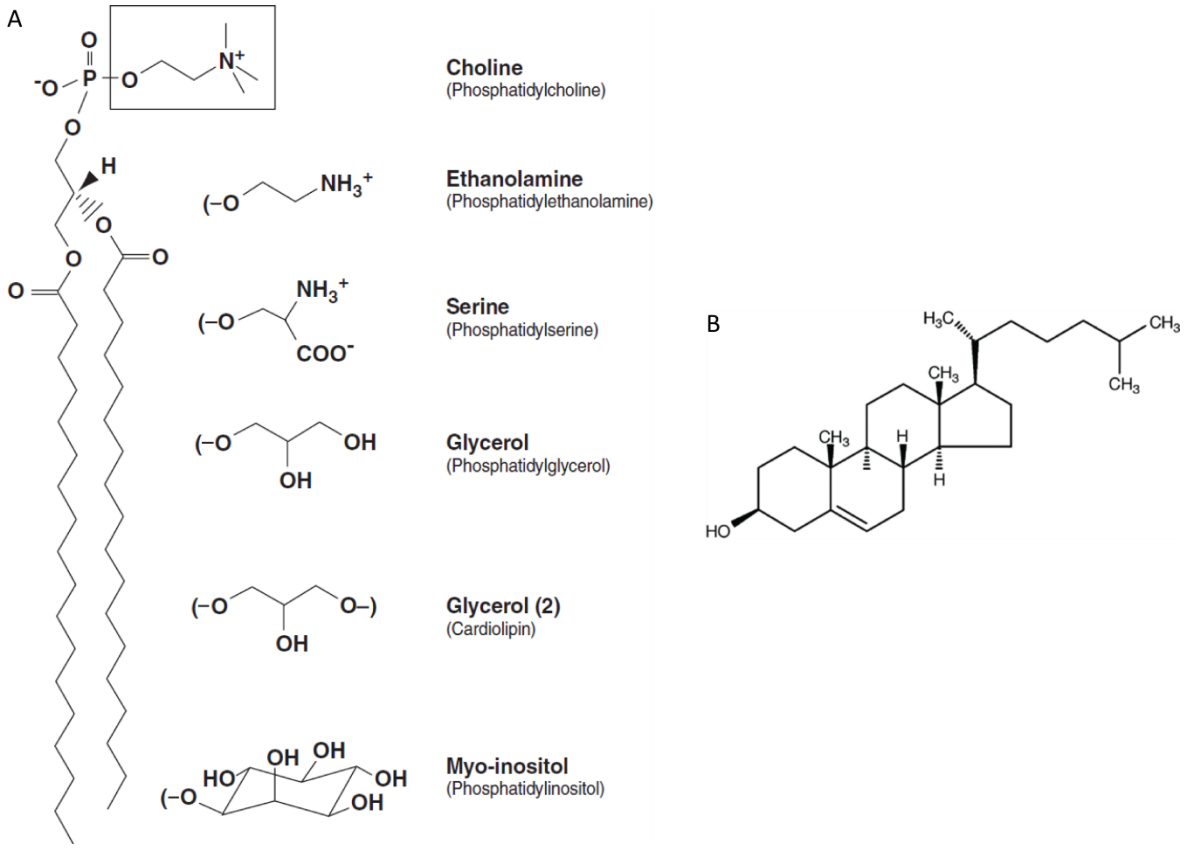

Figure 7 Chemical structures of lipid constituents of eukaryotic membranes. (A) Examples of phospholipids contained in eukaryotic biomembranes. Phospholipids are amphipathic molecules consisting of a polar head group and at least one hydrophobic hydrocarbon tail. The head group contains an alcohol, a phosphate, and glycerol or sphingosine. Here, several phospholipids derived from glycerol are depicted. The structure of these lipids differs in the alcohol moiety linked to the phosphate group. The complete structure shown on the left is the one of PC. By substitution of the boxed choline group with other alcohol residues, structures of different phospholipids are obtained. The names of the respective phospholipids are parenthesized. In phosphatidic acid, which is not shown here, choline is replaced by a hydroxyl group. As the glycerol moiety of cardiolipin joins two phosphatidic acid molecules, cardiolipin is also referred to as diphosphatidylglycerol. Figure taken from Dowhan *et al.* (2016). (B) Structure of cholesterol. Cholesterol is composed of four interlinked hydrocarbon rings, to which a hydroxyl group and a hydrocarbon tail are bound. While the hydroxyl group constitutes the polar part of the amphipathic molecule, the hydrophobic moiety is formed by the hydrocarbon rings and tail. Figure taken from Palmer (2004).

Phospholipids, which are abundant in all biomembranes, consist of a hydrophilic head group and at least one hydrophobic tail. The polar head is composed of an alcohol, a phosphate, and a glycerol or sphingosine, whilst each tail is formed by a fatty acid (Figure 7; Berg *et al.*, 2012). *Cis*-double bonds within the fatty acid carbon chain influence the lateral space required by a tail. Together with the overall length of the lipid molecule and the cross-sectional area of the hydrophilic head, the spatial

extent of the hydrophobic tails determines the molecular geometry of a phospholipid (Marsh, 1996; Alberts *et al.*, 2007; McMahon and Boucrot, 2015). Due to their molecular structure, phospholipids are generally depicted using the following shorthand: the hydrophilic head is pictured as a circle, and the hydrophobic tails are represented by straight or wavy lines connected with this circle.

Examples of phospholipids contained in eukaryotic membranes include phosphatidylethanolamine (PE), phosphatidylcholine (PC), phosphatidylserine (PS), sphingomyelin, and phosphatidylinositol (PI) (Table 1; Berg *et al.*, 2012). Commonly, PC and PE account for more than 50 % of the total phospholipid content of eukaryotic membranes hence playing a major role in determining structural properties of biomembranes (Gibellini and Smith, 2010). PS is the most abundant negatively charged membrane phospholipid in eukaryotes thus being an important mediator of electrostatic interactions between membranes and proteins (Lee *et al.*, 2006; Leventis and Grinstein, 2010). Sphingomyelin, which colocalizes with cholesterol in biomembranes, is assumed to be a regulator of cholesterol distribution (Slotte and Ramstedt, 2007). PI, despite representing only a minor component of biomembranes, has a unique role within eukaryotic cells. Its phosphorylated forms, called phosphoinositides, can be rapidly modified by phosphorylation and dephosphorylation of their head group (Figure 8), thereby activating or deactivating their function as protein binding sites. Therefore, phosphoinositides have regulatory functions in many cellular processes, e.g. intracellular signaling, membrane trafficking, or membrane adhesion of the cytoskeleton (Lemmon, 2003; Scrimgeour and Harwood, 2007).

Table 1 Lipid composition of various eukaryotic membrane systems. Data summarize the lipid constituents of the human erythrocyte plasma membrane (Tanford, 1980), the overall membranous system of Chinese hamster ovary (CHO) cells (Ohtsuka *et al.*, 1993), the inner and outer mitochondrial membrane of *Saccharomyces cerevisiae* (Zinser *et al.*, 1991), and the endoplasmic reticulum (ER) of murine L-cells (Murphy *et al.*, 2000). Numbers are expressed in mol% of total lipid. Blanks indicate that the respective lipid species was not analyzed. As exemplified below, phospholipids represent a group of lipid species abundant in all biomembranes.

	Erythrocyte	CHO Cells	Mitochondria		ER
			Outer	Inner	
PC	19	51	46	38	46
PE	18	21	33	24	21
PI	1	8	10	16	2
PS	9	7	1	4	2
Sphingomyelin	18	9	-	-	9
Cholesterol	25	-	0	0	20
Glycolipids	10	-	-	-	-
Others	0	4	10	18	-

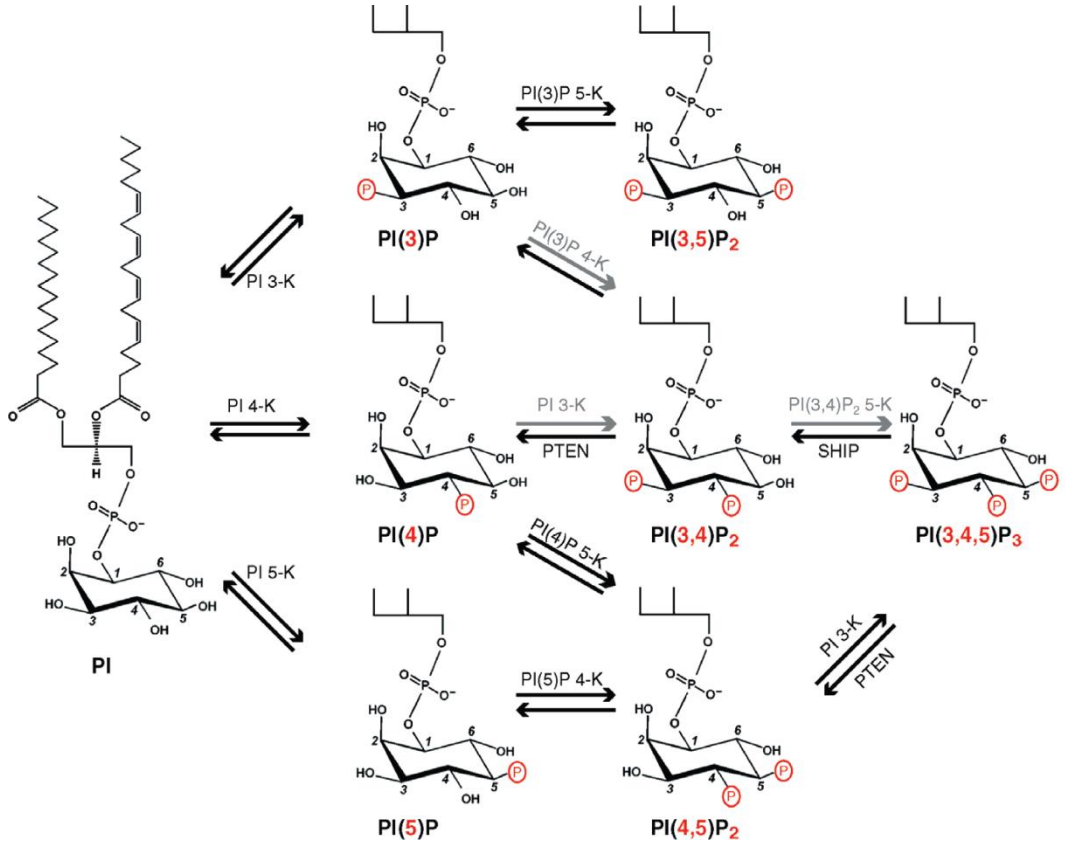

Figure 8 The phosphoinositide cycle in mammalian cells. Phosphatidylinositol (PI), a phospholipid constituent of biomembranes, can be phosphorylated at the 3, 4, and 5 position of its inositol ring. The resulting phosphorylated forms, called phosphoinositides, serve as protein binding sites and thereby regulate membrane functionality. Thus, the rapid activation and deactivation of these binding sites by phosphorylation and dephosphorylation play important regulatory roles within eukaryotic cells. The above scheme depicts the PI phosphorylation/dephosphorylation cycle in mammalian cells. The respective reactions are catalyzed by phosphatidylinositol kinases (K, the number behind the lipid name designates the position of phosphorylation/dephosphorylation), phosphatase and tensin homolog (PTEN), or SH2 domain-containing inositol 5'-phosphatase (SHIP). Gray arrows indicate paths which are less well-characterized or generate only a minor proportion of the respective phosphoinositide. Figure taken from Lemmon (2003).

The class of **glycolipids** comprises a heterogeneous group of lipids conjugated to one or more monosaccharide units. Like phospholipids, they are composed of at least one hydrophobic hydrocarbon tail and a polar head group, however with the hydrophilic head linked to sugar residues. *In vivo*, glycolipids are exclusively found in the non-cytosolic leaflet of lipid membranes. In addition to their importance in membrane stabilization and cell surface rigidization, they are also involved in cellular processes like cell-cell adhesion or signal transduction (Alberts *et al.*, 2007; Holst, 2008). One group of glycolipids comprises lipids called cerebrosides. These glycolipids solely contain one sugar unit and are a key component of the insulating myelin sheaths of nerve cells (Linington and Rumsby, 1977; Berg *et al.*, 2012).

Cholesterol, which constitutes up to 25 % of the lipids forming a eukaryotic biomembrane, consists of four interlinked hydrocarbon rings, which at one site of the molecule are attached to a hydrocarbon tail and at the opposite site carry a hydroxyl group. The hydrophilic hydroxyl group interacts with the head domains of adjacent membrane lipids, while the hydrophobic rings and tail

are embedded within the membrane core (Karp, 2005; Berg *et al.*, 2012). In biomembranes, cholesterol decreases the permeability for small water-soluble molecules and reduces membrane fluidity. Furthermore, it prevents crystallization of the hydrocarbon chains of phospholipids and glycolipids (Shin and Freed, 1989; Alberts *et al.*, 2007). Together with sphingomyelin, cholesterol is involved in the formation of membrane domains assumed to be a favorable location of certain membrane proteins (Slotte and Ramstedt, 2007; Goñi, 2014).

1.5.3 Self-Aggregation of Membrane Lipids

The common feature of all membrane lipids is their amphiphilicity, i.e. their composition of a hydrophilic and a hydrophobic moiety. In consequence, in an aqueous environment membrane lipids self-assemble into 3D structures shielding their hydrophobic parts from contact with water (Berg *et al.*, 2012).

In the course of self-assembly, membrane lipids can adopt distinct phases. Phases are defined as states of uniform physical properties, and the main phases of membrane lipids in water can be grouped into lamellar, micellar, inverse hexagonal, and inverse cubic phases (Figure 9).

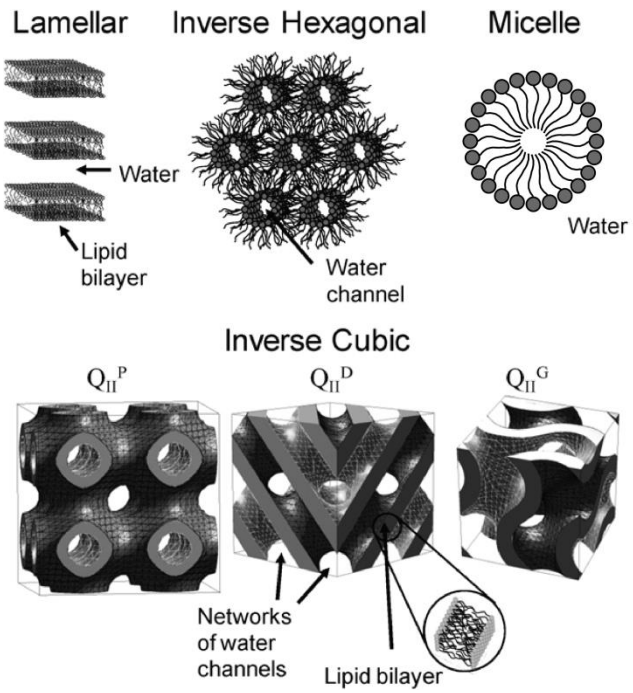

Figure 9 Main phases of membrane lipids dispersed in water. Due to their amphiphilicity, membrane lipids spontaneously self-assemble in an aqueous environment, thereby adopting distinct phases, i.e. states of uniform physical properties. Self-assembly is driven by hydrophobic interactions, thus lipids position with their polar moieties facing the lipid-water interface. The four major membrane lipid phases comprise lamellar, inverse hexagonal, micellar, and inverse cubic. In lamellar phases, membrane lipids form bilayers. Inverse hexagonal phases are characterized by the formation of water-filled tubes arranged in a hexagonal lattice. Micelles are spherical monolayer structures. Membrane lipids adopting inverse cubic phases arrange in diverse types of cubic lattices enclosing aqueous channels or cavities. Illustrations of lamellar, inverse hexagonal, and inverse cubic phases taken from, micellar phase redrawn in accordance with Squires *et al.* (2009).

Lamellar phases are characterized by the assembly of two layers of lipid molecules into a bilayer with the bilayer core harboring the hydrophobic moieties. Micelles display a spherical architecture with the hydrophobic carbohydrate chains buried in the interior. Inverse hexagonal phases consist of water-filled lipid tubes forming a hexagonal lattice. The lipid-water interface within the tubes is established by the hydrophilic lipid heads. In inverse cubic phases, lipids are organized in a cubic lattice enclosing aqueous cavities or channel. As in the case of inverse hexagonal phases, hydrophilic lipid heads face the water-filled space.

The phase spontaneously adopted by lipids is determined by various external factors including temperature, pressure, and the amount of surrounding water. Changes in these factors can result in a transition to another lipid phase. Temperatures at which such phase transitions occur are called phase transition temperatures. In addition to external conditions, the molecular geometry of lipids is a critical factor determining the lipid phase.

Phases commonly adopted by the majority of phospholipids and glycolipids are of lamellar nature. However, different lamellar phases exist each differing in the freedom of lipid movement. In general, biomembranes adopt the so-called liquid crystalline phase characterized by unhindered translational and rotational lipid movement (Goñi, 2014).

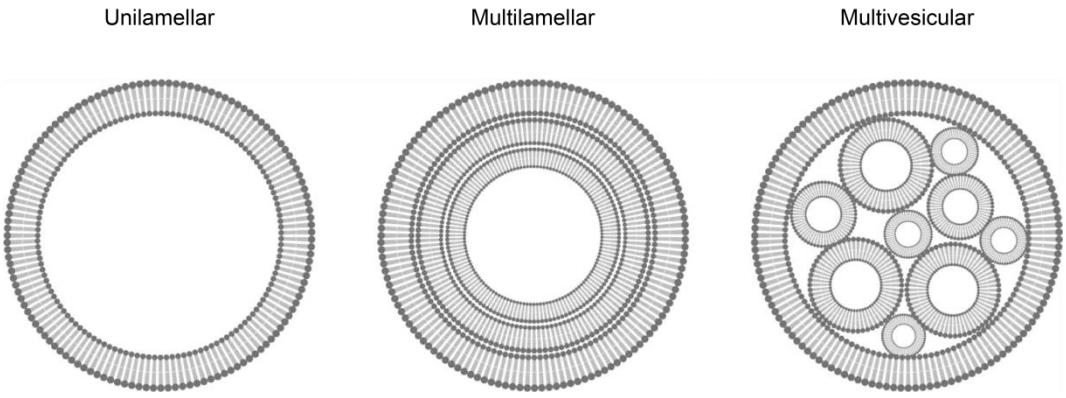

Figure 10 Vesicle formation by membrane lipids in the lamellar phase. To prevent contact of the hydrophobic bilayer core with water at bilayers edges, lipids in the lamellar phase form closed, self-healing compartments. *In vitro*, compartment formation enables the preparation of synthetic vesicles. Depending on the preparation technique applied, unilamellar, multilamellar, or multivesicular vesicles are obtained. While unilamellar vesicles consist of a single lipid bilayer, multilamellar and multivesicular vesicles are composed of several concentric or non-concentric spherical bilayers respectively. Figure taken from van Swaay and deMello (2013).

As the self-assembly of membrane lipids is predominantly driven by hydrophobic interactions, lipids in the lamellar phase, i.e. lipid bilayers, tend to form closed, self-healing compartments. Due to the absence of bilayer edges in these structures, the energetically unfavorable exposure of the hydrophobic bilayer core to the aqueous surroundings is avoided. *In vivo*, lipid self-assembly into closed structures enables the generation of sealed plasma membranes and the formation of distinct intracellular compartments (Berg *et al.*, 2012). *In vitro*, it is exploited to prepare synthetic vesicles with diameters ranging from 25 nm to 100 µm. Depending on the applied preparation technique,

vesicles can be unilamellar, i.e. be formed by a single bilayer, multilamellar, i.e. be composed of several concentric spherical bilayers, or multivesicular, i.e. contain several non-concentric spherical bilayers (Figure 10**;** van Swaay and deMello, 2013; Stano and Luisi, 2016).

1.5.4 The Fluid Mosaic Model of Biomembrane Structure

The structure and functional properties of biomembranes have been subject of intensive scientific research already beginning in the 1920s and still pursued today.

One of the early models of biomembrane architecture was proposed by Danielli and Davson (1935). According to their hypothesis, biomembranes are double layers of amphipathic lipid molecules with the polar parts of the lipids oriented towards the lipid-water interface and the hydrophobic lipid moieties embedded in the bilayer core. Additionally, the authors proposed the existence of a continuous protein film covering both faces of the membrane.

Based on the idea of a lipid bilayer forming the fundamental structure of biomembranes, Singer and Nicolson (1972) developed the fluid mosaic model, which to date is commonly utilized to explain biomembrane architecture. Unlike Danielli and Davson, Singer and Nicolson hypothesized biomembranes to be fluid bilayers composed of both lipids and integral proteins. They proposed lipids to be the major constituent of bilayers, forming a matrix in which integral proteins are either embedded or which these proteins completely span. The latter type of integral protein is termed transmembrane protein today. Similar to membrane lipids, integral membrane proteins can be glycosylated, i.e. biomembranes contain glycoproteins. In addition to the existence of integral proteins, Singer and Nicolson pointed out that peripheral membrane proteins are locally associated with the hydrophilic outer surfaces of biomembranes. In the fluid mosaic model, protein and lipid constituents of biomembranes are not expected to exhibit a lateral long-range order, i.e. a lateral order over distances of several 100 nm.

The characteristic feature of the model membrane proposed by Singer and Nicolson is the dynamic behavior of its constituents: lipid molecules and integral proteins perform unhindered 2D translational diffusion giving the membrane properties comparable to a 2D oriented viscous solution. Additionally, lipids and proteins freely rotate around axes perpendicular to the membrane plane. Importantly, the fluid mosaic model predicts that transbilayer rotations of membrane constituents do not proceed at significant rates. Thus, no substantial exchange of lipid and protein molecules between the two bilayer leaflets occurs, resulting in an asymmetry of the composition and structure of the distinct membrane leaflets.

Singer and Nicolson also speculated about a potential influence of protein-protein and protein-lipid interactions on biomembrane properties, for example due to the formation of aggregates. Further, they suggested the possibility of varying bilayer thickness at membrane areas surrounding large

integral proteins, and considered the potential existence of membrane lipid fractions not organized in a bilayer structure.

Following its publication, the fluid mosaic model has been complemented and partially modified by findings obtained through the scientific research of the past decades (Figure 11).

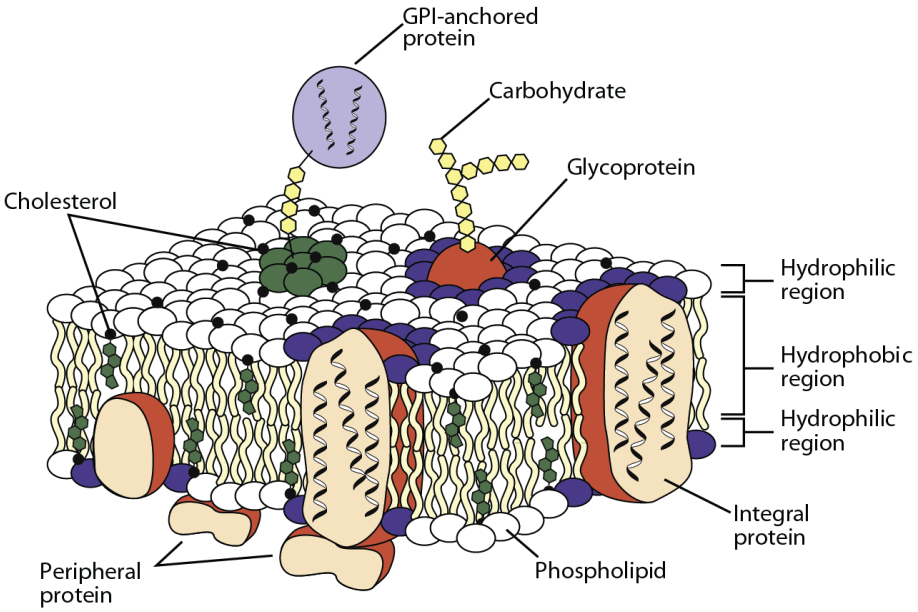

Figure 11 Adapted fluid mosaic model of the structure of eukaryotic membranes. Amphipathic membrane lipids form a bilayer in which a high density of integral proteins is embedded. Both membrane lipids and integral proteins can carry covalently linked carbohydrate chains. Peripheral membrane proteins transiently or irreversibly bind to the hydrophilic outer surfaces of the biomembrane. Due to the high spatial density of membrane proteins, protein-protein and protein-lipid interactions cause a restriction of lateral diffusion. Moreover, areas of specific chemical composition exist throughout the membrane plane. These so-called membrane domains presumably fulfill specific functions. Cholesterol is one of the constituents of biomembranes known to be involved in domain formation. In the above illustration, a glycosylphosphatidylinositol-anchored (GPI-anchored) protein, i.e. a protein covalently linked to a glycolipid, is shown to be associated with such a membrane domain. Figure taken from Dowhan *et al.* (2016).

One of the novel aspects of biomembrane architecture was the finding that in fact, integral membrane proteins are inserted into membranes at such high densities that hardly any membrane area is left unperturbed. In addition, the existence of bulky extra-bilayer membrane protein domains was discovered. As a consequence of this high spatial density of proteins, protein-protein and protein-lipid interactions cause a pronounced restriction of lateral diffusion within biomembranes (Engelman, 2005). Resulting diffusion coefficients were determined to range between 10^{-13} $m^2 \cdot s^{-1}$ and 10^{-12} $m^2 \cdot s^{-1}$ in the case of lipids, and between 10^{-15} $m^2 \cdot s^{-1}$ and 10^{-13} $m^2 \cdot s^{-1}$ for integral proteins (Edidin, 1974). Furthermore, it could be verified that the presence of large integral membrane proteins leads to variations in bilayer thickness. However, spatial and temporal fluctuations in membrane thickness occur rather frequently due to the high incidence of integral proteins (Holt and Killian, 2010; Goñi, 2014). Another finding complementing the fluid mosaic model was the discovery of transiently attached peripheral membrane proteins: depending on the prevailing physiological

conditions, certain proteins reversibly bind to biomembranes and return to the aqueous environment after detachment (Nicolson, 1976; Burn, 1988).

In addition to an impact of high membrane protein density, dynamics of biomembrane constituents are also altered in areas of different lipid phase. While the liquid crystalline phase is the phase primarily adopted by membrane lipids, further lipid phases, which exhibit different degrees of translational and rotational freedom, have been shown to be of physiological importance as well (de la Serna *et al.*, 2004; Zhang *et al.*, 2009). The combined effect of varying lipid phases, protein-protein interactions, and protein-lipid interactions gives rise to the formation of membrane domains, areas of specific chemical composition which presumably fulfill particular functions. These domains exist in a variety of sizes, with diameters supposably starting at less than 100 nm and reaching up to several µm. In contrast to the initial fluid mosaic model, the presence of such long-range order is now actually assumed to be a common feature of biomembranes (Pike, 2006; Goñi, 2014).

Apart from its importance in domain formation, the coexistence of different lipid phases within biomembranes is also thought to enable the transient generation of non-bilayer intermediate structures arising during processes like membrane fusion or fission (Chernomordik and Zimmerberg, 1995; Yang and Huang, 2003; Goñi, 2014).

Importantly, research of the past decades also elucidated geometric aspects of biomembrane architecture. Today, biomembranes are not considered plane objects but structures exhibiting dynamically modulated curvature (Goñi, 2014). The induction and sensing of bilayer curvature is an important aspect of the interaction of numerous proteins with biomembranes and will be described in greater detail in subsection 1.5.6.

Another modification of the fluid mosaic model is the fact that in biomembranes transbilayer rotations, so-called flip-flops, of lipids occur at significant rates. Occurrence of flip-flops is locally restricted and the resulting exchange of lipids between the bilayer leaflets is of transient nature. Transbilayer rotations can happen spontaneously or can be catalyzed by specific proteins (Contreras *et al.*, 2003, 2010).

1.5.5 Phospholipid Binding by Peripheral Membrane Proteins

Biomembranes are complex mixtures of manifold lipid and protein species and their constituents are involved in a wide range of intermolecular interactions (Goñi, 2014). As the present study is concerned with the binding of the motor protein myosin-XXI to phospholipid bilayers, the association of peripheral membrane proteins with membrane-embedded phospholipids will be addressed in this subsection.

Peripheral membrane proteins associate with membrane phospholipids via lipid binding domains. These domains are attracted to and bind to lipids by non-covalent forces, mainly electrostatic, van

der Waals, and hydrophobic interactions and hydrogen bonds. Frequently, membrane binding involves not a single type but a combination of these interactions. Phospholipid binding domains of peripheral membrane proteins exhibit various structures ranging from structurally defined globular domains to unstructured domains (Lemmon, 2008; Goñi, 2014).

Table 2 Globular phospholipid binding domains of peripheral membrane proteins. At present, globular phospholipid binding domains can be grouped into a minimum of 11 distinct classes. In the overview given below, general properties of the majority of domains of a specific class are summarized. Within some of these classes, variations concerning preferred ligands and ligand specificity exist. If not stated otherwise, lipid binding generally exhibits little or no target specificity or stereospecific lipid binding is limited to certain representatives of the respective domain class. Note that PX and FYVE domains primarily target PI(3)P with high stereospecificity. C1 domains, the targets of which do not belong to the class of phospholipids, are commonly considered as phospholipid binding domains as one of their targets, diacylglycerol, is only one phosphate group short of being classified as phospholipid (Lemmon, 2008). Abbreviations: ANTH: AP180 N-terminal homology; BAR: Bin-amphiphysin-Rvs; C1: protein kinase C conserved region 1; C2: protein kinase C conserved region 2; ENTH: epsin N-terminal homology; FERM: 4.1/ezrin/radixin/moesin; FYVE: Fab1/YOTB/Vac1/EEA1; PDZ: PSD-95/Dlg/ZO-1; PH: pleckstrin homology; PX: phox homology; PS: phosphatidylserine; $PI(4,5)P_2$: phosphatidylinositol 4,5-bisphosphate; PI(3)P: phosphatidylinositol 3-phosphate; $PI(3,4,5)P_3$: phosphatidylinositol 3,4,5-trisphosphate; $PI(3,4)P_2$: phosphatidylinositol 3,4-bisphosphate.

Domain	Typical Size [aa]	Structure	Preferred Lipid Target	References
ANTH	~280	α-helical solenoid	phosphoinositides	Ford *et al.* (2001), Itoh and De Camilli (2006)
BAR	~250-280	extended α-helical bundle	acidic phospholipids	Ren *et al.* (2006)
C1	~50	Zn^{2+} finger	diacylglycerol, phorbol esters	Zhang *et al.* (1995), Colón-González and Kazanietz (2006)
C2	~130	β-sandwich	PS, phosphoinositides	Sutton *et al.* (1995), Cho and Stahelin (2006)
ENTH	~140	α-helical solenoid	$PI(4,5)P_2$	Kay *et al.* (1999), Itoh *et al.* (2001)
FERM	~300	clover-shaped complex consisting of 3 α- and β-structured modules	phosphoinositides	Niggli *et al.* (1995), Pearson *et al.* (2000), Moleirinho *et al.* (2013)
FYVE	~70	Zn^{2+} finger	PI(3)P (highly stereospecific)	Kutateladze (2006)
PDZ	~90	β-sandwich capped by 2 α-helices	$PI(4,5)P_2$, $PI(3,4,5)P_3$	Gallardo *et al.* (2010)
PH	~120	β-sandwich capped by an α-helix	phosphoinositides	Lemmon and Ferguson (2000), Lemmon (2007)
PX	~110	α- and β-structured	PI(3)P (highly stereospecific)	Teasdale and Collins (2012)
Tubby	~260	β-sandwich enclosing a hydrophobic α-helix	$PI(3,4)P_2$, $PI(4,5)P_2$, $PI(3,4,5)P_3$	Boggon *et al.* (1999), Santagata *et al.* (2001)

At present, at least 11 distinct classes of globular phospholipid binding domains are known (Stahelin, 2009). An overview of these classes is given in Table 2. The interaction of globular binding domains with lipid bilayers can be mediated by both the attraction to general physical bilayer properties like surface charge, and the stereospecific recognition of particular lipid head groups. Interestingly, the contribution of these two modes of interaction to membrane association differs even between domains of the same class (Lemmon, 2008).

One example of a globular phospholipid binding domain is the phox homology (PX) domain, an approximately 110 aa long domain containing the consensus sequence R[Y/F]x_{23-30}Kx_{13-23}R (R: arginine, Y: tyrosine, F: phenylalanine, x: arbitrary aa, K: lysine). PX domains exhibit a highly conserved structure with an electropositive basic binding pocket that directly binds negatively charged phosphates of phosphoinositide head groups (Figure 12). Head group binding involves the establishment of electrostatic bonds, stacking interactions and the formation of hydrogen bonds, and is stereospecific in the majority of PX domains investigated so far. Commonly, phosphatidylinositol 3-phosphate (PI(3)P), which is primarily found in the cytosolic leaflet of early endosomes, is the preferred ligand of PX domains (Seet and Hong, 2006; Teasdale and Collins, 2012). Though, research has also revealed the existence of PX domains that do not exhibit a preference for a specific phosphoinositide binding partner, as for example the PX domain identified within the myosin-XXI converter region (Kanai *et al.*, 2001; Song *et al.*, 2001; Batters *et al.*, 2014). Interestingly, the insertion of hydrophobic amino acids into the lipid bilayer has been demonstrated to play an important role in the membrane association of certain PX domains (Stahelin *et al.*, 2003, 2007).

However, structured phospholipid binding domains do not only comprise globular domains. Amphipathic helices, which have been identified in many proteins and peptides, are α-helical motifs exhibiting two opposite faces, one concentrating hydrophobic amino acids and the other enriched in polar residues. Amino acid sequences forming amphipathic helices do not adopt a defined structure in solution. Instead, they fold into their helical conformation when inserting into a bilayer. When embedded in a bilayer, the hydrophobic face of the helix is buried inside the hydrophobic bilayer core while the polar face is located between the membrane lipid heads and at the lipid-water interface. Importantly, the folding of amphipathic helices into lipid bilayers depends on the presence of lipid packing defects and can thus only proceed in positively curved membranes (see subsection 1.5.6; Segrest *et al.*, 1990; Hristova *et al.*, 1999; Madsen *et al.*, 2010; Cui *et al.*, 2011).

Basic-hydrophobic-basic (BHB) domains are representatives of the group of unstructured lipid binding domains. These domains, which are formed by patches of hydrophobic amino acids enclosed by basic residues, are proposed to attach to membranes due to a combination of electrostatic attraction and insertion of hydrophobic moieties into the lipid bilayer (Figure 12; McLaughlin and Murray, 2005; Brzeska *et al.*, 2008).

The association of phospholipid binding domains with biomembranes can be regulated and tuned by several factors. The stereospecific recognition of phospholipids which are synthesized in a temporally or spatially restricted fashion controls the membrane binding reaction in space or time. Furthermore, the requirement for soluble second messengers like Ca^{2+} is an important regulator of bilayer binding. In addition, physical properties of biomembranes, e.g. charge or amphiphilicity, are capable of modulating attachment of phospholipid binding domains (Lemmon, 2008). In particular, membrane curvature has been demonstrated to play a crucial role in protein-bilayer association (e.g. Wetterau and Jonas, 1982; Davidson *et al.*, 1998; Bhatia *et al.*, 2009; Gerlach *et al.*, 2010) and will therefore be addressed in a separate subsection (see subsection 1.5.6).

Noteworthily, the attachment of certain peripheral membrane proteins to specific biomembranes is guaranteed by the coincidence detection of several membrane characteristics, i.e. of physical membrane properties, membrane constituents, or a combination of both. Coincidence detection can be implemented by cooperating lipid binding domains, cooperating lipid binding and protein binding domains, or even by a single lipid binding domain containing two distinct lipid binding sites (Lemmon, 2008). For example, the binding of sorting nexin 1 to endosomal membranes is regulated by the combined preference of its BAR domain for positive bilayer curvature and the recognition of PI(3)P and phosphatidylinositol 3,5-bisphosphate ($PI(3,5)P_2$) by its PX domain (Carlton *et al.*, 2004).

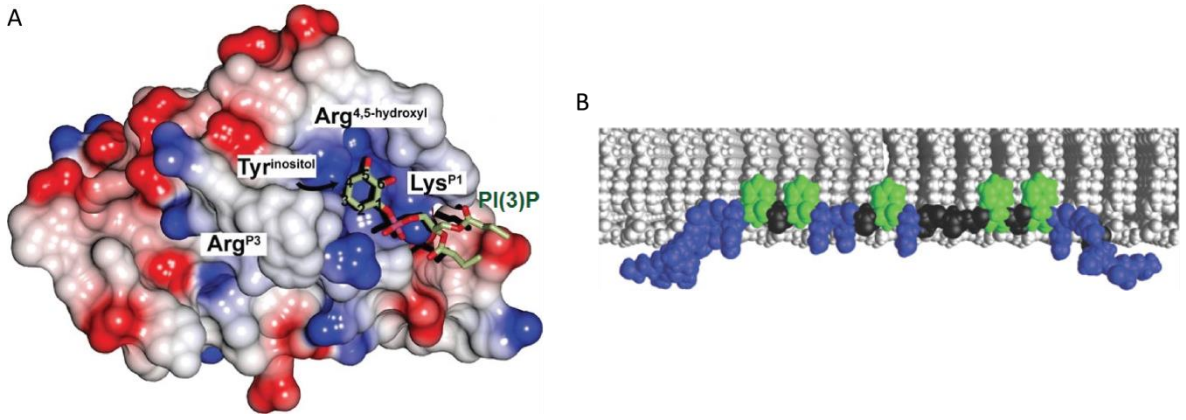

Figure 12 Membrane binding by PX and BHB domains. (A) Surface structure of the PX domain of the $p40^{phox}$ subdomain of NADPH oxidase in complex with PI(3)P. PI(3)P is located within the deep positively charged binding pocket of the PX domain. The conserved amino acids of the $R[Y/F]x_{23\text{-}30}Kx_{13\text{-}23}R$ consensus sequence and their interaction with PI(3)P are indicated: the N-terminal arginine (Arg^{P3}) electrostatically associates with the 3-phosphate group, the tyrosine ($Tyr^{inositol}$) side chain binds the inositol ring via a stacking interaction, lysine (Lys^{P1}) electrostatically interacts with the 1-phosphate, and the C-terminal arginine ($Arg^{4,5\text{-hydroxyl}}$) forms hydrogen bonds with the 4- and 5-hydroxyl groups of the inositol ring. Figure taken from Teasdale and Collins (2012). (B) Atomic model of the BHB domain of MARCKS bound to a lipid bilayer. The MARCKS BHB region consists of five hydrophobic (green) and 13 basic (blue) amino acid residues. Basic side chains mediate electrostatic interaction with the bilayer, while hydrophobic residues penetrate the bilayer core. Both in solution and when bound to membranes, the BHB domain adopts an elongated unstructured conformation. Figure taken from McLaughlin and Murray (2005).

1.5.6 Biomembrane Curvature

In eukaryotic cells, biomembranes define organelles and compartments highly variable in size ranging from vesicles of less than 100 nm in diameter to whole cells of a size of 10 µm and more. In addition, various organelles like the ER, the Golgi apparatus, or mitochondria form tubulated, folded, or disk-like structures. Furthermore, intracellular trafficking processes like endocytosis or vesicular transport between distinct organelles involve the generation of highly curved compartments (Karp, 2005; McMahon and Boucrot, 2015). Hence, membrane surfaces of diverse degrees of curvature are omnipresent within the intracellular environment.

In general, the term curvature refers to the reciprocal radius of curvature (Goñi, 2014). For vesicular lipid bilayers, the radius of curvature is identical to the vesicle radius, i.e. curvature of the bilayer surface increases with decreasing vesicle size. The terms negative and positive curvature refer to the spatial orientation of curved surfaces: convex surfaces are positively curved, while concave surfaces exhibit negative curvature (Antonny, 2011).

The local curvature of a biomembrane can be regulated by the constituents of the membrane itself and by forces exerted on the membrane by the cytoskeleton (McMahon and Boucrot, 2015).

The fundamental principle of curvature generation and stabilization by membrane constituents is the generation of a geometric asymmetry of the opposing membrane leaflets (Goñi, 2014). As the molecular geometry of lipids determines the shape of the monolayer they are incorporated in, such asymmetry can be imposed by the heterogeneous distribution of lipid species between the two leaflets of a biomembrane. Depending on the overall molecule length and the cross-sectional areas occupied by the hydrophilic and the hydrophobic moiety, membrane lipids favor the assembly into planar, negatively curved, or positively curved monolayers (Figure 13; Marsh, 1996; McMahon and Boucrot, 2015). The organization of lipids within monolayers is also referred to as lipid packing.

Apart from lipid constituents, membrane proteins can be involved in curvature generation and stabilization as well. Transmembrane proteins possessing a conical structure can simply bend the lipid bilayer they are integrated in due to their shape (Fertuck and Salpeter, 1974; Unwin, 2005; Fribourg *et al.*, 2014). In addition, the interaction of large integral proteins with membrane lipids can enforce a vertical expansion of the bilayer (Holt and Killian, 2010). Crowding and oligomerization of membrane proteins can also induce or stabilize membrane curvature, for example due to the accumulation of large extramembranous protein domains at one of the two bilayer faces (Ĉopiĉ *et al.*, 2012; McMahon and Boucrot, 2015). Further, biomembrane curvature is suggested to be regulated by protein scaffolding, i.e. the clustering of peripheral membrane proteins. In this case, peripheral proteins are thought to impose their surface shape on the membrane, however the exact mechanism underlying this process is still not clear. Another mechanism of curvature regulation by

peripheral membrane proteins is the insertion of hydrophobic motifs into the bilayer core (Campelo *et al.*, 2008; Stachowiak *et al.*, 2012; Kozlov *et al.*, 2014).

Biomembrane deformations of larger scale are mediated by the cytoskeleton. Forces required to change membrane shape are generated by the polymerization of filaments or by motor-driven translocation of membrane-associated filaments (Doherty and McMahon, 2008; Leduc *et al.*, 2010). The regulation of membrane shape by cytoskeletal components is crucial for the formation of membrane protrusions, as for example filopodia (see subsection 1.5.7).

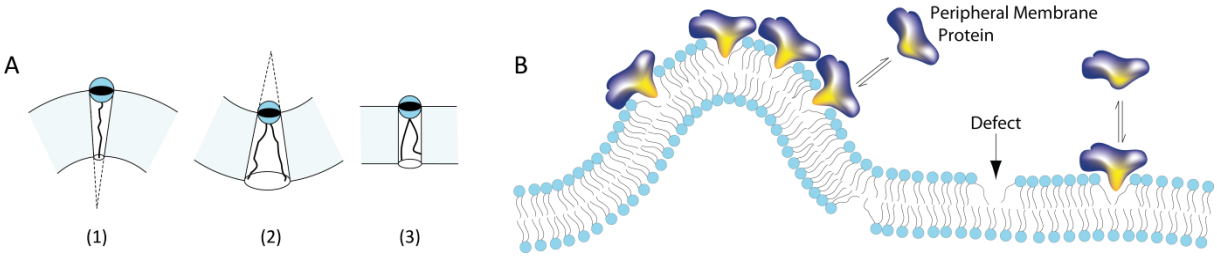

Figure 13 The curvature of biomembranes. (A) Regulation of membrane shape by lipid molecule geometry. Curvature can be imposed by an asymmetry of the distribution of lipid species between the two lipid monolayers of a membrane. According to their molecular shape, i.e. the overall molecule length and the cross-sectional areas occupied by the hydrophilic and the hydrophobic moieties, membrane lipids assemble into (1) positively curved (e.g. PI), (2) negatively curved (e.g. PE), or (3) planar monolayers (e.g. PC, PS). Figure taken from Goñi (2014). (B) Regulatory functions of membrane curvature. Bilayer shape is capable of controlling the spatial distribution (illustrated above) and the function of curvature sensitive lipid binding proteins. The upconcentration of proteins at bilayer surfaces of high positive curvature is assumed to be based on the hydrophobic insertion of protein motifs into the bilayer core. This insertion process requires the presence of lipid packing defects, the surface density of which increases with increasing membrane curvature. Figure taken from Hatzakis *et al.* (2009).

Importantly, the spatially and temporally controlled emergence of membrane curvature allows for the regulation of the localization or function of proteins which exhibit membrane curvature sensitivity (MCS). MCS can manifest in two different ways (Madsen *et al.*, 2010): firstly, lipid binding proteins can undergo structural adaptations in response to their association with curved bilayers. Thereby, bilayer curvature modulates functional properties of these proteins. This mechanism has for instance been shown to regulate the catalytic activity of certain membrane-associated enzymes like protein kinase C and *Thermomyces lanuginosa* lipase (Slater *et al.*, 1994; Cajal *et al.*, 2000). The second manifestation of MCS, which was considered in the present experimental work with myosin-XXI, is characterized by a curvature-dependent membrane association of proteins, which in turn can cause a targeted localization or redistribution of proteins within the cellular environment. In the following chapters, the term MCS will always refer to a curvature dependency of protein-bilayer binding. The N-BAR domain of endophilin A1 (eNBAR), i.e. the functional unit of N-terminal amphipathic helix and BAR domain, is one of the motifs identified as a curvature sensor of the second type. The investigation of vesicle binding by eNBAR revealed an upconcentration of this domain at the surfaces of small vesicles, i.e. at bilayers of high positive curvature (Bhatia *et al.*, 2009).

Furthermore, amphipathic helices have been demonstrated to exhibit enhanced binding to positively curved membranes (Cornell and Taneva, 2006; Drin *et al.*, 2007; Antonny, 2011).

Noteworthily, the sensing of positive bilayer curvature is proposed to be mediated by the insertion of hydrophobic motifs into the bilayer core (Figure 13). As this insertion is dependent on the presence of lipid packing defects, i.e. areas of packing mismatch where the hydrophobic bilayer interior is exposed to the aqueous environment, sensitivity for positive membrane curvature too is expected to rely on the presence of packing defects (Hatzakis *et al.*, 2009; Madsen *et al.*, 2010; Cui *et al.*, 2011).

Another interesting aspect of curvature-dependent bilayer binding is that to date several proteins have been identified as coincident sensors and inducers of membrane curvature (Wetterau and Jonas, 1982; Davidson *et al.*, 1998; Kurten *et al.*, 2001; Carlton *et al.*, 2004; Gerlach *et al.*, 2010; Varkey *et al.*, 2010). However, the existence of a functional relation between MCS and bilayer deformation is still under debate (e.g. Zimmerberg and Kozlov, 2006; Arkhipov *et al.*, 2009; Bhatia *et al.*, 2009; Madsen *et al.*, 2010).

Importantly, none of the above-mentioned manifestations of MCS has so far been found to exhibit a maximum effect within a specific range of bilayer curvature. Instead, increases in bilayer curvature always result in an enhanced efficiency of the regulation of protein function or localization (Madsen *et al.*, 2010).

1.5.7 Filopodia

In order to perform specific functions like cell motility, probing of the cell´s environment, secretion, or nutrient absorption, eukaryotic cells form plasma membrane protrusions supported by cytoskeletal filaments, e.g. actin-based microvilli and filopodia, or microtubule-based cilia and flagella (Alberts *et al.*, 2007).

In the present *in vivo* studies, fluorophore-labeled myosin-XXI was found to localize within the filopodia of transfected mammalian cells. Moreover, myosin-XXI was shown to increase the number and length of filopodia formed by transfected cells. As these findings connect myosin-XXI function with processes involved in the formation or maintenance of filopodia, a short description of the architecture of these membrane protrusions will be given here.

Filopodia are slender protrusions of the plasma membrane that are supported by tight parallel bundles of 10 to 20 actin filaments. They can grow up to several µm, occasionally several tens of µm, in length (Mattila and Lappalainen, 2008; Nambiar *et al.*, 2010). The formation of filopodia is a complex process promoted by many proteins and is still not understood completely. Simulation calculations (Peskin *et al.*, 1993; Mogilner and Oster, 1996) have shown that the force required to protrude the plasma membrane in order to form these rod-like structures is provided by the polymerization of actin at the membrane-facing barbed ends of actin filaments. As a whole, the

length of a filopodium is regulated by the balance between barbed end actin assembly and retrograde flow of actin (Mallavarapu and Mitchison, 1999). Retrograde flow is the rearward movement of F-actin toward the cell body and is assumed to be driven by myosins (Lin *et al.*, 1996; Suter and Forscher, 2000).

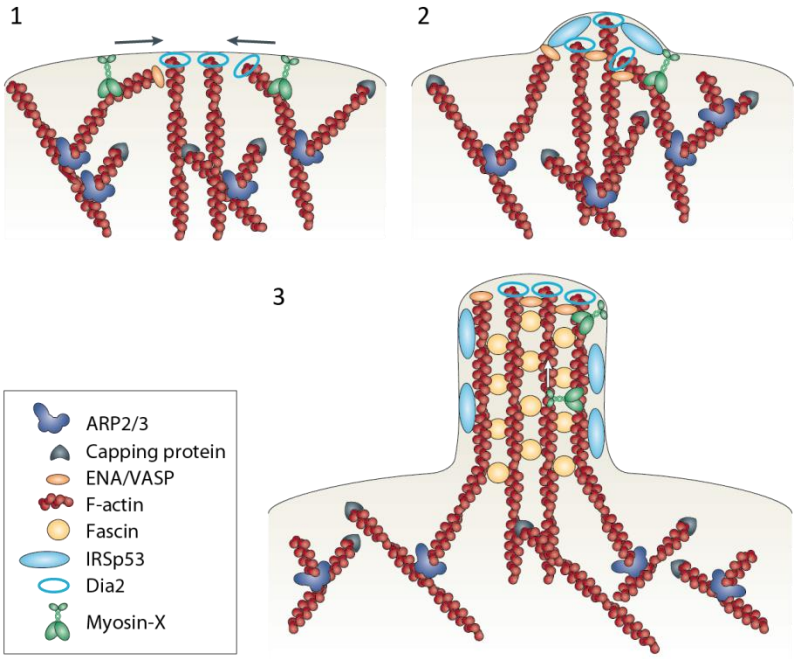

Figure 14 Model of filopodia formation. In this model, Mattila and Lappalainen (2008) propose a mechanism for the initiation and elongation of filopodia. (1) Uncapped actin filaments branching from the ARP2/3-regulated actin network or emerging from Dia2-induced nuclei are continuously elongated. Elongation is assisted by Dia2 and/or Ena/VASP family proteins. Barbed filament ends face the plasma membrane and are converged by myosin-X thereby creating an initiation site of filopodia formation. (2) As the nascent filopodium starts to protrude the plasma membrane, IRSp53 is recruited to the initiation site. Once IRSp53 has bound to the membrane, it either assists further membrane deformation or alternatively recruits additional components promoting filopodia formation. At this point in time, Ena/VASP proteins might also act as initial cross-linkers. (3) Fascin assembles actin filaments into stiff bundles. Myosin-X might now deliver adhesion molecules to the filopodia tip and/or link the actin bundle to the plasma membrane. Dia2 stays at the distal end of the filopodium. As part of a tip complex, it continues to promote actin polymerization. Figure taken from Mattila and Lappalainen (2008).

In addition to actin, several other molecular constituents have been shown to promote the initiation, elongation, and stabilization of filopodia taking action at different stages of filopodia assembly and growth: the formin Dia2 induces actin nucleation and facilitates addition of G-actin to the growing plus ends of filaments, while proteins of the Ena/VASP family prevent capping of the barbed filament ends thus preventing a polymerization halt. In addition, Ena/VASP family proteins presumably bundle nascent actin filaments (Krause *et al.*, 2003; Schirenbeck *et al.*, 2005, 2006). Other bundling proteins then cross-link elongating F-actin to bundles constituting the core of filopodia. One of these proteins is fascin, which mediates the generation of actin bundles of increased stiffness (DeRosier and Edds, 1980). Furthermore, actin-associated motor proteins are proposed to play a role in filopodia formation. Myosin-X, which has been demonstrated to localize within filopodia, is assumed to initiate filopodia by bundling F-actin at the plasma membrane, to enhance filopodia elongation by

transporting components involved in filopodia assembly, and to link integrins to the filopodial actin core (Sousa and Cheney, 2005; Tokuo *et al.*, 2007; Watanabe *et al.*, 2010). Also, it is suggested that proteins such as IRSp53, which contain lipid binding I-BAR (inverse BAR) domains, promote the formation of filopodia by protruding the plasma membrane owing to their membrane deforming capability (Scita *et al.*, 2008). In the case of IRSp53, an interaction of membrane-bound protein with other components of filopodia formation is considered as well. Adhesion molecules like integrins mediate the attachment of filopodia to the surrounding environment (Mattila and Lappalainen, 2008). A model of filopodia formation as proposed by Mattila and Lappalainen (2008) is depicted in Figure 14.

Importantly, the spatial distribution and the activity of many proteins implicated in filopodia assembly are regulated by phospholipid constituents of the plasma membrane. Phosphatidylinositol 4,5-bisphosphate ($PI(4,5)P_2$) represents one of these constituents as it controls the actin polymerization machinery (Hilpelä *et al.*, 2004).

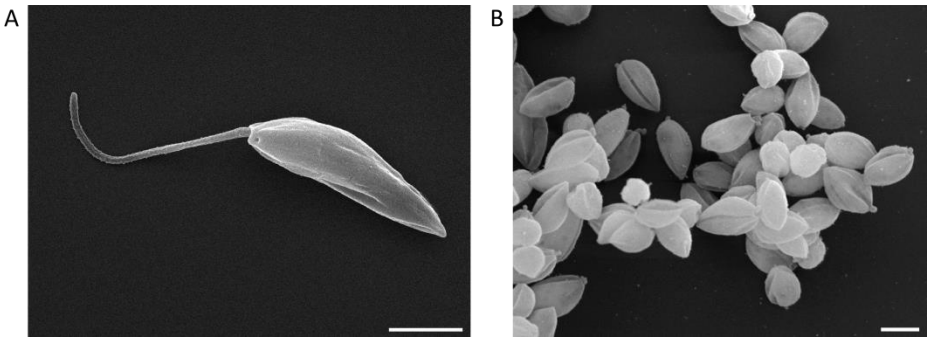

Figure 15 Forms of *Leishmania* throughout the parasitic life cycle. Scanning electron microscopy images of *Leishmania mexicana*. (A) The motile promastigote exhibits an elongated form with a fully developed flagellum. (B) Amastigotes display an ovoid form and development of a merely rudimentary flagellum inhibits motility. Scale bars: 2 µm. Images taken from The Cell Image Library (2016), Cell Image Library numbers: 10603 (A), 12403 (B).

1.6 Myosin-XXI and *Leishmania*

Myosin-XXI is a motor protein specifically expressed by eukaryotes belonging to the class of Kinetoplastea (Foth *et al.*, 2006). In the past years, this molecular motor was identified as a critical factor for the survival of *Leishmania donovani* (*L. donovani*), a parasite of clinical importance as it causes the human disease leishmaniasis (Rodrigues *et al.*, 2014). In agreement with its vital role, myosin-XXI was found to be involved in the essential biomembrane-associated cellular processes of endocytosis, exocytosis, intracellular vesicle trafficking, and flagellum formation (Katta *et al.*, 2010).

As the present study investigated the molecular bases of *L. donovani* myosin-XXI function, an introduction on the structure and the cellular role of this motor protein will be given in the following subsections. Further, cellular architecture and clinical relevance of *Leishmania* parasites will be described.

1.6.1 *Leishmania* and Their Parasitic Life Cycle

Leishmania are unicellular, uniflagellate parasites belonging to the family of Trypanosomatidae. Today, 21 species of the *Leishmania* genus are known to cause leishmaniasis, a human disease belonging to the group of neglected tropical diseases (Rodrigues *et al.*, 2014).

Leishmania undergo a digenetic life cycle involving two hosts: an insect vector, in which the parasites exist in an elongated, flagellate motile form called promastigote, and a mammalian vector, in which the parasites differentiate into their immotile amastigote form characterized by an ovoid shape and a rudimentary flagellum (Figure 15; Forestier *et al.*, 2011; Rodrigues *et al.*, 2014).

The *Leishmania* life cycle is characterized by multiple developmental stages within each host. Throughout one cycle, the parasites alternate between their two forms in order to adapt to their current habitat (Figure 16; Rodrigues *et al.*, 2014).

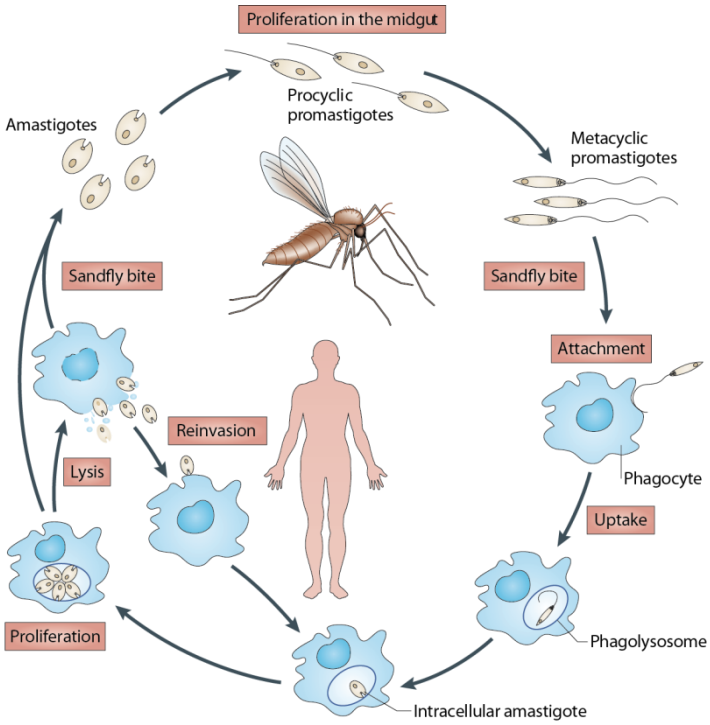

Figure 16 The life cycle of *Leishmania*. *Leishmania* amastigotes are transmitted from a mammalian host to a sandfly during its blood meal. In the sandfly midgut or hindgut, amastigotes transform into procyclic promastigotes, which reproduce and differentiate into infective metacyclic promastigotes. Upon inoculation into the following mammalian host, metacyclic promastigotes are ingested by phagocytes. Within these cells, promastigotes transform back into amastigotes and replicate. Rupture of infected cells releases *Leishmania* into the bloodstream resulting in the infection of further cells. Blood uptake by another sandfly initiates the next cycle. Figure taken from Kaye and Scott (2011).

Within the bloodstream of an infected mammalian host, *Leishmania* exist in their non-motile amastigote form. Amastigotes are ingested by a sandfly during its blood meal, and within the sandfly gut, they transform into non-infective, flagellated procyclic promastigotes, which quickly reproduce and subsequently differentiate into non-dividing, infective metacyclic promastigotes. Metacyclic promastigotes migrate to the proboscis from where they are inoculated into another mammalian

host during a subsequent blood meal. Within their new mammalian host, promastigotes attach to and are ingested by phagocytes. In phagolysosomes, *Leishmania* transform back into their amastigote form and replicate by binary fission. Once a large number of amastigotes has evolved, phagocytes rupture and release amastigotes into the bloodstream. Now, amastigotes can reinfect further host cells. Once blood of the infected mammalian host is consumed by another sandfly, life cycle of *Leishmania* is repeated (Bates, 1994; Kaye and Scott, 2011; Rodrigues *et al.*, 2014).

1.6.2 Clinical Relevance

According to the World Health Organization, about 12 million people worldwide currently suffer from leishmaniasis with an estimated number of 2 million new cases occurring per year (WHO, 2016). Furthermore, 350 million people are at risk of contracting the disease (WHO, 2010). In 2012, leishmaniasis was reported to affect patients in a total of 98 countries in five continents (Alvar *et al.*, 2012).

Leishmaniasis presents five main clinical manifestations, which are specified in Table 3.

Table 3 Main clinical manifestations of leishmaniasis. Leishmaniasis displays five main clinical manifestations causing distinct somatic symptoms, which are summarized below (WHO, 2010; Rodrigues *et al.*, 2014).

Clinical Manifestation	Symptoms
cutaneous leishmaniasis	• formation of localized ulcerating skin lesions • usually self-healing • formation of disfiguring scars
diffuse cutaneous leishmaniasis	• formation of non-ulcerative skin lesions • thickening of the eyebrows and ear lobes
mucocutaneous leishmaniasis	• formation of mucosal lesions of the mouth and the upper respiratory tract • obstruction and destruction of the nose, the pharynx, and the larynx lead to severe mutilation
visceral leishmaniasis (kala-azar)	• fever • weight loss • splenomegaly, hepatomegaly • lymphadenopathy • possible occurrence of post-kala-azar dermal leishmaniasis
post-kala-azar dermal leishmaniasis	• complication of visceral leishmaniasis, which appears up to years after apparent successful treatment • formation of lesions of skin and mucosa

1.6.3 Cytoskeleton and Molecular Motors of *Leishmania*

The cytoskeleton of *Leishmania* is mainly composed of microtubules, which generate a network spanning the cytoplasm but also form the subpellicular corset and the axoneme.

The subpellicular corset, which is essential for maintaining the shape of the parasites, is a cortical network of cross-linked microtubules. It is tied to the plasma membrane by thin filaments of 6 nm in diameter (Gull, 1999; Rodrigues *et al.*, 2014).

The axoneme is one of the basic structural elements of the flagellum, a dynamic whip-like membrane protrusion essential for motility, cellular organization, parasite attachment to the sandfly gut, and sensory perception. The flagellum originates from a structure called basal body and extends through the flagellar pocket, a large membrane invagination which is also the site of endocytosis and exocytosis. In their non-motile amastigote stage, *Leishmania* only carry a rudimentary flagellum, which contains an axoneme composed of a ring of nine canonical microtubule doublets. In the promastigote stage, the flagellum is fully developed and in addition to the nine canonical pairs of microtubules, harbors a microtubule doublet within its center (Field and Carrington, 2009; Gluenz *et al.*, 2010). Apart from the axoneme, the promastigote flagellum is composed of a second basic structure, the paraflagellar rod. The paraflagellar rod, a lattice-like array of filaments, is located alongside the axoneme with filaments of varying thickness interlinking both structures. It is composed of a large number of proteins many of which have not been identified yet, and has been shown to be crucial for parasite motility (Santrich *et al.*, 1997; Gull, 1999; Rodrigues *et al.*, 2014).

In agreement with microtubules representing the major cytoskeletal constituent, several microtubule-associated motor proteins have been identified in *Leishmania*, as for example a class XIII kinesin or two distinct dynein-2 heavy chains. Furthermore, processes like intraflagellar transport and flagellum assembly and disassembly are proposed to involve the activity of microtubule-associated molecular motors (Adhiambo *et al.*, 2005; Blaineau *et al.*, 2007; Cole and Snell, 2009).

In recent years, studies of *Leishmania* have also demonstrated the presence of actin within the parasites. In *L. donovani* promastigotes, actin was found to be distributed along the flagellum and to form granules, patches, and short filaments and bundles within the cytoplasm (Sahasrabuddhe *et al.*, 2004). Despite the fact that no evidence for the existence of a complex actin network within *Leishmania* has so far been reported, the presence of dynamic i.e. polymerizing and depolymerizing actin was shown to be essential for the formation of a functional flagellum, endocytosis, exocytosis, and intracellular vesicle transport (Tammana *et al.*, 2008; Katta *et al.*, 2010; Kumar *et al.*, 2012; Rodrigues *et al.*, 2014). Additionally, genetic analysis revealed that two myosin genes exist within the *Leishmania* genome with one gene encoding a class IB myosin and the other encoding myosin-XXI (El-Sayed *et al.*, 2005; Odronitz and Kollmar, 2007). While verification of myosin-Ib expression in

Leishmania has not been successful, myosin-XXI was demonstrated to be expressed in *Leishmania* and was shown to fulfil tasks critical for parasite survival (Katta *et al.*, 2009, 2010).

1.6.4 Myosin-XXI

Myosin-XXI is a kinetoplastid-specific motor protein, which had originally been classified as class XXI myosin but was assigned to class XIII in a later phylogenetic analysis (Foth *et al.*, 2006; Odronitz and Kollmar, 2007). As this motor protein is referred to as myosin-XXI in the literature cited in the present work, this nomenclature is retained.

Within the scope of this thesis, experimental studies of *L. donovani* myosin-XXI were performed. Accordingly, functional and structural properties of this specific motor protein will be described here.

The structure of 1050 aa long *L. donovani* myosin-XXI (Figure 17, Table C.1) comprises the typical domain sequence of myosins consisting of motor domain, neck region, and tail domain. The catalytic domain of myosin-XXI is preceded by an N-terminal SH3-like domain, the function of which still needs to be investigated (Odronitz and Kollmar, 2007; Batters *et al.*, 2014). The converter region (aa 662-747) in the C-terminal portion of the head is directly followed by an IQ motif (aa 754-769) within the neck of the motor protein. Noteworthily, several aa stretches resembling an IQ motif were identified within the myosin-XXI sequence but binding of calmodulin or calmodulin-like proteins was exclusively attributed to the region of aa 754 to 769. The neck domain was predicted to contain a coiled coil region, which is proposed to mediate dimerization.

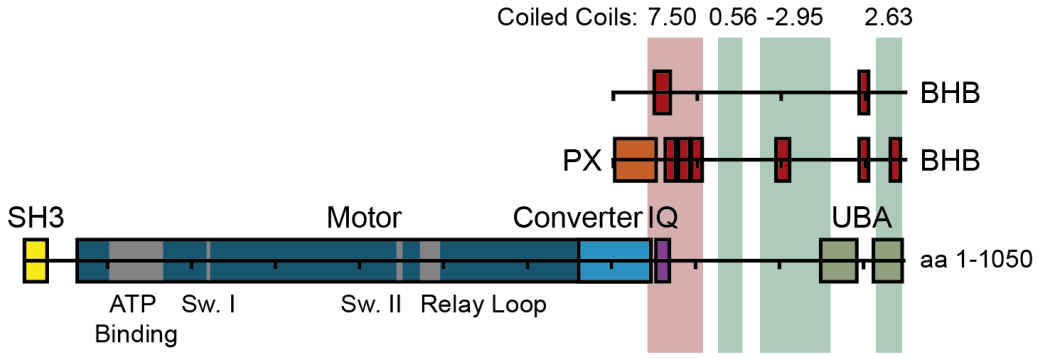

Figure 17 Structure of *L. donovani* myosin-XXI. *L. donovani* myosin-XXI consists of 1050 aa and exhibits the typical myosin structure comprising a motor, a neck, and a tail domain. At its N-terminus, the motor is preceded by an SH3-like domain. In a previous study of our lab (Batters *et al.*, 2014), the conserved structural motifs of the ATP/ADP binding pocket, switch I (Sw. I), switch II (Sw. II), and the relay loop were localized. Furthermore, the converter domain in the C-terminal part of the head was located. Within the neck domain of myosin-XXI, presence of a light chain binding IQ motif was demonstrated and existence of a coiled coil region was predicted. The latter is assumed to mediate dimer formation. Additional potential coiled coil regions were found within the tail domain. The indicated score, which can adopt values between 0 and 10, quantifies propensity of oligomerization. Positive values indicate dimerization, negative values imply trimer formation. Within the myosin-XXI converter, neck and tail, several lipid binding sites were identified. These sites comprise a PX domain and potential lipid binding motifs exhibiting a BHB sequence. BHB regions in the top row were determined by basic and hydrophobic score calculation, BHB regions in the bottom row were determined by sequence analysis. The indicated scale specifies intramolecular position in units of 100 aa.

Additional potential coiled coil regions were located within the myosin tail but have not been experimentally characterized (Batters *et al.*, 2012, 2014). In contrast to other myosins known to date, the C-terminus of the myosin-XXI tail contains two ubiquitin-associated (UBA) domains (Odronitz and Kollmar, 2007). UBA domains are typically found in proteins involved in the proteasomal degradation pathway, DNA excision repair, or protein kinase-dependent cell signaling (Hofmann and Bucher, 1996). However, the specific function of the myosin-XXI UBA domains is still to be investigated (Katta *et al.*, 2009).

As described in a previous publication of our lab (Batters *et al.*, 2014), myosin-XXI also contains binding sites for phospholipids. Basic and hydrophobic score calculations and sequence analyses revealed the existence of lipid binding domains within the tail, neck, and converter domain. These lipid binding sites comprise a converter-located PX domain and several potential lipid binding motifs displaying basic-hydrophobic-basic sequences. *In vitro* binding studies based on membrane lipid strips and co-sedimentation assays demonstrated that myosin-XXI is capable of associating with phospholipids via its PX domain and via several binding sites C-terminal of aa 730.

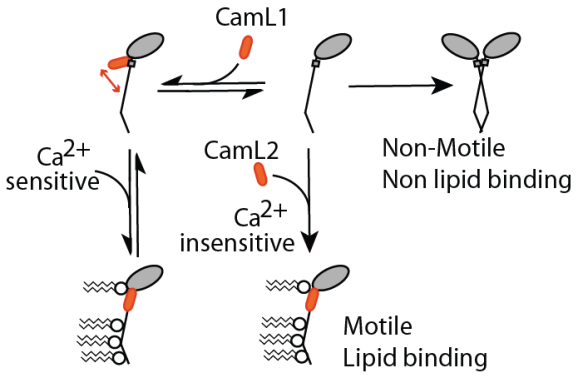

Figure 18 Model of the regulation of myosin-XXI dimerization, motility, and lipid binding. In this model, our research group proposes that the binding of calmodulin or calmodulin-like proteins to the myosin-XXI neck prevents dimerization thus keeping myosin-XXI in a monomeric, lipid binding state. Mechanical stabilization of the neck due to the association with calmodulin or calmodulin-like proteins generates a functional lever arm thus enabling myosin-XXI motility. Additionally, lipid binding sites of myosin-XXI are accessible in the motor protein´s monomeric conformation. For the calmodulin and calmodulin-like protein species investigated thus far binding to myosin-XXI requires presence of Ca^{2+}. However, association with myosin-XXI can be reversible or irreversible depending on the respective calmodulin or calmodulin-like protein. As illustrated above, *L. donovani* calmodulin-like protein 1 dissociates from the neck at low Ca^{2+} levels while in contrast, *L. donovani* calmodulin-like protein 2 stays irreversibly bound to myosin-XXI. Figure taken from Batters *et al.* (2014).

The investigation of myosin-XXI oligomerization states by our research group, which was implemented using size exclusion chromatography and Förster resonance energy transfer, led to the proposal of a model describing the regulation of myosin-XXI dimerization, motility, and lipid binding (Figure 18). According to this model, binding of calmodulin or calmodulin-like proteins to the IQ motif within the neck of myosin-XXI prohibits dimerization of the motor protein due to the impairment of coiled coil formation. In turn, the monomeric conformation of myosin-XXI ensures the accessibility of its lipid binding sites. Additionally, association of calmodulin or calmodulin-like proteins generates a

functional lever arm enabling myosin-XXI motility. Depending on the specific calmodulin or calmodulin-like protein, the interaction with the myosin-XXI IQ motif can be reversible or not. In agreement with this model, monomeric myosin-XXI was shown to induce gliding of actin filaments *in vitro* and to bind various phospholipids. Interestingly, myosin-XXI monomers were also capable to drive filament movement when bound to lipid vesicles (Batters *et al.*, 2012, 2014).

In *in vivo* studies, myosin-XXI was shown to be expressed throughout both stages of the *L. donovani* life cycle. Though, the expression level in promastigotes is approximately 20 times higher than in amastigotes. Immunofluorescence and immune-gold staining revealed that the distribution of myosin-XXI within the parasite differs for both stages: while in the amastigote, myosin-XXI is concentrated at the apical end of the cell, promastigotes exhibit a sparse myosin-XXI distribution throughout the cytoplasm and a pronounced concentration of the motor protein within the proximal part of the flagellum and along the proximal length of the paraflagellar rod (Figure 19; Katta *et al.*, 2009).

Gene knockout studies further demonstrated that in *L. donovani*, myosin-XXI and actin-based transport processes mediated by myosin-XXI play a critical role in endocytosis, exocytosis, intracellular vesicle trafficking, and development of a functional flagellum including paraflagellar rod formation. Importantly, a double knockout of both myosin-XXI gene copies could not be implemented thus demonstrating myosin-XXI to be essential for parasite survival (Katta *et al.*, 2010).

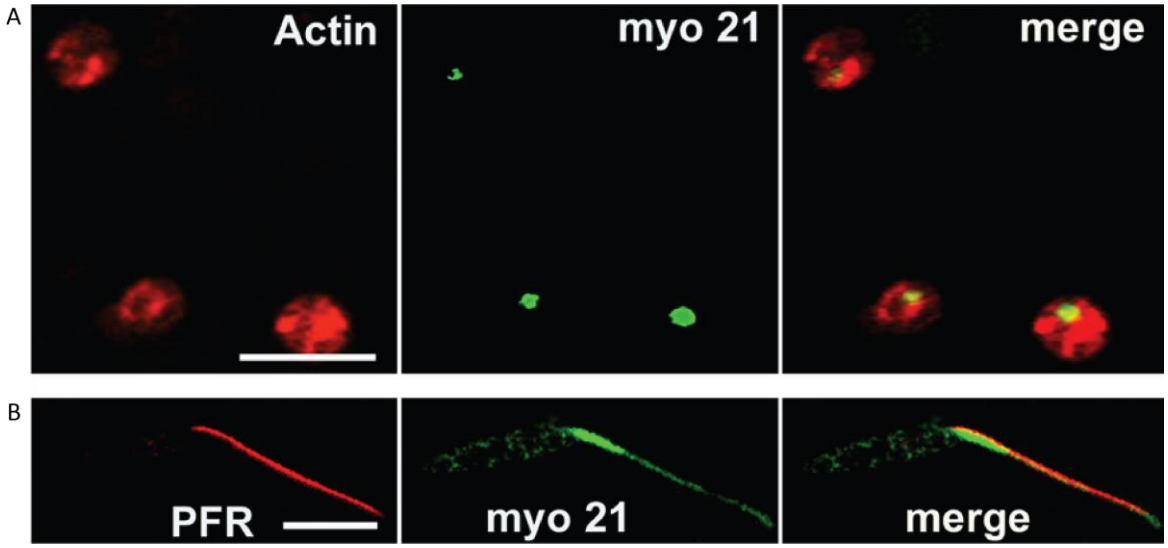

Figure 19 Cellular localization of myosin-XXI throughout the life cycle of *L. donovani* . While expression of myosin-XXI was verified in both the amastigote and the promastigote form of *L. donovani*, the observed cellular localization patterns differed between the two forms. (A) Images of *L. donovani* amastigotes immunostained for actin (red) and myosin-XXI (green). Myosin-XXI accumulates at the apical ends of the cells. (B) Images of an *L. donovani* promastigote immunostained for the paraflagellar rod (red) and myosin-XXI (green). Myosin-XXI is sparsely distributed throughout the cytoplasm and concentrates within the proximal part of the flagellum and along the proximal length of the paraflagellar rod. Scale bars: 5 µm. Images taken from Katta *et al.* (2009).

2 Research Objectives

Myosin-XXI, which had been identified in the genome of several trypanosomatids in 2005 (El-Sayed *et al.*, 2005), was initially characterized regarding its cellular localization and functions in *L. donovani* by *in vivo* studies of the Gupta research group (Katta *et al.*, 2009, 2010). These investigations revealed that myosin-XXI is absolutely essential for parasite survival and that endocytosis, exocytosis, vesicular trafficking, and flagellum formation in *L. donovani* depend on actin-based transport processes mediated by myosin-XXI.

The demonstrated vital necessity of myosin-XXI expression and the involvement of this cytoskeletal motor in such manifold cellular processes motivated the present study, which aimed to further elucidate the molecular bases of myosin-XXI´s physiological functionality. For this purpose, experimental work comprised both *in vivo* and *in vitro* approaches.

2.1 *In Vivo* Experimental Approaches

According to Katta *et al.* (2009), the distribution of myosin-XXI within *L. donovani* promastigotes is regulated by the motor protein´s tail domain. In the present study, myosin-XXI localization and functionality were aimed to be further elucidated by analyzing the cellular distribution of fluorescently labeled full-length myosin-XXI and myosin-XXI fragments, and by investigating the potential colocalization of these proteins with eukaryotic cellular structures and compartments. In order to inspect myosin-XXI constructs in a physiological environment devoid of endogenously expressed myosin-XXI, i.e. to avoid an influence of endogenous myosin-XXI on the experimental results, transfection studies in mammalian cells were carried out.

2.2 *In Vitro* Experimental Approaches

To more precisely characterize myosin-XXI in a controlled environment harboring only a limited number of interaction partners, the present study also comprised *in vitro* investigations. In order to determine the directionality of myosin-XXI translocation along filamentous actin, gliding filament assays with dual-labeled F-actin were performed. Further, as previous studies of our lab had revealed the existence of myosin-XXI lipid binding domains and had demonstrated the capability of vesicle-associated myosin-XXI to drive movement of actin filaments, the present work aimed to gain deeper insight into the dynamic behavior of the bilayer-bound complex of myosin-XXI and actin. Targeting at the elimination of spatial constraints by the limited size of vesicles, experimental set-ups were based on planar lipid bilayer systems. Since bilayer-related experiments yielded hints on an impact of bilayer shape on the binding of myosin-XXI, research objectives were complemented by the

clarification of a potential membrane curvature sensitivity of myosin-XXI. The latter aspect was tested with the help of Single Liposome Curvature assays.

3 Materials and Methods

3.1 Solutions, Gels, and Lipid Stocks

This section gives an overview about the preparation or treatment of buffers, medium, gels, and lipids utilized in the procedures and experiments described later.

Water (H_2O) used for the preparation of solutions or in experimental procedures was always double-distilled deionized water.

3.1.1 Buffers

Buffer solutions were prepared according to the following recipes:

2x SDS Gel Loading Buffer:

100 mM Tris-HCl (pH 6.8), 20 % (v/v) glycerol, 138.7 mM SDS, 0.2 % (w/v) bromphenol blue-xylene cyanol powder (Sigma-Aldrich), 200 mM β-mercaptoethanol

6x SDS Gel Loading Buffer:

375 mM Tris-HCl (pH 6.8), 50 % (v/v) glycerol, 346.8 mM SDS, 0.2 % (w/v) bromphenol blue-xylene cyanol powder (Sigma-Aldrich), 1.4 M β-mercaptoethanol

6x Gel Loading Buffer:

30 % (v/v) glycerol, 0.25 % (w/v) bromphenol blue-xylene cyanole powder (Sigma-Aldrich), 0.25 % (w/v) xylene cyanol

AB^-/2x BSA:

AB^-, 14.9 µM BSA

AB^-/BSA:

AB^-, 7.5 µM BSA

Actin Extraction Buffer (ACEX Buffer):

2 mM Tris-HCl (pH 8.0), 0.2 mM $CaCl_2$, 1 mM DTT, 0.2 mM ATP

ATP-Free Assay Buffer (AB^-):

25 mM imidazole, 25 mM KCl, 4 mM $MgCl_2$, 1 mM EGTA, pH 7.4

ATP-Supplemented Assay Buffer (AB^+):

25 mM imidazole, 25 mM KCl, 4 mM $MgCl_2$, 1 mM EGTA, 2 mM ATP, pH 8.0

Blocking Buffer:

TBS, 0.05 % (v/v) Tween 20, 5 % (w/v) skim milk powder

Blotting Buffer:

80 % (v/v) TG Buffer, 20 % (v/v) methanol

Carbonate Buffer:

480 mM $NaHCO_3$, pH 8.5

G-Actin Buffer:

2 mM Tris-HCl (pH 7.5), 0.2 mM $CaCl_2$, 0.2 mM ATP

GF 150 Buffer (Gel Filtration 150 Buffer):

50 mM Tris-HCl (pH 7.5), 150 mM NaCl

Guba-Straub Solution:

0.3 M KCl, 0.1 M KH_2PO_4, 50 mM K_2HPO_4, 1 mM ATP, 5 mM $MgCl_2$, 1 mM DTT, pH 6.5

High Salt Buffer:

40 mM Potassium Phosphate Buffer (pH 6.5), 1 M KCl, 4 mM $MgCl_2$, 2 mM DTT

His Low 500:

50 mM Tris-HCl (pH 7.5), 40 mM imidazole, 500 mM NaCl

His High 500:

50 mM Tris-HCl (pH 7.5), 400 mM imidazole, 500 mM NaCl

HNa 100:

10 mM HEPES (pH 7.0), 100 mM NaCl, 1 mM DTT, 1 mM EGTA

KMg 25:

10 mM MOPS (pH 7.0), 25 mM KCl, 1 mM DTT, 1 mM EGTA, 1 mM $MgCl_2$

KMg Activation Buffer:

KMg 25, 0.4 µM glucose oxidase, 1 mM ATP, 10 µM calmodulin, 5.6 mM glucose, 1.8 nM catalase

Lipid Buffer 150:

20 mM HEPES, 150 mM NaCl, 1 mM DTT, pH 7.4

Lipid Buffer 500:

20 mM HEPES, 500 mM NaCl, 1 mM DTT, pH 7.4

Lipid TBS:

10 mM Tris, 150 mM NaCl, pH 7.4

Low Salt Buffer:

20 mM Potassium Phosphate Buffer (pH 6.5), 40 mM KCl, 2 mM $MgCl_2$, 2 mM DTT

Lysis Buffer:

PBS, 50 % (v/v) 2x SDS Gel Loading Buffer

Motility Buffer:

AB^+, 7.2 µM BSA, 0.3 µM glucose oxidase, 38.1 nM catalase, 7.9 mM glucose, 9.5 mM DTT

Myosin-VI Buffer:

20 mM Tris-HCl (pH 7.5), 20 mM imidazole, 25 mM NaCl, 5mM $MgCl_2$, 1 mM EGTA, 10 mM DTT

Myosin Extraction Buffer:

90 mM KH_2PO_4, 60 mM K_2HPO_4, 300 mM KCl, pH 6.8

Myosin Preparation Solution:

50 mM Potassium Phosphate Buffer (pH 7.0), 5 mM DTT, 5 mM EDTA, 3 M KCl, pH 7.0

PBS/BSA:

PBS, 0.3 mM BSA

Phosphate-Buffered Saline (PBS):

2.7 mM KCl, 1.5 mM KH_2PO_4, 137.9 mM NaCl, 8.1 mM Na_2HPO_4

Potassium Phosphate Buffer:

mixture of 1 M KH_2PO_4 and 1 M K_2HPO_4 in a volume ratio depending on the desired pH

Rigor Buffer:

AB^-, 7.2 µM BSA, 0.3 µM glucose oxidase, 38.1 nM catalase, 7.9 mM glucose, 9.5 mM DTT

STORM Buffer:

Lipid TBS, 1.2 µM glucose oxidase, 160 nM catalase, 33.3 mM glucose, 80 mM DTT

Tris-Buffered Saline (TBS):

50 mM Tris, 150 mM NaCl, pH 7.6

Tris/Borate/EDTA Buffer (TBE Buffer):

1 mM EDTA (pH 8.0), 44.6 mM Tris, 44.5 mM boric acid, pH 8.3

Tris Glycine Buffer (TG Buffer):

1.3 M glycine, 125 mM Tris, 17.3 mM SDS, pH 8.3

Tris-HCl:

1 M Tris, HCl; amount of HCl depends on the desired pH

Wash Buffer:

TBS, 0.05 vol% Tween 20, 1 % (w/v) skim milk powder

3.1.2 Gels and Staining Solutions for Gel Electrophoresis

In order to separate DNA or proteins according to their molecular weight in gel electrophoresis, polyacrylamide gels for protein separation and agarose gels for DNA separation were prepared. Additionally, staining solutions for the visualization of protein or DNA bands were produced:

agarose gel:

TBE Buffer, 0.8 % to 1.2 % (w/v) agarose, $4 \cdot 10^{-3}$ % (v/v) Gel Red™ dye (Biotium)

Blue Stain Solution:

Destain Solution, 1.2 mM Coomassie Brilliant Blue G-250

Destain Solution:

45 % (v/v) methanol, 10 % (v/v) acetic acid

resolving gel:

375.9 mM Tris-HCl (pH 8.8), 1.0/1.3/2.0 M acrylamide, 24.4/32.5/48.8 mM bis-acrylamide, 3.5 mM SDS, 1.4 mM APS, 0.04 % (v/v) TEMED; acrylamide:bis-acrylamide molar ratio remains constant

stacking gel:

125.5 mM Tris-HCl (pH 6.8), 0.7 M acrylamide, 16.6 mM bis-acrylamide, 3.5 mM SDS, 4.4 mM APS, 0.1 % (v/v) TEMED

SYBR Green Staining Solution:

TBE, 1 % (v/v) 10,000X SYBR® Green I Nucleic Acid Gel Stain (Thermo Fisher Scientific)

3.1.3 Medium and Agar Plates

For *Escherichia coli* (*E. coli*) cell culture, medium and agar plates were prepared the following way:

2x YT Medium:

1.6 % (w/v) tryptone, 1.0 % (w/v) yeast extract, 85.6 mM NaCl, pH 7.5

Agar:

2x YT Medium, 1.5 % (w/v) bacterial agar

3.1.4 Other Solutions

In addition to the above-mentioned mixtures, the following solutions were utilized in sample preparation:

Mowiol Embedding Solution:

89.7 mM Tris-HCl (pH 8.5), 17.8 % (v/v) glycerol, 2.9 mM Mowiol® 4-88 (Sigma-Aldrich)

Oxidizing Solution:

0.5 mM $KMnO_4$, 16.6 mM $NaIO_4$, 1.8 mM K_2CO_3

3.1.5 Stock Solutions of Lipids and Lipophilic Fluorescent Dye

In experiments with lipid vesicles and planar lipid bilayers, the following lipids and carbocyanine dye were used:

phosphocholines (Sigma-Aldrich):

- 1-palmitoyl-2-oleoyl-*sn*-glycero-3-phosphocholine (POPC)

- 1,2-dioleoyl-*sn*-glycero-3-phosphocholine (DOPC)

phosphoinositides (Avanti Polar Lipids):

- L-α-phosphatidylinositol-4-phosphate (from porcine brain) (PI(4)P)
- 1,2-dihexanoyl-*sn*-glycero-3-phospho-(1'-myo-inositol-3',5'-bisphosphate) (denoted as PI(3,5)P_2)
- L-α-phosphatidylinositol-4,5-bisphosphate (denoted as PI(4,5)P_2)

conjugated phospholipids (Thermo Fisher Scientific):

- N-(biotinoyl)-1,2-dihexadecanoyl-sn-glycero-3-phosphoethanolamine (Biotin DHPE)
- Lissamine™ Rhodamine B 1,2-dihexadecanoyl-sn-glycero-3-phosphoethanolamine (Rhodamine DHPE)

other lipids:

- bovine brain extract (type I, Folch fraction I; Sigma-Aldrich)
- cholesterol (Sigma-Aldrich)

carbocyanine dye (Thermo Fisher Scientific):

- 3,3'-dihexadecyloxacarbocyanine perchlorate (DiO)

All lipids were obtained as dried powders, and stock solutions were prepared by dissolving these powders in chloroform in a concentration range between 40 µg/ml and 10 mg/ml. Stock solutions were stored at -20°C until use.

DiO dried powder was dissolved in dimethylformamide following manufacturer´s guidelines. Carbocyanine dye stock solution contained 40 µg/ml DiO and was stored at 4°C protected from light.

3.2 Cloning

To produce recombinant DNA constructs used in protein expression and mammalian cell transfections, respective DNA templates were amplified and cloned into vectors suitable for the intended use. Subsequently, the resulting recombinant constructs were further amplified and purified.

3.2.1 Amplification of DNA

Polymerase Chain Reaction (PCR)

Prior to cloning, DNA templates were amplified by polymerase chain reaction. PCR was executed as follows: DNA was mixed with primers (Sigma-Aldrich; Table A.3), deoxynucleotides (Thermo Fisher Scientific) and Phusion Hot Start II DNA Polymerase (Thermo Fisher Scientific) as recommended by suppliers, and the mixture was immediately subjected to heating and cooling according to the following touchdown PCR protocol:

1. T=98°C, Δt=45 s
2. 9 cycles (with a temperature decline of 1°C in step 2.2 after each cycle) of:
   2.1 T=98°C, Δt=15 s
   2.2 T=68°C, Δt=30s
   2.3 T=72°C, Δt=150 s
3. 29 cycles of:
   3.1 T=98°C, Δt=15 s
   3.2 T=60°C, Δt=30 s
   3.3 T=72°C, Δt=150 s
4. T=72°C, Δt=120 s

T denotes the temperature of each incubation step, Δt its duration. Once PCR was finished, agarose gel electrophoresis was performed as described in the next subsection. Subsequently, amplified DNA was purified and stored at -20°C until further processing. Purification was executed using the PureLink® Quick Gel Extraction and PCR Purification Combo Kit (Thermo Fisher Scientific) according to manufacturer´s protocol.

Agarose Gel Electrophoresis

To verify the presence of DNA molecules of the correct number of base pairs, samples were subjected to agarose gel electrophoresis. DNA samples were mixed with 6x Gel Loading Buffer in a 5:1 volume ratio, and samples and a molecular weight size marker were injected into the gel. Electrophoresis was executed in TBE Buffer at an electric current of 80 mA, and agarose gels were imaged in a ChemiDoc™ XRS+ gel imaging system (Bio-Rad).

3.2.2 Cloning and Isolation of Recombinant DNA

After a DNA template was amplified in polymerase chain reaction, it was inserted into a vector suitable for the intended use of the resulting recombinant plasmid. Following this, the plasmid was amplified in competent *E. coli,* and amplified plasmids were isolated by minipreparation or by maxipreparation. DNA constructs utilized in the transfection of mammalian cells or in the bacterial expression of proteins were readily processed at this point (Figure 20). In the case of DNA intended to be used for protein expression by insect cells, further treatment was necessary: The DNA template encoding the protein was transposed from the plasmid into a baculovirus shuttle vector (bacmid), which was in turn used to create a baculovirus required for the infection of insect cells (Figure 20).

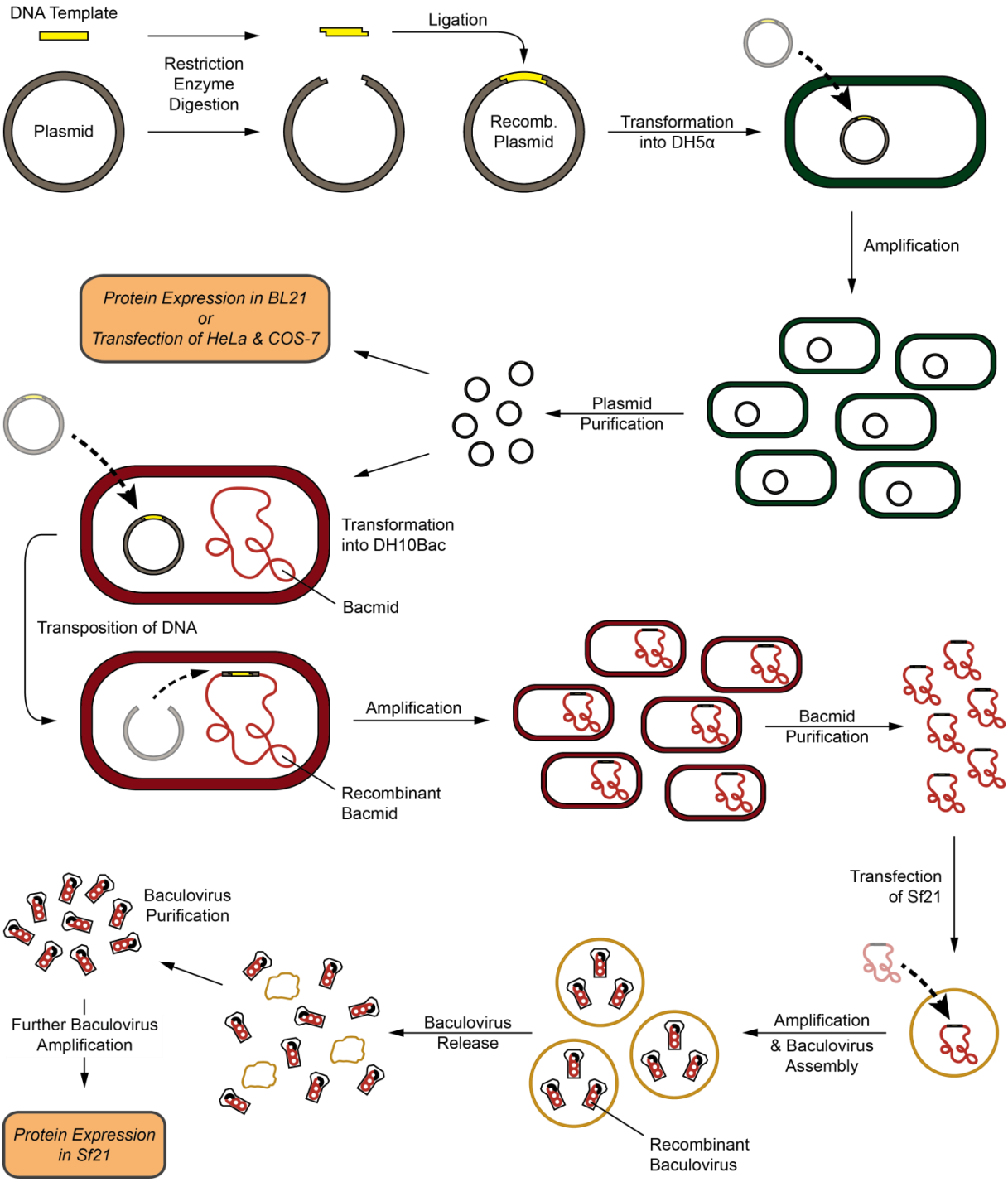

Figure 20 Cloning and isolation of recombinant plasmids for use in protein expression and mammalian cell transfections. In the above scheme, the principle steps performed during the creation, amplification, and isolation of recombinant DNA constructs are illustrated: once, the DNA template encoding the respective protein had been amplified by PCR, restriction enzyme digestion prepared both the template and the selected plasmid vector for subsequent ligation. In order to amplify the resulting recombinant plasmid, the latter was transformed into competent DH5α *E. coli* cells. Following multiplication of competent cells, the amplified plasmid was purified. At this point, cloning of recombinant constructs intended to be utilized in transfections of mammalian cells was completed. Further, proteins of a molecular weight below 100 kDa could now be expressed upon transformation of the purified plasmid into competent BL21 *E. coli*. Plasmids encoding proteins with a molecular weight exceeding 100 kDa had to be further processed. Respective recombinant constructs were transformed into DH10Bac™ Competent *E. coli*. Within these cells, the DNA template was transposed into a baculovirus shuttle vector, the so-called bacmid. After multiplication of *E. coli*, the bacmid was isolated and transfected into Sf21 cells, in which the bacmid was amplified and packaged in a baculovirus. Perishing Sf21 cells released the baculovirus into the surrounding medium, from where the virus was purified. Subsequent to two baculovirus amplification steps in Sf21, the baculovirus was ready to be used to induce protein expression in Sf21 cells.

Cloning and Isolation of Recombinant Plasmids

To prepare the insertion of a DNA template into a vector, both DNA constructs were subjected to restriction enzyme digestion applying identical enzymes. Restriction enzymes and associated reaction buffers were purchased from New England Biolabs and applied according to manufacturer´s guidelines. A summary of all restriction enzymes, DNA templates and vectors can be found in Table A.1 and Table A.2.

Following restriction enzyme digestion, digested DNA was isolated from remaining undigested DNA. For this purpose, DNA samples were mixed with SYBR Green Staining Solution and 6x Gel Loading Buffer in a volume ratio of 10:1:2 and subjected to agarose gel electrophoresis. DNA bands were visualized in a gel imaging system, and digested DNA was excised from the gel to be purified using the PureLink® Quick Gel Extraction and PCR Purification Combo Kit (Thermo Fisher Scientific).

In the next step, digested vectors and DNA templates were ligated by application of the Rapid DNA Ligation Kit (Thermo Fisher Scientific). Implementing manufacturer´s instructions, ligated DNA, i.e. recombinant plasmids, was then transformed into competent DH5α *E. coli* cells (Library Efficiency® DH5α™ Competent Cells; Thermo Fisher Scientific). After transformation, cells were plated on agar plates supplemented with 50 µg/ml antibiotic (kanamycin or ampicillin), and incubated at 37°C for at least 15 h. To amplify recombinant plasmids transformed into DH5α, colonies were picked from the incubated agar plates and each colony was transferred into 5 ml 2x YT Medium supplemented with 50 µg/ml antibiotic. Cultures were incubated in a dry block incubator at 200 rpm and 37°C overnight.

Recombinant DNA was purified from cell cultures using the PureLink® Quick Plasmid Miniprep Kit (Thermo Fisher Scientific). To verify the correct composition of the recombinant plasmid, purified plasmids were tested by another restriction enzyme digestion. Molecular sizes of the digestion products were determined in agarose gel electrophoresis. In addition, plasmids were sent to GATC Biotech for sequencing.

Depending on the amounts of recombinant DNA required in later procedures, plasmids could be further amplified. For this purpose, transformation into DH5α and subsequent amplification were repeated setting up bacterial cultures of larger volume. Recombinant DNA was isolated with the help of a PureLink® HiPure Plasmid Filter Maxiprep Kit and a PureLink™ HiPure Precipitator Module (Thermo Fisher Scientific) according to manufacturer´s guidelines.

DNA content of purified samples was determined by absorbance measurements at a wavelength of 260 nm in a Biophotometer® plus (Eppendorf).

Cloning and Isolation of Recombinant Baculoviruses

As expression in *E. coli* is not suitable for proteins of a molecular weight exceeding 100 kDa (Bell, 2001), expression in insect cells was chosen for large proteins. Accordingly, *L. donovani* full-length myosin-XXI (aa 1-1050, called FL-XXI here), the myosin-XXI motor truncation of aa 1-800 (Trunc-XXI), and chicken (*Gallus gallus*) myosin-VI were expressed with this method. As all myosin constructs were coexpressed with *Xenopus laevis* calmodulin, procedures described in the following subsections were also applied to calmodulin DNA.

To prepare DNA for the infection of insect cells, the Bac-to-Bac® Expression System (Thermo Fisher Scientific) was utilized. At first, the DNA template was cloned into the pFastBac™HT B plasmid following the procedures described earlier.

In the following step, the DNA template was transposed from the pFastBac™HT B plasmid into a baculovirus shuttle vector (bacmid). For this purpose, the recombinant plasmid was transformed into DH10Bac™ Competent *E. coli* (Thermo Fisher Scientific). This *E. coli* strain harbors the bMON14271 bacmid and expresses a transposase which transfers DNA from pFastBac™HT B into this bacmid. Transformation of the plasmid into DH10 Bac™ cells and subsequent bacmid purification were implemented following the protocol provided by the manufacturer. Purified bacmid was stored at -20°C.

Subsequently, recombinant bacmid was transfected into Sf21 cells (*Spodoptera frugiperda* ovary cells) using Cellfectin® II Reagent (Thermo Fisher Scientific) according to manufacturer´s instructions.

Regulated by the polyhedrin promoter and the simian virus 40 polyadenylation signal contained in the bacmid, Sf21 cells replicated bacmid DNA and expressed proteins required for the self-assembly of baculoviruses. Once characteristics of a late baculoviral infection phase could be observed, i.e. once sufficient amounts of baculovirus had been released into the medium, cells were sedimented by 15 min of centrifugation at 1,000 x g and 4°C. The supernatant, which contained the so-called passage 1 baculovirus, was transferred into a clean tube and stored at 4°C protected from light.

To increase the amount and titer of baculovirus, infection of Sf21 cells with passage 1 baculovirus was performed, again implementing manufacturer´s instructions. Sf21 cells in suspension culture were infected by simply adding baculovirus and incubated in a shaking incubator at 27°C and 140 rpm. Viability of Sf21 cells was examined with the help of a TC10™ Automated Cell Counter (Bio-Rad), and as soon as viability decreased to a value between 50 % and 60 %, cells were centrifuged at 1,000 x g and 4°C for 15 min. The supernatant, which contained the passage 2 baculovirus, was transferred into a clean tube and stored at 4 °C protected from light. Using passage 2 baculovirus, the amplification procedure described above was repeated resulting in a

passage 3 baculovirus stock, which was used for the infection of Sf21 cells for the purpose of protein expression.

3.3 Protein Expression and Purification

Depending on the molecular weight, different expression systems were applied to produce the proteins utilized in later experiments. In accordance with the literature (Bell, 2001), expression in *E. coli* was only applied for proteins with a molecular weight below 100 kDa, i.e. for the rat endophilin A1 N-BAR domain (aa 1-247) and all myosin-XXI fragments except for Trunc-XXI. FL-XXI (unlabeled or fused to eGFP (enhanced green fluorescent protein)), Trunc-XXI (unlabeled or fused to eGFP), and myosin-VI were coexpressed with calmodulin in Sf21 cells.

Independent from the expression system, all proteins except for calmodulin were expressed with a polyhistidine tag encoded by the vectors utilized. Accordingly, all proteins were purified by immobilized metal affinity chromatography. Expressed calmodulin was bound to myosin and thus did not need to be purified.

Actin and heavy meromyosin were not expressed in cell culture but purified from rabbit skeletal muscle tissue.

3.3.1 Protein Expression

E. coli Expression System

For bacterial expression of proteins, competent BL21 *E. coli* cells (One Shot® BL21 Star™ (DE3) Chemically Competent *E. coli*, Thermo Fisher Scientific) were used. According to manufacturer´s recommendations, DNA was transformed into BL21 cells and shake cultures in 2x YT Medium supplemented with 50 µg/ml antibiotic were prepared. After protein expression was induced by the addition of 1 mM IPTG, cultures were further incubated in a shaking incubator at 180 rpm and a temperature of 27°C for at least 4 more h. Finally, cells were sedimented at 2,000 x g and 4°C for 20 min. Resulting pellets were resuspended in 10 ml Buffer B per 500 ml culture. Buffer B was supplemented with one cOmplete™ EDTA-free protease inhibitor cocktail tablet (Roche) per 40 ml buffer. Resuspended pellets were stored at -80°C until protein purification.

Insect Cell Expression System

To express FL-XXI, Trunc-XXI, or myosin-VI in Sf21 cells, a 500 ml suspension culture of $0.8 \cdot 10^6$ ml^{-1} Sf21 cells was prepared. Cells were kept in Supplemented Grace´s Insect Medium (Thermo Fisher Scientific) enriched with 10 % (v/v) heat inactivated fetal bovine serum, 0.1 % (v/v) Pluronic® F-68, and 0.01 % (w/v) Normocin™. Since calmodulin is an important regulator of myosin motor function

(Cheung, 1980), the above-mentioned constructs were always coexpressed with calmodulin. For this purpose, 40 ml of myosin passage 3 baculovirus stock and 20 ml of calmodulin passage 3 baculovirus stock were added to the suspension culture and cells were incubated in a shaking incubator at 27°C and 140 rpm. After the first 72 h of incubation, cell viability was determined every 24 h using an automated cell counter. When cell viability was 50 % to 60 %, cells were centrifuged at 8,000 x g and 4°C for 20 min. After disposal of the supernatant, the pellet was resuspended in 40 ml Myosin Extraction Buffer. One cOmplete™ EDTA-free protease inhibitor cocktail tablet (Roche) was dissolved in the resuspension, and the solution was stored at -80°C until purification of the expressed protein.

3.3.2 Protein Purification

Purification of Proteins Expressed in Cell Culture

As all proteins expressed in BL21 or Sf21 cell culture contained a polyhistidine tag, these proteins were purified by immobilized metal affinity chromatography using a 5 ml Sepharose column functionalized with bivalent nickel ions (HisTrap FF, GE Healthcare).

Prior to purification, frozen pellets resultant from protein expression were thawed in a water bath at room temperature (RT). In the case of myosin-VI, thawed solution was additionally supplemented with 1 mM DTT, 1 mM ATP, 5 mM $MgCl_2$, and 1 mM calmodulin. Subsequently, samples were tip-sonicated (duration: 195 s, cycle: 50 %, power: 45 %; Bandelin Sonopuls HD 2070 ultrasonic homogenizer) while kept on ice. Myosin-VI samples were then left to incubate at 4°C for 30 min to 60 min, all other samples were further processed immediately. In the next step, samples were centrifuged at 33,000 x g and 4°C for 20 min, and resulting supernatants were filtered through a syringe filter of 450 nm pore diameter (Sarstedt).

Now, immobilized metal affinity chromatography was carried out a temperature of 4°C (Figure 21). All buffers utilized were supplemented with 1 mM DTT directly before use. After the Sepharose column was equilibrated in His Low 500 or PBS, the sample was loaded onto the column. Unbound constituents were removed by washing the column with His Low 500 or PBS respectively. Afterwards, the column was subjected to several washing steps with increasing volume fractions of His High 500 to elute bound protein by applying an increased imidazole concentration. During the elution process, fractions were collected which were then analyzed by sodium dodecyl sulfate-polyacrylamide gel electrophoresis (SDS-PAGE). Fractions exhibiting high content of desired protein and low contamination by other proteins were pooled and concentrated at 4°C and 7,000 x g using centrifugal filters of 30 kDa molecular weight cut-off (Amicon® Ultra Centrifugal Filters, Merck Millipore). ENBAR samples were not treated further at this point.

FL-XXI and its fragments were further purified by size exclusion chromatography with an agarose/dextran column (Superdex 200 10/300 GL, GE Healthcare). Size exclusion chromatography

was executed at 4°C and again the applied buffer was supplemented with 1mM DTT immediately before use. After the column was equilibrated in GF 150 Buffer, the sample was loaded onto the column and run through the matrix in a constant flow of GF 150 Buffer. Fractions were collected and subjected to SDS-PAGE. Fractions containing the least concentration of contaminant protein were pooled and concentrated as described above.

Following purification, proteins were flash-frozen in liquid nitrogen and stored at -80°C.

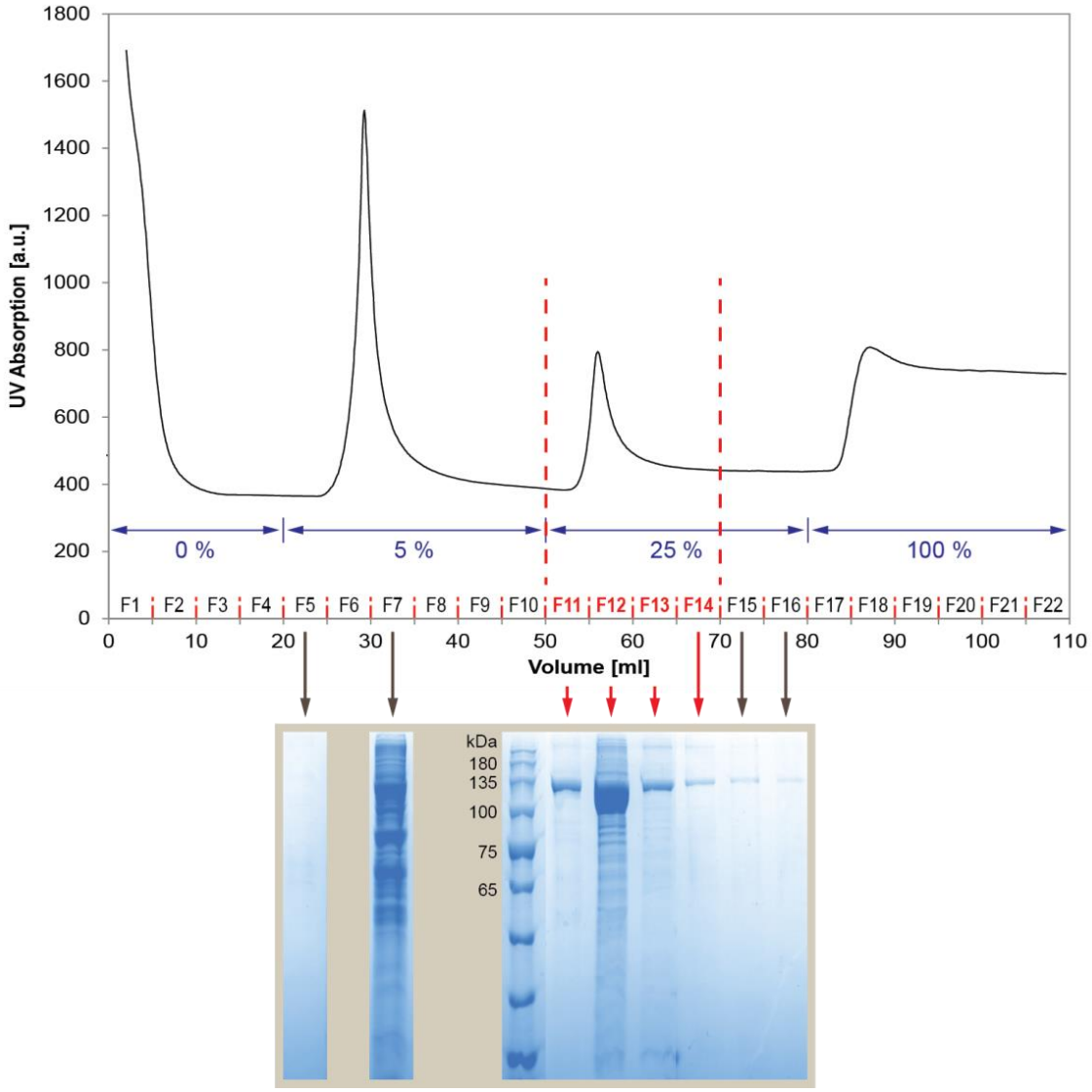

Figure 21 Protein purification by immobilized metal affinity chromatography. In the above figure, data obtained during the purification of a polyhistidine-tagged fusion protein of eGFP and full-length myosin-XXI (molecular weight: ~140 kDa) are depicted. The diagram displays UV absorbance of fractions collected during the purification process. Along the horizontal axis, buffer volume is quantified. Fractions collected are indicated as "F". The extent of UV absorption is a direct measure for the protein content of these fractions, however not for their purity. Before absorbance measurements were carried out, the sample intended for purification was loaded onto the Sepharose column. Subsequently, unbound constituents were removed from the column by washing with PBS. During the latter step (labeled as 0 %), UV detection was started. Following removal of unbound components, polyhistidine-tagged column-associated protein was eluted in several washing steps with increasing volume fractions of His High 500 (5 %, 25 %, and 100 %), i.e. with increasing imidazole concentrations. Collected fractions were then subjected to SDS-PAGE. In the lower panel, images of respective polyacrylamide gels are shown. Arrows assign fractions to corresponding lanes. Here, fractions 11 to 14 were pooled and further processed.

Purification of Proteins from Rabbit Skeletal Muscle

As purification techniques for the extraction of G-actin and HMM from rabbit skeletal muscle are well-established, these proteins were not expressed in cell culture. Instead, myosin-II glycerol stocks and acetone powder were prepared from muscle tissue and could be stored at -20°C for several months (Margossian and Lowey, 1982; Pardee and Spudich, 1982). Later, HMM could be prepared from myosin-II glycerol stock, and G-actin could be purified from acetone powder (Figure 22).

1. Purification of Myosin-II and Preparation of HMM:

Myosin-II was extracted from rabbit skeletal muscle as described by Margossian and Lowey (1982) with modifications. Prior to purification, all required buffers were freshly prepared and prechilled at 4°C. DTT and ATP contained in the buffers were added immediately before use. In short, dorsal lateral and hind leg muscles were excised from a rabbit, minced and stirred in Guba-Straub Solution to dissolve myosin-II. The mixture was centrifuged at 4,000 x g for 30 min, resulting in the separation of myosin-II, which was contained in the supernatant, and actin, which remained in the precipitate. Actin extraction from the precipitate will be described in the next subsection.

Myosin-II contained in the supernatant was further purified by filtration through minced moistened filter paper and extraction in prechilled H_2O. The resulting precipitate was dissolved in 20 ml of 3 M KCl per 100 ml of precipitate. After a 10 min centrifugation at 4,000 x g, the resulting supernatant was again subjected to an extraction in prechilled H_2O. Sedimented myosin-II was dissolved in Myosin Preparation Solution. A myosin-II glycerol stock was prepared by the addition of 50 % (v/v) of prechilled glycerol.

To prepare HMM from the myosin-II glycerol stock, chymotryptic digestion was applied. At first, myosin-II was extracted in ice-cold H_2O and the resulting precipitate was resuspended in High Salt Buffer. Subsequently, digestion was carried out applying 2 µM α–chymotrypsin. Digestion was stopped with the help of 1.3 mM trypsin-chymotrypsin inhibitor. To isolate HMM from undigested myosin-II and light meromyosin, the solution was dialyzed in Low Salt Buffer at 4°C overnight using a membrane with a 3.5 kDa molecular weight cut-off. The dialyzed sample was then subjected to a 45 min centrifugation at 21,000 x g and 4°C. The supernatant was supplemented with 30 % (w/v) sucrose, flash-frozen in liquid nitrogen, and stored at -80°C.

2. Purification of G-Actin:

G-actin was isolated from pretreated minced rabbit skeletal muscle obtained during the purification of myosin-II. The protocol for G-actin purification was adapted from Pardee and Spudich (1982). Buffers and solutions were freshly prepared and prechilled at 4°C prior to use. Precipitated muscle

mince was subjected to several extraction steps in 47.6 mM $NaHCO_3$, 1 mM EDTA (pH 7.0), H_2O, and acetone. By overnight drying in vacuo, the resulting residue was transformed into acetone powder.

Before actin was extracted from acetone powder, ACEX Buffer was freshly prepared and prechilled on ice. Thereafter, 6 g of powder were dissolved in 120 ml ACEX Buffer and stirred for 30 min. The solution was two times filtered through 4 layers of sterile cheesecloth and the flow-through was centrifuged at 33,000 x g for 15 min. The resulting supernatant was transferred into a beaker, and actin polymerization was induced by adjusting compound concentrations to 5 mM Tris, 50 mM KCl, 2 mM $MgCl_2$, and 1mM ATP. After the solution was stirred for 2 h, filamentous actin was separated from tropomyosin by salt-precipitation: KCl concentration was increased to 0.8 M, and pH was adapted to a value between 8.3 and 8.5 using 1 M KOH. Then, F-actin was precipitated by 40 min of centrifugation at 361,000 x g. The resulting pellet was incubated on ice in ACEX Buffer for several minutes. Afterwards, the softened pellet was gently homogenized in ACEX Buffer for 30 min. During homogenization, the sample was constantly kept on ice. In the next step, the resulting solution was dialyzed in ACEX Buffer overnight to depolymerize F-actin into its globular monomeric form. For this purpose, a membrane with a molecular weight cut-off of 3.5 kDa was utilized. Thereupon, the sample was centrifuged at 14,000 x g for 15 min and the pellet was discarded. The obtained G-actin solution was stored in liquid nitrogen until use.

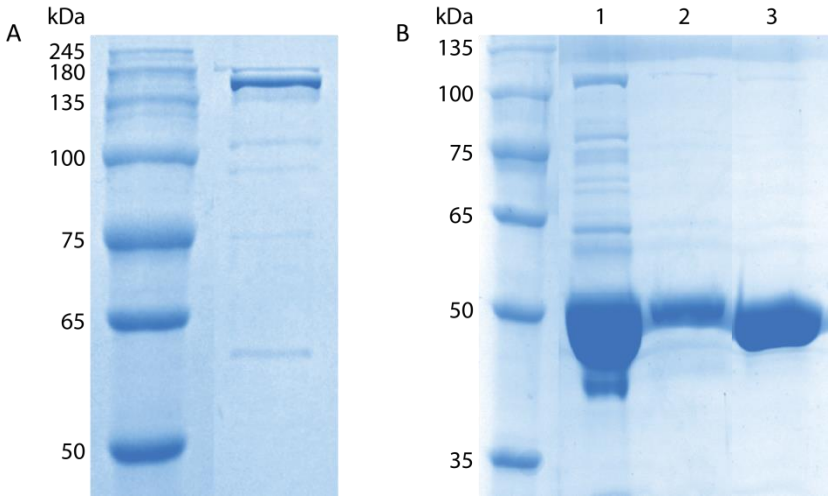

Figure 22 Purification of proteins from rabbit skeletal muscle. (A) Polyacrylamide gel of purified HMM (molecular weight: ~180 kDa). (B) Polyacrylamide gel of samples from different stages of the G-actin purification process: (1) before salt-precipitation, (2) after salt-precipitation, (3) after overnight dialysis (molecular weight of G-actin: 42 kDa).

Protein Detection and Determination of Concentration

Throughout and at the end of each purification process, presence and purity of the purified protein had to be verified. For this purpose, samples were subjected to SDS-PAGE. Following this, protein concentration was determined in light absorbance assays.

1. SDS-PAGE:

Discontinuous SDS-PAGE was performed according to Laemmli (1970) with modifications. Prior to SDS-PAGE, samples were mixed with 2x SDS Gel Loading Buffer or 6x SDS Gel Loading Buffer in a 1:1 or 5:1 volume ratio respectively. Proteins were linearized by a 5 min incubation in a heat block at 95°C.

Following this, samples were injected into a polyacrylamide gel composed of a stacking gel and a resolving gel. During gel electrophoresis, protein samples were concentrated into small bands in the stacking gel, and separated according to their molecular weight in the resolving gel. Concentration and separation process resulted from different pore sizes of stacking and resolving gel. Pore sizes were adjusted via acrylamide/bis-acrylamide content of the gels. To quantify the molecular weight of the proteins analyzed, a prestained molecular weight marker was always added to the gels. SDS-PAGE was carried out in TG Buffer at a voltage of 200 mV. Once gel electrophoresis was terminated, polyacrylamide gels were stained in Blue Stain Solution. Destain Solution was applied to remove dye from the polyacrylamide gel, leaving detectable protein bands for subsequent analysis. Gel imaging was performed in a gel imaging system.

2. Determination of Protein Concentration:

Protein concentration of purified samples was determined by light absorbance assays. In all of these assays, absorbance of the sample buffer was measured first to correct later detected absorbance values of the protein solution.

For concentration determination of HMM samples, absorbance $A_{(\lambda)}$ at a wavelength of λ=280 nm was measured with a UV-Vis spectrophotometer. Protein concentration c was then calculated from (Stoscheck, 1990):

$$c\left[\frac{mg}{ml}\right] = A_{(280\,nm)} \cdot l[cm] \tag{3}$$

In the above equation, l denotes the optical path length.

Determination of G-actin concentration was implemented by UV-Vis spectrophotometric measurement of the absorbance at wavelengths of 290 nm and at 310 nm, and the following calculation:

$$c\left[\frac{mg}{ml}\right] = \frac{A_{(290\,nm)} - A_{(310\,nm)}}{0.62} \tag{4}$$

For all other proteins, light absorbance measurements at 280 nm and 310 nm or Bradford Assays were performed. In the first case, light absorbance at the two wavelengths was measured and protein concentration was computed from Beer-Lambert law:

$$c = \frac{A_{(280\,nm)} - A_{(310\,nm)}}{\varepsilon \cdot l} \tag{5}$$

Here, ε represents the molar extinction coefficient and l again denotes the optical path length. Molar extinction coefficients were determined with the help of MacVector 13 software (MacVector). Implementation of Bradford assays was adapted from Bradford (1976). Samples were mixed with a Coomassie Brilliant Blue G-250-containing solution (Protein Assay Dye Reagent Concentrate, Bio-Rad) and photometric absorption measurements at a wavelength of 595 nm were performed. Protein concentration determination was based on the shift of the dye´s absorption maximum upon protein binding. Before the assay was performed with a sample of unknown protein concentration, measurements with BSA standards of concentrations c ranging from 0.2 mg/ml to 0.9 mg/ml were performed. Applying Microsoft Excel, the following linear fit with fit parameters m and n was adjusted to the data obtained from BSA standards:

$$A_{(595\ nm)} = c\left[\frac{mg}{ml}\right] \cdot m + n \tag{6}$$

In the next step, absorbance measurements of the samples with unknown protein content were performed. Concentrations were then calculated from equation (6) using the values of m and n obtained from fitting.

3.4 *In Vivo* Functional Protein Analysis

To gain insight into myosin-XXI´s potential functions in a cellular environment, transfections with various myosin-XXI DNA constructs were carried out. To avoid interference of endogenously expressed myosin-XXI, mammalian cell lines COS-7 (*Cercopithecus aethiops* kidney fibroblasts) and HeLa (human cervix epithelial carcinoma cells) were utilized in transfection experiments. In addition to the investigation of the cellular localization of myosin-XXI in fixed cell samples, the dynamic behavior of myosin-XXI was investigated with the help of live records of transfected cells. Further, the influence of myosin-XXI on the formation of membrane protrusions was studied by the analysis of filopodia length and density of fixed cells. Myosin-XXI expression of transfected HeLa and COS-7 cells was confirmed by western blotting.

3.4.1 Cell Culture and Transfections

Cells were grown at a temperature of 37°C in an atmosphere of 10 % CO_2 (COS-7) or 5 % CO_2 (HeLa) content. COS-7 cells were maintained in Minimum Essential Medium (Thermo Fisher Scientific), and HeLa cells were kept in Dulbecco´s Modified Eagle Medium (Thermo Fisher Scientific), each supplemented with 10 % (v/v) fetal bovine serum. Cells were not transfected before a minimum passage number of 6 and after a maximum passage number of 27. Prior to transfection, cells were seeded in 6-well plates and left to grow for 24 h. If cells were later to be fixed to prepare durable samples for confocal microscopy, wells were equipped with flamed clean circular coverslips

(diameter: 25 mm) before seeding (see subsection 3.5.1 for cleaning protocol). If live imaging was intended, cells were grown in glass bottom cell culture dishes. Transfection of plasmid DNA was implemented using Lipofectamine® 2000 Transfection Reagent (Thermo Fisher Scientific) following manufacturer´s instructions. Cells were incubated with Lipofectamine® 2000-DNA mixture for 4 h to 6 h. Afterwards, cells were left to grow for 24 h, 48 h, or 72 h before further treatment. Plasmids introduced into the cells contained a fluorophore sequence and DNA encoding a myosin-XXI construct. Furthermore, plasmids only encoding a fluorophore were used for control experiments. A detailed list of all plasmids used in transfections can be found in Table A.2. In addition to transfections with only one plasmid, mammalian cells were also co-transfected with either two plasmids or a plasmid and a baculovirus at a time. In co-transfection experiments, a plasmid containing myosin-XXI DNA and a construct for the staining of a certain cell structure were applied in order to acquire information about myosin-XXI cellular localization. The additional plasmid applied in co-transfections with two plasmids encoded a fusion protein of RFP (red fluorescent protein) and lifeact, a peptide used for staining of the actin cytoskeleton (Riedl *et al.*, 2008). Baculoviruses (Cell Light® Reagents BacMam 2.0, Thermo Fisher Scientific) used in co-transfections encoded markers for early endosomes, Golgi apparatus, and endoplasmic reticulum. They were added to transfected cells immediately after cells had been incubated with Lipofectamine® 2000-DNA mixture. Baculovirus concentrations used varied between $1.2 \cdot 10^6$ and $1.6 \cdot 10^6$ particles per 10^5 cells. In all transfections and co-transfections performed, plasmid DNA was applied at a concentration of 0.2 µg to 2.2 µg per 10^5 cells and DNA to Lipofectamine® 2000 ratios ranged between 1:1.3 µg/µl and 1:4.6 µg/µl.

Once transfection was completed, cells were either subjected to live imaging, lysed for western blotting, or fixed for later confocal microscopy. For fixation, cells were washed with PBS and incubated in 4 % (w/v) paraformaldehyde in PBS for 10 min to 15 min. Subsequently, samples were again washed with PBS and treated with 50 mM NH_4Cl in PBS for 15 min to 30 min. Following washing with PBS, samples were either further treated in a staining procedure (see subsection 3.4.2) or already mounted on microscope slides for microscopic inspection.

3.4.2 Staining of the Actin Cytoskeleton and Clathrin-Coated Vesicles

In order to gain information about the cellular localization of transfected myosin-XXI constructs, actin filaments and clathrin-coated vesicles within the cells were stained after transfection.

All incubation steps described below were carried out at RT in a humid atmosphere. All required solutions were prechilled on ice prior to use. To prepare cells for the uptake of staining reagents, cells were simultaneously permeabilized and blocked in PBS/BSA supplemented with 0.1 % (v/v) Triton X-100 for 15 min. Staining of actin filaments was implemented by treating permeabilized cells with 264 nM phalloidin-TRITC in PBS/BSA for 30 min. Immunostaining of clathrin-coated vesicles was

implemented with the help of anti-clathrin heavy chain rabbit polyclonal antibody (abcam) and cyanine 3-conjugated polyclonal goat anti-rabbit antibody (Jackson ImmunoResearch): initially, permeabilized cells were incubated with 1 µg/ml anti-clathrin antibody in PBS/BSA for 1 h. Following washing with PBS, samples were treated with 3 µg/ml secondary antibody in PBS/BSA for another hour. Subsequent to staining, samples were washed with PBS and were then mounted onto microscope slides.

3.4.3 Preparation of Durable Samples, Confocal Microscopy, and Analysis of Confocal Images

Coverslips with fixed transfected cells were attached to 26x76 mm^2 microscope slides (Menzel) using Mowiol Embedding Solution. Immediately before the solution was applied, approximately 3 % (m/v) 1,4-diazabicyclo[2.2.2]octane were added in order to improve lifetime of the dyes contained in the cell samples.

Confocal images of durable samples were recorded using a 60x or a 100x oil immersion objective. DsRed2 (*Discosoma* species red fluorescent protein 2) and RFP were excited with a 544 nm laser, ZsGreen1 (*Zoanthus* species green fluorescent protein 1) and eGFP excitation was implemented with a 488 nm laser.

To elucidate a possible impact of myosin-XXI on the formation and dynamics of membrane protrusions, filopodia density and length was analyzed for HeLa and COS-7 cells transfected with equal concentrations of vector encoding FL-XXI-ZsGreen1 fusion protein, Trunc-XXI-ZsGreen1 fusion protein, or solely ZsGreen1. Based on the literature (Berg and Cheney, 2002), filopodia were defined as membrane protrusions of a width smaller than 1 µm and a length greater than 0.75 µm. Density of filopodia was calculated as the ratio of filopodia number to membrane circumference in the xy-plane. Membrane circumference was measured with the help of NIS-Elements Advanced Research 4.00 software. Number of filopodia was deduced in the course of length determination. Two different approaches were deployed to measure filopodia length: In the analysis of HeLa cells, length of a filopodium was defined as the length of a straight line connecting the origin and the tip of a filopodium, and origin and tip of each filopodium were identified in z-series records. For COS-7 cells, filopodia lengths were automatically derived from average images of z-stack records. Average images were processed in ImageJ 1.46r by sharpening, manual removal of the image parts depicting the cell body, and converting remaining structures (i.e. filopodia) into single-pixel format. Lengths were then computed applying automated particle analysis. For better evaluation of the analysis results, fluorescence intensity signals of the cell bodies of analyzed cells were compared as a measure for different expression levels. Intensities were quantified with the NIS-Elements Advanced Research 4.00 software.

3.4.4 Live Imaging and Analysis of Records

Live images of transfected HeLa cells were recorded with the confocal microscopy system applying the same settings as stated in the previous subsection. During the imaging process, cells were maintained in phenol red free Minimum Essential Medium (Thermo Fisher Scientific) in a stage top incubation chamber which sustained a humid atmosphere of 37°C temperature and 5 % CO_2 content.

Records were analyzed regarding myosin-XXI movement and length changes of filopodia. Furthermore, the time course of the fluorescence intensity of myosin-XXI accumulations inside filopodia tips was measured. Myosin-XXI movement within filopodia shafts was analyzed with the SpotTracker plugin in ImageJ. Tracking was only applied during phases of constant filopodia length and position. The rates of length changes of filopodia were determined by tracking stable myosin-XXI accumulations inside the tips of filopodia, again utilizing the ImageJ SpotTracker plugin. Fluorescence intensities of myosin-XXI accumulations inside filopodia tips were quantified using the NIS-Elements Advanced Research 4.00 software. Intensity measurements were only carried out during phases of stable filopodia length and fixed tip position.

3.4.5 Cell Lysis and Western Blotting

Western blotting was utilized to verify the expression of FL-XXI-ZsGreen1 fusion protein, Trunc-XXI-ZsGreen1 fusion protein, and ZsGreen1 by HeLa and COS-7 cells transfected with the corresponding plasmid.

Once transfection procedure was finished, cells were washed in ice-cold PBS and scraped into ice-cold Lysis Buffer. Lysates were boiled at 95°C for 5 min and briefly tip-sonicated. Linearized samples were then subjected to SDS-PAGE. Proteins were subsequently transferred onto a nitrocellulose membrane by electroblotting in Blotting Buffer at a voltage of 100 V. Afterwards, the nitrocellulose membrane was blocked in Blocking Buffer at RT for 15 min. Then, the membrane was incubated with anti-RCFP rabbit polyclonal pan antibody (Clontech) at 4°C overnight. This primary antibody was supplied as serum and diluted 1:1,000 in Blocking Buffer. After washing with Wash Buffer, incubation with 0.1 µg/ml horseradish peroxidase-conjugated polyclonal goat anti-rabbit antibody (abcam) in Blocking Buffer was carried out for 1 h. Subsequent to washing with Wash Buffer, Clarity™ Western ECL Blotting Substrate (Bio-Rad) was applied to the membrane according to manufacturer´s instructions. Chemiluminescence signal was detected with the help of a gel imaging system.

3.5 *In Vitro* Functional Protein Analysis

In *in vitro* experiments, myosin-XXI motility on different surfaces, and its binding behavior to phospholipids were investigated. Gliding filament assays on nitrocellulose and on lipid vesicle-

covered surfaces were performed to gain information about the directionality of myosin-XXI movement along F-actin, and to verify that myosin-XXI is capable of inducing filament movement when bound to lipids. The dynamic behavior of the bilayer-bound actin-myosin-XXI complex and the capability of myosin-XXI to bind to planar lipid bilayers were investigated with the help of supported and tethered lipid bilayers. Furthermore, potential curvature sensitivity of myosin-XXI was elucidated in co-sedimentation assays and Single Liposome Curvature (SLiC) assays.

3.5.1 General Preparation Techniques

In order to execute the *in vitro* experiments described in later subsections, certain preparation techniques had to be performed repeatedly. These commonly used techniques are described in the following subsections.

Preparation of Coverslips and Flow Cells

Before coverslips were utilized in any experimental procedure, they were cleaned to avoid sample contamination. If not used in cell culture, coverslips were attached to microscope slides to form experimental chambers.

Coverslips were cleaned by applying an etch solution made of H_2O, 50 % (w/v) H_2O_2, and 30 % (w/v) NH_3 in a volume ratio of 5:1:1. Coverslips were incubated in this solution at a temperature of 70°C for 2 to 3 hours. Following this, coverslips were intensely washed with H_2O and with methanol. Coverslips were left to dry and stored at RT. Coverslips used in cell culture, were additionally sterilized by flaming, and were immediately transferred into sterile 6-well plates.

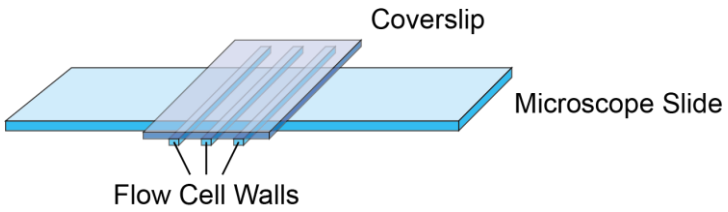

Figure 23 Construction of flow cells. Each flow cell was assembled from a cleaned coverslip mounted on a microscope slide. Flow cell walls enclosed two experimental channels, and consisted of glass or of a combination of double-sided tape and gaffer tape.

Flow cells (Figure 23) constructed from cleaned coverslips were mounted on 26x76 mm^2 microscope slides (Menzel). Flow cells used in gliding filament assays on nitrocellulose or lipid vesicles further were constructed using cleaned 24x40 mm^2 coverslips (Menzel) attached to the microscope slides with double-sided tape and gaffer tape. Prior to attachment to a microscope slide, coverslips were coated with 0.6 mg/ml nitrocellulose in pentyl acetate. Flow cells used for the preparation of supported lipid bilayers (SLB) or for SLiC assays were completely made from glass to assure integrity

of the flow cell throughout long incubation times: Flow cell walls consisted of 3x40 mm^2 coverslips (Menzel), and flow cells were closed with 26x40 mm^2 cleaned coverslips. UV glue (Loctite AA 350, Henkel) was utilized for the attachment of all components. In the case of SLiC assays, cleaned coverslips were additionally coated with polyethylene glycol (PEG) before attachment (see subsection 3.5.5).

Polymerization and Fluorescent Labeling of Actin

To investigate myosin-XXI in gliding filament assays, purified G-actin was polymerized to form filaments. To ensure visibility in total internal reflection fluorescence (TIRF) microscopy, actin was polymerized in the presence of fluorescently labeled phalloidin. Phalloidin was conjugated to tetramethylrhodamine B isothiocyanate (TRITC) or fluorescein isothiocyanate (FITC), and further served as stabilizing agent preventing depolymerization of filaments (Lengsfeld *et al.*, 1974). For studies of myosin directionality, polar labeling of actin with two dyes was implemented. For any other investigation, solely phalloidin-FITC was utilized for labeling.

1. Preparation of FITC-Labeled F-Actin:

Polymerization of actin was induced by the application of K^+, Mg^{2+}, and ATP as these constituents had been shown to promote formation of actin filaments (Straub, 1943; Price, 1946; Feuer *et al.*, 1948). For this purpose, purified G-actin was mixed with 10 times concentrated AB^+ in a 9:1 volume ratio and incubated on ice for 1 h. Subsequently, the resulting F-actin solution was diluted by a factor of 60 in AB^-. Diluted F-actin and phalloidin-FITC were mixed in equimolar concentrations of actin monomers and phalloidin. The mixture was incubated on ice for 2 more hours. F-actin was stored at 4°C until use.

2. Preparation of Dual-Labeled F-Actin:

To attain a polar labeling of actin filaments with two distinct fluorescent dyes, actin was consecutively incubated with phalloidin-TRITC and phalloidin-FITC. The development of the applied method was based on a protocol published by Herm-Götz *et al.* (2002). At first, purified monomeric actin was diluted in G-Actin Buffer to a final G-actin concentration of 1.9 µM. Following a 15 min incubation on ice, polymerization was induced by the addition of 100 mM solid KCl, and the sample was incubated at RT for 10 min. Phalloidin-TRITC was added to the actin solution so that molar ratio of phalloidin to G-actin was 1:1. The mixture was left to incubate on ice overnight. The next morning, the solution was supplemented with human plasma gelsolin and incubated on ice for 30 min. Gelsolin is a capping protein preventing polymerization at the barbed end (also called plus end) of F-actin (Harris and Weeds, 1984). Molar ratio of gelsolin to G-actin was adjusted to a value between 1:10

and 1:100. In the next step, a 10- to 15-fold excess of purified G-actin was added to the capped actin seeds. After a 5 min incubation on ice, actin polymerization was again induced by the application of 100 mM solid KCl. Then, phalloidin-FITC was added in an equimolar amount to unlabeled G-actin. The mixture was left to incubate on ice for 1 h to 3 h. This procedure resulted in actin filaments exhibiting TRITC-labeled barbed ends and FITC-labeled pointed ends (also called minus-ends). Filaments were stored at 4 °C. Samples had to be used within 48 h as gelsolin also exhibits an actin severing activity causing disassembly of filaments even in the presence of phalloidin (Norberg *et al.*, 1979; Allen and Janmey, 1994).

Preparation of Unilamellar Vesicles

In order to prepare unilamellar vesicles, lipid composition had to be determined. Molar ratios of the different lipids and carbocyanine dyes were specified and required volumes of stock solutions were calculated using the molecular weight values stated by the suppliers. For bovine brain extract, only lipid composition was declared by the manufacturer: Extract consists of phosphatidylserine (PS), cerebrosides and phosphatidylinositol (PI) in a molar ratio of 5:4:1. For this reason, molecular weight M of bovine brain extract was estimated as:

$$M = 0.5 \cdot M_{PS} + 0.4 \cdot M_C + 0.1 \cdot M_{PI} = 815.48 \, \frac{g}{mol} \tag{7}$$

Molecular weights M_{PS} of PS (824.97 g/mol), M_C of cerebrosides (781.95 g/mol), and M_{PI} of PI (902.13 g/mol) were adopted from porcine brain PS, porcine brain cerebrosides, and bovine liver PI as stated by Avanti Polar Lipids.

To prepare unilamellar vesicles, stock solutions were mixed in the desired molar ratios, and evaporated in a vacuum concentrator at 30 °C until complete removal of all solvents. Thereafter, the resulting lipid cake was resuspended in aqueous buffer (Lipid TBS, Lipid Buffer 500, Lipid Buffer 150, or HNa 100). The resulting solution was subjected to multiple freeze-thaw cycles using liquid nitrogen and a water bath. Temperature of the water bath ranged between 50°C and 65°C depending on the phase transition temperatures of the lipids contained in the solution.

3.5.2 Gliding Filament Assays

In gliding filament assays, functionality of myosin-XXI was investigated by immobilizing myosin on a surface, adding actin filaments and monitoring filament movement in the presence of ATP. Assays were performed in flow cells made from nitrocellulose-coated coverslips. All buffers used were degassed before the experiments and sample preparation was carried out at RT. Filament movement was recorded by a Nikon 1AR TIRF microscopy system using a 100x Nikon Apochromat oil immersion objective (NA 1.49). Fluorophore excitation was achieved by 488 nm and 544 nm laser irradiation.

Gliding Filament Assays on Nitrocellulose-Coated Glass Surfaces

Gliding filament assays on nitrocellulose-coated glass surfaces (Figure 24) were carried out to determine myosin directionality, and to verify functionality of myosin-XXI samples prior to use in further experiments.

Assays were carried out according to Kron and Spudich (1986) with modifications. In short, a 240 nM dilution of myosin-XXI in AB^- and a 26 nM (monomer concentration) dilution of F-actin in AB^-/BSA were prepared. Myosin-XXI was then injected into the flow chamber and incubated for 3 min. Afterwards, the nitrocellulose surface was blocked with AB^-/BSA for 3 min. F-actin solution was added and left to incubate for another 3 min. The chamber was then rinsed with Rigor Buffer and transferred to the TIRF microscope to verify binding of actin filaments. Filament movement was initiated by the addition of 1 mM ATP in Rigor Buffer.

Gliding filament assays with HMM and myosin-VI followed the same procedure with the following modifications: For HMM assays, protein solutions were diluted to concentrations of 140 nM HMM and 8 nM G-actin. Furthermore, 10 µM ATP was applied to induce motor motility. Experiments with myosin-VI were implemented using 2.3 µM myosin-VI and 7 nM G-actin. Assay Buffer was replaced by Myosin-VI Buffer, and ATP concentration was increased to 10 mM. ATP concentration was adapted for each myosin to reduce the frequency of filament rupture.

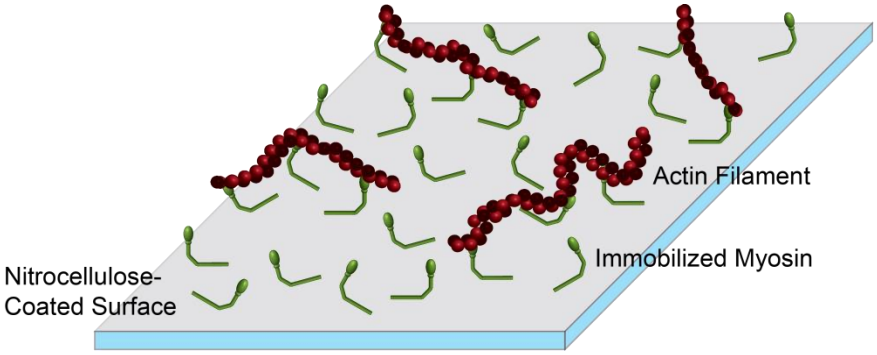

Figure 24 Gliding filament assay on a nitrocellulose-coated glass surface. In this assay, myosin was unspecifically bound to a coverslip treated with nitrocellulose. Subsequently, BSA was applied to block the sample surface. In the next step, fluorescently labeled F-actin was added, which attached to immobilized myosin molecules. Upon addition of ATP, filament gliding could be observed with the help of fluorescence microscopy.

Gliding Filament Assays on Lipid Vesicles

To confirm myosin-XXI´s vesicle binding capability and motor motility in a lipid-bound state, gliding filament assays on lipid vesicle-coated surfaces were carried out.

Prior to the experiments, vesicles were treated in an ultrasonic bath (Sonorex RK 100 H, Bandelin) at RT for 10 min and extruded through a polycarbonate membrane at least 21 times (membrane pore diameter: 30, 100, 200, 400, 800, or 1000 nm). Vesicle solutions were diluted in Lipid Buffer 500 to attain lipid concentrations of 10 µg/ml or 40 µg/ml. Lipids were then injected into a flow chamber

and incubated at RT for 10 min. The flow cell was then rinsed with AB^-/2x BSA and incubated for 5 to 10 min. BSA was applied to prevent nonspecific protein binding to the nitrocellulose surface. FL-XXI was diluted in AB^- to a final concentration of 0.4 µM, rinsed into the chamber, and incubated for 3 min. An 8.6 nM (monomer concentration) dilution of FITC-labeled F-actin in AB^-/2x BSA was prepared and added to the sample. After another 3 min of incubation, the flow cell was rinsed with Rigor Buffer and filament binding to the surface was confirmed by TIRF microscopy. Subsequently, Motility Buffer was flushed into the chamber and filament movement was recorded.

Lipid vesicles utilized in gliding filament assays contained POPC, 1.2 mol% Rhodamine DHPE, and 4.8 mol% to 9.7 mol% of a phosphoinositide (PI(4)P, or PI(3,5)P_2). Rhodamine DHPE allowed visual verification of vesicle binding to the nitrocellulose surface. PI(4)P and PI(3,5)P_2 were added as myosin-XXI binding to those phospholipids had been demonstrated (Batters *et al.*, 2014). As a negative control, vesicles merely composed of POPC and 1.1 mol% Rhodamine DHPE were used.

Analysis of Filament Movement

Myosin directionality was determined using NIS-Elements Advanced Research 4.00 software (Nikon) for analysis. Filament movement was manually tracked and color of the leading filament end was registered. For a filament to be taken into account for analysis, movement of the filament had to be detectable in at least 3 consecutive frames, and the filament´s entire length had to be visible for at least 3 consecutive frames of filament movement. Furthermore, each filament had to exhibit exactly two distinct parts of different labeling, and each of these parts had to be of at least 2 pixels of length along the filament axis.

To determine the speed of gliding filaments, ND2 files generated by the Nikon software were converted into GMV files in ImageJ 1.46r with the help of a self-written macro. Filaments could then be manually tracked using GMimPro image sequence processor (Mashanov and Molloy, 2007). Tracks of filament movement persisting for less than 5 consecutive frames were excluded from the analysis. Average filament gliding speed was calculated as the mean of the speed values of all single steps of all tracked filaments.

3.5.3 Binding of Myosin-XXI to Planar Lipid Bilayers

To elucidate the dynamic behavior of the actin-myosin-XXI complex and to investigate the capability of myosin-XXI to bind to planar lipid bilayers systems, two types of bilayers were prepared (Figure 25): supported lipid bilayers consist of a lipid double layer directly applied to the surface of the substrate. Tethered lipid bilayers are lifted from the substrate and attached to the substrate surface by singular molecular anchors. Before these bilayers were utilized in experiments with

myosin-XXI, presence of a fluid membrane was verified by Fluorescence Recovery after Photobleaching (FRAP) tests.

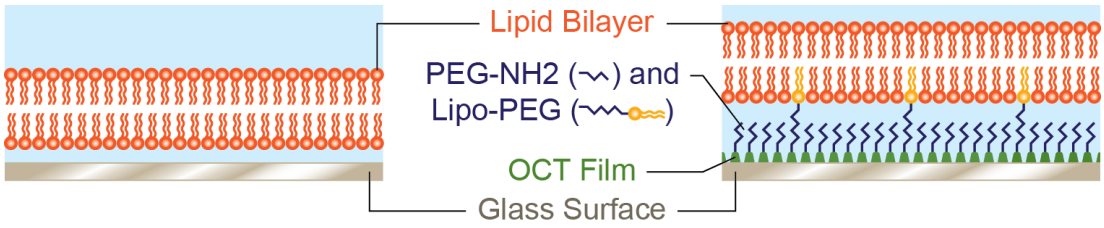

Figure 25 Types of planar lipid bilayers. In order to perform bilayer binding experiments, two types of planar lipid bilayers were prepared: supported bilayers (left) consist of a lipid double layer directly located on the surface of a coverslip, while tethered bilayers (right) are attached to a PEG-coated glass surface via Lipo-PEG anchors. PEG/Lipo-PEG coating required preceding chemical treatment of coverslips resulting in the self-assembly of an OCT film. Presence of the PEG cushion beneath tethered lipid bilayers passivated the glass surface thus reducing unspecific attachment of proteins.

Preparation of Planar Lipid Bilayers

1. Preparation of Supported Lipid Bilayers:

In order to prepare supported lipid bilayers, unilamellar vesicles containing Rhodamine DHPE were produced. Rhodamine DHPE was added to permit later FRAP measurements of the readily formed bilayers. In advance to some experiments, vesicles were additionally treated in an ultrasonic bath at RT for 10 min. Furthermore, some of the lipid solutions were then centrifuged at 4°C and at least 13,000 x g for 15 min or longer to remove lipid aggregates. Immediately before bilayer preparation, vesicles were diluted in aqueous buffer to a concentration between 0.02 mg/ml and 2.0 mg/ml. Buffers used were HNa100 and Lipid Buffer 500. SLB were prepared in glass flow cells made with uncoated cleaned coverslips.

First, a flow cell was filled with buffer and thereafter, diluted lipid solution was flushed in. Vesicles were left to attach to the glass surface during an incubation period of at least 30 min at RT in a humid environment. Once attachment had occurred, bilayer formation resulted from rupture of the vesicles. Rupture was achieved by simply incubating flow cells until bilayer formation could be observed, or by rinsing flow chambers with H_2O thus exposing vesicles to an osmotic shock. Prior to experimental use, bilayers were again rinsed with buffer.

2. Preparation of Tethered Lipid Bilayers:

Tethered lipid bilayers were prepared in a two-step procedure: At first, coverslips (20x15 mm^2; Carl Roth) were passivated and functionalized with tethers. In the second step, phospholipids were applied.

For the purpose of substrate passivation and creation of tethers, coverslips were prepared according to Daniel *et al.* (2007) and Wasserman *et al.* (1989) with modifications. All equipment used in this procedure was incubated at 120°C for several hours prior to use to remove all water. Coverslips were

prepared for coating by several cleaning procedures. After they were cleaned with acetone, isopropanol, and H_2O, coverslips were subjected to RCA cleaning (RCA: Radio Corporation of America): coverslips were consecutively incubated in a solution of H_2O, 30 % H_2O_2, 25 % NH_3 (5:1:1 volume ratio) at 80°C, a solution of H_2O, 30 % H_2O_2, 37 % HCl (5:1:1 volume ratio) at 120°C, and again in a solution of H_2O, 30 % H_2O_2, 25 % NH_3 at 80°C, each for 30 min. Afterwards, coverslips were dried under a stream of nitrogen and incubated at 120 °C and at a pressure of 40 mbar for 5 min in a vacuum drying oven to remove remaining water.

Dried clean coverslips were then coated with a self-assembled octenyltrichlorosilane (OCT) film by incubating them in 0.2 % (v/v) OCT in anhydrous hexadecane while kept in a nitrogen atmosphere overnight. After a 3 min ultrasound treatment in chloroform, coverslips were dried under a stream of nitrogen and incubated at RT and 40 mbar for 1 h. To oxidize OCT films, coverslips were incubated in Oxidizing Solution overnight. Subsequently, coverslips were successively cleaned in the following solutions for several seconds: 0.4 M $NaHSO_3$, H_2O, 1 M HCl, H_2O, and ethanol.

After drying with nitrogen and in the vacuum drying oven at 40 mbar at RT, OCT surfaces were functionalized with amino-terminated polyethylene glycol conjugated to phosphoethanolamine (1,2-distearoyl-*sn*-glycero-3-phosphoethanolamine-N-[amino(polyethylene glycol)-2000], Avanti Polar Lipids; called Lipo-PEG here). For this purpose, coverslips were incubated in a solution containing 15.2 mM N-hydroxysuccinimide (NHS) and 78.2 mM 1-ethyl-3-(3-dimethylaminopropyl)carbodiimide hydrochloride (EDC) at RT for 2 h. After coverslips were washed with H_2O and dried under a stream of nitrogen, they were placed in 1 mg/ml Lipo-PEG in dimethylformamide at RT overnight. During the following reaction, NHS was removed and partially replaced by Lipo-PEG. Lipo-PEG would later serve as an anchor for tethering the lipid bilayer to the coverslip. The next day, coverslips were washed with chloroform and dried under a stream of nitrogen.

Subsequently, silanes not linked to Lipo-PEG were conjugated to amino-terminated polyethylene glycol (alpha-methoxy-omega-amino poly(ethylene glycol)-750, Rapp Polymere; called PEG-NH_2 here). Therefore, coverslips were again treated with NHS/EDC solution. Then, OCT films were incubated in 10 mg/ml PEG-NH_2 in Carbonate Buffer overnight to replace NHS by PEG-NH_2. The resulting PEG-NH_2 cushion passivated the glass surface in later experiments, creating a lipid bilayer lifted from the glass surface and simultaneously reducing nonspecific binding of proteins to the coverslips. After the overnight incubation, coverslips were cleaned using H_2O and chloroform, dried under a stream of nitrogen, and finally, remaining solvents were removed by a 1 h incubation at RT and 40 mbar. Coated coverslips were stored at RT until use.

In the second step of tethered bilayer preparation, passivated coverslips were coated with a phospholipid film. For this purpose, lipid stock solutions were mixed, and solvents were evaporated in a vacuum concentrator at 30 °C. Dried lipids were resuspended in isopropanol. The lipid solution

was then uniformly spread on the coverslips utilizing a spin coater. Subsequently, isopropanol was thoroughly evaporated by 150 min of incubation in a vacuum drying oven at 40 mbar at RT. Each lipid-coated coverslip was then inserted into a polymer slide containing a channel (µ-Slide I 0.8 Luer Uncoated, ibidi) via a rectangular opening milled out of the bottom of the slide (Figure 26). Coverslips were fixated using Microset 101RF Fluid silicone glue (Microset), and experimental chambers were stored in a desiccator at RT. Immediately before experimental use, chambers were carefully flushed with 25 ml of degassed Lipid Buffer 500 to rehydrate the dried lipid films.

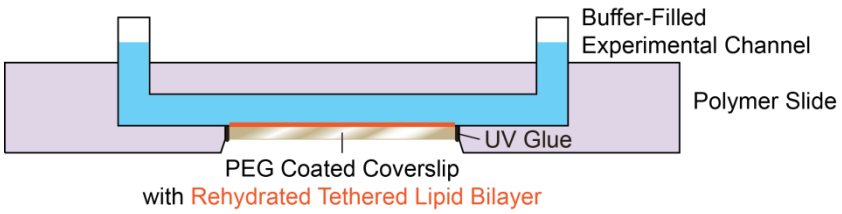

Figure 26 Polymer slides used for the preparation of tethered lipid bilayer samples. Tethered lipid bilayers were prepared with the help of prefabricated polymer slides containing an experimental channel. Prior to use, each polymer slide was modified by the removal of a rectangular piece of material from its base. Subsequently, a coverslip coated with a dried tethered bilayer film was inserted, and fixated using silicone glue. Eventually, the experimental channel was carefully flushed with degassed buffer in order to rehydrate the lipid film.

FRAP Experiments and Calculation of Lateral Diffusion Constants

Fluorescence Recovery after Photobleaching experiments (Figure 27) were performed with a Nikon A1R confocal microscope system using a 60x Nikon Apochromat oil immersion objective (NA 1.40) or a 100x oil immersion objective. Rhodamine DHPE contained in the bilayers was excited by 544 nm or 561 nm laser light, bleaching was implemented with a 405 nm laser. Using the manufacturer´s software (NIS-Elements Advanced Research 4.00), in each field of view two regions of interest (ROI) were defined. For the Reference ROI solely the time course of fluorescence intensity was recorded. At the same time, the so-called Stimulation ROI was actually used for FRAP measurements: Following 60 s of fluorescence intensity measurement, the majority of fluorophores within this region was bleached. Instantly after photobleaching, recovery of the fluorescence signal by lateral diffusion of non-bleached Rhodamine DHPE was monitored. Regions of interest always had a circular shape with radii ranging from 8 µm to 9 µm.

Before FRAP of the Stimulation ROI was analyzed, a time-dependent correction factor $\alpha_{(t)}$ was calculated which accounted for photobleaching inherent to the imaging process:

$$\alpha_{(t)} = \frac{F_{ref(0)}}{F_{ref(t)}} \tag{8}$$

Here, $F_{ref(t)}$ denotes the fluorescence intensity of the Reference ROI at a time t. $F_{ref(0)}$ is the intensity at time t=0 s, i.e. at the beginning of the record.

The correction factor $\alpha_{(t)}$ was multiplied with the intensity data $F_{stim(t)}$ obtained from the measurements of the Stimulation ROI:

$$F_{(t)} = \alpha_{(t)} \cdot F_{stim(t)} \tag{9}$$

Thus, $F_{(t)}$ describes the time course of the corrected intensity curve of the Stimulation ROI.

Curves $F_{(t)}$ were now subjected to an analysis derived from Axelrod *et al.* (1976) and Soumpasis (1983). Accordingly, intensity curves $F_{(t)}$ of FRAP experiments can be fitted by the following function:

$$F_{(t)} = F_{(\infty)} - \left[F_{before} - F_{PB}\right] \cdot \left[1 - e^{-\frac{2\tau_D}{t - t_{PB}}} \cdot \left(I_1\left(\frac{2\tau_D}{t - t_{PB}}\right) + I_0\left(\frac{2\tau_D}{t - t_{PB}}\right)\right)\right] \tag{10}$$

where $F_{(\infty)}$ is the fluorescence intensity after termination of fluorescence recovery, F_{before} is the intensity before photobleaching, and F_{PB} is the fluorescence intensity measured immediately after photobleaching. $F_{(\infty)}$ and F_{PB} were determined as average intensities of 15 s to 30 s intervals. The parameter t_{PB} is the point in time where photobleaching is executed. The constant τ_D is the characteristic diffusion time and the parameter to be determined by fitting. I_1 and I_0 are modified Bessel functions. Fits were adapted to experimental data with the help of the solver Add-in in Microsoft Excel.

Lateral diffusion constants D could then be calculated from τ_D and the ROI radius R:

$$D = \frac{{\tau_D}^2}{4R} \tag{11}$$

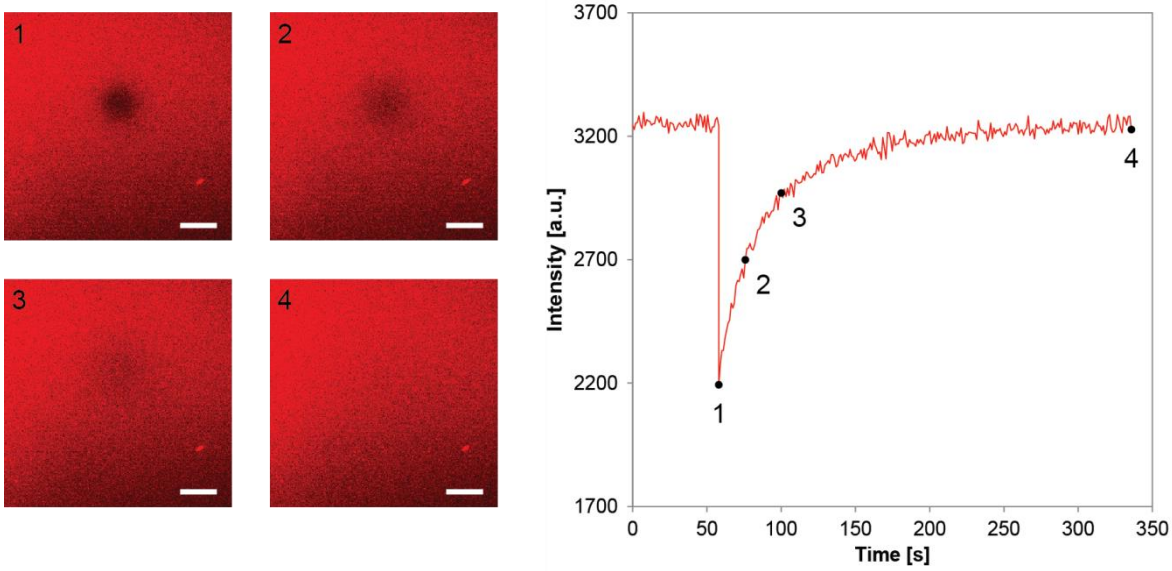

Figure 27 FRAP. In Fluorescence Recovery after Photobleaching experiments, bilayer fluidity was verified by bleaching bilayer-incorporated Rhodamine DHPE. Immediately after applying the bleaching laser to a defined circular ROI, a marked decrease in the fluorescence signal detected within this defined region was observed (1). Due to lateral diffusion of unbleached Rhodamine DHPE, the fluorescence signal recovered (2, 3) until finally almost reaching its initial level (4). Confocal images on the left show FRAP records of a supported bilayer composed of 73.0 mol% POPC, 26.0 mol% cholesterol, and 1.0 mol% Rhodamine DHPE. The diagram on the right depicts the corresponding intensity measurement of the selected ROI. Scale bars: 20 µm.

Binding of Myosin-XXI to Lipid Bilayers

After ATPase activity and motility of FL-XXI had been tested in gliding filament assays on nitrocellulose surfaces, filament gliding was intended to be reproduced on lipid bilayers composed of bovine brain extract, or a combination of POPC or DOPC with other phospholipids. These other lipids were 9.5 mol% bovine brain extract, or 1.6 mol% to 9.7 mol% of a phosphoinositide (PI(4)P, PI(3,5)P_2, or PI(4,5)P_2). Bovine brain extract and the mentioned phosphoinositides were chosen as myosin-XXI binding to them had been demonstrated before (Batters *et al.*, 2014). POPC/Rhodamine DHPE bilayers were used as negative controls.

In addition to the investigation of the behavior of the actin-myosin-XXI complex, bilayer binding of myosin-XXI alone was tested with the help of FRAP experiments.

1. Investigation of the F-Actin-Myosin-XXI Complex:

In a first approach adapted from Zot *et al.* (1992), the procedure of gliding filament assays on nitrocellulose was transferred to supported lipid bilayers: at first 0.1 µM to 7.5 µM myosin-XXI in AB^- was injected into a flow chambers in which an SLB had been prepared. Following this, 8.6 nM (monomer concentration) FITC-labeled F-actin in AB^- or AB^-/BSA was flushed into the flow cell. After Rigor Buffer was added and actin binding was verified by inspection with a TIRF microscope using a 488 nm laser and a 100x oil immersion objective, Motility Buffer was injected and filament behavior was observed. In some experiments, the aforementioned procedure was complemented by blocking with AB^-/BSA to prevent protein binding to the glass surface at areas not completely bilayer-covered. Furthermore, experiments omitting myosin-XXI addition were performed to assure actin´s inability to bind to lipid bilayers in the absence of myosin.

The second method for binding F-actin-myosin-XXI complexes to planar lipid bilayers was adapted from Pyrpassopoulos *et al.* (2012). 0.5 µM to 7.5 µM myosin-XXI and 8.6 nM to 28.7 nM (monomer concentration) FITC-labeled F-actin were premixed in an ATP-supplemented buffer (Motility Buffer or KMg Activation Buffer) and incubated on ice for 3 min. The mixture was then added to a supported or a tethered lipid bilayer and the sample was observed using the TIRF microscope.

2. Investigation of Myosin-XXI:

In two additional set-ups, bilayer binding of FL-XXI in the absence of F-actin was studied. Here, the diffusive behavior of a fusion protein of FL-XXI and eGFP was investigated with the help of FRAP utilizing a 488 nm laser for imaging and a 405 nm laser or bleaching. Bilayers studied consisted of bovine brain extract and 1.2 mol% Rhodamine DHPE.

In the first experimental set-up, myosin-XXI was added to readily formed SLB. 10 nM to 15 µM myosin-XXI in aqueous buffer (Rigor Buffer without BSA, Lipid Buffer 500, or Lipid Buffer 150) was

carefully injected into the flow cell and incubated at RT for at least 3 min. FRAP tests of the bilayer and of myosin-XXI were repeatedly performed over a time span of several hours. It was further investigated whether rinsing the flow chamber with buffer after incubation of myosin-XXI influenced myosin´s diffusive behavior. In addition to the procedure described so far, in some experiments the impact of blocking with AB^-/2x BSA prior to myosin application was tested.

To set-up the second type of experiment, 5 nM to 5 µM myosin-XXI and 0.1 mg/ml to 0.4 mg/ml lipid vesicles were mixed in buffer (Lipid Buffer 500 or Lipid Buffer 150), and the mixture was incubated at RT for 10 min. All vesicles used in this type of experiment had been treated with ultrasound at RT for 10 min. Before myosin-lipid mixture was injected into a flow cell, the flow cell was rinsed with buffer. The sample was left to incubate at RT for at least 30 min. Bilayer formation was surveyed over a time period of several hours using the confocal microscope and a 100x oil immersion objective. In some experiments, bilayer formation was promoted by applying an osmotic shock to the vesicles by rinsing the flow chamber with H_2O.

3.5.4 Co-Sedimentation Assays

Co-sedimentation assays were performed to test if proteins intended to be investigated in SLiC assays are capable of binding lipid vesicles.

Experimental procedure was adapted from Spudich *et al.* (2007). In summary, 2 µM protein and 0.2 mg/ml unilamellar vesicles were mixed in Lipid TBS, and incubated at RT for 10 min. Following this, samples were centrifuged at 4°C at 160,000 x g for 20 min. Supernatants were carefully removed from the samples, and pellets were resuspended in Lipid TBS. Supernatants and resuspended pellets were then subjected to SDS-PAGE. After imaging of gels with a gel imaging system, intensities of the protein bands were determined with the help of Image Lab 5.0 software (Bio-Rad). Vesicles used in co-sedimentation assays were identical to the ones utilized in SLiC assays, i.e. lipid composition and treatment prior to experimental use correspond to the descriptions given in the following subsection.

3.5.5 Single Liposome Curvature Assays

Once protein binding to vesicular bilayers had been verified in co-sedimentation assays, proteins were further investigated in Single Liposome Curvature assays to identify a potential curvature sensitivity of binding events (Figure 28).

As negative control, SLiC assays with streptavidin conjugated to Alexa Fluor® 488 (Thermo Fisher Scientific) were performed (Hatzakis *et al.*, 2009; Larsen *et al.*, 2015). As positive control, experiments with eGFP-eNBAR fusion protein were carried out (Bhatia *et al.*, 2009). Finally, lipid binding behavior of eGFP fusion proteins with FL-XXI and with myosin-XXI fragments was investigated.

Flow cells prepared for SLiC assays were always assembled using PEG-coated coverslips in order to minimize nonspecific protein binding to the glass surface and to avoid deformation of vesicles by immobilization (Bendix *et al.*, 2009). In order to quantify diameters of the utilized unilamellar vesicles, size calibration was performed with the help of Stochastic Optical Reconstruction Microscopy (STORM).

PEG Coating of Coverslips

For the purpose of PEG coating, coverslips were silanized using Vectabond™ reagent (Vector Laboratories) following manufacturer´s instructions. In the next step, a 100 mM $NaHCO_3$ solution was freshly prepared to dissolve a mixture of 250 mg/ml PEG succinimidyl carbonate (alpha-methoxy-omega-carboxylic acid succinimidyl ester poly(ethylene glycol)-5000, Iris Biotech; called PEG-NHS here) and 12.5 mg/ml biotinylated PEG (alpha-biotin-omega-carboxy succinimidyl ester poly(ethylene glycol)-5000, Iris Biotech; called Biotin-PEG here). Coverslips were then covered with the PEG-NHS/Biotin-PEG solution and incubated at RT for 3 h. Once incubation was finished, coverslips were washed in 100 mM $NaHCO_3$ and H_2O to remove unbound PEG. Coated coverslips were stored in a desiccator at RT until they were used for the construction of flow cells.

Sample Preparation and Imaging

For all SLiC assays, unilamellar vesicles composed of 97.2 mol% bovine brain extract, 1.2 mol% Rhodamine DHPE, and 1.6 mol% Biotin DHPE were prepared. Before resulting lipid solutions were used in SLiC assays, they were treated in an ultrasonic bath at RT for 10 min, and extruded through a polycarbonate membrane of 800 nm pore diameter 21 times. Biotin DHPE contained in the lipid mixture enabled vesicles to bind to Biotin-PEG molecules on the surface of coated coverslips via a biotin-streptavidin-biotin link. Sample preparation techniques were adapted from Bhatia *et al.* (2009).

For all proteins except for Alexa Fluor® 488 streptavidin, 2 nM to 320 nM protein and 0.1 µg/ml vesicles were mixed in degassed Lipid TBS and left to incubate at RT for 1 h. Meanwhile, a flow cell with a PEG-coated coverslip was prepared. Immediately after construction, chambers were filled with 15.1 µM BSA in Lipid TBS and left to incubate at RT for 15 min. Following this, flow chambers were rinsed with Lipid TBS, and 1.7 µM streptavidin in PBS was flushed in. After another 15 min of incubation, the flow cell was again rinsed with Lipid TBS, the protein-lipid mixture was added, and the chamber was sealed with vacuum grease. The sample was again incubated for 15 min to allow vesicles to bind to the PEG surface. This first method of sample preparation was also applied when assays solely with vesicles were performed, e.g. when samples for size calibration were prepared. In these cases, lipid concentrations ranged from 10 ng/ml to 1 µg/ml.

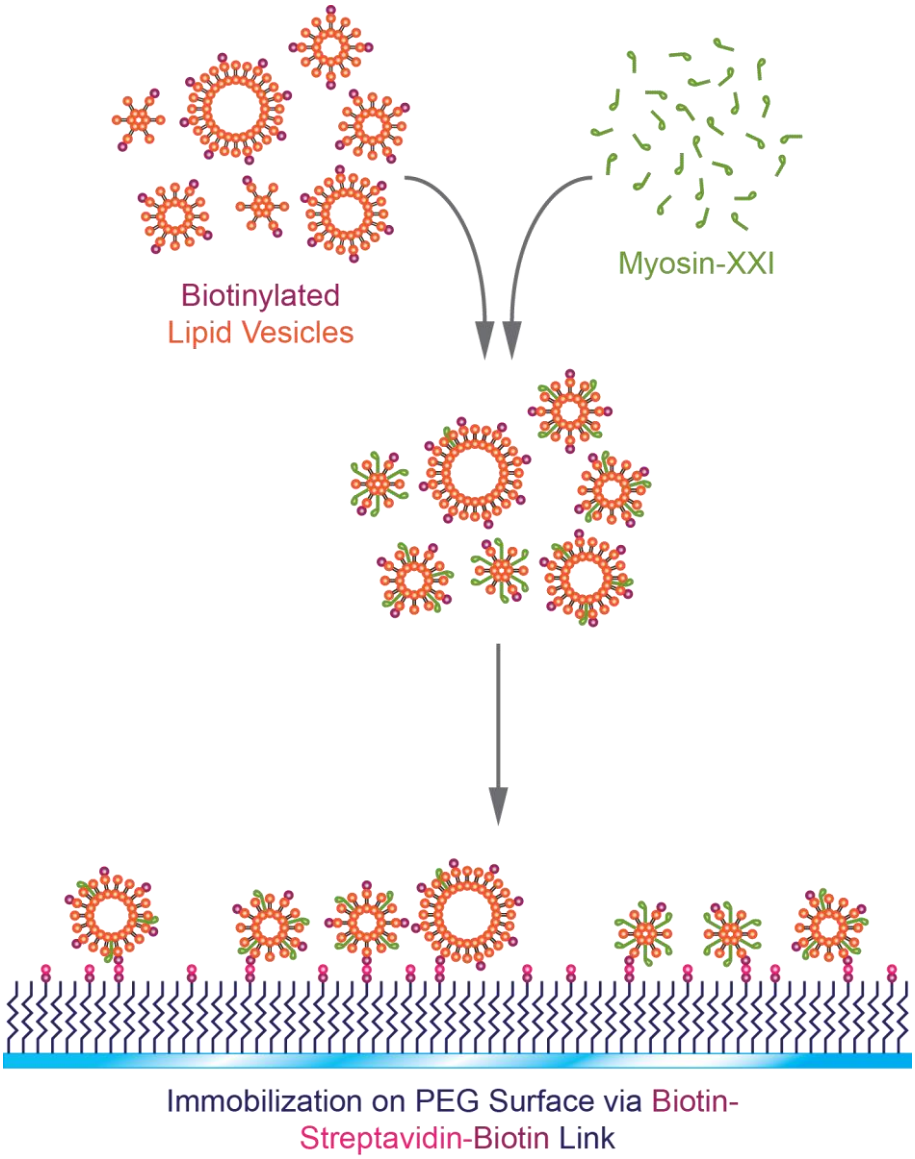

Figure 28 SLiC assay. With the help of Single Liposome Curvature assays, proteins were tested for their capability to sense bilayer curvature. For this purpose, the protein under investigation was incubated with a lipid solution composed of vesicles of various diameters. Further, protein and vesicles were labeled with distinguishable fluorophores. As vesicular bilayers contained Biotin DHPE, vesicles could be immobilized on a biotinylated PEG surface via biotin-streptavidin-biotin links. Using confocal microscopy, surface densities of vesicle-bound protein could then be determined.

For SLiC assays with Alexa Fluor® 488 streptavidin, a modified procedure of sample preparation was applied. The reason for this was the fact that Alexa Fluor® 488 streptavidin bound to the vesicular bilayers by binding to Biotin DHPE. As Biotin DHPE also served as link between vesicles and the PEG surface, premixing of Alexa Fluor® 488 streptavidin and lipid solutions impeded vesicle immobilization on the PEG surface. Thus, once PEG surfaces were incubated with 15.1 µM BSA and 16.7 µM streptavidin, flow chambers were three times flushed with Lipid TBS to remove unbound streptavidin, and 0.1 µg/ml unilamellar vesicles were injected. Samples were incubated at RT for 15 min and rinsed with Lipid TBS afterwards. Then, 1 µM Alexa Fluor® 488 streptavidin in Lipid TBS was rinsed into the flow chambers, and samples were incubated for 30 min. Unbound Alexa Fluor®

488 streptavidin was removed by rinsing the flow cell with Lipid TBS three times, and chambers were sealed with vacuum grease.

Imaging of samples was performed with the confocal microscope using the 100x oil immersion objective. Protein and lipid vesicles were recorded in two distinct channels. Rhodamine linked to DHPE was excited with a 544 nm laser, eGFP and Alexa Fluor® 488 fluorescence were excited by a 488 nm laser.

Data Analysis

All images taken were processed and analyzed in a multi-step procedure modified from Bhatia *et al.* (2009). At first, image files were converted from ND2 format to TIF format using NIS-Elements Advanced Research 4.30 software. Analysis was then carried out in ImageJ 1.46r: the GaussFit OnSpot plugin was applied to fit 3D Gaussian profiles to all intensity peaks present in an image. Fit parameters, integrated intensities, and positions of the corresponding intensity maxima were automatically listed into text files. As binding of protein to a lipid vesicle was identified as a colocalization of the intensity peaks in the protein channel and in the lipid channel of one confocal image, positions of intensity maxima in associated TIF files were matched. For this purpose, a LabVIEW program was designed which calculated the distance between maxima positions in the two imaging channels. A maximum distance of $\sqrt{2}$ pixels was applied to identify binding events, and data of colocalizing intensity maxima were saved in another text file. In a second analysis step, positions of all intensity maxima in each TIF file were determined in ImageJ, and position and amplitude of every maximum were listed in a text file. Again using the above-mentioned LabView program, colocalizing peaks in the protein and the lipid channel were assigned and their data were saved. Finally, lists containing Gaussian profile parameters and lists containing intensity amplitudes were merged into one file using the LabVIEW program one more time. Identical binding events could be identified due to their identical positions of intensity maxima.

With the help of the data contained in this merged file, each vesicle could now be assigned a fluorescence intensity I_V of the vesicle itself and an intensity I_P of the protein molecules bound to its surface. According to Kunding *et al.* (2008), the diameter d of a vesicle imaged by confocal microscopy can be calculated from:

$$d = c \cdot \sqrt{I_V} \tag{12}$$

with c representing a constant calibration factor.

As vesicular bilayers possess a spherical shape, their surface area A_V is determined by the diameter d and thus can be calculated from the intensity I_V:

$$A_V = \pi \cdot d^2 = \pi \cdot c^2 \cdot I_V \tag{13}$$

Equation (13) describes the relation between the surface area of a uniformly labeled spherical shell and the fluorescence signal in confocal microscopy.

Since proteins binding to immobilized vesicles form a spherical shell, (13) is equally valid for the fluorescence intensity signal I_P originating from bound proteins:

$$A_P \propto I_P \tag{14}$$

In the above equation, A_P denotes the surface area formed by the protein envelope.

Assuming a uniform distribution of protein bound to a vesicular bilayer surface, the number N_P of bound protein molecules satisfies the following relation:

$$N_P \propto A_P \tag{15}$$

In conclusion, N_P is directly proportional to the fluorescence intensity I_P:

$$N_P \propto I_P \tag{16}$$

As the surface density ρ of protein molecules bound to a vesicle is defined as the ratio of protein molecule number to vesicle surface area

$$\rho = \frac{N_P}{A_V} \tag{17}$$

the ratio ρ_R of fluorescence intensities I_P to I_V is a direct measure for this surface density:

$$\rho \propto \rho_R = \frac{I_P}{I_V} \tag{18}$$

The course of the intensity ratio ρ_R as a function of the vesicle diameter d illustrates the binding affinity of the tested protein for bilayers of different curvature and thus identifies proteins as curvature sensors or non-sensors. When the curve $\rho_{R(d)}$ is normalized to a value $\rho_{R(d^*)}$ at a specific vesicle diameter d*, curvature sensitivity of different proteins can be compared. Therefore, curves $\rho_{R(d)}$ obtained for the investigated proteins were normalized to the mean value $\overline{\rho_R}$ of intensity ratios at vesicle diameters between 250 nm and 350 nm resulting in the calculation of normalized protein densities $\rho_{norm(d)}$:

$$\rho_{norm(d)} = \frac{\rho_{R(d)}}{\overline{\rho_R}} \tag{19}$$

Before curves $\rho_{norm(d)}$ were deduced from the data obtained from image analysis, data had to be filtered for noise. Noise could for example result from protein aggregation at areas of defective PEG coating. Hence, data were filtered by the following parameters: ratio $A = \sigma_x/\sigma_y$ of Gaussian profile widths σ_x in x-dimension and σ_y in y-dimension, total Gaussian profile width σ, minimum integrated intensity, and minimum amplitude of intensity maxima. In addition, values $\rho_{R(d)}$ deviating by more than a factor of 7.5 from the mean of their 8 adjoining data points were excluded.

Size Calibration of Unilamellar Vesicles

To quantify diameters of unilamellar vesicles used in SLiC assays, calibration measurements were carried out. As stated in equation (12), the diameter d of a fluorophore-labeled vesicle equals the product of a constant calibration factor c and the square root of the intensity signal I_V detected from that vesicle in confocal microscopy. Accordingly, a calibration factor can be determined when related intensity values I_v and diameters d can be assigned to each other. This assignment was implemented by consecutive imaging of identical fields of view of samples of immobilized unilamellar vesicles in confocal microscopy and in STORM.

Intensity values I_V were determined with the help of confocal microscopy as described above. Diameters d were determined by using a STORM system included in the Nikon A1R confocal microscopy set-up and a 100x oil immersion objective. For STORM, the 544 nm laser was utilized. The application of an additional laser of different wavelength for fluorophore deactivation was not required as rhodamine exhibited fluorescence intermittency, i.e. rhodamine switched between its emitting and its dark state while constantly irradiated by the 544 nm laser. To avoid overlapping of fluorescence signals from adjacent vesicles, unilamellar vesicles were imaged at a lipid concentration of 10 ng/ml. A reduction of photobleaching was achieved by a buffer exchange applied directly before imaging: Lipid TBS in the flow chambers was replaced by STORM Buffer which contained an oxygen scavenging system.

Images recorded in STORM mode were analyzed in the following procedure: At first, fluorophore positions were reconstructed with the help of NIS-Elements Advanced Research 4.30 software. Coordinates of fluorophore positions were saved in a text file which was then processed in ImageJ 1.46r. Employing a self-written macro, single fluorophores were assembled to 2D objects. In the next step, Gaussian Blur filter was applied, and ellipses were fitted to each 2D object with the help of automated particle analysis. Positions of the 2D objects (i.e. vesicle positions) and lengths of the major and minor axes of the correlating ellipses were saved in a text file. The diameter d of each vesicle could then be calculated as:

$$d = \frac{a+b}{2} - r \tag{20}$$

with a representing the length of the major ellipse axis and b the length of the minor axis. The variable r represents the approximate size of a single rhodamine molecule imaged by the STORM system. Subtraction of r was required as rhodamine molecules detected at the circumference of the xy-projection of a vesicle resulted in an apparent increase in vesicle size. As only intact lipid vesicles were intended to be included in the analysis, only objects with a maximum axis ratio a/b of 2.0 were taken into account.

Vesicle positions in confocal and in STORM images were matched to generate a list of correlating intensities I_V and diameters d. For each data pair (d_i,I_{Vi}), a calibration factor c_i was calculated

according to equation (20), and the final calibration factor c was determined as the arithmetic mean of all calibration factors c_i.

4 Results

4.1 Cellular Localization of Myosin-XXI in Transfected Mammalian Cells

In order to gain information about potential cellular functions of distinct myosin-XXI domains, transfection experiments with HeLa and COS-7 cells were performed.

Myosin-XXI constructs investigated in *in vivo* experiments were designed considering the structural motifs and domains identified within myosin-XXI (Figure 29, Table C.1).

	Cytoplasm			Plasma Membrane	Filopodia
	Diffuse	Clusters	Spherical		
FL-XXI	✓	✓	✓	✓	✓
Trunc-XXI	✓	✓	✓	✓	✓
aa 46-1050	✓	✓	✓		
aa 46-800	✓	✓	✓		
aa 1-753	✓	✓	✓		
aa 1-704	✓	✓	✓		
aa 46-753	✓	✓	✓		
aa 46-704	✓	✓	✓		
aa 730-1050	✓				
XXI-830 Tail	✓				
XXI-930 Tail	✓				
aa 730-936	✓				
aa 830-936	✓				
aa 730-836	✓				

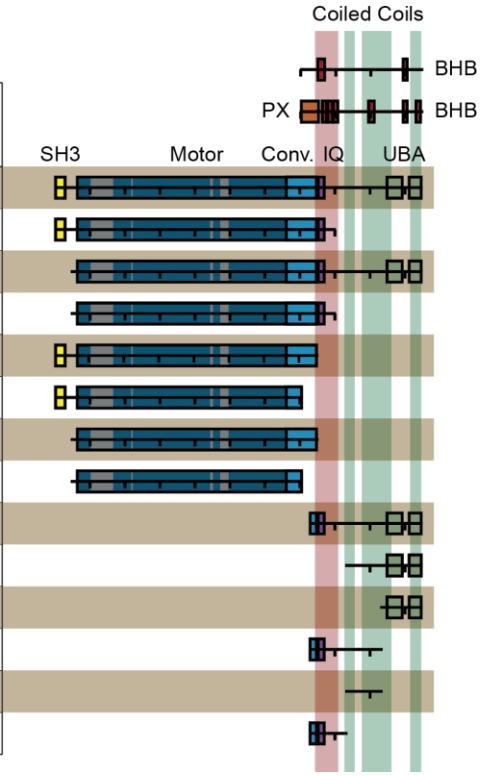

Figure 29 Myosin-XXI constructs investigated in transfection experiments with HeLa and COS-7 cells. The table above lists all parts of the myosin-XXI DNA sequence that were transfected into mammalian cells (FL-XXI: full-length myosin-XXI of aa 1-1050, Trunc-XXI: motor truncation of aa 1-800, XXI-830 Tail: tail fragment of aa 830-1050, XXI-930 Tail: tail fragment of aa 930-1050). Myosin DNA was cloned into vectors already containing fluorophore DNA. The respective fusion proteins exhibited different cellular localizations within HeLa and COS-7: within the cytoplasm, fusion proteins were found to display a diffuse distribution frequently associated with staining of the nucleus. Additionally, FL-XXI and myosin-XXI fragments containing major parts of the motor domain accumulated in clusters in the vicinity of the nucleus and in spherical structures. FL-XXI and Trunc-XXI exhibited the most striking localization pattern forming protein populations along the plasma membrane and along the shafts and at the tips of filopodia. The schematic overview on the right illustrates the so far identified structural motifs encoded by the corresponding myosin-XXI constructs.

According to previous studies of our research group (Batters *et al.*, 2012, 2014), myosin-XXI possesses an N-terminal SH3-like domain (aa 11-37), followed by the catalytic motor domain (aa 65-747) including a converter region at aa 662-747. Starting at aa 705, i.e. already beginning within the converter domain, a PX domain (aa 705-752) and several other potential lipid binding domains have been identified. Furthermore, an IQ motif (aa 754-769), several potential

oligomerization sites and two UBA domains have been located in the neck and tail region of myosin-XXI. For the oligomerization site at aa 744-809, dimerization of full-length myosin-XXI has already been demonstrated.

In experiments with immortal mammalian cells, *in vivo* localization of myosin-XXI and myosin-XXI fragments depending on the structural motifs contained in the respective constructs were examined. For this purpose, transfections with plasmids encoding a fusion protein of a fluorophore (ZsGreen1, eGFP, or DsRed2) and myosin-XXI or a myosin-XXI fragment were performed. A summary of all myosin-XXI constructs tested can be found in Figure 29. In addition to transfections with plasmids encoding myosin-XXI fusion proteins, control experiments were performed with plasmids just containing fluorophore DNA.

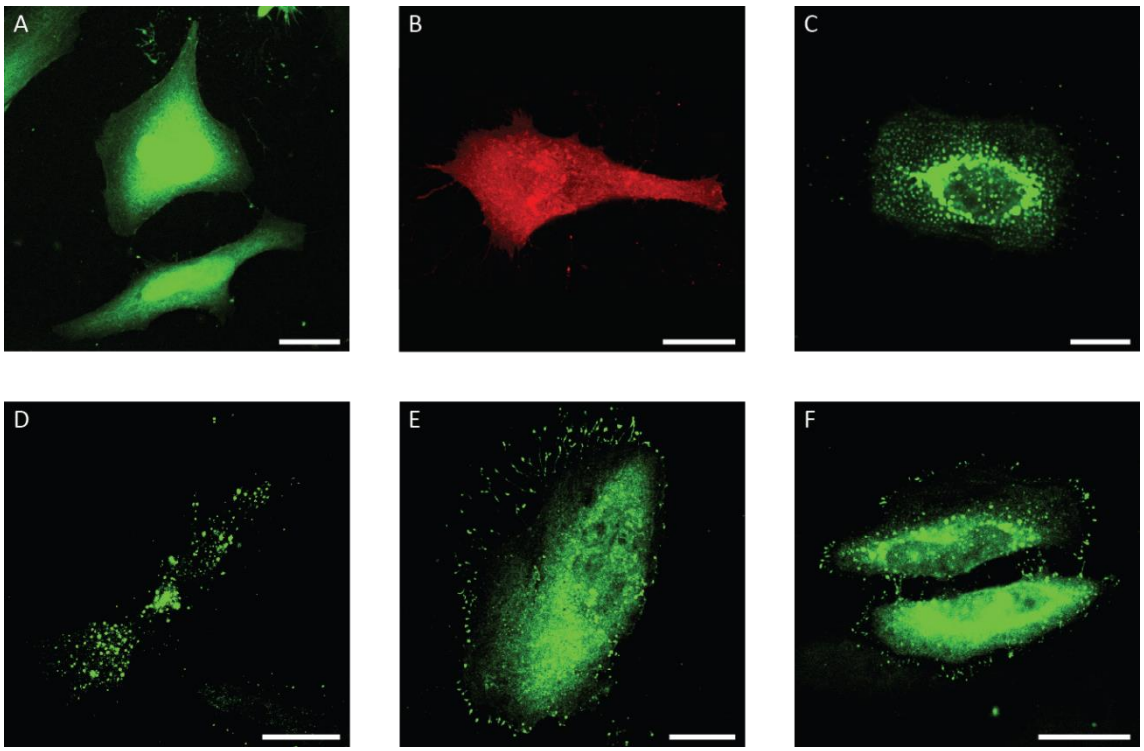

Figure 30 Localization of FL-XXI and myosin-XXI fragments in transfected HeLa cells. In transfected mammalian cells, fusion proteins of a fluorophore and FL-XXI or a myosin-XXI fragment were detected at different cellular localizations depending on the structural motifs of myosin-XXI present in the protein. Above, representative confocal images of transfected HeLa cells are shown. (A) In control experiments with plasmids solely encoding a fluorophore (here: ZsGreen1), uniform staining of the cytoplasm with frequent staining of the nucleus was detected. (B) A diffuse cytoplasmic distribution was displayed by all myosin-XXI fusion proteins tested and was the only localization found for myosin-XXI tail constructs (here: aa 730-936). (C) Accumulations in clusters close to the nucleus were found for all constructs containing the major part of the myosin-XXI motor domain (here: FL-XXI) and were related to high expression levels of fusion proteins. (D) Fusion proteins containing the major part of the motor domain (here: FL-XXI) also formed spherical accumulations in the cytoplasm. (E, F) FL-XXI (E) and Trunc-XXI (F) were the only constructs capable of concentrating along the plasma membrane and within filopodia. Scale bars: 20 µm.

When inspected by confocal microscopy, cells solely transfected with fluorophore encoding plasmids exhibited a uniform staining of the cytoplasm associated with a frequent staining of the nucleus. In fact, an identical staining pattern was observed for all plasmids encoding fusion proteins of the

myosin-XXI tail constructs (Figure 30, Figure 31). Tail fragments investigated were aa 730-1050, aa 830-1050 (called XXI-830 Tail here), aa 930-1050 (called XXI-930 Tail here), aa 730-936, aa 730-836, and aa 830-936.

For the other myosin-XXI constructs studied, apart from a diffuse cytoplasmic distribution, four additional cellular localizations were identified: clusters in the vicinity of the nucleus, spherical accumulations within the cell body, spherical accumulations along the plasma membrane, and accumulations within the shafts and inside the tips of filopodia. All of these cellular localizations were found in both, HeLa and COS-7 cells (Figure 30, Figure 31). Clusters in the vicinity of the nucleus were discovered to be a result of strong protein expression, with their incidence increasing with increasing concentrations of plasmid DNA applied during the transfection procedure. Further, clusters were only found in cells which also contained spherical myosin-XXI accumulations within the cytoplasm.

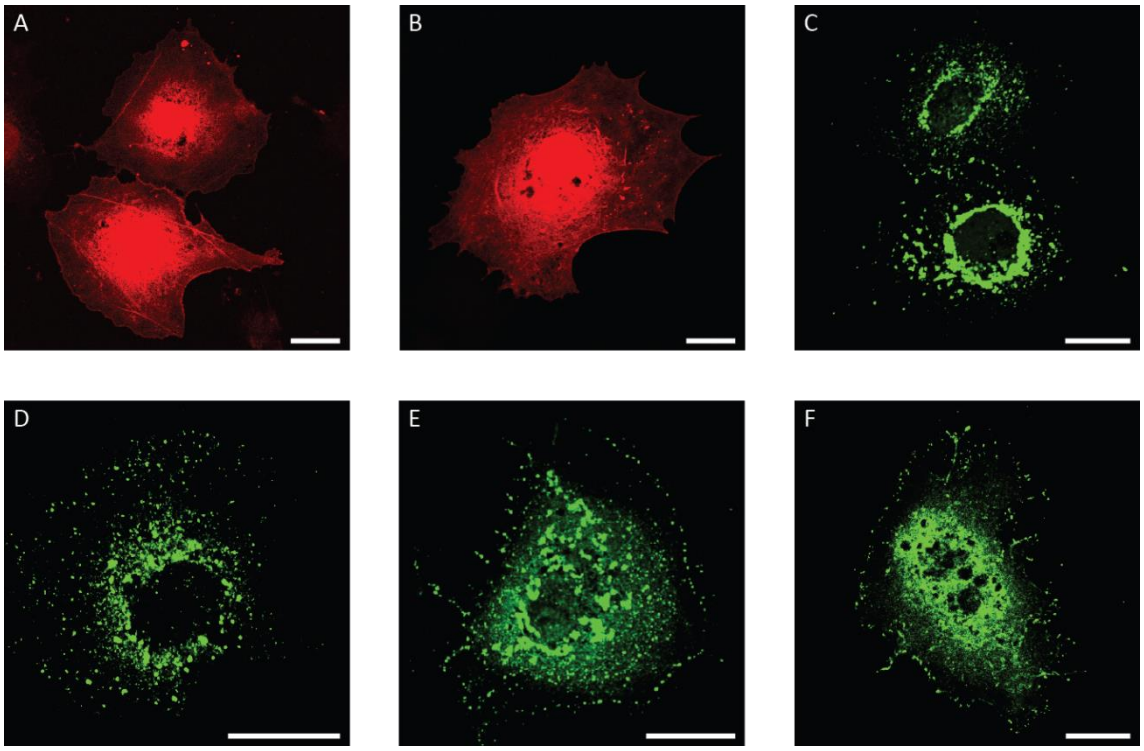

Figure 31 Localization of FL-XXI and myosin-XXI fragments in transfected COS-7 cells. As in the case of HeLa cells, localization of fluorophore-fused FL-XXI and myosin-XXI fragments in transfected COS-7 cells was found to depend on the myosin-XXI structural motifs contained in the fusion proteins. Above, representative confocal images of transfected COS-7 cells are shown. (A) In control experiments, expression of fluorophore (here: DsRed2) caused a uniform staining of the cytoplasm associated with nucleus staining. (B) Expression of myosin-XXI tail constructs (here: XXI-830 Tail) resulted in a homogenous cytoplasmic distribution of fluorescent protein as well. (C, D) Myosin-XXI constructs containing the major part of the motor were additionally detected in clusters in the vicinity of the nucleus (C, here: FL-XXI) and spherical accumulations within the cytoplasm (D, here: aa 1-704). (E, F) FL-XXI (E) and Trunc-XXI (F) were detected within filopodia and in accumulations along the plasma membrane. Scale bars: 20 µm.

Myosin-XXI constructs located at one of the above-mentioned defined localizations comprised the full-length molecule (FL-XXI), and three motor truncations: Trunc-XXI (comprising aa 1-800) which also contained part of the myosin tail, the motor truncation of aa 1-754 which

terminated right after the converter, and the motor truncation of aa 1-704 which was truncated within the converter domain N-terminal of the PX domain. Furthermore, defined localization patterns were also observed when the first 45 amino acids, i.e. the SH3-like domain, were deleted from these four constructs.

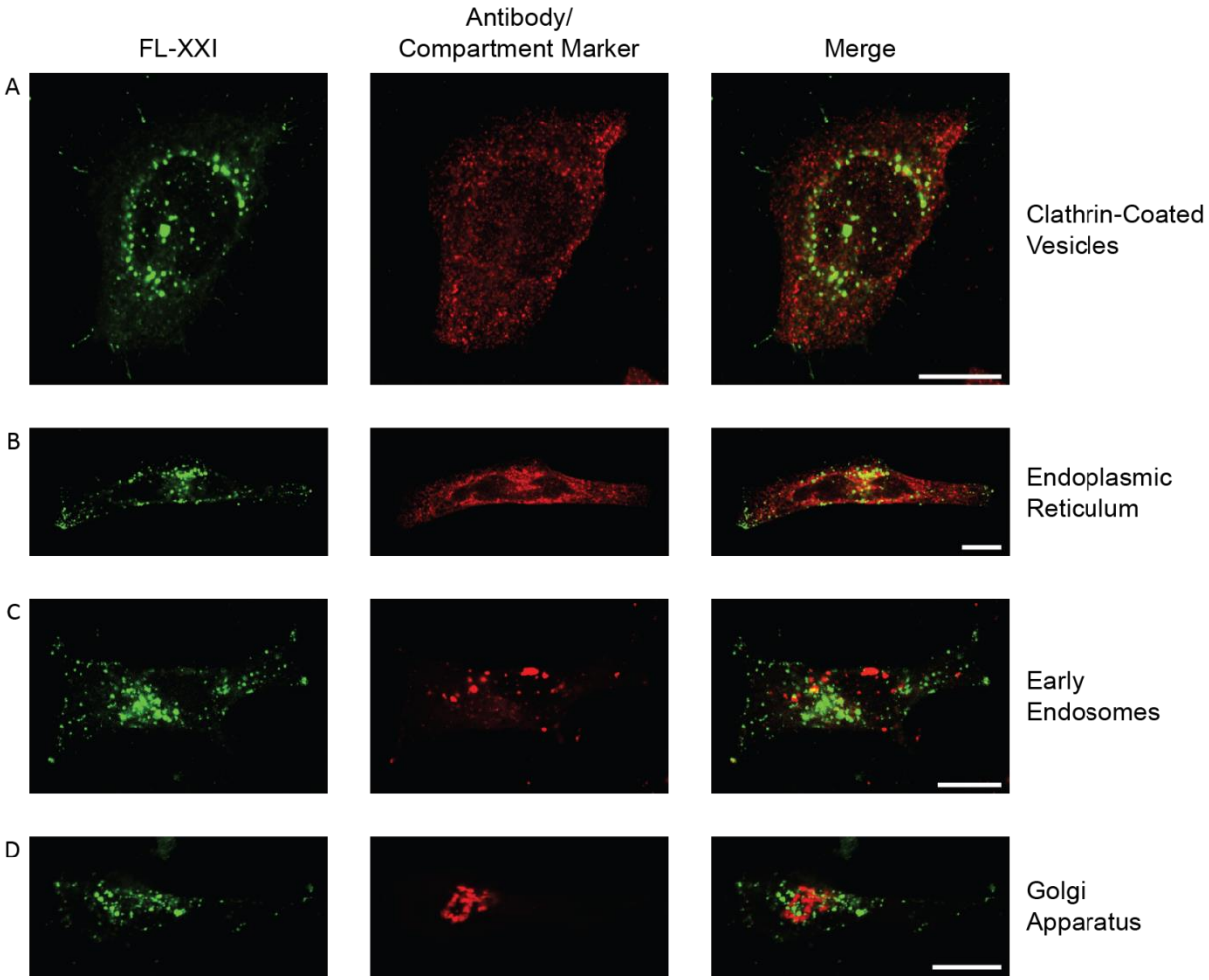

Figure 32 Staining of clathrin-coated vesicles, endoplasmic reticulum, early endosomes and Golgi apparatus in FL-XXI-transfected HeLa cells. (A) Clathrin-coated vesicles (red) were stained by application of anti-clathrin heavy chain antibody and cyanine 3-conjugated secondary antibody. (B, C, D) Endoplasmic reticulum, early endosomes and Golgi apparatus (red) were stained in co-transfection experiments with baculoviruses encoding markers for the respective organelle. No colocalization of full-length myosin-XXI (green) with either one of the stained organelles was discovered. Scale bars: 15 µm.

To summarize, while fluorophore-labeled myosin-XXI tail fragments displayed the identical cellular localization as mere fluorophores, the presence of a major part of the motor domain resulted in a more differentiated cellular distribution of fusion proteins. The respective part of the motor comprised almost the complete head domain and thus included the ATP binding loop, switch I, switch II, the relay loop, and half of the converter.

While all motor-containing constructs were observed to accumulate in clusters and spherical structures within the cytoplasm, only FL-XXI and Trunc-XXI (i.e. a minimum construct of SH3-like

domain, motor and the neck and tail region from aa 748 to aa 800) additionally generated accumulations within filopodia and along the plasma membrane.

Further investigation of filopodial protein accumulations by live imaging and statistical analysis of fixed cells, resulted in additional findings: in transfected HeLa cells, accumulations of FL-XXI and Trunc-XXI were present in both, substrate-attached and freely moving filopodia. Moreover, statistical analysis of 20 HeLa cells for each of these two constructs, i.e. of 1231 filopodia of FL-XXI-transfected cells and 1302 filopodia of Trunc-XXI-transfected cells respectively, revealed that myosin-XXI accumulations in filopodia tips were present in 54 % of filopodia of FL-XXI-transfected HeLa cells, and in 25 % of filopodia of Trunc-XXI-transfected HeLa cells. However, it needs to be noticed that despite equal transfection conditions, HeLa cells transfected with Trunc-XXI exhibited a lower average fluorescence intensity signal per area of cell body cross section (~900 a.u./µm^2) than FL-XXI-transfected ones (~1,500 a.u./µm^2). Consequently, the average expression level in Trunc-XXI-transfected HeLa cells was lower than in FL-XXI-transfected ones. Thus, in comparison to cells expressing FL-XXI, amounts of fusion protein available for the formation of filopodial accumulations were lower in cells expressing Trunc-XXI.

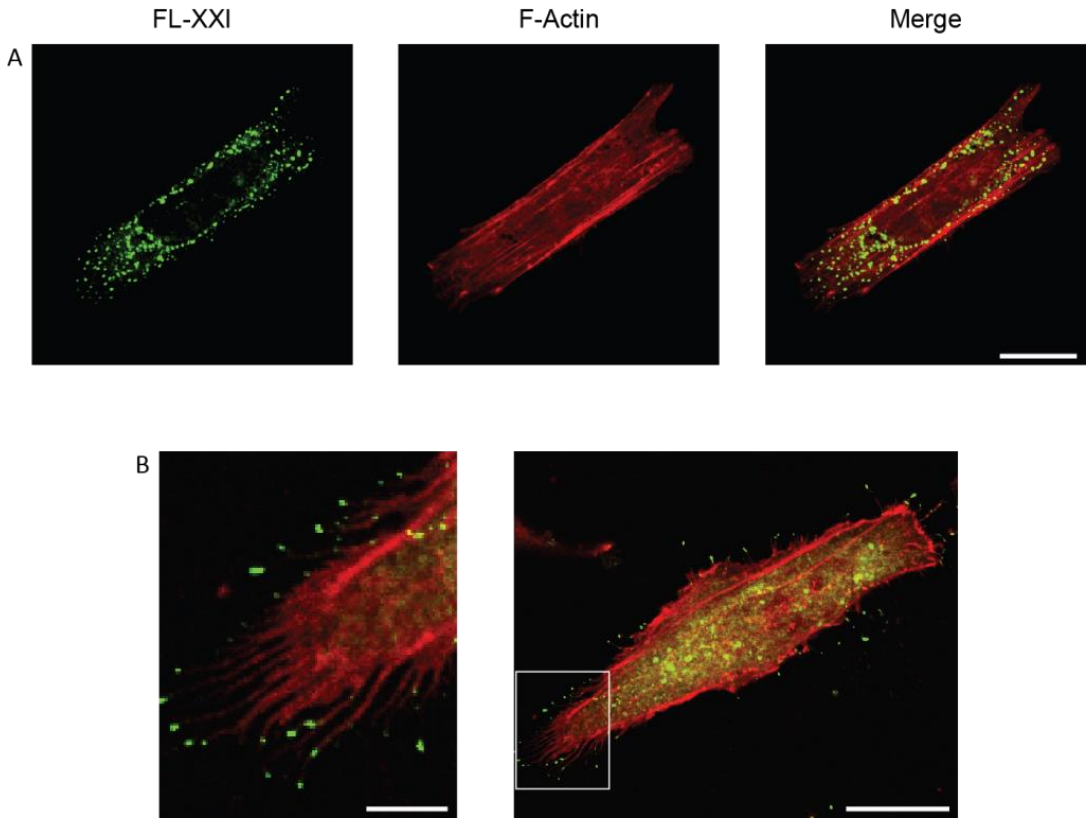

Figure 33 F-actin staining with lifeact-RFP fusion protein within FL-XXI-transfected HeLa cells. Co-transfection of HeLa cells with plasmids encoding FL-XXI (green) and lifeact-RFP fusion protein (red) were performed to simultaneously visualize full-length myosin-XXI and actin filaments. (A) No colocalization of FL-XXI and the actin cytoskeleton within the cell body was observed. (B) However, FL-XXI was detected within filopodia displaying striking accumulations at the filopodia tips. Scale bars: 20 µm, for magnified section: 5 µm.

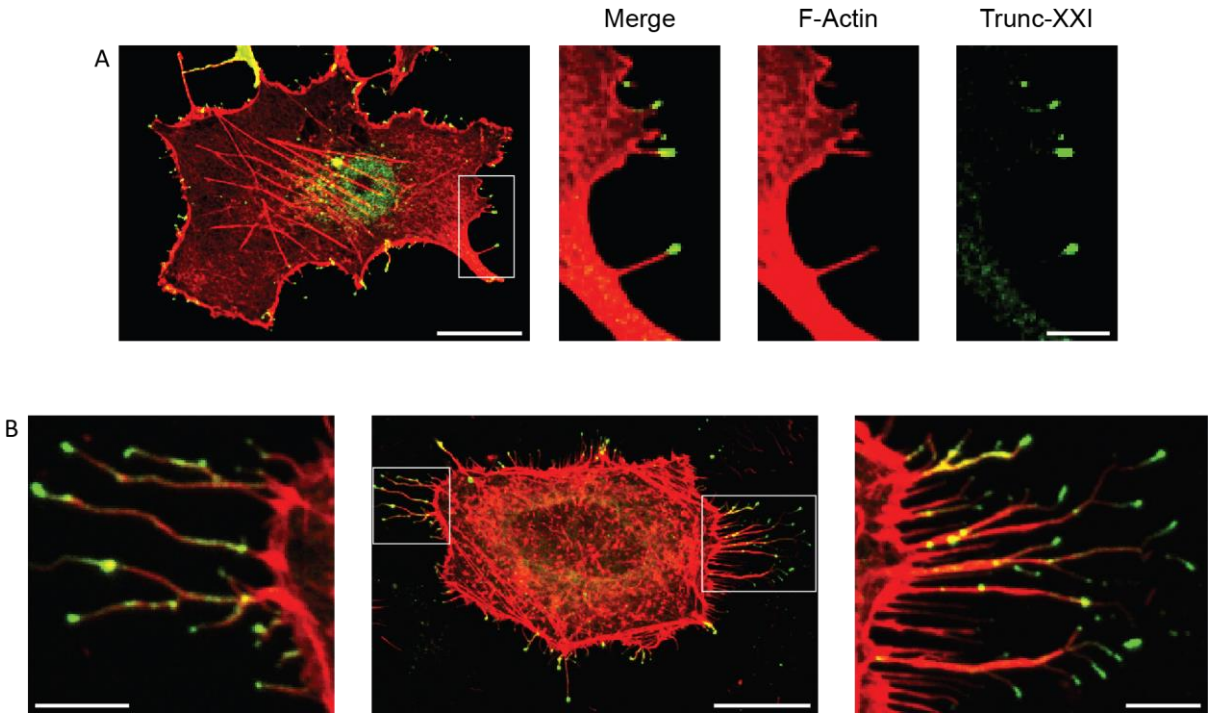

Figure 34 F-actin staining with phalloidin-TRITC within FL-XXI- and Trunc-XXI-transfected HeLa and COS-7 cells. The actin cytoskeleton of FL-XXI- and Trunc-XXI-transfected (both green) HeLa and COS-7 cells was stained with TRITC-conjugated phalloidin (red) after transfection. (A) A COS-7 cell showing accumulations of Trunc-XXI within filopodia. Phalloidin-TRITC staining revealed that Trunc-XXI localized at the filopodia tips. (B) A HeLa cell expressing FL-XXI. Protein was detected along the shafts of filopodia and at the barbed ends of the intrafilopodial actin cores. Scale bars: 20 µm, for magnified sections: 5 µm.

In order to elucidate the exact localization of FL-XXI and Trunc-XXI in transfected COS-7 and HeLa cells, co-transfection experiments and different staining procedures were carried out.

Co-transfections with baculoviruses encoding markers for early endosomes, endoplasmic reticulum, and Golgi apparatus did not reveal any colocalization of the myosin-XXI constructs with these cellular compartments. Immunostaining of clathrin-coated vesicles yielded the same result (Figure 32).

Actin staining with phalloidin-TRITC and co-transfections with a plasmid encoding a fusion protein of RFP and lifeact, a peptide which binds to the actin cytoskeleton (Riedl *et al.*, 2008), led to the finding that FL-XXI and Trunc-XXI did not colocalize with F-actin in the cell body but colocalized with actin filaments along the whole length of filopodia (Figure 33, Figure 34).

To verify that the observations described above can be assigned to an expression of FL-XXI or Trunc-XXI fusion protein, western blots of lysates of transfected HeLa and COS-7 cells were performed (Figure 35). Application of anti-RCFP antibody confirmed the expression of ZsGreen1 fusion proteins with the molecular weights expected for fusion constructs containing full-length myosin-XXI or the myosin-XXI motor truncation of aa 1-800 respectively.

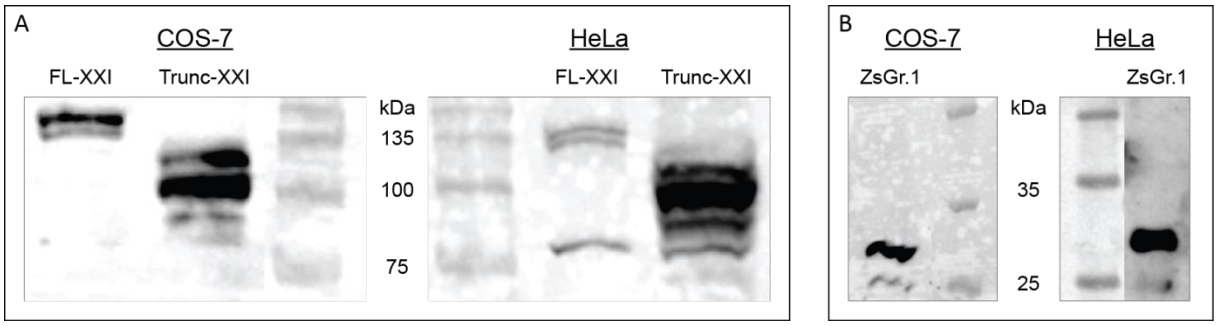

Figure 35 Western blots of lysates of HeLa and COS-7 cells transfected with FL-XXI, Trunc-XXI, or ZsGreen1. To verify expression of the correct protein, transfected HeLa and COS-7 cells were lysed and subjected to western blotting. ZsGreen1 and ZsGreen1 in FL-XXI and Trunc-XXI fusion proteins were detected with the help of anti-RCFP antibody. (A) Detection of FL-XXI and Trunc-XXI fusion protein. Observed bands correspond to the expected molecular weights (FL-XXI: ~140 kDa, Trunc-XXI: ~120 kDa). (B) Detection of ZsGreen1 (ZsGr.1). The resulting protein band is located at ~30 kDa, thus verifying ZsGreen1 expression.

4.2 Dynamics of Myosin-XXI in Mammalian Cells

Live imaging of HeLa cells co-transfected with plasmid encoding lifeact-RFP fusion protein and FL-XXI or Trunc-XXI construct was performed to gain insights into the dynamics of myosin-XXI within a cellular environment.

In live records, two motile myosin-XXI populations were observed in transfected HeLa cells: spherical accumulations of myosin-XXI within the cell body and myosin-XXI-associated structures inside the shafts of filopodia.

Intrafilopodial dynamics of FL-XXI and Trunc-XXI were subsequently subjected to a more detailed evaluation. Thereby, it was found that within filopodia, clusters of myosin-XXI frequently moved from the tip toward the cell body. These moving clusters could clearly be identified in temporally resolved intensity profiles covering the whole length of filopodia (Figure 36). Additionally, tracking algorithms could be applied to the clusters, resulting in speeds of 24.3±15.5 nm/s (mean ± s.d.; 20 tracks) for FL-XXI-transfected cells and 34.6±17.1 nm/s (46 tracks) for Trunc-XXI-transfected cells. Furthermore, it was detected that clusters of myosin moving rearward along the shafts of filopodia frequently elongated and occasionally split up. In contrast to myosin´s rearward movement toward the cell body, movement of myosin-XXI fusion protein toward the filopodia tips could not be resolved in live confocal microscopy. Nevertheless, rearward movement did not result in a permanent disappearance of the protein accumulations in filopodia tips. Instead, apart from decreases in the fluorescence intensity signals in the tips, significant intensity increases were detected (Figure 36).

Furthermore, in addition to myosin-XXI movement within filopodia, stability of myosin-XXI accumulations within filopodia tips was monitored. It was observed that accumulations remained at the tips even throughout phases of filopodial length changes. Determination of the rates of length changes of filopodia with myosin-XXI tip accumulations led to the following results: for FL-XXI, average extension rate of 54 analyzed filopodia was 21.3±13.1 nm/s (mean ± s.d.), and average

retraction rate was 22.8±13.1 nm/s. For Trunc-XXI, changes in length of 113 evaluated filopodia were faster, with an average speed of 28.8±18.1 nm/s when extending, and 25.1±13.6 nm/s when retracting (Figure 37).

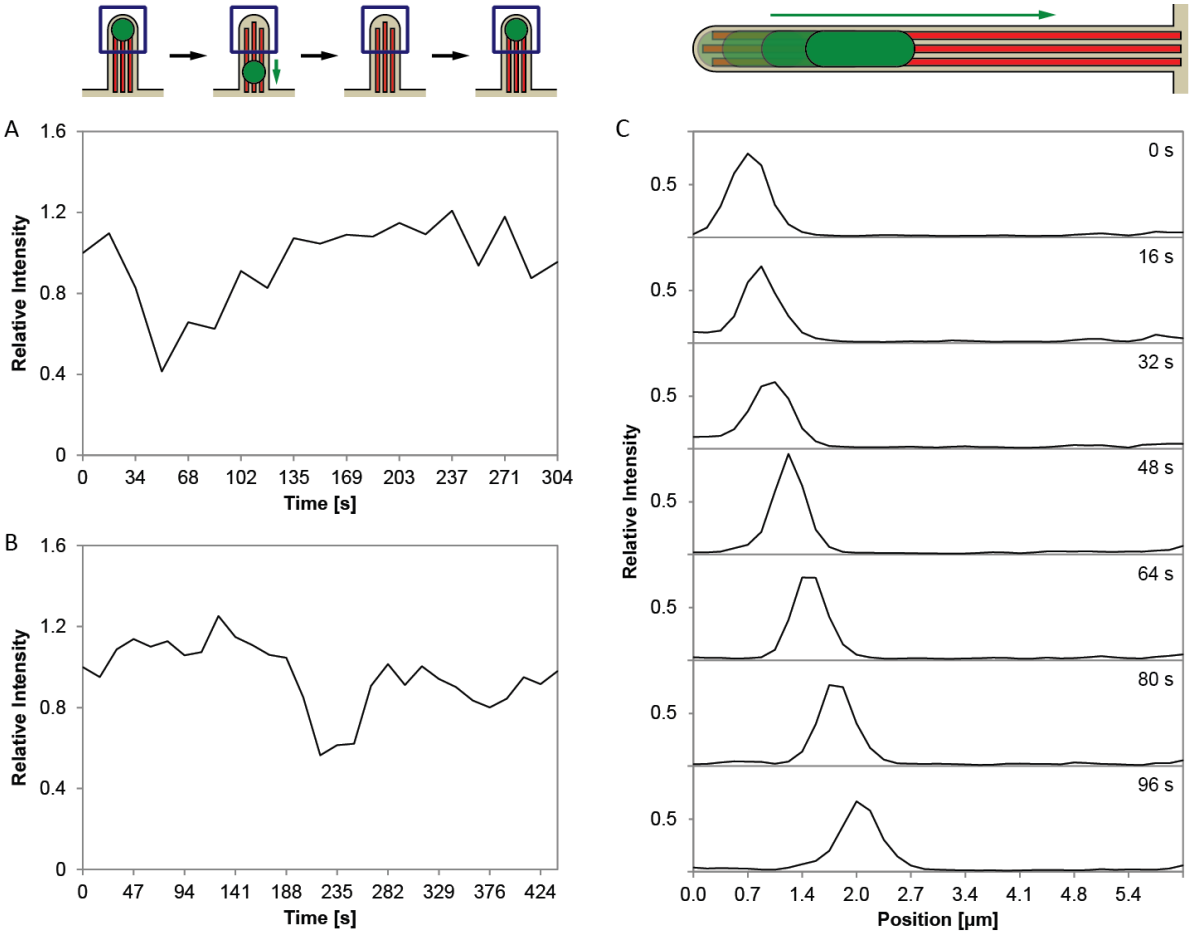

Figure 36 Time course of fluorescence intensities in filopodia of Trunc-XXI-transfected HeLa cells. Fluorescence signals of motile Trunc-XXI populations were measured during phases of constant filopodia length. Illustrations symbolize corresponding movement of Trunc-XXI accumulations (green) along the filopodial actin core (red). The blue box depicts the region of intensity measurements of filopodia tips. (A, B) Representative Intensity signals detected in two filopodia tips of distinct HeLa cells. Following intensity decreases caused by Trunc-XXI travelling rearward to the cell body, intensity signals recovered thus proving forward movement of Trunc-XXI into the filopodia tips. Intensity values were normalized to the first data point. (C) Fluorescence intensity distribution along the whole length of a single filopodium. The position of 0 µm designates the distal end of the filopodium. At the beginning of the measurement (t=0 s), an accumulation of Trunc-XXI was present at the filopodium´s tip. This accumulation detached from the tip and moved rearward along the shaft of the filopodium. Data were normalized to the 1.05-fold of the maximum intensity value detected.

4.3 Myosin-XXI Influenced Average Length and Density of Filopodia in Transfected HeLa and COS-7 Cells

As FL-XXI and Trunc-XXI fusion proteins exhibited a pronounced accumulation at the tips of filopodia of transfected HeLa and COS-7 cells, and as it had been shown that myosin-X transfected into HeLa and COS-7 cells accumulated in filopodia tips and additionally influenced the average length and density of filopodia (Berg and Cheney, 2002; Zhang *et al.*, 2004; Watanabe *et al.*, 2010), an analysis of

length and density of filopodia of FL-XXI- and Trunc-XXI-transfected HeLa and COS-7 cells was performed in the present study.

In the course of this analysis, COS-7 and HeLa cells transfected with plasmids encoding ZsGreen1, ZsGreen1-FL-XXI fusion protein, and ZsGreen1-Trunc-XXI fusion protein were evaluated. Identical transfection conditions were applied for all three constructs. Transfections with plasmid only encoding the ZsGreen1 fluorophore were performed to compensate for a potential effect of the treatments of the cells during the transfection procedure. As a result, the effect solely caused by FL-XXI or Trunc-XXI could be quantified.

To ensure that transfected cells expressed the intended protein, lysates of transfected cells were subjected to western blotting (Figure 35), which revealed the expression of ZsGreen1 and ZsGreen1 fusion proteins of the correct molecular weight.

In the following subsections, a detailed description of the results of filopodia length and density analysis will be given.

A

	FL-XXI	Trunc-XXI
Extension Rate [nm/s]	21.3±13.1	28.8±18.1
Retraction Rate [nm/s]	22.8±13.1	25.1±13.6

B

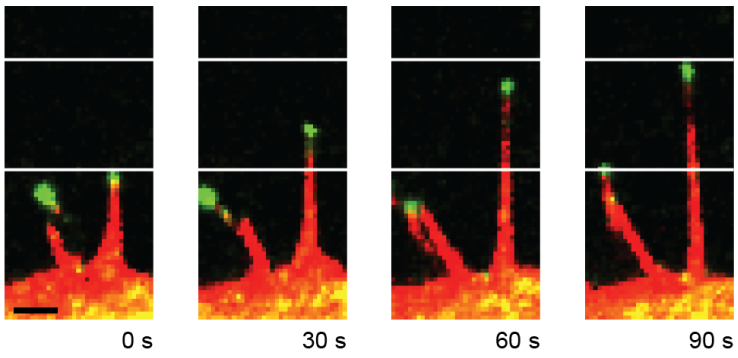

Figure 37 Filopodial length changes in FL-XXI- and Trunc-XXI-transfected HeLa cells. Dynamics of filopodia and persistence of myosin-XXI accumulations at filopodia tips were investigated with the help of live records of HeLa cells co-transfected with a plasmid encoding lifeact-RFP fusion protein and FL-XXI or Trunc-XXI respectively. (A) Extension and retraction rates of filopodia containing FL-XXI or Trunc-XXI tip accumulations. Cells expressing Trunc-XXI exhibited higher average length change rates than FL-XXI-expressing ones. (B) Image sequence of a filopodia tip containing Trunc-XXI. The protein accumulation remained at the tip even throughout a filopodial extension phase. Scale bar: 1.5 µm.

4.3.1 Transfection with FL-XXI or Trunc-XXI Resulted in an Increase in Filopodia Length

Filopodia length determination was performed for 6 HeLa and 10 COS-7 cells for each transfection construct respectively. In total, 319 (HeLa) and 276 (COS-7) filopodia were analyzed for the ZsGreen1 control, 418 (HeLa) and 417 (COS-7) filopodia for Trunc-XXI, and 333 (HeLa) and 264 (COS-7) filopodia for FL-XXI.

Analysis yielded the result that for both, COS-7 and HeLa cells, the average filopodia length increased when cells were transfected with one of the myosin-XXI constructs.

For COS-7 cells, in comparison to the control, a length increase of about 16.6 % for Trunc–XXI and approximately 22.2 % for FL-XXI (Figure 38) was revealed. This increase could be assigned to a more frequent occurrence of filopodia with a length of at least 2 µm in myosin-XXI-expressing cells (Figure 39).

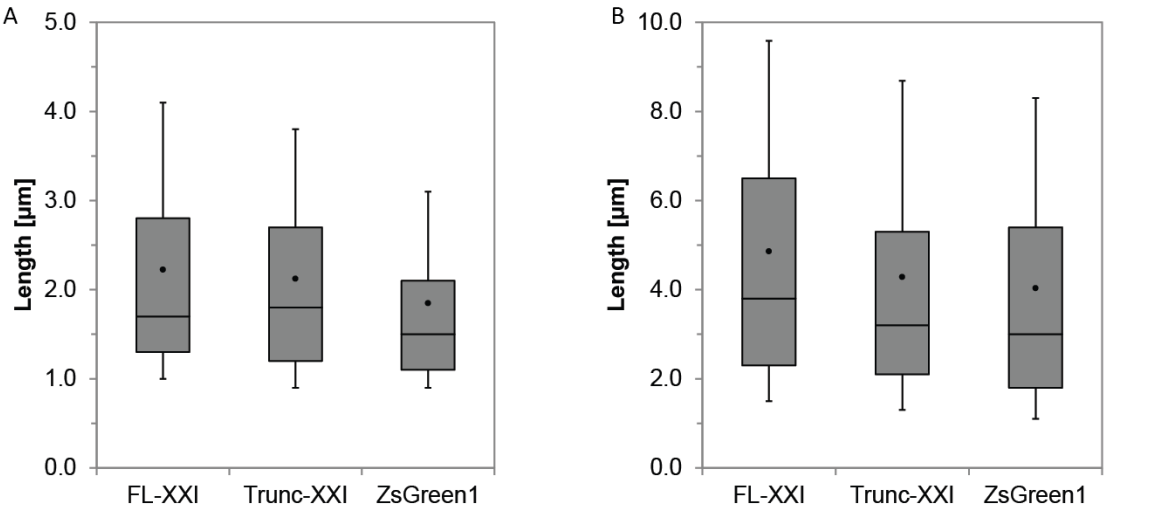

C

	FL-XXI	Trunc-XXI	ZsGreen1
L [µm]	2.2	2.1	1.8
ΔL [%]	22.2	16.6	-

D

	FL-XXI	Trunc-XXI	ZsGreen1
L [µm]	4.9	4.3	4.0
ΔL [%]	22.5	7.5	-

Figure 38 Increase in average filopodia length in FL-XXI- and Trunc-XXI-transfected HeLa and COS-7 cells. The average length of filopodia formed by cells expressing FL-XXI or Trunc-XXI fusion protein was determined. To eliminate a potential effect of the transfection procedure, cells expressing ZsGreen1 were used as negative control. (A, B) Box whisker plots of filopodia lengths of COS-7 (A) and HeLa cells (B). Middle lines of the boxes represent mean filopodia lengths, black circular markers show average lengths. Lower and upper line of the boxes depict 25th and 75th quartile. Upper and lower whiskers illustrate 10th and 90th percentile. For both cell lines, significant increases in average filopodia length were observed when cells were transfected with FL-XXI or Trunc-XXI. (C, D) Average filopodia lengths L of FL-XXI-, Trunc-XXI-, and ZsGreen1-transfected COS-7 (C) and HeLa cells (D). ΔL denotes the average length increase observed for filopodia of FL-XXI- and Trunc-XXI-expressing cells relative to the control.

Fluorescence intensities per area of cell body cross section were ~1,200 a.u./µm^2 for FL-XXI-transfected COS-7 cells, ~1,400 a.u. /µm^2 for Trunc-XXI-transfected COS-7 cells, and ~7,900 a.u. /µm^2 for the ZsGreen1 control. Thus, FL-XXI- and Trunc-XXI-transfected cells exhibited lower expression levels than the control. The fact that average filopodia lengths were yet higher in FL-XXI- and Trunc-XXI-expressing COS-7 cells than in control cells further confirmed FL-XXI or Trunc-XXI expression as primary cause of filopodia elongation. In addition, expression levels in FL-XXI-transfected COS-7 were lower than expression levels in Trunc-XXI-transfected cells. However, length

increase induced by FL-XXI was higher than the one induced by Trunc-XXI thereby indicating an impact of the expressed fusion protein on the extent of filopodia elongation.

In transfected HeLa cells, average length increase of filopodia was 7.5 % for Trunc-XXI-expressing cells and 22.5 % for FL-XXI-expressing cells when compared to the control (Figure 38). In comparison to cells only transfected with ZsGreen1 construct, HeLa cells transfected with either myosin-XXI construct more often exhibited a length of 10 µm and above (Figure 39).

In the case of HeLa cells, fluorescence intensities per area of cell body cross section were ~1,700 a.u./µm^2 for FL-XXI, ~1,100 a.u. /µm^2 for Trunc-XXI, and ~1,300 a.u. /µm^2 for ZsGreen1. Hence, similar to Trunc-XXI-expressing COS-7 cells, Trunc-XXI-expressing HeLa cells exhibited a lower expression level than the control. Nevertheless, Trunc-XXI again induced an elongation of filopodia in comparison to the control. FL-XXI-transfected HeLa cells, which showed a higher expression level of myosin-XXI fusion protein than Trunc-XXI-transfected cells, displayed an even higher increase in average length of filopodia.

As HeLa cells were not analyzed in an automated approach, in addition to the evaluation of the average length of the entirety of filopodia of transfected cells, a distinction between filopodia with (FL-XXI: 179 filopodia; Trunc-XXI: 104 filopodia) and without (FL-XXI: 154 filopodia; Trunc-XXI: 314 filopodia) protein accumulations at their tips could be made. According to this more detailed analysis (Figure 39), the increase in average filopodia length of FL-XXI- and Trunc-XXI-expressing HeLa cells resulted from an elongation of filopodia containing myosin-XXI tip accumulations: while protein accumulation-free filopodia exhibited an average length up to 7.5 % smaller than the average length of the control, filopodia containing FL-XXI or Trunc-XXI tip populations displayed a length increase of 43 % (FL-XXI) to 53 % (Trunc-XXI). A comparison of length distributions of filopodia with and without myosin-XXI at their tips demonstrated that the length increase of filopodia containing FL-XXI or Trunc-XXI can be assigned to a reduced occurrence of filopodia of 2 µm of length or shorter.

Overall, analysis of filopodia lengths of transfected mammalian cells demonstrated that the expression of either FL-XXI or Trunc-XXI resulted in an elevated average length of filopodia. In addition, analysis results indicated differing capabilities of both fusion proteins to induce an elongation of filopodia and provided hints that filopodial elongation was related to the presence of fusion protein accumulations within the distal ends of filopodia.

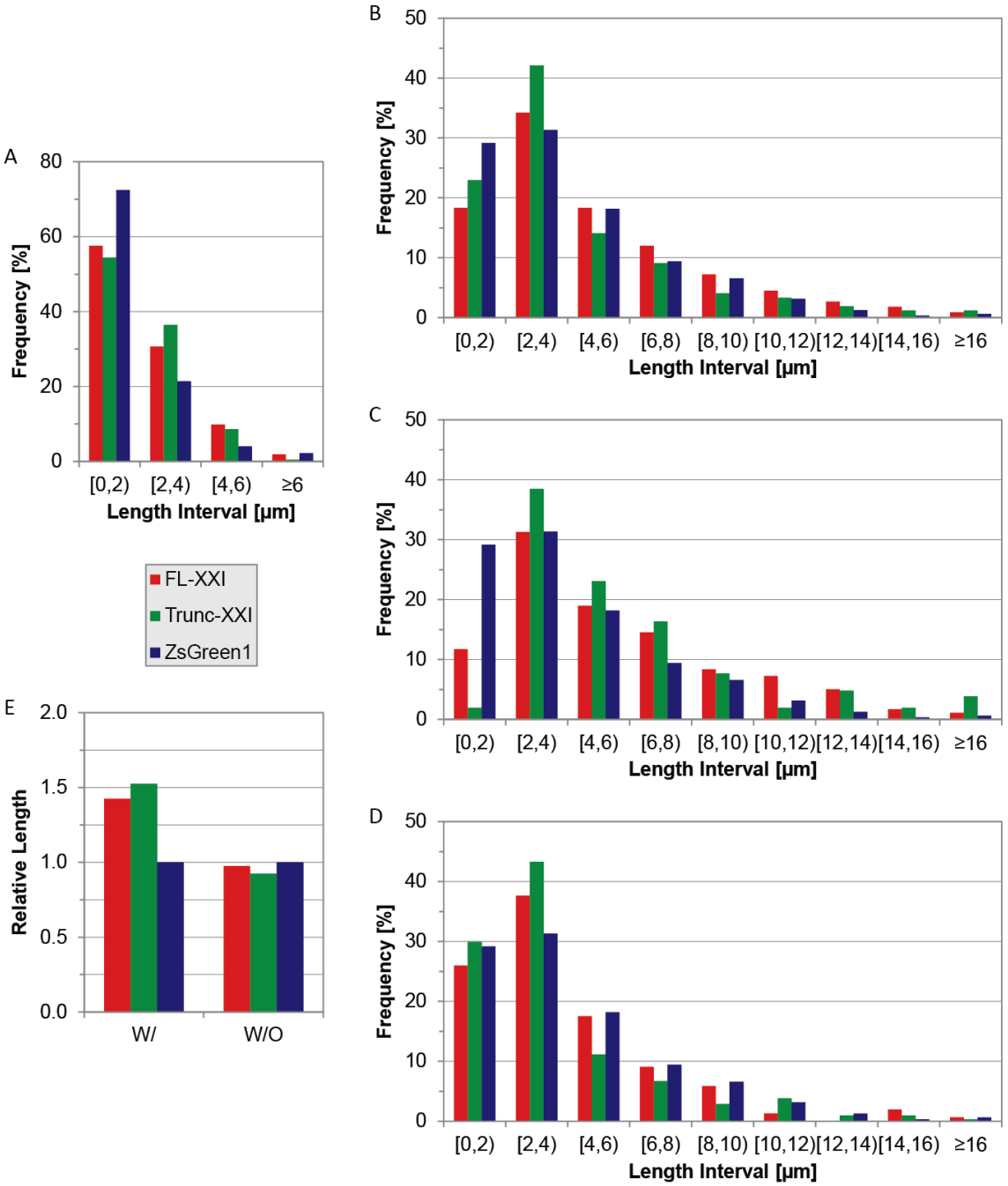

Figure 39 Filopodial length distributions of FL-XXI- and Trunc-XXI-transfected HeLa and COS-7 cells. The frequency of filopodia lengths was determined within length intervals of 2 µm. Filopodia of cells expressing FL-XXI or Trunc-XXI fusion protein were compared to those of cells solely expressing ZsGreen1. ZsGreen1-expressing cells were selected as control to compensate for a potential influence of the transfection procedure on filopodia formation. (A, B) Length distributions of filopodia of transfected COS-7 (A) and HeLa cells (B). In comparison to the control, transfection of COS-7 cells with either FL-XXI or Trunc-XXI resulted in an increased incidence of filopodia with a length of 2 µm or longer. In the case of HeLa cells, filopodia of FL-XXI- and Trunc-XXI-expressing cells more frequently exhibited a length of at least 10 µm when compared to filopodia of the control. (C, D, E) A more detailed analysis of filopodia lengths of transfected HeLa cells. In this analysis, filopodia of FL-XXI- and Trunc-XXI-expressing cells were classified into filopodia exhibiting and filopodia not exhibiting accumulations of fusion protein at their tips. Importantly, protein accumulations at the distal filopodia ends were not detected in ZsGreen1-expressing cells, thus length distribution and average length of control filopodia are identical in each diagram. (C, D) Length distributions of filopodia. In comparison to accumulation-free filopodia (D), a reduced occurrence of lengths of 2 µm and below was observed for filopodia containing protein tip populations (C). (E) Average lengths of filopodia normalized to the control. In consequence of the lower incidence of short filopodia, the average length of filopodia with (w/) FL-XXI or Trunc-XXI accumulations was found to exceed the average length of control filopodia by more than 40 %. In contrast, filopodia without (w/o) FL-XXI or Trunc-XXI tip populations were 7.5 % shorter than control filopodia. Accordingly, the overall increase in average filopodia lengths of FL-XXI- and Trunc-XXI-expressing HeLa cells is related to an elongation of filopodia containing FL-XXI or Trunc-XXI accumulations.

4.3.2 Transfection with FL-XXI or Trunc-XXI Resulted in an Increase in Filopodia Density

Filopodia density, i.e. the number of filopodia per cell circumference, was determined for 20 HeLa and 10 COS-7 cells for each transfection plasmid respectively.

For both cell types, density of filopodia increased upon transfection with FL-XXI or Trunc-XXI: for COS-7 cells density increases of 29 % (FL-XXI) and 100 % (Trunc-XXI) were observed (Figure 40). As mentioned before, detected fluorescence intensity signals of cell bodies were ~1,200 a.u./µm^2 (FL-XXI), ~1,400 a.u. /µm^2 (Trunc-XXI), and ~7,900 a.u. /µm^2 (ZsGreen1) respectively. As in the case of average filopodia length, an effect of myosin-XXI on filopodia was detected although average expression levels of COS-7 cells transfected with one of the myosin-XXI constructs were lower than the average ZsGreen1 expression level. The strongest impact on filopodia density was detected for Trunc-XXI, which on average was also expressed at a higher level than FL-XXI.

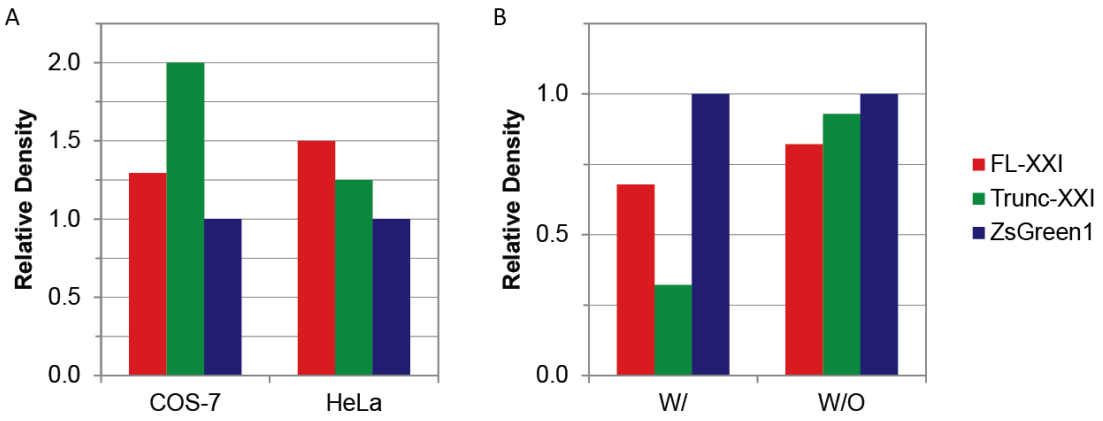

Figure 40 Filopodial density increase in HeLa and COS-7 cells upon transfection with FL-XXI and Trunc-XXI. In the diagrams above, average numbers of filopodia per membrane circumference of cells expressing FL-XXI, Trunc-XXI, or ZsGreen1 are compared. ZsGreen1-transfected cells served as negative control. Determined densities were normalized to the filopodia density of the control. (A) Average density of filopodia of HeLa and COS-7 cells. For both myosin-XXI constructs and both cell lines, determined filopodia densities were increased by at least 25 % in comparison to the control. (B) A more detailed analysis of filopodia densities of FL-XXI- and Trunc-XXI-transfected HeLa cells. In this analysis, filopodia exhibiting accumulations of fusion protein at their tips were distinguished from accumulation-free filopodia. Importantly, protein tip populations were not observed in ZsGreen1-expressing cells, therefore only one constant value for the density of control filopodia was obtained. Evaluation revealed that relative to the control, filopodia number per membrane length was reduced by more than 7 % for both filopodia with (w/) and filopodia without (w/o) myosin-XXI accumulations. Hence, an increase in filopodia density was only observed when considering the entirety of filopodia of FL-XXI- or Trunc-XXI-expressing HeLa cells.

In experiments with HeLa, cells displayed a filopodia density increase of 50 % (FL-XXI) and 25 % (Trunc-XXI) when transfected with one of the myosin constructs (Figure 40). For HeLa cells analyzed regarding filopodia density, average intensity levels of cell bodies were ~1,500 a.u. /µm^2 (FL-XXI), ~900 a.u. /µm^2 (Trunc-XXI), and ~3,200 a.u. /µm^2 (ZsGreen1). Again, an effect of myosin-XXI on filopodia density was observed even though average expression levels of FL-XXI- and Trunc-XXI-transfected HeLa cells were lower than average expression level of ZsGreen1. A comparison of the data obtained for FL-XXI and Trunc-XXI showed that both the increase in filopodia density and the

average expression level of FL-XXI-expressing HeLa cells exceeded those of Trunc-XXI-expressing cells.

A more detailed analysis of HeLa cells regarding the accumulation of myosin-XXI fusion protein at the tips of filopodia revealed that in FL-XXI- and Trunc-XXI-transfected cells, neither the density of filopodia without protein tip accumulations nor the density of filopodia containing these accumulations coincided with the overall filopodia density observed for ZsGreen1-expressing cells (Figure 40). Instead, the density of filopodia containing myosin-XXI as well as the density of accumulation-free filopodia was more than 7 % smaller than the average density of filopodia of ZsGreen1-transfected cells. An increase in filopodia density of FL-XXI- and Trunc-XXI-expressing HeLa in comparison to the control was only observed when considering all filopodia of these cells.

Summarizing, evaluation of the densities of filopodia in transfected mammalian cells showed that both FL-XXI and Trunc-XXI induce an increase in the number of filopodia per membrane circumference. Unlike in the case of myosin-XXI-induced increases in filopodia length, no clear relation between elevated filopodia densities and the occurrence of fusion protein accumulations within the filopodia tips was found.

4.4 Myosin-XXI Moved Towards the Plus End of Dual-Labeled Actin Filaments

As described in section 4.2, motile populations of fluorophore-labeled full-length myosin-XXI were detected during live imaging of transfected HeLa cells. In subsequent gliding filament assays with dual-labeled F-actin, directionality of motor movement along filamentous actin was determined.

In order to verify the applied method, directionality was first deduced for HMM and myosin-VI, i.e. for motor proteins of known direction of movement. For HMM, 70 dual-labeled filaments from 10 different samples were analyzed. 69 (98.6 %) of these filaments exhibited a leading pointed end, thus HMM was identified as plus end-directed motor. The evaluation of 80 filaments from 8 myosin-VI samples resulted in 93.8 %, i.e. 75, of the filaments exhibiting a leading barbed end (Figure 41). Therefore, myosin-VI motor movement was determined as minus end-directed.

As these findings were in agreement with the literature (Huxley, 1969; Sheetz and Spudich, 1983; Wells *et al.*, 1999), gliding filament assays with full-length myosin-XXI were performed. 6 samples were prepared and 76 filaments were analyzed. 73 of these filaments (96.1 %) showed a leading pointed end. Therefore, myosin-XXI was identified as a plus end-directed actin-associated motor protein (Figure 41).

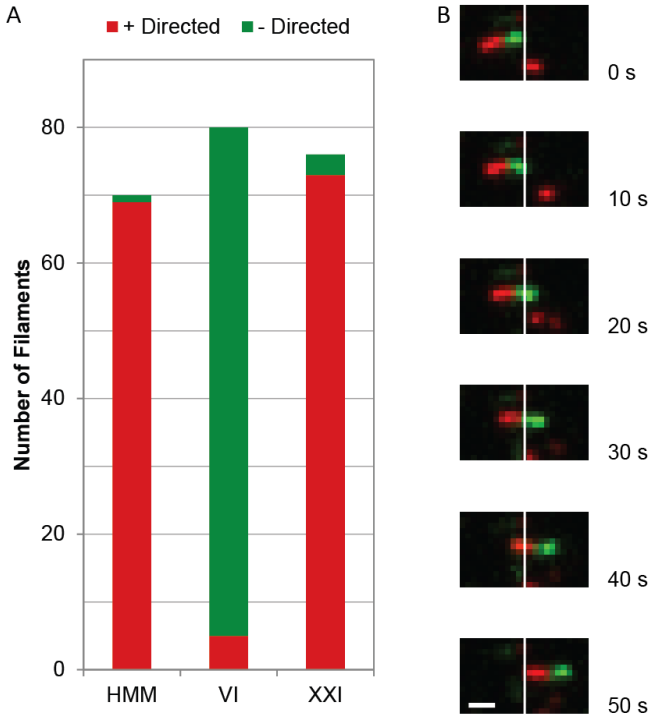

Figure 41 Determination of motor directionality in gliding filament assays with dual-labeled F-actin. (A) Number of filaments indicating plus end- or minus end-directed movement of HMM, chicken myosin-VI, and *L. donovani* myosin-XXI. Identification of HMM as plus end-directed and of myosin-VI as minus end-directed motor verified the applied method. Myosin-XXI was found to be a plus end-directed actin-associated motor. (B) Sequential images of dual-labeled filamentous actin sliding on a surface covered with myosin-XXI: the leading FITC-labeled pointed filament end (green) demonstrates movement of myosin-XXI towards the TRITC-labeled barbed end (red). Scale bar: 0.5 µm.

4.5 Myosin-XXI Binding to Planar Lipid Bilayers

Previous research of our lab had demonstrated that myosin-XXI binds to various phospholipids. Moreover, when bound to vesicular lipid bilayers this motor protein can bind actin filaments and induce filament gliding (Batters *et al.*, 2014). Therefore, the further investigation of the dynamic behavior of the bilayer-bound actin-myosin-XXI complex was one of the scientific objectives of the present study.

In addition, as ZsGreen1-FL-XXI fusion protein was observed to accumulate along the plasma membrane of HeLa and COS-7 cells in present transfection experiments (see section 4.1), the question arose whether myosin-XXI is capable of binding to lipid constituents of the plasma membrane and thus whether myosin-XXI binds to planar lipid bilayers.

In order to elucidate both aspects, the dynamics of the bilayer-associated actin-myosin-XXI complex and myosin-XXI´s capability of binding to lipid bilayers of planar geometry, gliding filament experiments on planar lipid bilayers were performed. In the investigation of the actin-myosin-XXI complex, usage of planar bilayer systems eliminated spatial constraints by the limited size of previously applied lipid vesicles.

Prior to experiments involving myosin-XXI, applied bilayer preparation techniques were tested for the fluidity of the resulting bilayers. For this purpose, FRAP experiments were carried out and lateral

diffusion constants were determined. In the following step, it was tested whether myosin-XXI produced movement of F-actin when bound to planar lipid bilayers. As the investigations of the actin-myosin complex did not result in filament movement, bilayer binding of myosin-XXI alone was tested.

4.5.1 Lateral Diffusion Constants of Planar Lipid Bilayers

To verify that the applied preparation techniques resulted in the formation of lipid bilayers exhibiting reasonable fluidity, Fluorescence Recovery after Photobleaching was tested and lateral diffusion coefficients were computed (Figure 42).

Tested lipid bilayer samples comprised supported lipid bilayers and one tethered lipid bilayer. SLB samples included 6 samples with a lipid composition of 97.3 mol% POPC, 1.5 mol% Biotin DHPE, 1.2 mol% Rhodamine DHPE, and 5 samples composed of 73.0 mol% POPC, 26.0 mol% cholesterol, 1.0 mol% Rhodamine DHPE. For each SLB, 24 measurements were performed and subsequently evaluated (Table D.1). In the case of tethered bilayer experiments, only one sample was prepared due to high material costs. The lipid mixture applied contained 94.0 mol% POPC, 4.8 mol% PI(3,5)P_2, and 1.2 mol% Rhodamine DHPE. Here, 5 measurements were carried out and analyzed (Table D.1).

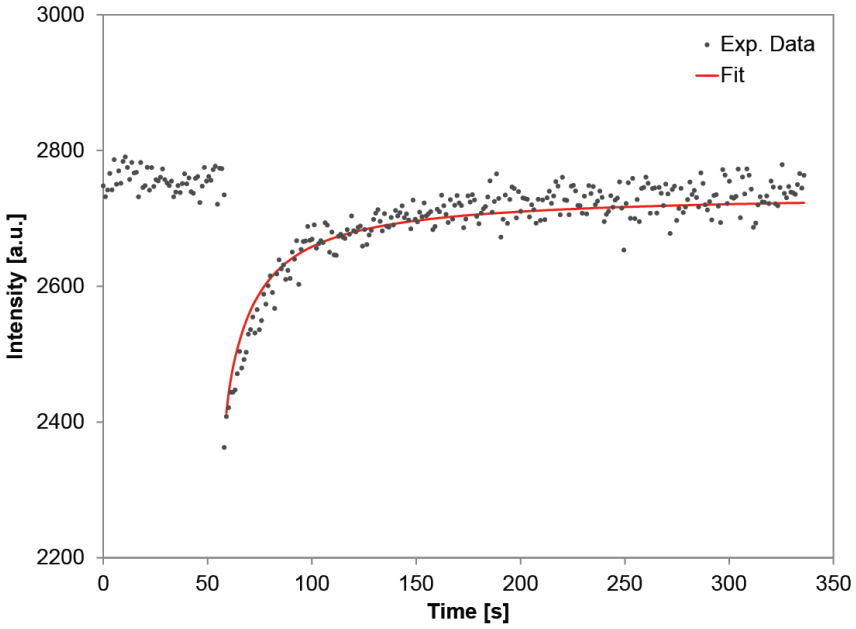

Figure 42 FRAP measurement of a supported lipid bilayer and applied fit function. A supported lipid bilayer composed of 73.0 mol% POPC, 26.0 mol% cholesterol, and 1.1 mol% Rhodamine DHPE was subjected to bleaching and recovery of the fluorescence signal was recorded. Experimental data depicted above are already corrected for photobleaching inherent to the imaging process. These corrected data were fitted by a function containing the characteristic diffusion time τ_D as fitting parameter. The lateral diffusion constant D was calculated from $D = {\tau_D}^2 \cdot (4R)^{-1}$ with R representing the radius of the bleached area. Fitting resulted in D=1.49·10^{-12} m^2·s^{-1}. The average lateral diffusion constant determined from the results of 24 measurements of 5 samples of this particular lipid composition was calculated as 1.21±0.33·10^{-12} m^2·s^{-1} (mean ± s.d.).

Analysis of FRAP experiments resulted in the following lateral diffusion coefficients D: for supported POPC/Biotin DHPE/Rhodamine DHPE bilayers, D was determined as 1.50±0.50·10^{-12} m^2·s^{-1}

(mean ± s.d.) resembling the diffusion coefficient of $1.42\pm0.13\cdot10^{-12}$ $m^2\cdot s^{-1}$ reported for a supported POPC bilayer containing $6.5\cdot10^{-6}$ mol% TRITC-conjugated DHPE (Schmidt *et al.*, 1996). In the case of supported POPC/cholesterol/Rhodamine DHPE bilayers, a diffusion coefficient of $1.21\pm0.33\cdot10^{-12}$ $m^2\cdot s^{-1}$ was deduced agreeing with a value of $D=1.20\pm0.50\cdot10^{-12}$ $m^2\cdot s^{-1}$ published for a supported bilayer of 79.5 mol% POPC, 20 mol% cholesterol, and 0.5 mol% 1-palmitoyl-2-(16-doxyl stearoyl)phosphatidylcholine. Furthermore, the reduced fluidity of POPC/cholesterol/Rhodamine DHPE bilayers in comparison to POPC/Biotin DHPE/Rhodamine DHPE bilayers corresponds to the membrane stiffening effect of cholesterol (Shin and Freed, 1989). FRAP measurements of the tethered POPC/PI(3,5)P_2/Rhodamine DHPE bilayer resulted in $D=1.45\pm0.19\cdot10^{-12}$ $m^2\cdot s^{-1}$, which was found to be in good agreement with the publication of Daniel *et al.* (2007) stating that tethered bilayer systems display lateral fluidities similar to those of supported lipid bilayer systems.

In summary, the applied preparation techniques were found to produce lipid bilayers suitable for utilization in further experiments. In addition, fluidity of all bilayers used in the assays described below was verified by the presence of a FRAP effect prior to experimental use.

4.5.2 Myosin-XXI Did Not Induce Filament Gliding on Planar Lipid Bilayers

To investigate whether full-length myosin-XXI binds to lipid bilayers and once bound maintains its ATPase activity and motility, FL-XXI was tested for its capability to induce actin filament movement on surfaces covered with planar lipid bilayers.

Before gliding filament experiments were carried out, the following negative control assays were performed: to verify that FL-XXI attachment to the sample surface requires phospholipid binding, FL-XXI and actin filaments were incubated on POPC/Rhodamine DHPE bilayers, i.e. bilayers not containing any of the lipids previously shown to bind myosin-XXI (Batters *et al.*, 2014). Further, SLB binding of actin alone was tested to exclude the possibility that actin itself binds to planar lipid bilayers. In both cases, no attachment of actin filaments to lipid bilayers was detected in TIRF microscopy. Thus, FL-XXI was not capable of binding to planar lipid bilayers in the absence of myosin-XXI binding lipids, and actin itself did not bind to planar lipid bilayers.

In gliding filament experiments on bilayers containing phospholipids for which FL-XXI binding had been demonstrated in a previous study of our research group (Batters *et al.*, 2014), actin filaments were found to attach to the sample surface. Thus, binding of FL-XXI to phospholipids enabled the attachment of the actomyosin complex to bilayer-covered surfaces. Unexpectedly, F-actin did not show any movement at all, neither directed gliding nor diffusive motion. Together with the fact that the presence of myosin-XXI was required for the binding of actin to surfaces of bilayer samples, this finding indicated that F-actin bound to FL-XXI, which in turn bound to immobile structures on the sample surface. In this configuration, myosin-XXI did not induce movement of filaments.

The observations described above were made for different experimental set-ups and modifications of the sample preparation procedure thereby repeatedly verifying the phospholipid-mediated attachment of FL-XXI to immobile structures.

First, two different approaches for the attachment of the actomyosin complex to planar lipid bilayers were applied. In one approach, FL-XXI was incubated with a planar lipid bilayer and filamentous actin was subsequently added. In the other approach, FL-XXI and actin filaments were premixed, incubated and added to a lipid bilayer.

Moreover, gliding filament experiments were performed using two different types of planar lipid bilayers: supported lipid bilayers, which were directly applied to the coverslip surface, and tethered lipid bilayers, which were separated from the glass surface by a PEG cushion, which reduced nonspecific binding of proteins to the coverslip. For SLB, additional passivation of the coverslip surface by BSA blocking was tested. In addition, various lipid compositions of bilayers were investigated in the present work:

- DOPC/2.0 mol% PI(4,5)P_2
- DOPC/2.0 mol% PI(3,5)P_2
- POPC/PI(3,5)P_2, with PI(3,5)P_2 content ranging between 4.8 mol% and 9.7 mol%
- POPC/PI(4)P, with PI(4)P content ranging between 1.6 mol% and 9.7 mol%
- POPC/9.5 mol% bovine brain extract
- bovine brain extract

To allow for the verification of bilayer fluidity by FRAP tests, all of the lipid mixtures stated above were supplemented with Rhodamine DHPE.

Finally, buffer conditions during bilayer preparation and gliding filament experiments were modified, and various concentrations of myosin-XXI and actin were tested.

In summary, FL-XXI was shown to attach to immobile structures on the surfaces of planar lipid bilayer samples under various experimental conditions. When associated with these structures, myosin-XXI was incapable of driving actin filament movement.

4.5.3 Myosin-XXI Did Not Bind to Planar Lipid Bilayers

Subsequent to gliding filament tests, binding of myosin-XXI to planar lipid bilayers was further investigated in experiments with a fusion protein of FL-XXI and eGFP.

In the first experimental set-up, fluorophore-labeled myosin-XXI was added to already formed SLB. In the second set-up, FL-XXI fusion protein was incubated with unilamellar vesicles, and after the mixture was injected into a flow cell, bilayer formation was monitored. In both cases, presence of a fluid lipid bilayer was tested by FRAP measurements. Additionally, FRAP signals of eGFP fused to myosin-XXI were measured to explore whether FL-XXI was bound to the SLB.

When myosin-XXI was added to readily prepared SLB, fluidity of the bilayers was preserved. Nevertheless, no FRAP signal was detected for eGFP indicating that myosin-XXI did not bind to SLB. Furthermore, rinsing of the bilayers with buffer resulted in a pronounced removal of FL-XXI-eGFP fusion protein from the sample. Fluorescence signal of the remaining fusion protein did not recover when bleaching was carried out and thus the remaining protein was immobile (Figure 43). These observations again demonstrated that myosin-XXI did not bind to planar lipid bilayers but instead attached to immobile structures on the sample surface.

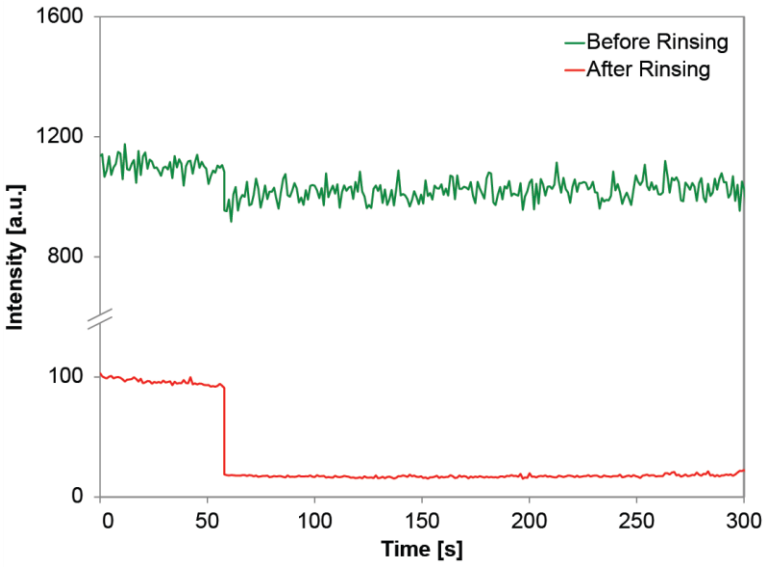

Figure 43 FRAP measurements of eGFP-FL-XXI fusion protein incubated with a supported lipid bilayer. Fusion protein of eGFP and FL-XXI was added to a readily prepared supported lipid bilayer composed of 98.8 mol% bovine brain extract and 1.2 mol% Rhodamine DHPE. EGFP was bleached and time course of the fluorescence intensity was recorded. Experimental data depicted above are already corrected for photobleaching inherent to the imaging process. The first FRAP experiment (green curve) was performed after fusion protein had been incubated with the bilayer without further treatment. EGFP fluorescence signal only exhibited a small decrease and fluorescence recovery was not observed. Therefore, reduction of the fluorescence signal can be assigned to bleaching of immobilized fusion protein within the region of interest. The absence of a FRAP signal can be attributed to eGFP-FL-XXI fusion protein not binding to the bilayer. Fluorescence recovery due to the 3D diffusion of fusion protein in the solution above the bilayer was not temporally resolved by the microscope set-up utilized. The second FRAP measurement (red curve) was carried out after the sample was rinsed with buffer. Again, no fluorescence recovery was observed. Due to the removal of fusion protein in solution, eGFP signal was almost completely eliminated by a single application of the bleaching laser.

When eGFP-labeled myosin-XXI and lipid vesicles were incubated and subsequently injected into a flow cell to generate a lipid bilayer with FL-XXI bound to it, formation of a fluid bilayer was only observed for the lowest myosin-XXI concentration (5 nM). For myosin-XXI concentrations of 50 nM and higher, bilayer formation was not observed. In agreement with this, no FRAP signal of lipids was detected. Independent from the formation of a fluid phospholipid bilayer, no fluorescence recovery was detected for eGFP when bleaching was applied. Thus, although formation of fluid bilayers from myosin-XXI-lipid mixtures occurred for appropriate lipid to FL-XXI molar ratios, myosin-XXI did not bind to the resulting SLB.

In addition, modifications of the sample preparation methods (e.g. application of different buffers, BSA blocking of bilayers prior to the addition of myosin-XXI) did not result in a binding of myosin-XXI-eGFP fusion protein to the investigated lipid bilayers.
Thus, myosin-XXI was not capable of binding to planar lipid bilayers.

4.6 Myosin-XXI Produced Filament Gliding When Bound to Lipid Vesicles

In a previous study of our lab, myosin-XXI was demonstrated to bind to lipid vesicles, i.e. curved lipid bilayers, and to exhibit motility in a lipid-bound state (Batters *et al.*, 2014).
To verify that the FL-XXI samples produced in the present study exhibited functional lipid binding and were motile when bound to lipids, gliding filament assays on vesicle-covered surfaces were carried out. For this purpose, unilamellar vesicles were attached to nitrocellulose-coated coverslips, and FL-XXI and F-actin were added.
In negative control experiments, vesicles merely composed of POPC and Rhodamine DHPE were utilized. The lack of filament binding observed in control samples confirmed that in the absence of myosin-XXI binding lipids, FL-XXI did not bind to the areas of sample surfaces in the interstices between lipid vesicles (Figure 44).

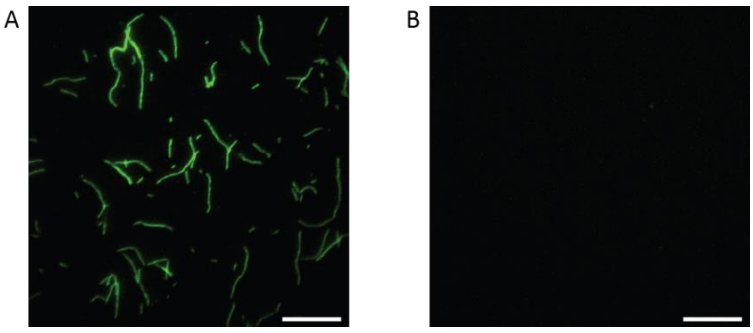

Figure 44 Gliding filament assays with myosin-XXI on lipid vesicle-covered surfaces. Unilamellar vesicles were immobilized on nitrocellulose-coated surfaces and subsequently, FL-XXI and FITC-labeled filamentous actin were added. Images display the FITC imaging channel. (A) Gliding filament assays on vesicles containing 94.0 mol% POPC, 1.2 mol% Rhodamine DHPE, and 4.8 mol% PI(3,5)P_2. Observation of filament attachment and gliding verified the binding of myosin-XXI to vesicular bilayers and the motility of the motor protein in a lipid-bound state. (B) Negative control experiment utilizing vesicles composed of 98.9 mol% POPC and 1.1 mol% Rhodamine DHPE. The absence of bound actin filaments verified that FL-XXI did not bind to the sample surface in the interstices between vesicles. Scale bars: 10 µm.

In assays with vesicles containing POPC, Rhodamine DHPE, and PI(4)P or PI(3,5)P_2, gliding of actin filaments was observed (Figure 44). Phosphoinositide content of the tested lipid mixtures was 4.8 mol% or 9.7 mol% and vesicle populations of different average size were prepared by extrusion through polycarbonate membranes of various pore diameters. For vesicles containing 4.8 mol% PI(3,5)P_2 extruded through a membrane of 100 nm pore diameter, filament movement was tracked and analysis resulted in an average gliding speed of 63.0±27.7 nm/s (mean ± s.d.; 255 filaments from 7 samples).

Overall, gliding filament assays on unilamellar vesicles confirmed functional lipid binding by FL-XXI and motor motility of the lipid-bound protein. Furthermore, they indicated that myosin-XXI binding and thereby filament gliding only occurred on vesicular bilayers, i.e. on bilayers of positive curvature.

4.7 Vesicle Binding by Fluorescently Labeled FL-XXI and Myosin-XXI Fragments

In order to elucidate whether bilayer curvature influenced lipid binding by myosin-XXI, Single Liposome Curvature assays with FL-XXI and myosin-XXI fragments were performed.

Before respective proteins were examined in SLiC assays, they were tested for their ability to bind to unilamellar vesicles in co-sedimentation assays. Centrifugation of protein-vesicle mixtures and subsequent analysis of the protein content of resulting pellets and supernatants allowed for the verification of protein binding via the quantification of the fraction of protein detected in the precipitate.

Proteins examined comprised fusion proteins of eGFP and FL-XXI or a myosin-XXI fragment. Myosin-XXI fragments included Trunc-XXI, three tail constructs, and two converter domain constructs. Tail fragments analyzed were XXI-830 Tail (aa 830-1050), XXI-930 Tail (aa 930-1050), and XXI-809 Tail (aa 809-1050). Converter domain constructs consisted of aa 600 to 758 of the myosin-XXI sequence. One construct (XXI-Conv. WT) contained the wild-type sequence, the second one (XXI-Conv. M) was modified by a double-amino acid substitution in the PX domain replacing arginine and tyrosine (aa 705 and aa 706) by leucine and serine. This mutation had been demonstrated to reduce but not completely eliminate the phospholipid binding capacity of the myosin-XXI converter domain (Batters *et al.*, 2014). Furthermore, co-sedimentation assays with a fusion protein of eGFP and the endophilin A1 N-BAR domain were carried out. The latter fusion protein was expressed and purified in order to be used as positive control in SLiC assays.

For each protein tested, 5 co-sedimentation assays with vesicles consisting of 97.2 mol% bovine brain extract, 1.2 mol% Rhodamine DHPE, and 1.6 mol% Biotin DHPE were performed (Table E.2). Additionally, 3 negative controls were carried out (Table E.1). For the latter, solutions solely containing protein were subjected to the sedimentation procedure. Analysis of the protein content in supernatants and pellets revealed that in the negative controls, i.e. in the absence of lipids, on average less than 2 % of the protein contained in the solution was sedimented (Figure 45).

A

Fraction of Protein in the Precipitate [%]			
eNBAR	FL-XXI	Trunc-XXI	XXI-930 Tail
0.0±0.0	1.6±1.5	1.3±2.4	0.0±0.0

Fraction of Protein in the Precipitate [%]			
XXI-830 Tail	XXI-809 Tail	XXI-Conv. WT	XXI-Conv. M
0.0±0.0	0.0±0.0	0.0±0.0	0.0±0.0

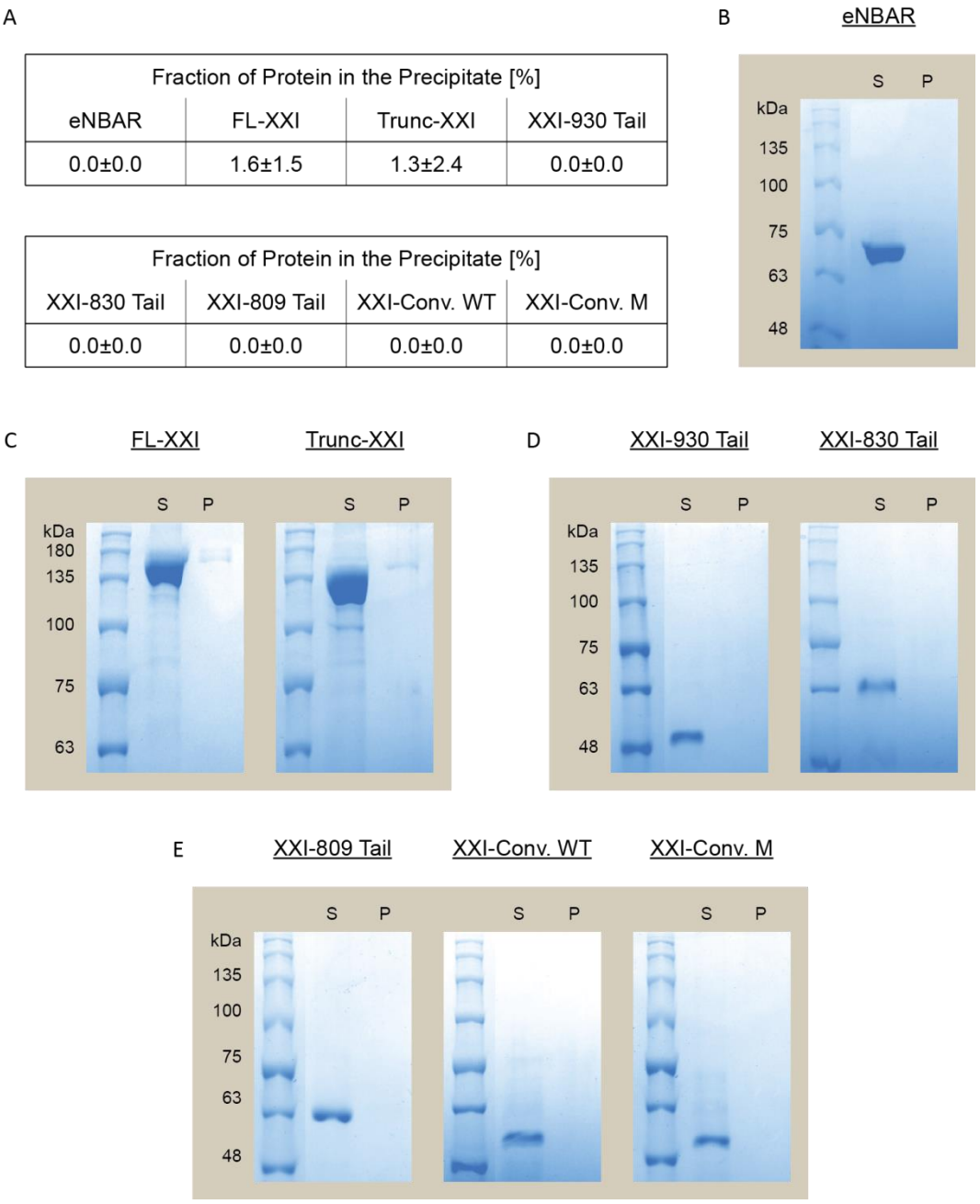

Figure 45 Negative control sedimentation assays of fusion proteins of eGFP and eNBAR, FL-XXI, and myosin-XXI fragments. Prior to co-sedimentation experiments with protein-vesicle mixtures, protein samples were ultracentrifuged in the absence of lipids. Resulting supernatants (S) and pellets (P) were analyzed by SDS-PAGE. (A) Results of the analyses of polyacrylamide gels. On average, less than 2 % of the amount of protein contained in the samples was detected in the sediment. Numbers are mean ± s.d. of 3 sedimentation assays. (B-E) Representative images showing polyacrylamide gels of sedimentation samples of eNBAR (B), FL-XXI and Trunc-XXI (C), XXI-930 Tail and XXI-830 Tail (D), XXI-809 Tail, XXI-Conv. WT and XXI-Conv. M (E).

In the presence of lipids, the fraction of protein detected in the pellet increased for the following proteins indicating a capability of these proteins to bind to bovine brain extract vesicles (Figure 46): for eNBAR, which did not precipitate in negative control experiments, percentage of protein in the pellet increased to 82.9 % ± 4.0 % (mean ± s.d.). The capability of eNBAR to bind to the applied vesicles is in agreement with published data (Bhatia *et al.*, 2009). FL-XXI protein content in the sediment increased from 1.6 % ± 1.5 % in negative controls to 22.4 % ± 5.0 %. In the case of

Trunc-XXI, fraction of precipitated protein increased by 10 % to 13.3 % ± 3.6 %. XXI-830 Tail and XXI-930 Tail, which did not show any precipitation in negative control experiments, exhibited proportions of sedimented protein of 67.0 % ± 4.6 % and 75.8 % ± 28.6 % respectively.

A

Fraction of Protein in the Precipitate [%]			
eNBAR	FL-XXI	Trunc-XXI	XXI-930 Tail
82.9±4.0	22.4±5.0	13.3±3.6	75.8±28.6

Fraction of Protein in the Precipitate [%]			
XXI-830 Tail	XXI-809 Tail	XXI-Conv. WT	XXI-Conv. M
67.0±4.6	0.0±0.0	0.0±0.0	0.0±0.0

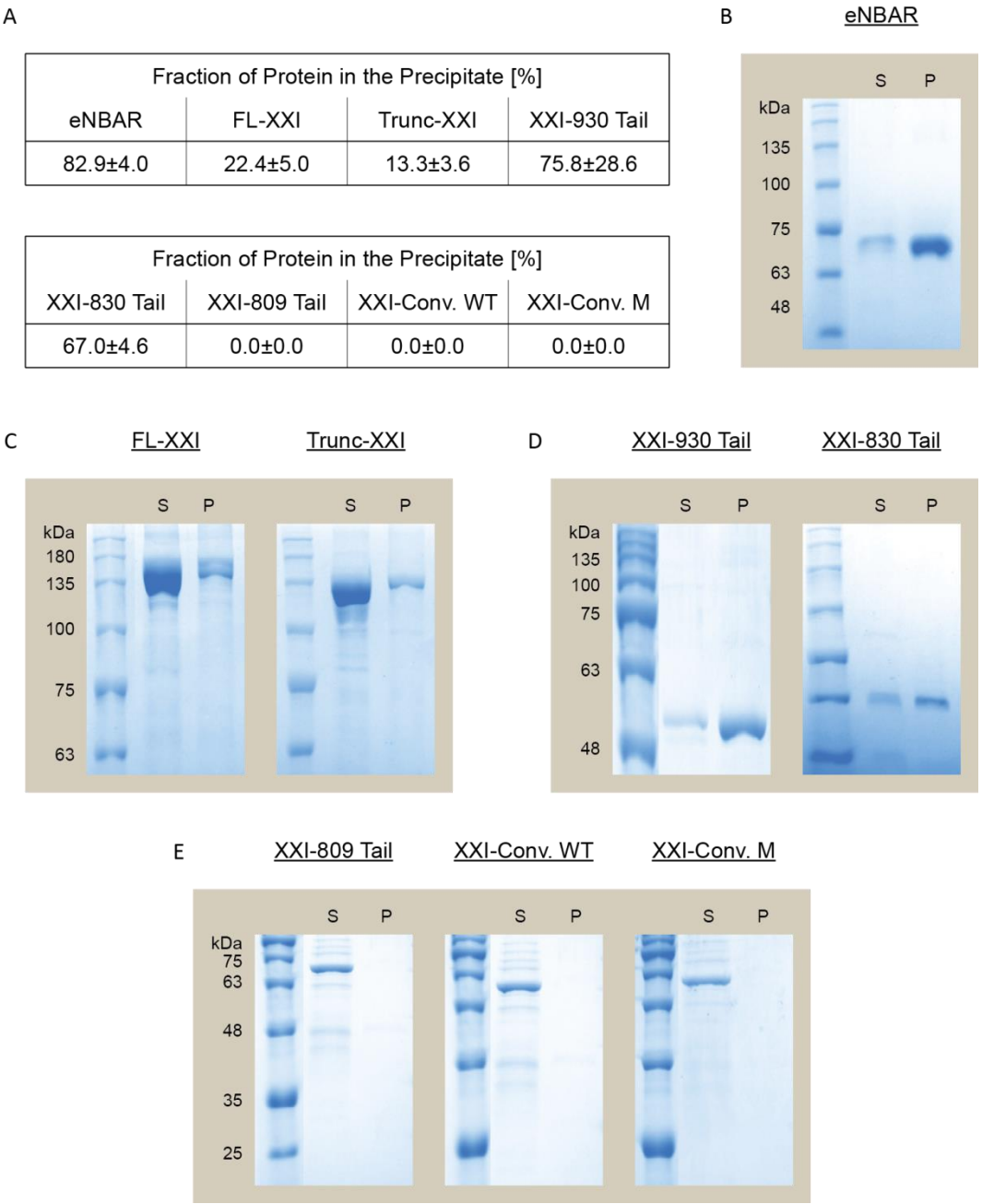

Figure 46 Co-sedimentation assays of bovine brain extract vesicles with fusion proteins of eGFP and eNBAR, FL-XXI, and myosin-XXI fragments. To test the respective proteins for their capability to bind to unilamellar vesicles, proteins were incubated with bovine brain extract vesicles and subjected to ultracentrifugation. Resulting supernatants (S) and pellets (P) were analyzed by SDS-PAGE. (A) Results of the analyses of polyacrylamide gels. In comparison to negative control assays, where on average less than 2 % of the protein content of the samples was found to precipitate, significant fractions of eNBAR, FL-XXI, Trunc-XXI, XXI-930 Tail, and XXI-830 Tail sedimented in the presence of lipids. In contrast, no precipitation of XXI-809 Tail, XXI-Conv. WT, or XXI-Conv. M was observed. Numbers are mean ± s.d. of 5 co-sedimentation assays. (B-E) Representative images showing polyacrylamide gels of co-sedimentation samples of eNBAR (B), FL-XXI and Trunc-XXI (C), XXI-930 Tail and XXI-830 Tail (D), XXI-809 Tail, XXI-Conv. WT and XXI-Conv. M (E).

In addition to the verification of protein-vesicle binding, the extent of protein precipitation in the presence of lipids also permitted a comparison of the investigated proteins´ binding affinities for vesicular bovine brain extract bilayers: while eNBAR, XXI-830 Tail, and XXI-930 Tail fractions in the precipitate were comparably high, sedimentation of FL-XXI and Trunc-XXI was significantly less pronounced. Thus, binding affinities of eNBAR, XXI-830 Tail, and XXI-930 Tail for vesicular bovine brain extract bilayers were higher than those of FL-XXI and Trunc-XXI.

In co-sedimentation assays with XXI-809 Tail, XXI-Conv. WT and XXI-Conv. M, no sedimentation of protein in the presence of lipids was discovered (Figure 46). Thus, these three myosin-XXI fragments did not bind bovine brain extract vesicles although each of the constructs contained at least one domain previously shown to be capable of phospholipid binding (Batters *et al.*, 2014).

4.8 Myosin-XXI Binding to Curved Lipid Bilayers

As experiments studying the lipid bilayer binding capability of myosin-XXI yielded the result that FL-XXI did not bind to planar lipid bilayers but did bind to lipid vesicles, the question arose whether geometrical aspects influenced lipid binding by myosin-XXI.

Research of past years has shown that several lipid binding motifs found in different proteins are sensors of membrane curvature and bind lipid bilayers in a curvature-dependent manner (e.g. Drin *et al.*, 2007; Bhatia *et al.*, 2009; Mehrotra *et al.*, 2014; Snead *et al.*, 2014; Prévost *et al.*, 2015). Accordingly, FL-XXI and myosin-XXI fragments were tested for their sensitivity for positively curved lipid bilayers.

For this purpose, Single Liposome Curvature assays were performed: immobilized rhodamine-labeled unilamellar vesicles with eGFP- or Alexa Fluor® 488-labeled protein bound were imaged in 2-channel confocal microscopy. Densities of protein bound to the surface of vesicular bilayers were quantified by the intensity ratio

$$\rho_R = \frac{I_P}{I_V} \tag{21}$$

of fluorescence signals detected from vesicles (I_V) and protein (I_P). With the help of the average intensity ratio $\overline{\rho_R}$ at vesicle diameters between 250 nm and 350 nm, normalized protein densities

$$\rho_{norm(d)} = \frac{\rho_{R(d)}}{\overline{\rho_R}} \tag{22}$$

were computed permitting comparison of results obtained for different proteins. In addition, diameters of vesicles were calculated from

$$d = c \cdot \sqrt{I_V} \tag{23}$$

with c denoting a constant calibration factor. This calibration factor was determined by combined imaging of unilamellar vesicles by confocal microscopy and STORM.

In the following subsections, results of calibration measurements and of SLiC assays will be described.

4.8.1 Size Calibration of Unilamellar Vesicles

In order to assign diameters to unilamellar vesicles imaged in SLiC assays, 34 fields of view of 20 samples of immobilized vesicles were consecutively imaged in confocal microscopy and STORM. To avoid overlapping of fluorescence signals in STORM, low phospholipid concentrations were applied for sample preparation.

In total, image analysis resulted in the determination of calibration factors for 50 distinct vesicles (Figure 47) ranging from 1.2 nm/(a.u.)$^{0.5}$ to 8.1 nm/(a.u.)$^{0.5}$. By calculation of the arithmetic mean, the final calibration factor was determined as c=3.6±1.6 nm/(a.u.)$^{0.5}$ (mean ± s.d.).

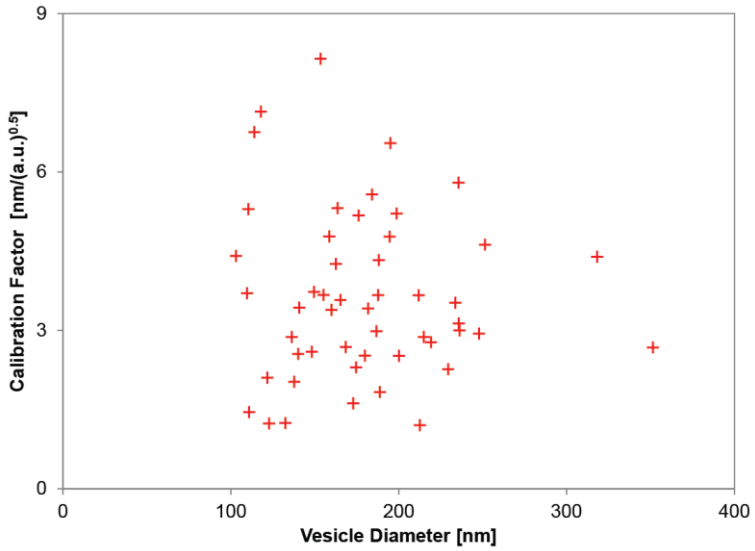

Figure 47 Size calibration of unilamellar vesicles. To enable the assignment of specific diameters to vesicles utilized in SLiC assays, calibration measurements were performed. Identical fields of view of samples containing fluorescently labeled bovine brain extract vesicles were consecutively imaged by confocal microscopy and STORM. In the subsequent analysis, related intensity signals I_V detected in confocal microscopy and diameters d determined with the help of STORM were assigned to each other and calibration factors were calculated from $d = c \cdot \sqrt{I_V}$. As depicted in the above diagram, calibration factors for 50 distinct vesicles of different diameters were deduced. By calculation of the arithmetic mean, a final calibration factor of 3.6±1.6 nm/(a.u.)$^{0.5}$ (mean ± s.d.) was determined.

4.8.2 Positive Curvature Promoted Binding of Myosin-XXI to Lipid Bilayers

In SLiC assays, impact of bilayer curvature on the bilayer binding capability of fusion proteins of eGFP and FL-XXI, Trunc-XXI, XXI-830 Tail, and XXI-930 Tail was tested. As positive control, SLiC assays with eGFP-eNBAR fusion protein were performed. In negative control assays, binding of Alexa Fluor® 488-conjugated streptavidin to Biotin DHPE contained in the vesicular bilayers was examined.

Prior to the investigation of the above-mentioned proteins, 2-channel confocal imaging of unilamellar vesicles dual-labeled with Rhodamine DHPE and DiO was carried out in order to verify the

image analysis method developed for assay evaluation. Vesicles examined were composed of 94.7 mol% bovine brain extract, 1.6 mol% Biotin DHPE, 1.2 mol% Rhodamine DHPE, and 2.5 mol% DiO. Analysis followed the identical procedure as applied to images of SLiC assay samples, with DiO fluorescence replacing the protein signal. Evaluation of 4 samples (1,123 data points) resulted in a normalized DiO surface density curve $\rho_{norm(d)}$ displaying an increase in DiO density of a maximum factor of 8.2 for small vesicles relative to vesicles with diameters ranging from 250 nm to 350 nm (Figure 48). The magnitude of this increase is in agreement with published data of dual-labeled vesicular bilayers (Larsen *et al.*, 2011). According to Larsen *et al.*, increases in dye surface densities are related to the inhomogeneous distribution of lipid species and dyes inevitable in the vesicle preparation process. As the signal increase of the DiO surface density curve generated by the image analysis method developed in the present study lies within the range of the expected increase, the analysis method is suitable for the evaluation of SLiC assays. In addition, the curve $\rho_{norm(d)}$ obtained from vesicular bilayers dual-labeled with Rhodamine DHPE and DiO presented a useful reference to assess the reasonability of results received from the analysis of samples of vesicle-bound protein.

In the following step, negative control experiments with Alexa Fluor® 488-conjugated streptavidin were executed. Normalized streptavidin densities deduced from 4 samples (296 data points) exhibited a 12.9-fold signal multiplication for protein bound to vesicles of small diameters (Figure 48). Accordingly, streptavidin results clearly resembled the curve of dual-labeled unilamellar vesicles validating the applied analysis procedure.

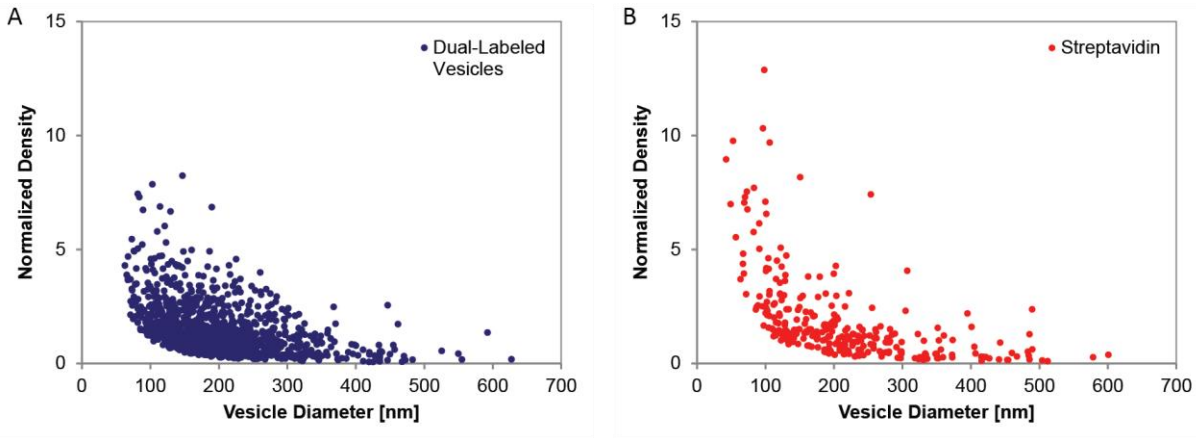

Figure 48 Imaging of dual-labeled vesicles and SLiC assays of streptavidin. Diagrams show densities of DiO and Alexa Fluor® 488-conjugated streptavidin on the surfaces of vesicular bilayers normalized to the values obtained for vesicles of the reference size, i.e. of diameters from 250 nm to 350 nm. (A) Dual-labeled vesicles composed of bovine brain extract, Biotin DHPE, Rhodamine DHPE, and DiO were immobilized, imaged by confocal microscopy, and analyzed regarding surface density of DiO molecules. Relative to the reference size, an 8.2-fold increase in the DiO surface density was detected for small vesicles. This seeming curvature dependence of the DiO signal results from an inhomogeneous distribution of lipid species and dyes inherent to the vesicle production process. The magnitude of the signal increase lies within the expected range. (B) Analysis results of SLiC assays of Alexa Fluor® 488 streptavidin bound to vesicular bilayers of bovine brain extract supplemented with Rhodamine DHPE and Biotin DHPE. Streptavidin surface density exhibited an increase by a factor of 12.9 for vesicles of small diameters thus resembling results obtained for dual-labeled vesicles. Therefore, SLiC assays of Alexa Fluor® 488 streptavidin presented a suitable negative control.

Subsequent to negative control assays, positive control experiments with 12 samples (406 data points) containing eNBAR fusion protein were carried out and evaluated. For small vesicles, normalized protein density was up to 130.4 times higher than for vesicles of the reference size (Figure 49). Thus, increase in protein signal of eNBAR significantly exceeded the signal increase observed for streptavidin. Consequently, eNBAR was identified as a sensor of positive bilayer curvature, which corresponds to findings published by Bhatia *et al.* (2009).

SLiC assays with FL-XXI (14 samples, 115 data points) resulted in a curve $\rho_{norm(d)}$ with a protein density increase of up to a factor of 59.9 (Figure 49). As in the case of eNBAR, this increase was significantly higher than the protein density increase found for the negative control suggesting that full-length myosin-XXI bound to phospholipid bilayers in a curvature-dependent manner. In SLiC assays with FL-XXI, it was noticed that FL-XXI did not bind to bovine brain extract vesicles very efficiently leaving observable amounts of fusion protein in solution. The low efficiency of the FL-XXI-bovine brain extract binding reaction limited the number of data points obtainable from one sample. This effect could only be restrictedly compensated by increasing FL-XXI concentration as unbound FL-XXI fusion protein caused an elevation of noise level.

On the contrary, in SLiC assay samples of Trunc-XXI, protein-vesicle binding was found to be remarkably efficient thereby generating a sufficient number of data points for a Trunc-XXI concentration (7 nM) almost 10-fold lower than the applied FL-XXI concentration (64 nM). Analysis of 10 samples (181 data points) containing Trunc-XXI fusion protein showed that the number of protein molecules bound to the surface of small vesicles exceeded the average reference protein surface density by the 192.1-fold hence demonstrating the curvature sensitivity of Trunc-XXI (Figure 49). Notably, Trunc-XXI was not detected to be bound to vesicles of diameters above 350 nm.

The investigation of eGFP fusion proteins of XXI-830 Tail and XXI-930 Tail showed that both of the tail fragments too were capable of sensing curvature of phospholipid bilayers. For XXI-830 Tail, 4 samples (240 data points) were evaluated yielding protein surface density increases of a maximum factor of 131.7 for small vesicles (Figure 49). Analysis of 4 samples (318 data points) containing XXI-930 Tail fusion protein revealed that up to 110.7 times more protein molecules bound to lipid vesicles of diameters below 250 nm (Figure 49).

Summarizing the results of SLiC assay experiments, myosin-XXI-lipid bilayer binding was promoted by positive bilayer curvature. In addition, fragments of myosin-XXI containing lipid binding motifs also exhibited curvature-dependent bilayer binding behavior.

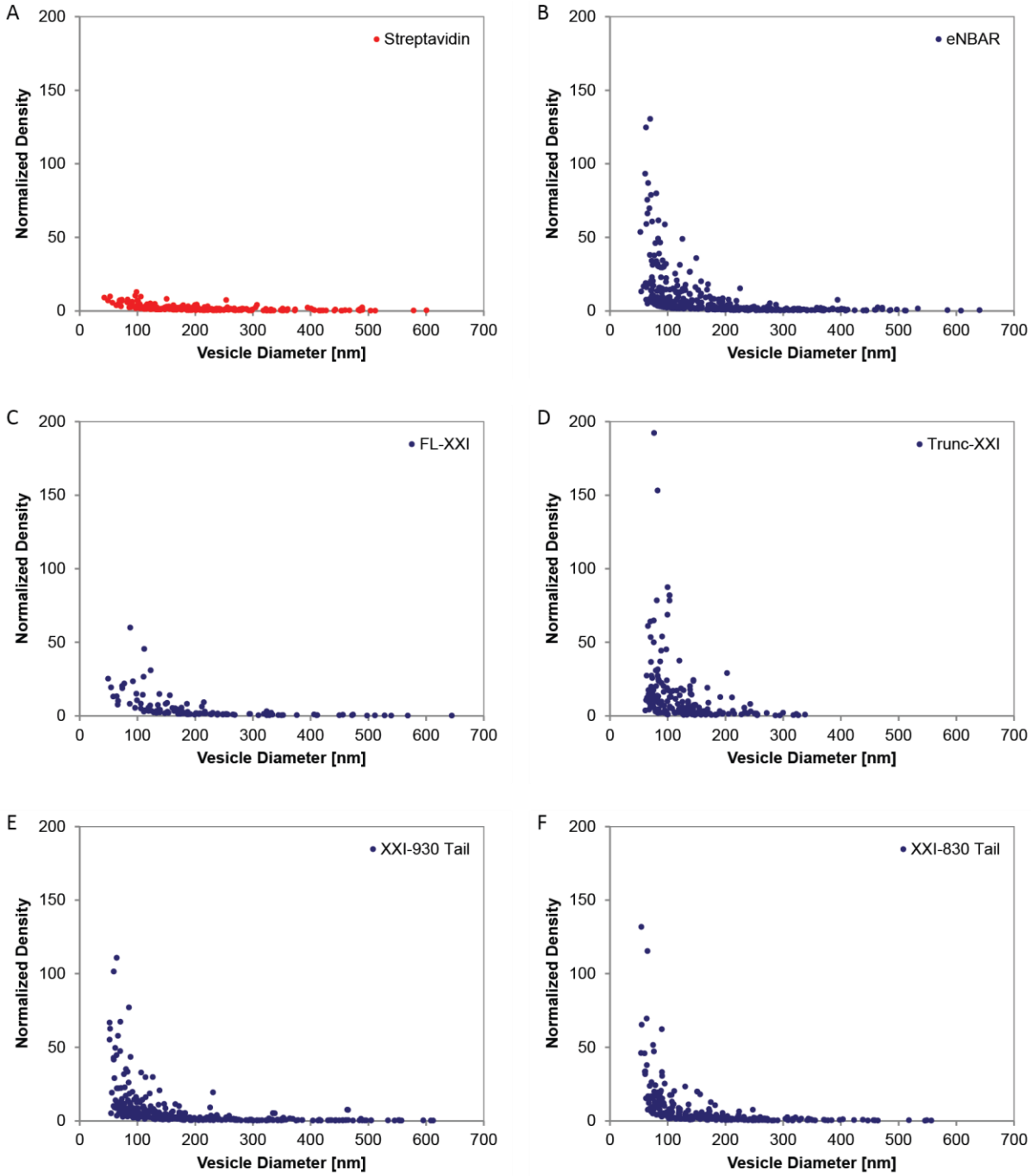

Figure 49 SLiC assays of fusion proteins of eGFP and eNBAR, FL-XXI, Trunc-XXI, XXI-930 Tail, and XXI-830 Tail. Diagrams show normalized surface densities of proteins bound to vesicular bilayers composed of bovine brain extract, Rhodamine DHPE, and Biotin DHPE. As normalization factor, average protein density detected for vesicles in the diameter interval of 250 nm to 350 nm was applied. (A) Density curve for Alexa Fluor® 488-conjugated streptavidin, which served as negative control. (B) When bound to vesicles of small size, eNBAR exhibited an up to 130.2-fold higher surface density. Thus, eNBAR was identified as a sensor of positive bilayer curvature. (C, D, E, F) Normalized surface density curves of FL-XXI (C), Trunc-XXI (D), XXI-930 Tail (E), and XXI-830 Tail (F). All myosin-XXI constructs exhibited a significant increase in the number of protein molecules bound per bilayer surface area for decreasing vesicle diameters. Surface densities increased by a factor of 59.9 (FL-XXI), 192.1 (Trunc-XXI), 110.7 (XXI-930 Tail), and 131.7 (XXI-830 Tail) respectively. Accordingly, all of the tested myosin-XXI fusion proteins bind phospholipid bilayers dependent on positive curvature.

5 Discussion

5.1 Cellular Localization Patterns and Dynamics of Myosin-XXI Constructs in Transfected HeLa and COS-7 Cells

5.1.1 General Discussion of Cellular Localization Patterns

Mammalian cell lines have frequently been used as model systems to investigate biochemical properties and cellular functions of different myosin motors (e.g. Tsakraklides *et al.*, 1999; Les Erickson *et al.*, 2003; Zhang *et al.*, 2004; Belyantseva *et al.*, 2005; Bohil *et al.*, 2006; Kerber *et al.*, 2009; Watanabe *et al.*, 2010). In the present study, plasmids encoding fusion proteins of a fluorophore and different myosin-XXI constructs were transfected into HeLa and COS-7 cells to examine myosin-XXI *in vivo*.

For all myosin constructs investigated, a diffuse distribution of fusion protein in the cytoplasm frequently paired with staining of the nucleus was detected. This staining pattern was also observed when HeLa and COS-7 cells were transfected with plasmids solely encoding a fluorophore. Therefore, a homogeneous cytoplasmic localization most probably does not represent a cellular localization specific for myosin-XXI or myosin-XXI fragments. Noteworthily, a diffuse distribution in the cytoplasm was the only localization detected for myosin-XXI tail constructs, i.e. all myosin constructs merely containing amino acids C-terminal of aa 729. In contrast, transfection experiments of the Gupta research group had demonstrated that in *L. donovani* promastigotes a myosin-XXI tail construct of aa 751 to aa 1050 was capable of localizing at the same distinct cellular locations as FL-XXI (Katta *et al.*, 2009). In addition, the tail domain had been identified as a prerequisite for the proper distribution of myosin-XXI within the promastigote. Thus, it can be concluded that in *L. donovani*, the tail domain mediates the transport of myosin-XXI via a cellular pathway that does not exist in HeLa and COS-7 cells (see subsection 5.1.2).

Contrary to the myosin-XXI tail constructs, myosin-XXI fusion proteins containing the major part of the motor domain including the ATP binding loop, switch I, switch II, the relay loop, and half of the converter were detected at distinct cellular locations when expressed in HeLa and COS-7. These locations were related to structural motifs outside the motor domain that were present in the respective proteins.

Motor-containing fusion proteins were found to accumulate in clusters and spherical structures within the cytoplasm of transfected cells. However, the nature of these myosin-XXI accumulating structures has to remain unclear as immunostaining for clathrin-coated vesicles and co-transfection experiments with baculoviruses encoding markers for early endosomes, Golgi apparatus, and endoplasmic reticulum did not reveal any colocalization of myosin-XXI with the respective organelles.

Since clusters were found to occur at high expression levels of fusion proteins and were only observed when cytoplasmic spherical myosin-XXI accumulations were present as well, clusters might result from fusion or incorporation of the smaller spherical myosin-XXI-related structures. Thus, clusters and spherical structures might potentially be part of the same cellular functional pathway. Remarkably, localization in clusters and spherical structures was independent of the presence of the myosin-XXI SH3-like or tail domain indicating that myosin binding to other cellular constituents than actin was not involved in this localization process. Therefore, myosin-XXI fusion proteins were most likely unspecifically enclosed in yet unidentified cellular compartments.

In addition to the cytoplasmic accumulations described above, Trunc-XXI and FL-XXI exhibited cellular localizations not observed for any other myosin-XXI construct tested: both fusion proteins were detected along the plasma membrane and inside filopodia of COS-7 and HeLa cells. This localization pattern will be discussed in the subsequent subsection.

5.1.2 Accumulation of FL-XXI and Trunc-XXI along the Plasma Membrane and Inside Filopodia

Of all the myosin-XXI constructs studied, FL-XXI and Trunc-XXI exhibited the most striking localization pattern. In both, HeLa and COS-7 cells, FL-XXI and Trunc-XXI fusion proteins were observed to accumulate at the tips of filopodia and to be distributed along the filopodia shafts. In addition, both proteins were found to accumulate in a dot-like appearance along the plasma membrane. Possibly, these accumulations at the plasma membrane are areas of newly emerging filopodia thus resulting from the same processes that leads to filopodial localization.

The localization of motor proteins inside the tips and along the shafts of filopodia of transfected mammalian cells has already been described for several myosins, including myosin-X (Berg and Cheney, 2002), myosin-Va (Tsakraklides *et al.*, 1999), and myosin-IIIa (Les Erickson *et al.*, 2003). As in the case of these myosins, for myosin-XXI presence of the motor domain is a prerequisite for the formation of filopodial myosin populations. Thus, identical to myosin-X, -Va, and -IIIa, myosin-XXI is likely to processively move toward the tips of filopodia under its own motor power. Further, active myosin-XXI movement along actin bundles inside filopodia agrees with myosin-XXI´s demonstrated plus end-directionality (see section 5.2), since within filopodia barbed ends of actin filaments point toward the cell periphery (Lewis and Bridgman, 1992).

The present finding that myosin-XXI needs its motor domain to reach distinct cellular locations in HeLa and COS-7 cells is seemingly contradictory to the results of transfection experiments with *L. donovani* promastigotes reported by Katta *et al.* (2009), as the latter demonstrated that proper myosin-XXI distribution within the parasite is independent of the myosin head. However, it can be argued that due to the absence of a fully developed actin network in *L. donovani*, the capability of

myosin-XXI to processively move along filamentous actin might not be sufficient for the movement of this myosin to specific cellular locations within the parasite. Instead, as indicated by the observations made by Katta *et al.*, other transport mechanisms evolved in the parasite to enable distribution of myosin-XXI. Moreover, the unspecific localization pattern of myosin-XXI tail constructs observed in the present transfection experiments with HeLa and COS-7 cells suggests that tail-mediated myosin-XXI transport in *L. donovani* is based on processes that might possibly be specific for *Leishmania* or lower eukaryotic species. As microtubules represent the main constituent of the trypanosomatid cytoskeleton (Gull, 1999) myosin-XXI might for example be transported with the help of a kinesin or dynein motor protein not found in HeLa or COS-7.

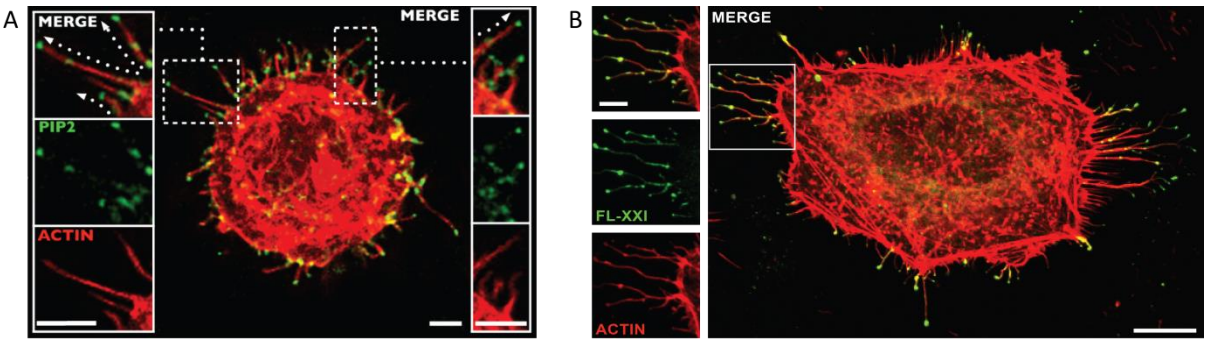

Figure 50 Cellular localization patterns of PI(4,5)P_2 and myosin-XXI. Confocal microscopy images of localization patterns of BODIPY-labeled PI(4,5)P_2 (BODIPY: dipyrromethene boron difluoride) (A) and ZsGreen1-labeled FL-XXI (B) in mammalian cells (both green). Actin cytoskeletons of the cells (red) were labeled with the help of phalloidin conjugated to ATTO 647 (A) or TRITC (B) respectively. Both PI(4,5)P_2 and FL-XXI were found to localize along the shafts of filopodia and to form pronounced accumulations at the distal filopodia ends. (A) NIH-3T3 cell treated with artificial vesicles containing fluorescent conjugates of PI(4,5)P_2 and phalloidin. Artificial vesicles were internalized by the cell via the endocytic pathway. Within early endosomes, vesicles dissociated and induced pore formation of the endosome membrane thereby causing the release of PI(4,5)P_2 into the cytoplasm. Scale bars: 5 µm. Images taken from Chierico *et al.* (2014). (B) HeLa cell transfected with a ZsGreen1-FL-XXI fusion construct and subjected to staining of F-actin after fixation. The localization pattern observed for FL-XXI was identical to the one found for Trunc-XXI. Scale bars: 20 µm, for magnified section: 5 µm.

Interestingly, the staining pattern of HeLa and COS-7 cells expressing a fusion protein of ZsGreen1 and FL-XXI or Trunc-XXI strongly resembles the staining pattern of fluorescently labeled PI(4,5)P_2 in NIH-3T3 cells (*Mus musculus* embryonic fibroblasts) observed by Chierico *et al.* (2014; Figure 50). The authors report that after fluorescent PI(4,5)P_2 was internalized by the cells via endocytosis of synthetic vesicles, PI(4,5)P_2 was found to form accumulations inside filopodia tips and domains along filopodia shafts. Considering the fact that the PI(4,5)P_2 binding capability of FL-XXI and Trunc-XXI has been demonstrated in a previous study of our lab (Batters *et al.*, 2014), myosin-XXI expressed by transfected HeLa and COS-7 cells might hence be bound to PI(4,5)P_2 within filopodia. In addition, irrespective of a potential intrafilopodial PI(4,5)P_2-myosin-XXI interaction, the striking similarity of PI(4,5)P_2 and myosin-XXI localization patterns in mammalian cells indicates that myosin-XXI is localized at regulatory sites of filopodia formation, stabilization or elongation as PI(4,5)P_2 is involved in the regulation of actin polymerization in filopodia (Lee *et al.*, 2010; Chierico *et al.*, 2014). In fact,

the assumption of myosin-XXI accumulation at such regulatory sites is further supported by the similarity of the FL-XXI and Trunc-XXI localization pattern with the reported cellular distribution of myosin-X: according to data published by Berg and Cheney (2002), myosin-X localized within filopodia of transfected COS-7, HEK-293 (human embryonic kidney epithelial cells) and NIH-3T3 cells, and furthermore influenced the length and density of filopodia in these cells.

To elucidate an involvement of myosin-XXI in the formation or elongation of filopodia of transfected HeLa and COS-7 cells, length and density analyses of filopodia were performed. Respective results will be discussed in subsection 5.1.4.

Comparison of cellular localizations of FL-XXI and Trunc-XXI with those of other myosin-XXI constructs also containing the motor domain reveals that the motor is not the only domain required for FL-XXI and Trunc-XXI to reach their filopodial destination. Additionally, the SH3-like domain and the neck and tail region from aa 748 to aa 800 have to be present in the protein. Within this region, an IQ motif, a dimerization site, and three lipid binding motifs have been identified.

According to previously published work of our group (Batters *et al.*, 2014), dimerization of myosin-XXI results in the formation of a non-motile state. Therefore, it can be concluded that dimer formation is not involved in the *in vivo* processive movement of myosin-XXI. This conclusion is further supported by the fact that dimer formation of Trunc-XXI could not be observed *in vitro* (Batters *et al.*, 2012). The requirement for a monomeric conformation implies that both FL-XXI and Trunc-XXI are capable of forming arrays of myosin molecules bound to cargo to enable processive motility *in vivo*. This again demonstrates cargo binding to be a mechanism enabling processive motor movement as for example already shown for myosin-VI (Iwaki *et al.*, 2006). Furthermore, cargo-mediated processivity explains the necessity of the presence of a minimum myosin-XXI tail fragment for FL-XXI and Trunc-XXI to reach filopodia. It is worth mentioning that actin binding by a second actin binding site within the myosin tail is another mechanism discussed to play a role in processive movement of monomeric myosins (Les Erickson *et al.*, 2003). However, Katta *et al.* (2010) verified the absence of an actin binding site C-terminal of the myosin-XXI motor domain.

In order for myosin-XXI to retain a motile monomeric state, calmodulin binding is required (Batters *et al.*, 2014) revealing that the IQ motif within the neck region of aa 754 to aa 769 is a prerequisite for FL-XXI and Trunc-XXI to move processively. In agreement with this, a myosin-XXI construct (aa 1-753) not containing the N-terminal part of the tail failed to reproduce the filopodial localization. However, unlike FL-XXI isolated Trunc-XXI was found to be incapable of binding calmodulin. Therefore, it is likely that cargo binding by Trunc-XXI causes a conformational change resulting in the accessibility of the calmodulin binding site.

Transfection experiments with constructs (aa 46-800, aa 46-1050) obtained by a deletion of the SH3-like domain from FL-XXI and Trunc-XXI revealed that the SH3-like domain too is a prerequisite

for FL-XXI and Trunc-XXI to generate the observed staining pattern. SH3 domains are known to be important mediators of protein-protein interactions also regulating protein conformation and function by intramolecular binding to other domains (Cohen *et al.*, 1995; Andreotti *et al.*, 1997; Geli *et al.*, 2000; Ago *et al.*, 2003). In fact, studies of *Dictyostelium discoideum* myosin-II indicated that the N-terminal SH3-like domain of class-II myosins stabilizes the head domain thereby facilitating nucleotide binding, actin binding, and motility (Fujita-Becker *et al.*, 2006). Thus, it is possible that the myosin-XXI SH3-like domain interacts with another structural motif within the motor domain, thereby maintaining FL-XXI and Trunc-XXI in a conformation enabling motility.

In order to determine, whether FL-XXI and Trunc-XXI differ in their capability to localize inside filopodia, transfected HeLa cells were analyzed regarding the incidence of protein accumulations within filopodia tips. It was observed that FL-XXI was present in 54 % of the filopodia tips while Trunc-XXI was detected in 25 % of the tips. Hence, FL-XXI potentially localizes within filopodia more efficiently. This might be related to a higher cargo binding capability of the full-length myosin resulting in better motility or a more effective binding to molecular components of filopodia. However, it needs to be noticed that despite equal transfection conditions, higher average fluorescence intensities of the cell bodies of FL-XXI-transfected cells in comparison to Trunc-XXI-transfected HeLa also indicate the possibility that the higher abundance of filopodial FL-XXI accumulations is related to a higher expression level of FL-XXI.

5.1.3 Dynamics of FL-XXI and Trunc-XXI in Transfected HeLa Cells

Since transfection experiments with COS-7 and HeLa cells yielded hints towards an involvement of FL-XXI and Trunc-XXI in specific cellular processes especially within filopodia, live imaging of HeLa cells transfected with FL-XXI or Trunc-XXI was performed. Records revealed that both spherical myosin-XXI accumulations in the cytoplasm and myosin-XXI populations within filopodia were motile.

In filopodia, fluorescent puncta of protein were observed to move rearward from the cell periphery to the cell body, and tracking of these puncta resulted in average rearward speeds of 24.3±15.5 nm/s (mean ± s.d.) for FL-XXI and 34.6±17.1 nm/s for Trunc-XXI. These values resemble speeds of rearward movement of fluorophore-labeled myosin-Va in HeLa (10-20 nm/s (Kerber *et al.*, 2009)), myosin-XVa in HeLa (~20 nm/s (Belyantseva *et al.*, 2005)), and myosin-X in HeLa and COS-7 (in HeLa: 15 nm/s (Berg and Cheney, 2002)), in COS-7: ~30 nm/s (Watanabe *et al.*, 2010)). Moreover, it can be argued that rearward movement of myosin-XXI results from a coupling of myosin to the retrograde actin flow in filopodia as the speed of intrafilopodial retrograde actin flow in HeLa cells was determined to range between 0 nm/s and 55 nm/s (Mallavarapu and Mitchison, 1999).

In a model described by Sousa and Cheney (2005; Figure 51), myosin-X moves toward the tips of filopodia using its own motor power and, once myosin-X stops moving actively, it is transported

back toward the cell body by coupling to rearward actin flow. During both processes, active movement and passive transport, myosin-X is involved into the delivery of cargo from the cell body to the filopodia tips and vice versa. Respective cargo is proposed to comprise integral membrane and cytoplasmic proteins which are related to the formation or stabilization of filopodia. Similar to myosin-X, active and passive forms of movement might be associated with the intrafilopodial motility of myosin-XXI in transfected HeLa and COS-7 cells. Furthermore, considering the fact that myosin-XXI increases the average length and density of filopodia in these cells, it is likely that similar to myosin-X, myosin-XXI transports components that are part of the filopodial architecture.

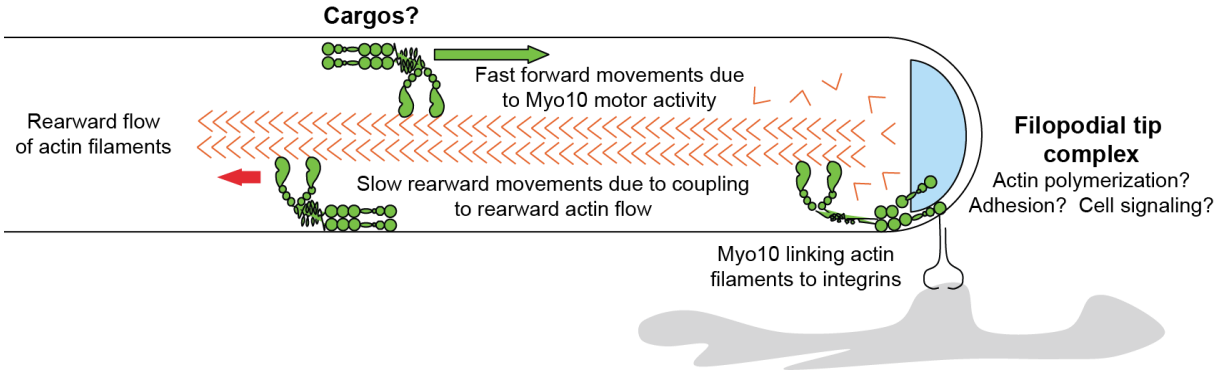

Figure 51 Model of intrafilopodial movement of and cargo transport by myosin-X. This model proposed by Sousa and Cheney (2005) states that myosin-X (green) moves into the tips of filopodia by actively walking toward the barbed ends of actin filaments. At the distal end of the filopodial actin core, where actin monomers (red) attach to the filaments, myosin-X might regulate the polymerization process as constituent of a filopodial tip complex (blue). Retrograde movement of myosin-X results from a termination of active motor movement combined with a coupling to rearward actin flow. Potential cargo of intrafilopodial transport by myosin-X is hypothesized to comprise integral membrane and cytoplasmic proteins regulating filopodia formation or stabilization. In addition, myosin-X possibly links filopodial actin to substrate-attached integrins. Figure taken from Sousa and Cheney (2005).

The assumption of active myosin-XXI movement to the tips of filopodia implies that in order to reach the filopodia tips, myosin-XXI has to be capable of moving faster than the rearward actin flow and faster than the elongation of filopodia by the polymerization of actin. A comparison of the speed of rearward actin flow in HeLa (0 nm/s to 55 nm/s) and of maximum actin assembly rates of approximately 30 nm/s in the tips of growth cone filopodia (Mallavarapu and Mitchison, 1999) with the average filament gliding speed of 63.0 nm/s observed in gliding filament assays with FL-XXI on vesicle-covered surfaces verifies that myosin-XXI is indeed capable of moving with the required speed.

Interestingly, unlike retrograde movement of FL-XXI and Trunc-XXI, a tip-directed intrafilopodial motility of these fusion proteins was not detected in confocal live imaging. The occurrence of myosin accumulations in filopodia tips despite the absence of an observable movement toward the cell periphery was also reported for a myosin-XVa-GFP fusion protein expressed by COS-7 cells (Belyantseva *et al.*, 2005). Belyantseva *et al.* concluded that myosin-XVa travels to the tips of filopodia as single molecule or in small groups. The same mechanism can be assumed for myosin-XXI,

especially since the time course of the fluorescence intensities of FL-XXI or Trunc-XXI accumulations in filopodia tips did not only exhibit significant decreases but also showed increases of up to 520 % hence clearly verifying a movement of fusion protein into the tips. Importantly, as processive translocation of myosin-XXI is most probably dependent on the formation of arrays of molecular motors (see subsection 5.1.2), FL-XXI and Trunc-XXI are likely to move toward the distal filopodia ends in small groups and not as single molecules.

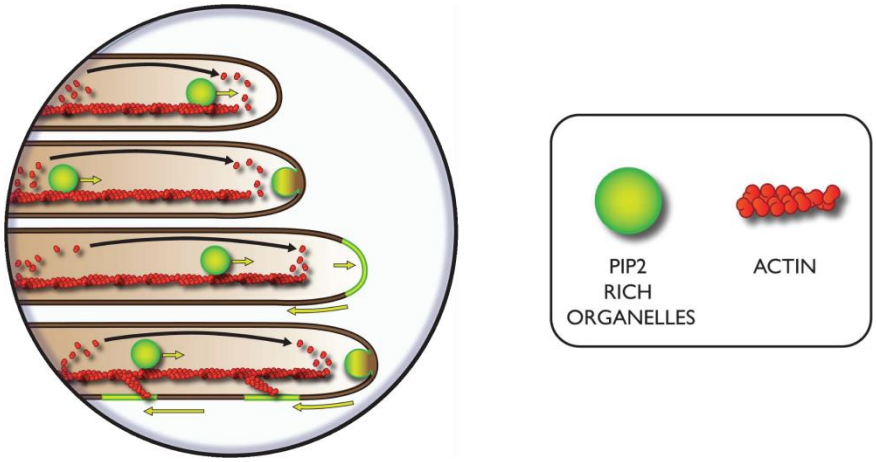

Figure 52 Model of intrafilopodial PI(4,5)P_2 movement. In NIH-3T3 cells, PI(4,5)P_2 was found to be associated with motile structures travelling toward the cell periphery (Chierico *et al.*, 2014). Accordingly, Chierico *et al.* (2014) deduced a model proposing that PI(4,5)P_2 (PIP2) is incorporated into organelles which are propelled to filopodia tips probably by the motor activity of myosins. Subsequently, organelles merge with the plasma membrane forming PI(4,5)P_2 rich domains. These domains are transported back to the cell body via a coupling to rearward actin flow. Figure taken from Chierico *et al.* (2014).

As already mentioned before, cellular localization patterns of FL-XXI and Trunc-XXI strongly resemble the distribution of PI(4,5)P_2 in NIH-3T3 cells described by Chierico *et al.* (2014; Figure 50). Interestingly, PI(4,5)P_2 was also found to be associated with motile structures travelling to the tips of filopodia. From the observed PI(4,5)P_2 dynamics, Chierico *et al.* deduced a model stating that PI(4,5)P_2 is incorporated into organelles which are propelled toward the cell periphery and merge with the plasma membrane at the filopodia tip, whereupon resulting PI(4,5)P_2 rich membrane domains are transported back toward the cell body (Figure 52). In this model, vesicular PI(4,5)P_2 transport is proposed to possibly involve myosin activity, and rearward PI(4,5)P_2 movement is assumed to be coupled to retrograde actin flow. In conclusion, PI(4,5)P_2 and myosin-XXI movement in filopodia are likely to be associated with correlating transport mechanisms. Accordingly, myosin-XXI fusion proteins might be bound to PI(4,5)P_2-enriched organelles travelling toward the tips of filopodia, and FL-XXI and Trunc-XXI rearward movement might be linked to PI(4,5)P_2 transport back to the cell body. In the first case, a low surface density of organelle-bound FL-XXI and Trunc-XXI would explain why myosin-XXI movement toward filopodia tips was not detected in live imaging. In the case of rearward movement, PI(4,5)P_2 and myosin-XXI might be propelled back to the cell body in

a multi-molecular complex which links curvature sensitive FL-XXI and Trunc-XXI (see subsection 5.3.4) to planar membrane domains via protein-protein interactions. Noteworthily, in *L. donovani* an involvement of myosin-XXI and PI(4,5)P_2 in related transport processes within membrane protrusions might account for the suggested regulatory role of PI(4,5)P_2 in flagellar development (Wei *et al.*, 2008).

To further elucidate a potential role of myosin-XXI in the formation, elongation or stabilization of membrane protrusions, in addition to an evaluation of FL-XXI and Trunc-XXI populations moving along the shafts of filopodia, accumulations of myosin-XXI fusion proteins at the filopodia tips were analyzed. It was found that myosin-XXI presence at the distal filopodia ends persisted during phases of filopodial length changes, indicating two possible scenarios: firstly, FL-XXI and Trunc-XXI possibly remain at the barbed ends of filopodial actin bundles due to their active plus end-directed movement, which as described before can reach speeds faster than the *in vivo* actin assembly rate. Secondly, myosin-XXI fusion proteins might as well be bound to constituents of the plasma membrane. Owing to the sensitivity of FL-XXI and Trunc-XXI for positively curved bilayers, plasma membrane binding then has to be mediated by protein-protein interaction, e.g. by an interaction with integral membrane proteins. The latter is a binding mechanism already demonstrated for myosin-X, which was shown to bind to integrins in the filopodial plasma membrane (Zhang *et al.*, 2004). A protein-mediated attachment of myosin-XXI to the plasma membrane further represents a potential explanation how myosin-XXI is stably fixed at the proximal region of the *L. donovani* promastigote flagellum.

The occurrence of stable myosin-XXI accumulations at filopodia tips further suggests that FL-XXI and Trunc-XXI could be capable of influencing actin polymerization, since distal ends of filopodia have been identified as sites of actin assembly (Okabe and Hirokawa, 1991). As the flagellum of *L. donovani* contains actin (Sahasrabuddhe *et al.*, 2004), regulation of actin polymerization by myosin-XXI might play a role in myosin-XXI-dependent formation of a functional flagellum.

To gain additional insight into a potential involvement of myosin-XXI in the modulation of intrafilopodial actin dynamics, length change rates of filopodia containing FL-XXI or Trunc-XXI respectively were determined. Analysis of the trajectories of permanent fusion protein accumulations at the tips of extending and retracting filopodia yielded average length change rates between 20 nm/s and 30 nm/s, with Trunc-XXI-expressing cells exhibiting higher average speeds of extension (approximate increase: 35 %) and retraction (approximate increase: 10 %) than FL-XXI-expressing HeLa. This dependency of filopodial length change rates on the fusion protein expressed cannot be explained by a difference in the motor activity of the two proteins as past research of our lab had even demonstrated that Trunc-XXI exhibits a slightly reduced actin-activated ATPase rate in comparison to FL-XXI (Batters *et al.*, 2012). Thus, the observed divergence indicates that myosin-XXI

actually influences actin dynamics within filopodia. Interestingly, similar observations were made for myosin-X in transfected COS-7 cells (Watanabe *et al.*, 2010): variations in the length of filopodia of cells expressing the full-length protein proceeded slower than length changes in cells transfected with a truncated myosin-X construct lacking the C-terminal FERM domain. In this case, the absence of the FERM domain was suggested to result in the incapability of the myosin-X motor truncation to link the filopodial actin core to substrate-attached integrins in the plasma membrane. The fact that Trunc-XXI and FL-XXI too merely differ in their tail domains indicates that the detected shift in filopodial length change rates is as well related to an interaction with binding partners. However, this interaction might not be restricted to intrafilopodial transport processes. Instead, Kozlov and Bershadsky (2004) proposed that myosins might actively promote actin polymerization by exerting tensile forces on capping proteins at the barbed ends of actin bundles. Yet, further investigations on myosin-XXI binding partners will have to be carried out in order to elucidate how this motor protein regulates actin assembly or disassembly.

In summary, analysis of live records of HeLa cells expressing FL-XXI or Trunc-XXI revealed that myosin-XXI is likely to be involved in processes regulating the assembly of membrane protrusions. Analyses of filopodia length and density of transfected HeLa and COS-7 cells, which are described in the next subsection, further confirmed this conclusion.

5.1.4 Induction of Filopodial Length and Density Increases in FL-XXI- and Trunc-XXI-Transfected HeLa and COS-7 Cells

In order to gain further information on a potential involvement of myosin-XXI in the formation, stabilization, or elongation of membrane protrusions, HeLa and COS-7 cells transfected with FL-XXI and Trunc-XXI were analyzed regarding average filopodia length and density.

The present work shows that myosin-XXI, similar to myosin-X in COS-7 cells (Berg and Cheney, 2002; Zhang *et al.*, 2004; Bohil *et al.*, 2006; Watanabe *et al.*, 2010), is capable of changing the average length and density of filopodia. For myosin-X, it was shown that localization of myosin inside the tips of filopodia was not sufficient to increase filopodial number and length (Bohil *et al.*, 2006). While tip localization only required head, neck and predicted coiled coil region of myosin-X, the MyTH4-FERM (MyTH4: myosin tail homology 4) domain cassette was essential for changes in length and density of filopodia (Berg and Cheney, 2002; Zhang *et al.*, 2004; Bohil *et al.*, 2006; Watanabe *et al.*, 2010). In contrast, myosin-XXI localization in filopodia was always accompanied by an elevated average density and length of filopodia. This suggests that the myosin-XXI tail region C-terminal of aa 800 does not fulfill essential functions in the initiation and elongation of actin-based membrane protrusions.

Nevertheless, FL-XXI-transfected cells were found to produce longer filopodia than Trunc-XXI-transfected ones even in the case of COS-7 cells, which exhibited lower average FL-XXI expression

levels than Trunc-XXI expression levels. Therefore, it can be concluded that the C-terminal part of the myosin-XXI tail is not essential for filopodia elongation but might increase the efficiency of the underlying processes.

Interestingly, a more detailed analysis of transfected HeLa cells revealed that filopodia not displaying myosin-XXI fusion protein accumulations in their tips exhibited an average length up to 7.5 % smaller than the average filopodia length of the control, i.e. of HeLa merely expressing ZsGreen1. In contrast, filopodia containing FL-XXI or Trunc-XXI populations within their tips, showed an increase in average length of up to 53 % relative to the control. Thus, FL-XXI and Trunc-XXI localization at the distal ends of filopodia is likely to be related to the elongation of filopodia indicating that myosin-XXI is capable of mediating processes promoting actin polymerization. As already described earlier (see subsection 5.1.3), potential roles of myosin-XXI therefore comprise the mechanical regulation of actin assembly by the exertion of a tensile force on capping proteins and the transport of cargo involved in the enhancement of actin polymerization comparable for example to intrafilopodial VASP transport by myosin-X (Tokuo and Ikebe, 2004).

In fact, the involvement of myosin-XXI-cargo or -capping protein binding in the regulation of filopodia length might explain the more pronounced elongation effect of FL-XXI: as in the case of differing filopodial extension and retraction rates of FL-XXI- and Trunc-XXI-transfected HeLa cells, it can be argued that a truncation of the myosin-XXI tail domain reduces efficiency of interaction with binding partners. Thereby, mechanical regulation of capping proteins and transport mediated by myosin-XXI would be impaired.

In addition to an elongation of already existing filopodia, interaction of FL-XXI and Trunc-XXI with binding partners might also play a role in elevating the filopodia density of HeLa and COS-7 cells: by forming a link between the filopodial actin core and integral membrane proteins, myosin-XXI could amplify the adhesion force between actin and the plasma membrane thus further reducing coalescence of neighboring filopodia. Noteworthily, mediation of cytoskeleton plasma membrane adhesion is proposed to be a critical function of myosins in the formation and maintenance of membrane protrusions (Tyska *et al.*, 2005; Nambiar *et al.*, 2010) and is assumed to be a potential function of myosin-X-integrin interaction within filopodia (Zhang *et al.*, 2004). Furthermore, an involvement of myosin-XXI in the tethering of intrafilopodial actin bundles to the plasma membrane could provide an additional explanation for the resembling cellular localization patterns of FL-XXI, Trunc-XXI, and PI(4,5,)P_2, which has been shown to be a crucial regulator of cytoskeleton-plasma membrane interaction (Raucher *et al.*, 2000).

Another myosin-XXI-related mechanism potentially influencing the density of filopodia is an actin bundling activity similar to that proposed for myosin-X (Figure 53; Tokuo *et al.*, 2007): based on its plus end-directionality, dimeric myosin-X actively travels to the plasma membrane and subsequently

bundles adjacent actin filaments in a yet unknown process. Thereby, initiation sites for the formation of filopodia are created. In the case of FL-XXI and Trunc-XXI, actin bundling would be mediated by arrays of monomers as array formation is expected to be a prerequisite for processive movement of FL-XXI and Trunc-XXI (see subsection 5.1.2). In agreement with a contribution of myosin-XXI to the initiation of filopodia, FL-XXI and Trunc-XXI were found to accumulate along the plasma membrane of transfected mammalian cells.

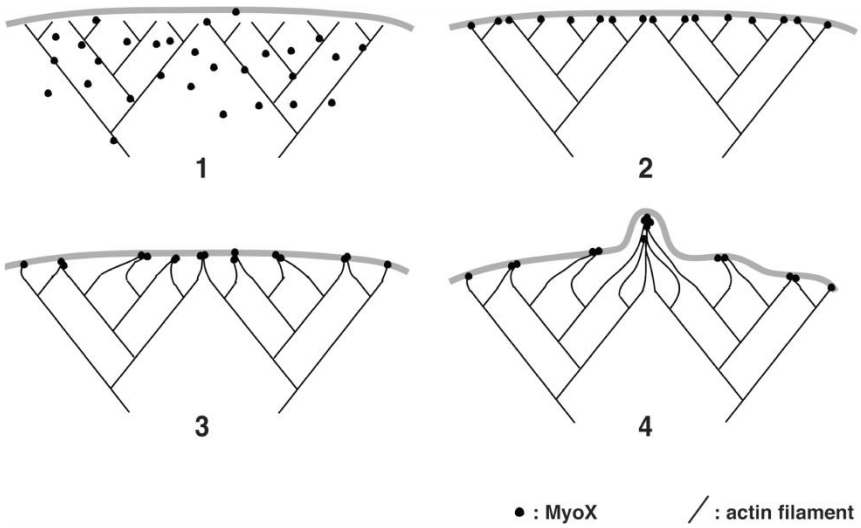

Figure 53 Model of filopodia initiation by myosin-X. In the model depicted above, Tokuo *et al.* (2007) hypothesize how myosin-X induces the formation of filopodia. 1: Myosin-X (MyoX) exists in a monomeric and a dimeric form. Monomers are distributed throughout the cytoplasm while dimers associate with actin filaments and perform processive movement. 2: Once monomers have assembled to dimers, dimeric myosin-X walks toward the barbed ends of F-actin. 3: In a yet unspecified process, myosin-X motor power drives lateral movement of barbed actin filament ends. 4: Filament drift results in convergence of filament ends thereby creating initiation sites of filopodia formation. Figure taken from Tokuo *et al.* (2007).

Moreover, both processes, tethering of actin to the plasma membrane and initiation of filopodia formation, coincide with the fact that no obvious relation between FL-XXI and Trunc-XXI accumulation within the filopodia tips and the increase in filopodia density was found.

However, as both mechanisms described above involve the interaction of FL-XXI and Trunc-XXI with binding partners, at present it still remains unclear why the extent of the filopodial density increase was observed to be independent from the myosin-XXI construct and thereby independent from the myosin-XXI tail region C-terminal of aa 800: HeLa cells transfected with FL-XXI exhibited an almost twofold higher expression level than HeLa transfected with Trunc-XXI, and FL-XXI expression caused a two times higher filopodial density increase compared to Trunc-XXI expression. In contrast, despite comparable expression levels in COS-7 cells, FL-XXI caused a more than threefold smaller increase in the density of filopodia of COS-7 than Trunc-XXI.

Overall, the impact of FL-XXI and Trunc-XXI on filopodia length and density clearly indicates that myosin-XXI is capable of promoting the elongation, initiation, and possibly even the stabilization of actin-based membrane protrusions.

5.1.5 Conclusions on Functions of Myosin-XXI in *L. donovani*

Studies of the intracellular architecture of trypanosomatids revealed that microtubules represent the main cytoskeletal constituent in these parasites and form the flagellar axoneme (Gull, 1999). However, flagellar development and functionality are based on complex processes involving various proteins (Landfear and Ignatushchenko, 2001; Emmer *et al.*, 2010; Maric *et al.*, 2010) and in recent years, it was discovered that actin is not only present within the *L. donovani* cell body and flagellum (Sahasrabuddhe *et al.*, 2004) but that actin polymerization and depolymerization are prerequisites for the formation of a functional flagellum (Tammana *et al.*, 2008; Kumar *et al.*, 2012). In addition, Katta *et al.* (2010) demonstrated that actin-based cargo transport by myosin-XXI too is essential for the development of the flagellum. Restriction of actomyosin-associated trafficking processes by a double gene knockout of the ADF/cofilin gene or a single gene knockout of the myosin-XXI gene resulted in a reduction of flagellar length and the elimination of *L. donovani* promastigote motility. Moreover, respective mutants exhibited defective endocytosis, exocytosis, and intracellular vesicle transport. Hence, the interplay between actin dynamics and actin-associated myosin-XXI transport is critical for the survival of *L. donovani*.

In transfection experiments with mammalian cell lines HeLa and COS-7, FL-XXI and several myosin-XXI fragments were tested for their cellular localization to draw conclusions about potential *in vivo* functions of the full-length molecule and particular structural motifs.

It was found that exclusively FL-XXI and Trunc-XXI colocalized with the actin core of filopodia and accumulated in filopodia tips, probably due to active movement powered by myosin-XXI motor activity. Thus, unlike in *L. donovani* promastigotes (Katta *et al.*, 2009), the C-terminal myosin-XXI tail region is not required for the two constructs to reach their cellular destination in HeLa and COS-7. Further, results of analyses of filopodial length change rates and of average filopodia lengths of transfected mammalian cells indicate a regulatory function of FL-XXI and Trunc-XXI in the polymerization of actin. Hence, it can be concluded that even though myosin-XXI structural motifs N-terminal of aa 751 are not essential for myosin localization within *L. donovani* promastigotes, together with the N-terminal part of the myosin-XXI neck and tail region they are critical for a potential regulation of actin assembly by myosin in the parasite. Overall, the respective regulatory part of myosin-XXI comprises an SH3-like domain, the motor domain including the converter, an IQ motif, a PX domain, several other lipid binding domains, and a dimerization site are located.

Intrafilopodial movement of FL-XXI and Trunc-XXI observed in live images of transfected HeLa cells and the increased average length of filopodia containing accumulations of either one of the myosin-XXI fusion proteins lead to the conclusion that regulation of actin dynamics by myosin-XXI might result from a transport of constituents involved in actin polymerization. Likewise, in *L donovani* myosin-XXI might transport components that regulate the assembly or analogically the disassembly

of filamentous actin. Interestingly, in addition to dynamic actin and actin-based myosin-XXI trafficking expression of the actin-depolymerizing factor ADF/cofilin has been shown to be another prerequisite for the formation of a functional flagellum (Tammana *et al.*, 2008) possibly indicating an interaction of myosin-XXI, actin and ADF/cofilin in the process of flagellum formation.

In addition to an involvement in transport processes, a potential role of FL-XXI and Trunc-XXI in the elongation of filopodia and other cellular processes dependent on dynamic actin is to interact with capping proteins thus facilitating actin assembly. However, in *Leishmania* no actin capping proteins have been identified so far (Gupta *et al.*, 2015).

The observation that FL-XXI and Trunc-XXI not only elongated filopodia of transfected HeLa and COS-7 cells but also increased filopodia density implies that myosin-XXI might contribute to the initiation and stabilization of filopodia. Initiation could be promoted by an actin bundling activity of myosin-XXI which might as well play a role in the formation of granular actin structures detected in the *L. donovani* flagellum and in other compartments of the promastigote (Sahasrabuddhe *et al.*, 2004). Filopodia stabilization might result from a binding of FL-XXI and Trunc-XXI to integral membrane proteins creating an adherent force between the plasma membrane and intrafilopodial actin thereby preventing coalescence of neighboring filopodia. As trypanosomatids only possess a single flagellum, prevention of the merging of membrane protrusions is not a potential function of myosin-XXI in *L. donovani*. Instead, by forming an interlink between actin and cellular membranes myosin-XXI might be involved in the actin-mediated tethering of subpellicular microtubules to the *L. donovani* plasma membrane proposed by Sahasrabuddhe *et al.* (2004).

In fact, further indications on an interaction of myosin-XXI with membrane components are provided by the strong resemblance of the cellular localization patterns of FL-XXI and Trunc-XXI with the $PI(4,5)P_2$ distribution in NIH-3T3 cells. Considering the fact that myosin-XXI as well as $PI(4,5)P_2$ are critical factors in flagellar development, an interplay of these two constituents in *L. donovani* appears to be probable.

To summarize, results of mammalian cell transfections imply that myosin-XXI is potentially involved in the regulation of actin polymerization in *L. donovani* and that this regulatory function is mediated by the N-terminal 800 amino acids of the motor protein i.e. by the aa sequence referred to as Trunc-XXI. In addition, myosin-XXI could possibly play a role in the formation of actin bundles and interact with cellular membranes. Membrane interaction might amongst others be mediated by $PI(4,5)P_2$.

5.2 Determination of Myosin Directionality in Gliding Filament Assays with Dual-Labeled Actin Filaments

In the course of this work, based on a protocol published by Herm-Götz *et al.* (2002) a method for the determination of the directionality of actin-based motor movement was developed. After the formation of TRITC-labeled actin seeds, actin polymerization was limited to the pointed ends of filaments by the application of gelsolin capping protein. This way, actin monomers newly added to the seeds selectively bound to the minus end, which was then specifically labeled with the help of phalloidin-FITC. This procedure resulted in the formation of filamentous actin exhibiting a polar fluorescent labeling.

Analysis of gliding filament assays with myosin-VI and HMM identified myosin-VI as minus end-directed and HMM as plus end-directed motor protein agreeing with the literature (Huxley, 1969; Sheetz and Spudich, 1983; Wells *et al.*, 1999) and thus demonstrating that the developed actin staining protocol is a useful tool for the determination of myosin directionality.

In the case of gliding filament assays with dual-labeled actin filaments driven by full-length myosin-XXI, evaluation of TIRF microscopy records revealed that myosin-XXI is a plus end-directed actin-based motor protein. This finding coincides with the current state of knowledge that myosin-VI is the only native myosin moving along filamentous actin in a minus end-directed fashion (O´Connell *et al.*, 2007).

It is noteworthy that in *L. donovani*, existence of a trypanosomatid actin species has been demonstrated but that this actin species was only found to form granules, patches, or filaments and bundles of small length (Sahasrabuddhe *et al.*, 2004; Kapoor *et al.*, 2008). The existence of a complex actin network as formed in higher eukaryotic cells has so far not been reported (Rodrigues *et al.*, 2014). Accordingly, directed movement along filamentous actin was demonstrated not to play a major role for myosin-XXI to reach its cellular localizations (Katta *et al.*, 2009). In *L. donovani* promastigotes, myosin-XXI was found to be sparsely distributed in the cytoplasm and to be concentrated in the proximal region of the flagellum and along the proximal length of the paraflagellar rod (Katta *et al.*, 2009). Myosin-XXI detected at the flagellar base was found to be stably attached to this region via its tail domain (Katta *et al.*, 2009) most probably leaving the myosin head free to rotate. Hence, on the basis of their findings indicating the necessity of actomyosin-based transport for the formation of a flagellum, Katta *et al.* (2010) proposed a model in which this stationary myosin-XXI subpopulation propels actin-bound cargo into or out of the flagellum. In this scenario, the demonstrated plus end-directed movement of myosin-XXI along F-actin could possibly play a role in determining the direction of cargo transport.

5.3 Myosin-XXI Binding to Phospholipid Bilayers

5.3.1 Myosin-XXI Binding to Planar Lipid Bilayers

In a previous study of our research group (Batters *et al.*, 2014), myosin-XXI was found to be capable of binding actin filaments and of driving filament movement when associated with vesicular lipid bilayers. Additionally, in present transfection experiments fusion proteins of ZsGreen1 and FL-XXI or Trunc-XXI accumulated along the plasma membrane of HeLa and COS-7 cells. Therefore, the association of myosin-XXI with lipid bilayers was further investigated in the present work. In this context, myosin-XXI´s capability to associate with planar lipid bilayers was examined and dynamics of the bilayer-bound actin-myosin-XXI complex was aimed to be further elucidated.

In experiments on both supported lipid bilayers and tethered lipid bilayers, it was observed that FL-XXI only bound to the sample surface in the presence of phospholipids shown to bind myosin-XXI. Therefore, it can be concluded that lipid binding was involved in the attachment of myosin-XXI. However, in FRAP experiments with eGFP-FL-XXI fusion protein incubated with supported lipid bilayers no 2D lateral diffusive movement of fusion protein was detected implying that myosin-XXI did not bind to the intact fluid part of the bilayer. Instead, observations made when FL-XXI and F-actin were incubated with bilayers indicate that myosin-XXI bound to immobile structures on the surface of the sample. As binding of FL-XXI to vesicular bilayers has successfully been implemented in our lab (see sections 4.6 and 4.7; Batters *et al.*, 2014), lipid binding of myosin-XXI is most likely influenced by bilayer geometry. Probably, myosin-XXI incubated with planar lipid bilayers bound to phospholipids at areas of bilayer discontinuities where positive bilayer curvature occurs (Figure 54). Noteworthily, several proteins like α-synuclein, apolipoprotein A-1, negative factor, and sorting nexin 1 which bind to bilayers in a curvature-dependent manner have already been shown to be capable of deforming membranes (Wetterau and Jonas, 1982; Davidson *et al.*, 1998; Kurten *et al.*, 2001; Carlton *et al.*, 2004; Gerlach *et al.*, 2010; Varkey *et al.*, 2010). Thus, it is possible that myosin-XXI does not passively bind to regions of positive bilayer curvature but actively induces these binding sites. In subsection 5.3.4 geometrical aspects of bilayer binding by myosin-XXI will be discussed in further detail.

In agreement with the observations described above, formation of supported planar lipid bilayers from solutions containing vesicles and FL-XXI was not observed unless FL-XXI concentration was very low. Accordingly, bilayer formation only occurs when vesicles are associated with minor amounts of protein. This inhibitory effect of FL-XXI could result from a curvature stabilizing function of bilayer-associated myosin comparable to the curvature stabilizing action of sorting nexin 1 (Carlton *et al.*, 2004), endophilin A1 (Farsad *et al.*, 2001), or the syndapin 1 BAR domain (Ramesh *et al.*, 2013).

However, it cannot be ruled out that the absence of bilayer formation was caused by the prevention of vesicle attachment to the glass surfaces of flow cells due to the presence of myosin-XXI.

Interestingly, myosin-XXI immobilized on planar bilayer-covered surfaces despite being capable of binding F-actin does not induce gliding of filaments. Since FL-XXI was found to propel filamentous actin when bound to lipid vesicles (see section 4.6; Batters *et al.*, 2014), absence of myosin-XXI motility in planar bilayer samples is most probably caused by steric hindrance.

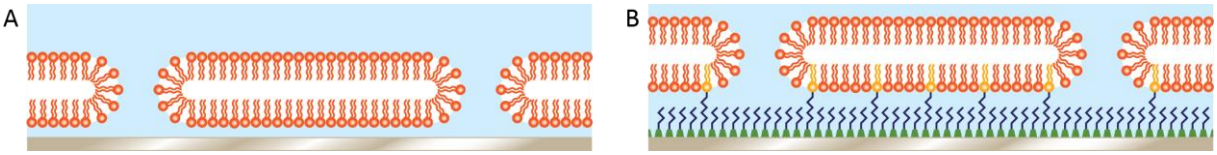

Figure 54 Illustration of discontinuities of supported and tethered planar lipid bilayers. At discontinuities of supported (A) and tethered (B) planar lipid bilayers, hydrophobic tails of the lipid molecules are shielded from the aqueous environment by the formation of curved bilayer edges. These curved regions might provide binding sites for curvature sensitive lipid binding proteins.

5.3.2 Myosin-XXI Binding to Vesicles

As described in the preceding subsection, the incapability of myosin-XXI to bind to planar lipid bilayers indicates that bilayer curvature might represent a crucial factor for the attachment of myosin-XXI. Consistently, studies of our research group have shown that FL-XXI binds vesicular bilayers of bovine brain extract and actually induces actin filament gliding in a vesicle-bound state (Batters *et al.*, 2014).

In the course of the present work, co-sedimentation assays and gliding filament assays on surfaces covered with unilamellar vesicles confirmed the previous finding of myosin-XXI binding to bovine brain extract, PI(4)P, and PI(3,5)P_2, and verified the utilized FL-XXI samples to be functional in respect of lipid binding. The observed binding of FL-XXI to vesicle-incorporated PI(4)P and PI(3,5)P_2 was in line with previously published findings obtained with the help of membrane lipid strips (Batters *et al.*, 2014). In addition, the present negative control experiments demonstrated that in the absence of myosin-XXI binding phospholipids, FL-XXI does not bind to vesicle-covered surfaces. Hence, filament gliding observed on vesicles containing myosin-XXI binding phospholipids was in fact driven by lipid-bound FL-XXI.

Overall, the verification of FL-XXI binding to vesicular lipid bilayers provides further evidence for a curvature dependence of the lipid bilayer binding capability of myosin-XXI.

Additionally, vesicle-based gliding assays demonstrated that lipid-bound FL-XXI is capable of efficiently propelling filamentous actin and that the lipid-bound state of myosin-XXI seems to be of advantage for driving filament movement: in the present experiments, the average gliding speed of F-actin on vesicles containing 4.8 mol% PI(3,5)P_2 was observed to be 3.5 times higher than the previously published speed of filament gliding on nitrocellulose-coated surfaces (18±3 nm/s (mean ±

s.d.; Batters *et al.*, 2014)). Accordingly, the present finding coincides with the previously reported enhanced motility of myosin-XXI when bound to bovine brain extract vesicles.

Furthermore, co-sedimentation assays with unilamellar vesicles composed of bovine brain extract, Rhodamine DHPE, and Biotin DHPE and fusion proteins of eGFP and several myosin-XXI constructs revealed differing capabilities of FL-XXI and the respective myosin-XXI fragments to bind vesicular bovine brain extract bilayers and thus indicated a potential influence of intermolecular interactions on myosin-XXI-lipid binding (Figure 55).

In agreement with published results (Batters *et al.*, 2014), FL-XXI, Trunc-XXI, XXI-830 Tail, and XXI-930 Tail were observed to bind to bovine brain extract vesicles in the present study.

However, fusion constructs of the myosin-XXI converter domain (XXI-Conv. WT, XXI-Conv. M) did not exhibit any binding in the present experiments. As the myosin-XXI PX domain is the only lipid binding domain so far identified within the respective amino acid sequence (aa 600-758; Batters *et al.*, 2014), this observation might imply that the binding of myosin-XXI to bovine brain extract does not involve the PX domain. Otherwise, similar to PX domains of other proteins, functionality of the myosin-XXI PX domain might depend on intramolecular or intermolecular interactions (Seaman and Williams, 2002; Ago *et al.*, 2003) and these interactions might not be promoted by the converter constructs or the experimental settings.

In previous binding tests using membrane lipid strips, unlabeled myosin-XXI converter constructs exhibited strong binding affinities for several phosphoinositides including PI(4)P (Batters *et al.*, 2014). In addition, the wild-type construct was detected to bind phosphatidylserine in these tests. Accordingly, as bovine brain extract contains phosphatidylserine as its major constituent and further contains phosphatidylinositol including phosphorylated forms like PI(4)P (Low, 1990), detection of a binding reaction between bovine brain extract vesicles and XXI-Conv. WT or XXI-Conv. M might be expected. The absence of an association of the myosin-XXI converter constructs with bovine brain extract vesicles observed in the present study might therefore result from differences in the applied experimental approaches. In membrane lipid strip tests, unlabeled proteins were used while in the present experiments, fluorescently labeled converter constructs were investigated. As shown by our research group, presence of a fluorophore label can induce dimerization of myosin-XXI constructs, which in turn severely impairs lipid binding (Batters *et al.*, 2014). Thus, the incapability of XXI-Conv. WT and XXI-Conv. M to bind to vesicular bovine brain extract bilayers in the present study might result from the presence of the eGFP label.

It should be mentioned that the results of vesicle binding experiments and membrane lipid strip tests have been reported to occasionally differ. This variability is presumed to arise from the different geometrical arrangements of the binding partners in the two experimental set-ups (Cozier *et al.*, 2002; Zhan *et al.*, 2002; Seet and Hong, 2006).

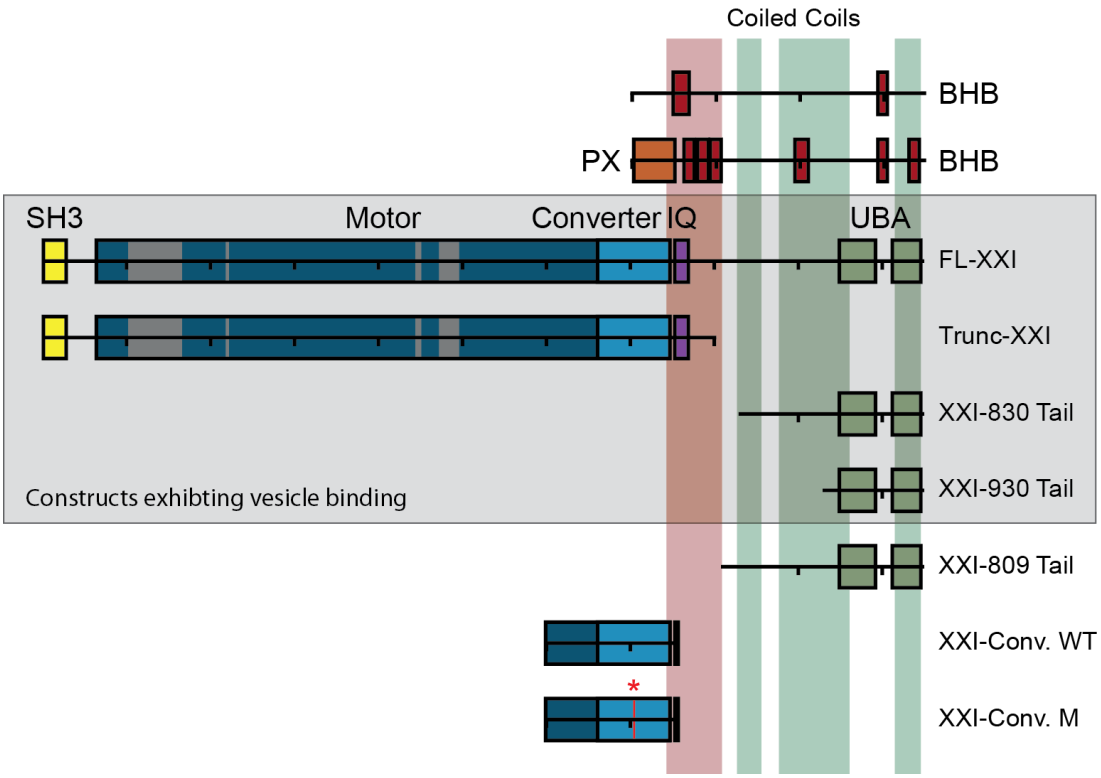

Figure 55 Lipid binding domains of myosin-XXI constructs tested in co-sedimentation and SLiC assays. The above scheme summarizes the lipid binding domains contained in the myosin-XXI constructs tested in the present co-sedimentation and SLiC assays. Respective lipid binding sites of myosin-XXI had been identified in a previous study of our lab (Batters *et al.*, 2014). They comprise a PX domain and several potential lipid binding motifs exhibiting a BHB sequence. BHB regions in the top row had been determined by calculation of a basic and hydrophobic score, BHB regions in the bottom row had been deduced from sequence analysis. In the present study, co-sedimentation assays were carried out to test all of the myosin-XXI constructs depicted above for their capability to bind to bovine brain extract vesicles. The asterisk above the scheme of the mutated myosin-XXI converter construct (XXI-Conv. M) indicates the position of the respective PX domain mutation. Co-sedimentation experiments showed that FL-XXI, Trunc-XXI, XXI-830 Tail, and XXI-930 Tail bound to the respective vesicles. With the help of SLiC assays, the latter fusion proteins were then investigated for curvature sensitive bilayer binding.

Similar to XXI-Conv. WT and XXI-Conv. M, XXI-809 Tail did not display binding to bovine brain extract vesicles in the present study. Again, this might be caused by the presence of the fluorescent label. However, it is conceivable that XXI-809 Tail represents a myosin-XXI fragment incapable of binding to vesicular bilayers. Noteworthily, a dependency of the vesicle binding capability on the protein architecture flanking a lipid binding site has for example already been demonstrated for the centaurin β2 BAR domain (Peter *et al.*, 2004) and the amphipathic helix motif of nucleoporin 133 (Doucet *et al.*, 2015): in the case of the centaurin β2 BAR domain, the presence of the adjacent PH domain significantly enhanced vesicle binding; in the case of the nucleoporin 133 amphipathic helix, the efficiency of vesicle binding was markedly reduced in the absence of the spatial constraint by the beta-propeller domain surrounding this motif. Accordingly, to be capable of binding to vesicular bilayers the XXI-809 Tail construct might require the presence of N-terminal structural myosin-XXI motifs. Since XXI-830 Tail was found to bind to bovine brain extract vesicles, in the absence of the N-terminal part of myosin-XXI the region of aa 809 to aa 829 possibly influences lipid binding sites

within the tail, for example by forming intramolecular bonds resulting in a change of the protein´s conformation.

Overall, vesicle-based experiments performed in the present work clearly show that myosin-XXI and specific fragments of the motor protein are capable of associating with curved lipid bilayers. Together with the demonstrated incapability of myosin-XXI to bind to lipid bilayers of planar geometry, these findings strongly indicate a curvature-dependent bilayer association of myosin-XXI. Consequently, in the next step binding of myosin-XXI to curved bilayer surfaces was further investigated with the help of Single Liposome Curvature assays.

5.3.3 Investigation of Curvature Sensitivity in Single Liposome Curvature Assays

Single Liposome Curvature assays have been demonstrated to be a highly sensitive tool for the detection of a protein´s preference for curved bilayer geometries (Bhatia *et al.*, 2009; Hatzakis *et al.*, 2009; Madsen *et al.*, 2010; Larsen *et al.*, 2015).

In order to analyze SLiC assays, an image processing routine was established and verified with the help of samples of immobilized dual-labeled vesicles. Furthermore, size calibration measurements were performed to enable the determination of vesicle diameters. Subsequently, negative and positive control experiments were carried out.

DiO surface densities derived from assays with dual-labeled vesicles and calculated calibration factors were found to display variations within an order of magnitude. Similarly, Larsen *et al.* (2011) had detected the surface density of a fluorescent dye in dual-labeled vesicular bilayers to exhibit variations of up to an order of magnitude and assigned this effect to an inhomogeneous distribution of lipid species and dyes inevitable in the vesicle preparation process. Accordingly, results of calibration measurements and control experiments with Rhodamine DHPE/DiO-labeled vesicles lie within a reasonable range thus verifying the suitability of the image analysis procedure developed in the course of this work. Importantly, the inhomogeneous distribution of lipids and dyes during vesicle preparation only causes an uncertainty in the size determination of lipid vesicles via fluorescence measurements by confocal microscopy but does not introduce any bias (Larsen *et al.*, 2011). Hence, the use of an average calibration factor for vesicle size determination is legitimate and used as standard method in the evaluation of SLiC assays (Kunding *et al.*, 2008; Bhatia *et al.*, 2009; Hatzakis *et al.*, 2009; Madsen *et al.*, 2010; Larsen *et al.*, 2015).

SLiC assays with Alexa Fluor® 488-conjugated streptavidin, which has been proven to represent a suitable negative control (Hatzakis *et al.*, 2009; Larsen *et al.*, 2015), yielded a protein surface density curve resembling the DiO density curve derived from assays with dual-labeled vesicles. The respective Alexa Fluor® 488 streptavidin surface density increase was found to be 12.9-fold, again lying within the range of signal fluctuation considered to be reasonable. Thus, usage of Alexa

Fluor® 488 streptavidin as a negative control was justified, and once again the developed analysis method was verified.

Finally, as a positive control a fusion protein of eGFP and eNBAR was investigated in SLiC assays. In agreement with published data (Bhatia *et al.*, 2009), eNBAR exhibited an increase in surface density of the order of two magnitudes. The divergence in signal increase between published results (approximately 100-fold; Bhatia *et al.*, 2009) and data obtained in the present study (approximately 130-fold) is most probably caused by differences in the image analysis procedure.

5.3.4 Curvature Sensitivity of FL-XXI and Myosin-XXI Fragments

As discussed before, experiments investigating the binding of myosin-XXI to planar and vesicular lipid bilayer systems repeatedly indicated a membrane curvature sensitivity of myosin-XXI. In order to elucidate this issue, SLiC assays with fusion constructs of eGFP and FL-XXI, Trunc-XXI, XXI-930 Tail, or XXI-830 Tail were performed (Figure 55).

Trunc-XXI, XXI-930 Tail, and XXI-830 Tail were found to clearly exhibit MCS, preferentially binding vesicles of small diameter, i.e. of high positive curvature. With a surface density increase of a factor of approximately 190 upon binding to small vesicles, Trunc-XXI was identified as the strongest sensor of curvature among the fusion proteins tested. Signal increases observed for myosin-XXI tail constructs were approximately 110-fold (XXI-930 Tail) and 130-fold (XXI-830 Tail) respectively. In the case of FL-XXI, results only exhibited a tendency toward membrane curvature sensitivity. Due to the low efficiency of the FL-XXI-vesicle binding reaction, which was also observed in co-sedimentation assays (see section 4.7), analysis of SLiC assays with FL-XXI fusion protein generated only a limited number of data points. Nevertheless, a surface density increase of a factor of almost 60 when binding to vesicles of small diameter strongly indicates a capability of sensing curvature.

Interestingly, analysis of SLiC assays with Trunc-XXI yielded a sufficient number of data points although Trunc-XXI concentration (7 nM) in SLiC assay samples was almost 10-fold lower than FL-XXI concentration (64 nM). Moreover, Trunc-XXI binding to bovine brain extract vesicles was observed to be even less efficient than FL-XXI binding in co-sedimentation assays (see section 4.7). This discrepancy might result from the effect of fractional binding: as described in Bhatia *et al.* (2009) and Madsen *et al.* (2010), due to a yet unidentified mechanism binding of certain proteins to vesicular bilayers exhibits a high temporal heterogeneity. Even for vesicles of the same diameter, binding of these proteins occurs at different points in time varying by several minutes to hours. Thus, depending on the incubation time a certain fraction of vesicles might not be associated with any protein. Since incubation times of protein-lipid mixtures in SLiC assays and in co-sedimentation assays varied sixfold, enhanced Trunc-XXI binding to bovine brain extract vesicles observed in SLiC assays might be caused by pronounced fractional binding.

Another interesting outcome of SLiC assays with Trunc-XXI fusion protein was that vesicles of a diameter larger than 350 nm did not bind this protein with surface densities above threshold level. Thus, due to the marked preference of Trunc-XXI for associating with small vesicles, interaction with vesicles of diameters above 350 nm was considerably limited. The fact that such a pronounced reduction in protein surface density at high vesicle diameters was not observed for any other of the fusion proteins investigated corresponds well with the identification of Trunc-XXI as the strongest sensor of bilayer curvature among the tested proteins.

The curvature sensing capability of FL-XXI and myosin-XXI fragments demonstrated in the present work can be explained by the nature of the actual and potential lipid binding sites identified within the myosin-XXI sequence. According to previous research of our lab (Batters *et al.*, 2014), myosin-XXI contains a PX domain and several basic-hydrophobic-basic regions, i.e. patches of hydrophobic amino acids surrounded by basic residues (Figure 55). Such BHB sequences, which potentially bind to lipid membranes by a combination of electrostatic attraction and bilayer penetration by hydrophobic side chains, are located within the Trunc-XXI construct as well as within XXI-930 Tail and XXI-830 Tail. According to a model proposed by Hatzakis *et al.* (2009), membrane binding by the insertion of hydrophobic moieties is always associated with a sensitivity for positive curvature, as bilayer penetration is dependent on the presence of lipid packing defects and the surface density of packing defects increases with increasing positive bilayer curvature. Therefore, bilayer binding by myosin-XXI via BHB motifs is expected to exhibit MCS. Noteworthily, structural and lipid binding studies of the PX domains of NADPH oxidase and Bem1p indicated that the interaction of at least certain PX domains with lipid membranes involves the insertion of hydrophobic amino acids as well (Bravo *et al.*, 2001; Stahelin *et al.*, 2003, 2007). Therefore, the myosin-XXI PX domain might also contribute to the regulation of bilayer association by geometric aspects. However, if the myosin-XXI PX domain does not exhibit curvature sensitivity, the additional presence of curvature-dependent BHB lipid binding sites might regulate PX domain-bilayer binding by imposing a geometric constraint thus further specifying target membranes of myosin-XXI. In fact, coincidence detection of distinct membrane properties like lipid composition, charge, or curvature by cooperating lipid binding motifs is a mechanism assumed to be employed by a variety of membrane binding proteins and has already been demonstrated to regulate the interaction of sorting nexin 1 with endosomal membranes (Carlton and Cullen, 2005; Carlton *et al.*, 2004).

The detection of curvature-dependent bilayer binding by Trunc-XXI as well as by XXI-830 Tail and XXI-930 Tail proves that myosin-XXI contains at least two distinct lipid binding motifs capable of MCS. In the case of myosin-Ia, Mazerik and Tyska (2012) identified two spatially separated BHB lipid binding sites involved in myosin-Ia enrichment at microvillar membranes, and hypothesized that the existence of multiple lipid binding domains might represent an adaptation to the myosin chemo-

mechanical cycle. Depending on the respective conformational state of myosin-Ia, membrane association might primarily be mediated by either one of the two binding sites. Regarding myosin-XXI, observations made during gliding filament assays on vesicle-covered surfaces and published data (Batters *et al.*, 2014) demonstrated that myosin-XXI is capable of exhibiting ATPase activity when bound to phospholipid vesicles. Thus, it is possible that the existence of multiple curvature sensitive lipid binding motifs in myosin-XXI too represents a mechanism to stably bind the motor protein to membranes throughout its ATPase cycle, in this case explicitly to membranes of positive curvature.

In addition, MCS of myosin-XXI raises the question whether this motor protein by itself is capable of inducing curvature, i.e. of deforming lipid membranes, particularly as membrane shaping by myosins is so far assumed to result from pulling forces caused by the movement of membrane-bound motor proteins along the actin cytoskeleton (Farsad and De Camilli, 2003; Anitei and Hoflack, 2011). To date, even though several proteins have been reported to display coincident curvature sensing and induction (Wetterau and Jonas, 1982; Davidson *et al.*, 1998; Kurten *et al.*, 2001; Carlton *et al.*, 2004; Gerlach *et al*, 2010; Varkey *et al.*, 2010), the question if curvature sensitivity is always associated with a capability to deform membranes is still under debate (e.g. Zimmerberg and Kozlov, 2006; Arkhipov *et al.*, 2009; Bhatia *et al.*, 2009; Madsen *et al.*, 2010). In the present experiments investigating whether FL-XXI binds to planar lipid bilayers, FL-XXI was found to be immobilized on bilayer-covered surfaces in the presence of myosin-XXI binding phospholipids thus indicating the possibility of membrane pore formation by myosin-XXI. However, as SLiC assays demonstrated that FL-XXI favors positively curved bilayers, pore formation by FL-XXI appears to be rather unlikely as it involves impression of the bilayer, i.e. generation of negative curvature. Hence, further investigations will be required to clarify if myosin-XXI is capable of modulating membrane shape.

In transfection experiments, HeLa and COS-7 cells expressing a fusion protein of ZsGreen1 and FL-XXI or Trunc-XXI were found to display protein accumulations along the proximal part of the plasma membrane and at the distal ends of filopodia. Due to the preferred association of FL-XXI and Trunc-XXI with bilayers of positive curvature, i.e. with convex membrane surfaces, direct binding of FL-XXI and Trunc-XXI to the plasma membrane along the cell body or at filopodia tips is highly improbable as the respective membrane surfaces exhibit virtually no curvature (along the cell body) or a concave shape (at filopodia tips). In fact, atomistic simulation calculations have shown that the number and size of membrane defects required for hydrophobic insertion, which in the case of FL-XXI and Trunc-XXI is expected to be involved in membrane binding, severely decreases with decreasing membrane curvature thus strongly impeding membrane penetration (Cui *et al.*, 2011). Therefore, localization of FL-XXI and Trunc-XXI in the vicinity of the plasma membrane might be mediated by an interaction of myosin-XXI with membrane-associated proteins or might not be

physically linked to the plasma membrane surface. Further, curvature dependency of the myosin-XXI-bilayer binding reaction implies a high probability of FL-XXI and Trunc-XXI association with lipid vesicles, e.g. PI(4,5)P_2-enriched vesicles travelling to the tips of filopodia.

5.3.5 Conclusions on Membrane Binding by Myosin-XXI in *L. donovani*

When lipid binding by myosin-XXI was first investigated in our lab (Batters *et al.*, 2014), membrane lipid strip tests revealed that FL-XXI binds to various phospholipids including several phosphoinositides like PI(4)P, PI(4,5)P_2, or PI(3,5)P_2, and that FL-XXI does not display any specificity for a particular lipid. Consequently, the question arose how myosin-XXI is targeted to distinct cellular membranes within *L. donovani*.

In the present study, SLiC assays with fusion proteins of eGFP and FL-XXI, Trunc-XXI, XXI-930 Tail, or XXI-830 Tail demonstrated a property of myosin-XXI which regulates the motor protein´s attachment to lipid bilayers according to bilayer geometry: membrane curvature sensitivity. Due to this sensitivity for membrane shape, myosin-XXI is directed to highly convex cellular membranes, e.g. vesicular compartments. In agreement with this, myosin-XXI was shown to be crucial for endocytosis, exocytosis, and intracellular trafficking in *L. donovani* promastigotes (Katta *et al.*, 2010). In fact, MCS might even be a critical factor for the recruitment of myosin-XXI to sites of endocytosis and for the motor protein´s stable association with vesicular cargo.

In addition to a geometrical constraint, MCS also allows for the regulation of myosin-XXI localization by variations in the lipid composition of membranes. Curvature-dependent bilayer binding by myosin-XXI is expected to be mediated by hydrophobic insertion, which is a process depending on the presence of lipid packing defects (Hatzakis *et al.*, 2009) and hence can be modulated by the molecular shape of the lipids contained in the bilayer. Accordingly, lysophospholipids, which exhibit a conical shape with the cross-sectional area of the head exceeding the one of the hydrophobic tail region, reduce the occurrence of lipid packing defects thus impeding insertion of hydrophobic moieties. In fact, lysophospholipids have been shown to prevent folding of the amphipathic helix of phosphocholine cytidylyltransferase into the bilayer of synthetic vesicles (Davies *et al.*, 2001). In *L. donovani*, preconditions for a lysophospholipid-mediated control of myosin-XXI localization potentially exist as lyso-PI has been shown to be a constituent of the parasite´s membranes (Kaneshiro *et al.*, 1986).

The observation that Trunc-XXI as well as XXI-930 Tail and XXI-830 Tail display curvature-dependent vesicle binding demonstrates that at least two spatially separated lipid binding sites capable of MCS exist within the myosin-XXI sequence. As gliding filament assays on vesicle-covered surfaces proved that FL-XXI efficiently propels F-actin in a membrane-bound state, it is conceivable that the presence of multiple lipid binding sites adapted to the attachment to convex membrane surfaces sustains the

stability of myosin-XXI association with vesicles during conformational changes throughout the myosin chemo-mechanical cycle. Such a stabilizing effect might actually be important for myosin-XXI-mediated transport processes which have been shown to be critical for endocytosis, exocytosis, intracellular trafficking, and flagellum assembly in the parasite (Katta *et al.*, 2010).

However, independent from the underlying mechanism a stable membrane attachment of myosin-XXI throughout its ATPase cycle, which was indicated by the observation of effective actin filament movement by vesicle-bound FL-XXI, could enable myosin-XXI to transport membrane patches to the flagellum during flagellar elongation as hypothesized by Katta *et al.* (2010).

Summarizing, investigation of the bilayer binding behavior of FL-XXI and myosin-XXI fragments by demonstrating MCS of multiple lipid binding domains within the myosin-XXI sequence revealed how the localization of myosin-XXI might be regulated in the parasite and how stable membrane attachment of the motor throughout its chemo-mechanical cycle might potentially be achieved.

6 Summary, Conclusions and Future Perspectives

The aim of the present study was to further elucidate the molecular bases of the physiological function of *L. donovani* myosin-XXI. This myosin plays an important role in the parasite as it is a multifunctional motor protein essential for survival. It mediates actin-based transport processes critical for endocytosis, exocytosis, vesicle transport, and flagellum formation (Katta *et al.*, 2010). In the following chapter, general conclusions derived from *in vivo* and *in vitro* experiments will be summarized, and their importance for myosin-XXI functionality in *L. donovani* will be outlined. Additionally, potential future scientific perspectives will be proposed.

6.1 Directionality of Myosin-XXI Translocation along F-Actin

In the present work, using gliding filament assays the direction of myosin-XXI translocation along filamentous actin was determined for the first time. For this purpose, a novel protocol for the polar fluorescent labeling of F-actin was developed. Gliding filament assays with molecular motors of known directionality, namely HMM and myosin-VI, proved the developed labeling method to be suitable for the determination of myosin directionality, and thus to be favorable for future use in our laboratory. The application of dual-labeled F-actin in gliding filament assays based on myosin-XXI revealed that myosin-XXI is a plus end-directed cytoskeletal motor, a finding which coincides with the present state of knowledge that, with the exception of myosin-VI, myosins move along F-actin in a plus end-directed fashion (O´Connell *et al.*, 2007).

6.2 Functionality and Cellular Localization of Myosin-XXI

In order to explore myosin-XXI functionality and cellular localization in *in vivo* systems devoid of endogenously expressed myosin-XXI, mammalian cell transfection experiments were performed. Cells were transfected with vectors encoding fusion constructs of a fluorophore and myosin-XXI or a myosin-XXI fragment to characterize the full-length motor protein as well as distinct protein domains.

Overall, fluorescent myosin-XXI fusion proteins were detected at one or several of the following cellular localizations: homogeneously distributed throughout the cytoplasm with frequent nucleus staining, in clusters and spherical structures within the cytoplasm, in dot-like accumulations along the plasma membrane, and within filopodia. The most striking cellular distribution was observed for FL-XXI and Trunc-XXI as they were the only fusion proteins capable of localizing at the plasma membrane and in filopodia. Phalloidin-TRITC staining of the actin cytoskeleton revealed that FL-XXI and Trunc-XXI colocalized with the filopodial actin core. Both myosin-XXI constructs contain the

SH3-like domain, the complete motor domain, and the neck and tail region of aa 748 to aa 800. This region comprises an IQ motif, a dimerization site, and three lipid binding sites.

The necessity of the full myosin head domain for FL-XXI and Trunc-XXI to reach the tips of filopodia led to the conclusion that these fusion proteins most probably employ their own motor power to actively move along the filopodial actin core. Consistently, vesicle-based gliding filament assays demonstrated that myosin-XXI is capable of translocating along F-actin with an average speed of 63.0 nm/s, i.e. faster than rearward actin flow and filopodial actin assembly. Thus, myosin-XXI is capable of reaching the distal ends of filopodia and of maintaining its position at the filopodia tips.

In order to actively translocate along actin filaments, myosin-XXI has to perform processive movement. The observation that FL-XXI and Trunc-XXI were the only tested myosin-XXI constructs containing the motor domain that localized within filopodia indicated that the SH3-like domain and the above-mentioned neck and tail region of aa 748 to aa 800 are necessary for processive motility of myosin-XXI. Considering the previously published finding of our lab (Batters *et al.*, 2014) that dimerization forces myosin-XXI into an immotile state, dimer formation could be ruled out to be involved in processive movement. Instead, requirement of the neck and tail region of aa 748 to aa 800 can be explained by the previously demonstrated regulatory effect of the myosin-XXI IQ motif (aa 754-769), which inhibits dimerization of myosin-XXI by associating with calmodulin or calmodulin-like proteins (Batters *et al.*, 2014). The necessity of a monomeric myosin-XXI conformation implies that in order to move processively, FL-XXI and Trunc-XXI form arrays of myosin molecules bound to cargo. This hypothesis is in line with the present finding that a minimum tail segment is required for myosin-XXI constructs to reach the tips of filopodia. The observation that the N-terminal SH3-like domain is essential for the translocation of myosin-XXI fusion proteins as well, led to the conclusion that the SH3-like domain might mediate intramolecular interactions maintaining the motor proteins in a conformation suitable for processive motility.

The filopodial localization pattern of FL-XXI and Trunc-XXI observed in the present study strongly resembles cellular localizations reported for $PI(4,5)P_2$ and myosin-X (Berg and Cheney, 2002; Chierico *et al.*, 2014), which are both proposed to be involved in processes regulating the generation, stabilization, or elongation of filopodia. According to this striking similarity, myosin-XXI is likely to have an impact on regulatory processes controlling the structure of filopodia. Indeed, live imaging of HeLa cells expressing either FL-XXI or Trunc-XXI revealed that both fusion proteins are capable of moving along intrafilopodial actin bundles, and of forming stable protein accumulations at the distal filopodia ends. In fact, translocation of FL-XXI and Trunc-XXI from the tips of these membrane protrusions to the cell body could clearly be observed by confocal microscopy. The evaluation of live images showed that FL-XXI and Trunc-XXI accumulations at filopodia tips, i.e. at sites of actin polymerization, were capable of persisting during phases of filopodia length changes. Further,

average filopodia extension and retraction rates of transfected HeLa cells were found to depend on the expressed fusion protein. Overall, these findings hint toward an influence of myosin-XXI on filopodial actin dynamics and thus on the assembly of actin-based membrane protrusions.

The latter conclusion was subsequently further confirmed by the results obtained from the analyses of filopodia lengths and densities in HeLa and COS-7 cells transfected with FL-XXI or Trunc-XXI. Expression of either myosin-XXI fusion protein resulted in a significant increase in average filopodia length, and this increase was found to be related to the presence of fusion protein accumulations within the distal ends of membrane protrusions. Hence, it may be concluded that myosin-XXI promotes actin assembly at filopodia tips, for example by delivering cargo facilitating actin polymerization. The different extent of filopodial elongation induced by FL-XXI and Trunc-XXI demonstrated that the myosin-XXI tail region C-terminal of aa 800 is not critical for the elongation process yet it increases the efficiency of the underlying mechanism. In addition to an increase in average length, the average number of filopodia per membrane circumference was also found to be enhanced in FL-XXI- and Trunc-XXI-transfected mammalian cells. Thus, myosin-XXI either initiates filopodia formation, e.g. by bundling actin filaments, or stabilizes already existing membrane protrusions, for instance by contributing to adhesion forces between actin and constituents of the plasma membrane. Alternatively, cargo transport by myosin-XXI might support the supply with components required for filopodia generation or stabilization.

In summary, the results of mammalian cell transfection experiments provide strong evidence for a significant impact of myosin-XXI and myosin-XXI-mediated transport on the assembly of actin within membrane protrusions. Further research may identify constituents that interact with myosin-XXI throughout the related cellular processes.

6.3 Myosin-XXI Binding to Planar Lipid Bilayers

As previous studies of our research group (Batters *et al.*, 2014) had revealed the existence of multiple lipid binding sites within myosin-XXI and had proven the capability of vesicle-attached myosin-XXI to drive gliding of F-actin, the present study aimed to further investigate the dynamic behavior of the bilayer-bound actin-myosin-XXI complex. To circumvent spatial constraints due to the limited size of vesicles, the present experiments were performed using supported and tethered planar lipid bilayers. Additionally, investigation of actomyosin association with planar lipid bilayers was intended to clarify whether myosin-XXI was potentially capable of binding to the plasma membranes of transfected mammalian cells, thus providing a possible explanation for the observed dot-like accumulations of FL-XXI and Trunc-XXI along the plasma membranes of HeLa and COS-7.

However, when incubated with planar lipid bilayers neither the actin-myosin-XXI complex nor myosin-XXI alone attached to the intact fluid part of the applied bilayers. This effect was independent

of lipid composition and buffer conditions. Conversely, when myosin-XXI functionality was examined in gliding filament assays on vesicle-covered surfaces, myosin-XXI could successfully be bound to vesicular lipid bilayers and furthermore propelled subsequently added filamentous actin. These observations led to the presumption that bilayer curvature might be a regulatory factor in myosin-XXI-membrane association. In order to test this hypothesis, fluorescently labeled full-length myosin-XXI and myosin-XXI fragments were subjected to SLiC assays, once their capability to bind to bovine brain extract vesicles had been tested in co-sedimentation assays.

6.4 Myosin-XXI Binding to Curved Lipid Bilayers

In agreement with previous findings (Batters *et al.*, 2014), co-sedimentation assays performed in the present study demonstrated that fluorescently labeled FL-XXI, Trunc-XXI, XXI-930 Tail, and XXI-830 Tail associated with vesicles prepared from bovine brain extract. In contrast, fluorescent XXI-Conv. WT and XXI-Conv. M were found not to attach to the applied vesicles despite the fact that the unlabeled myosin-XXI converter constructs had previously been shown to bind lipid constituents of bovine brain extract. Hence, it is very likely that the eGFP label of the converter constructs used in the present experiments inhibited lipid binding. In fact, fluorophore-related inhibition of lipid binding had previously been observed for an RFP-labeled myosin-XXI tail construct and could be assigned to the induction of dimer formation (Batters *et al.*, 2014). In co-sedimentation assays with XXI-809 Tail, no attachment of fusion protein to vesicles was detected. Apart from a potential influence of the fluorescent label, it might be assumed that the presence of the aa stretch of residues 809 to 829 hindered the association with vesicular bilayers. Considering the demonstrated vesicle binding capability of XXI-830 Tail, it is conceivable that in the absence of the N-terminal parts of myosin-XXI, aa 809 to aa 829 affect tail-located lipid binding sites, for example due to intramolecular interactions.

In SLiC assays, FL-XXI, Trunc-XXI, XXI-930 Tail, and XXI-830 Tail were entirely identified as sensors of positive bilayer curvature. Thereby, myosin-XXI is the first myosin demonstrated to exhibit a capability to sense the curvature of lipid bilayers. Surface densities of vesicle-bound myosin-XXI constructs were found to display ~60-fold (FL-XXI), ~190-fold (Trunc-XXI), ~110-fold (XXI-930 Tail), and ~130-fold (XXI-830 Tail) increases for small, i.e. highly curved, vesicles relative to vesicles of the reference size. It should be mentioned that for assays with FL-XXI, the low efficiency of the FL-XXI-vesicle binding reaction resulted in the generation of a comparably small number of data points, which in turn potentially masks the full extent of the curvature sensitivity of full-length myosin-XXI. The present observation of curvature-dependent bilayer association of FL-XXI and the myosin-XXI fragments agrees with the types of lipid binding sites so far identified within the myosin-XXI sequence, namely a PX domain and multiple basic-hydrophobic-basic regions (Batters *et al.*, 2014). For representatives of both classes of lipid binding motifs, experimental studies have shown that

membrane binding involves the insertion of hydrophobic residues into the lipid bilayer core (Stahelin *et al.*, 2003, 2007; McLaughlin and Murray, 2005), a mechanism which is proposed to require positive membrane curvature (Hatzakis *et al.*, 2009; Madsen *et al.*, 2010; Cui *et al.*, 2011). The demonstrated preference of myosin-XXI for bilayers of positive curvature also explains the motor protein´s incapability to bind to the applied supported and tethered planar bilayers. Additionally, it negates the possibility of a direct association of FL-XXI or Trunc-XXI with lipids contained in planar or concave cellular membranes. Thus, FL-XXI and Trunc-XXI detected in accumulations along the plasma membrane and in the filopodia tips of transfected mammalian cells were not bound to lipid constituents of the plasma membrane. Instead, these myosin-XXI constructs might associate with membrane proteins. The evident capability of Trunc-XXI and the tested myosin-XXI tail constructs to sense bilayer curvature proves that a minimum of two distinct curvature sensitive lipid binding domains exists within myosin-XXI. Since myosin-XXI drives filament movement in a vesicle-bound state, the presence of at least two such domains might guarantee the stability of the motor protein´s attachment to convex bilayer surfaces during the conformational changes inherent to the myosin chemo-mechanical cycle.

Further clarification of the mechanisms regulating bilayer association of each individual lipid binding motif of myosin-XXI represents a promising future research objective possibly yielding information on how this motor protein is recruited to distinct cellular targets. In this context, a potential role of coincidence detection of distinct membrane properties like curvature and charge by separate lipid binding domains might be an interesting research focus. Additionally, as a relation between the sensing and the induction of bilayer curvature has been observed for several proteins (e.g. Kurten *et al.*, 2001; Carlton *et al.*, 2004; Gerlach *et al.*, 2010), and as a functional coupling of these two processes is actually taken into consideration for certain lipid binding motifs (e.g. Zimmerberg and Kozlov, 2006; Madsen *et al.*, 2010), a closer inspection of a potential membrane deforming activity of myosin-XXI is of great interest for future investigations.

6.5 Functionality of Myosin-XXI in *L. donovani*

In the present study, mammalian cell transfection experiments provided further insight into the function of myosin-XXI under physiological conditions. Unlike in *L. donovani* promastigotes, where myosin-XXI localization had been demonstrated to be exclusively mediated by the tail domain (Katta *et al.*, 2009), targeting of myosin-XXI to distinct cellular locations in mammalian cells was shown to require the presence of the N-terminal parts of the motor protein (aa 1-800). Moreover, results of the present work indicate that the distribution of myosin-XXI within mammalian cells is related to processive actin-based movement of the molecular motor. Therefore, tail dependency of myosin-XXI localization within *L. donovani* cannot be assigned to a lack of processivity. Conversely,

the apparent absence of a complex actin cytoskeleton within the parasite (Rodrigues *et al.*, 2014) can be concluded to be associated with the necessity of an alternative transport mechanism in which the tail domain links myosin-XXI to respective binding partners. Such a mechanism might involve microtubule-dependent kinesins or dyneins.

The present transfection experiments further revealed that the respective N-terminal parts of myosin-XXI enable the motor protein to influence the structure of filopodia in mammalian cells. Analyses of live confocal images and of average filopodia lengths and densities indicated a regulatory function of the motor protein in the actin polymerization process at the distal ends of membrane protrusions. Hence, as actin represents a constituent of the *L. donovani* flagellum (Sahasrabuddhe *et al.*, 2004), myosin-XXI-mediated flagellar assembly might involve the regulation of actin polymerization.

In vitro approaches applied in the present study provided valuable insights into the lipid bilayer association of myosin-XXI. Positive bilayer curvature was revealed as a key factor in myosin-XXI-bilayer attachment, and thus membrane shape is likely to play a role in the control of myosin-XXI distribution within *L. donovani*. Therefore, membrane geometry potentially contributes to the recruitment of the motor protein to its cellular sites of action, e.g. to sites of endocytosis or to vesicular cargo. Furthermore, curvature sensitivity of myosin-XXI could enable regulation of myosin localization in *L. donovani* by bilayer-incorporated lysophospholipids. Owing to their molecular shape, these phospholipids are capable of impeding the association of convex membrane surfaces with proteins sensing positive curvature (Davies *et al.*, 2001).

SLiC assays additionally revealed the existence of at least two separate curvature sensitive lipid binding motifs within myosin-XXI, a structural property that might ensure the stable attachment of myosin-XXI to convex membranes (e.g. vesicles) throughout the motor protein´s ATPase cycle. In turn, stable membrane attachment might be essential for myosin-XXI-mediated transport processes required for functional endocytosis, exocytosis, vesicular trafficking, and flagellum formation in *L. donovani*.

In summary, the present study provides significant new knowledge on the molecular bases of the physiological roles of *L. donovani* myosin-XXI and thereby also gives general information on motor proteins of the myosin superfamily. The demonstrated regulatory role of myosin-XXI in the assembly of actin-based cellular structures once more illustrates the importance of the interplay between actin and myosins even in organisms like *L. donovani*, which exhibit a primarily microtubule-based cytoskeleton. Moreover, by demonstrating for the first time that membrane association of myosins can be controlled by the shape of the lipid bilayer, the present work revealed an interesting novel aspect of the targeting and thus the functionality of myosins.

7 References

Adhiambo, C., Forney, J. D., Asai, D. J., and LeBowitz, J. H. (2005). The two cytoplasmic dynein-2 isoforms in *Leishmania mexicana* perform separate functions. *Molecular and Biochemical Parasitology*, *143*(2), 216–225.

Ago, T., Kuribayashi, F., Hiroaki, H., Takeya, R., Ito, T., Kohda, D., and Sumimoto, H. (2003). Phosphorylation of $p47^{phox}$ directs phox homology domain from SH3 domain toward phosphoinositides, leading to phagocyte NADPH oxidase activation. *Proceedings of the National Academy of Sciences of the United States of America*, *100*(8), 4474–4479.

Alberts, B., Johnson, A., Lewis, J., Raff, M., Roberts, K., and Walter, P. (2007). *Molecular biology of the cell* (Fifth Edition). New York: Garland Science.

Allen, P. G., and Janmey, P. A. (1994). Gelsolin displaces phalloidin from actin filaments. *Journal of Biological Chemistry*, *269*(52), 32916–32923.

Alvar, J., Vélez, I. D., Bern, C., Herrero, M., Desjeux, P., Cano, J., Jannin, J., den Boer, M., and the WHO Leishmaniasis Control Team (2012). Leishmaniasis worldwide and global estimates of its incidence. *PLoS ONE*, *7*(5), e35671.

Andreotti, A. H., Bunnell, S. C., Feng, S., Berg, L. J., and Schreiber, S. L. (1997). Regulatory intramolecular association in a tyrosine kinase of the Tec family. *Nature*, *385*(6611), 93–97.

Anitei, M., and Hoflack, B. (2011). Bridging membrane and cytoskeleton dynamics in the secretory and endocytic pathways. *Nature Cell Biology*, *14*(1), 11–19.

Antonny, B. (2011). Mechanisms of membrane curvature sensing. *Annual Review of Biochemistry*, *80*, 101–123.

Arkhipov, A., Yin, Y., and Schulten, K. (2009). Membrane-bending mechanism of amphiphysin N-BAR domains. *Biophysical Journal*, *97*(10), 2727–2735.

Axelrod, D., Koppel, D.E., Schelessinger, J., Elson, E., and Webb, W. W. (1976). Mobility Measurement by Analysis of Fluorescence Photobeaching Recovery Kinetics. *Biophysical Journal*, *16*, 1055–1069.

Bates, P. A. (1994). The developmental biology of *Leishmania* promastigotes. *Experimental Parasitology*, *79*(2), 215–218.

Batters, C., Brack, D., Ellrich, H., Averbeck, B., and Veigel, C. (2016). Calcium can mobilize and activate myosin-VI. *Proceedings of the National Academy of Sciences of the United States of America*, *113*(9), E1162–E1169.

Batters, C., Ellrich, H., Helbig, C., Woodall, K. A., Hundschell, C., Brack, D., and Veigel, C. (2014). Calmodulin regulates dimerization, motility, and lipid binding of *Leishmania* myosin XXI. *Proceedings of the National Academy of Science of the United States of America*, *111*(2), E227–E236.

Batters, C., Woodall, K. A., Toseland, C. P., Hundschell, C., and Veigel, C. (2012). Cloning, Expression, and Characterization of a Novel Molecular Motor, *Leishmania* Myosin-XXI. *Journal of Biological Chemistry*, *287*(33), 27556–27566.

Bell, P. A. (2001). Chapter 15 - E.coli Expression Systems. In A. S. Gerstein (Ed.), *Molecular Biology Problem Solver: A Laboratory Guide* (Vol. 7, pp. 461–490). New York: John Wiley & Sons, Inc.

Belyantseva, I. A., Boger, E. T., Naz, S., Frolenkov, G. I., Sellers, J. R., Ahmed, Z. M., Griffith, A. J., Friedman, T. B. (2005). Myosin-XVa is required for tip localization of whirlin and differential elongation of hair-cell stereocilia. *Nature Cell Biology*, *7*(2), 148–156.

Bendix, P. M., Pedersen, M. S., and Stamou, D. (2009). Quantification of nano-scale intermembrane contact areas by using fluorescence resonance energy transfer. *Proceedings of the National Academy of Sciences of the United States of America*, *106*(30), 12341–12346.

Berg, J. S., and Cheney, R. E. (2002). Myosin-X is an unconventional myosin that undergoes intrafilopodial motility. *Nature Cell Biology*, *4*(3), 246–250.

Berg, J. S., Powell, B. C., and Cheney, R. E. (2001). A millennial myosin census. *Molecular Biology of the Cell*, *12*(4), 780–794.

Berg, J. M., Tymoczko, J. L., and Stryer, L. (2012). *Biochemistry* (Seventh Edition). New York: W. H. Freeman.

Bhatia, V. K., Madsen, K. L., Bolinger, P.-Y., Kunding, A., Hedegård, P., Gether, U., and Stamou, D. (2009). Amphipathic motifs in BAR domains are essential for membrane curvature sensing. *The EMBO Journal*, *28*, 3303–3314.

Blaineau, C., Tessier, M., Dubessay, P., Tasse, L., Crobu, L., Pagès, M., and Bastien, P. (2007). A Novel Microtubule-Depolymerizing Kinesin Involved in Length Control of a Eukaryotic Flagellum. *Current Biology*, *17*(9), 778–782.

Bloemink, M. J., and Geeves, M. A. (2011). Shaking the myosin family tree: Biochemical kinetics defines four types of myosin motor. *Seminars in Cell and Developmental Biology*, *22*(9), 961–967.

Boggon, T. J. (1999). Implication of Tubby Proteins as Transcription Factors by Structure-Based Functional Analysis. *Science*, *286*(5447), 2119–2125.

Bohil, A. B., Robertson, B. W., and Cheney, R. E. (2006). Myosin-X is a molecular motor that functions in filopodia formation. *Proceedings of the National Academy of Sciences of the United States of America*, *103*(33), 12411–12416.

Bradford, M. M. (1976). A rapid and sensitive method for the quantitation of microgram quantities of protein utilizing the principle of protein-dye binding. *Analytical Biochemistry*, *72*(1–2), 248–254.

Bravo, J., Karathanassis, D., Pacold, C. M., Pacold, M. E., Ellson, C. D., Anderson, K. E., Butler, P. J. G., Lavenir, I., Perisic, O., Hawkins, P. T., Stephens, L., and Williams, R. L. (2001). The crystal structure of the PX domain from $p40^{phox}$ bound to phosphatidylinositol 3-phosphate. *Molecular Cell*, *8*(4), 829–839.

Brzeska, H., Hwang, K. J., and Korn, E. D. (2008). *Acanthamoeba* myosin IC colocalizes with phosphatidylinositol 4,5-bisphosphate at the plasma membrane due to the high concentration of negative charge. *Journal of Biological Chemistry*, *283*(46), 32014–32023.

Burn, P. (1988). Amphitropic proteins: a new class of membrane proteins. *Trends in Biochemical Sciences*, *13*(3), 79–83.

Cajal, Y., Svendsen, A., Girona, V., Patkar, S. A., and Alsina, M. A. (2000). Interfacial control of lid opening in *Thermomyces lanuginosa* lipase. *Biochemistry*, *39*(2), 413–423.

Campelo, F., McMahon, H. T., and Kozlov, M. M. (2008). The Hydrophobic Insertion Mechanism of Membrane Curvature Generation by Proteins. *Biophysical Journal*, *95*(5), 2325–2339.

Carlier, M.-F. (1998). Control of actin dynamics. *Current Opinion in Cell Biology*, *10*(1), 45–51.

Carlton, J., Bujny, M., Peter, B. J., Oorschot, V. M. J., Rutherford, A., Mellor, H., Klumperman, J., McMahon, H. T., Cullen, P. J. (2004). Sorting Nexin-1 Mediates Tubular Endosome-to-TGN Transport through Coincidence Sensing of High-Curvature Membranes and 3-Phosphoinositides. *Current Biology*, *14*(20), 1791–1800.

Carlton, J. G., and Cullen, P. J. (2005). Coincidence detection in phosphoinositide signaling. *Trends in Cell Biology*, *15*(10), 540–547.

Cheney, R. E., and Mooseker, M. S. (1992). Unconventional myosins. *Current Opinion in Cell Biology*, *4*(1), 27–35.

Cheney, R. E., Riley, M. A., and Mooseker, M. S. (1993). Phylogenetic analysis of the myosin superfamily. *Cell Motility and the Cytoskeleton*, *24*(4), 215–223.

Chernomordik, L. V., and Zimmerberg, J. (1995). Bending membranes to the task: structural intermediates in bilayer fusion. *Current Opinion in Structural Biology*, *5*(4), 541–547.

Cheung, W. Y. (1980). Calmodulin plays a pivotal role in cellular regulation. *Science*, *207*(4426), 19–27.

Chierico, L., Joseph, A. S., Lewis, A. L., and Battaglia, G. (2014). Live cell imaging of membrane/cytoskeleton interactions and membrane topology. *Scientific Reports*, *4*, 6056.

Cho, W., and Stahelin, R. V. (2006). Membrane binding and subcellular targeting of C2 domains. *Biochimica et Biophysica Acta - Molecular and Cell Biology of Lipids*, *1761*(8), 838–849.

Cohen, G. B., Ren, R. B., and Baltimore, D. (1995). Modular binding domains in signal transduction proteins. *Cell*, *80*, 237–248.

Cole, D. G., and Snell, W. J. (2009). SnapShot: Intraflagellar Transport. *Cell*, *137*(4), 1–2.

Colón-González, F., and Kazanietz, M. G. (2006). C1 domains exposed: From diacylglycerol binding to protein-protein interactions. *Biochimica et Biophysica Acta - Molecular and Cell Biology of Lipids*, *1761*(8), 827–837.

Contreras, F. X., Sánchez-Magraner, L., Alonso, A., and Goñi, F. M. (2010). Transbilayer (flip-flop) lipid motion and lipid scrambling in membranes. *FEBS Letters*, *584*(9), 1779–1786.

Contreras, F. X., Villar, A. V., Alonso, A., Kolesnick, R. N., and Goñi, F. M. (2003). Sphingomyelinase activity causes transbilayer lipid translocation in model and cell membranes. *Journal of Biological Chemistry*, *278*(39), 37169–37174.

Cooke, R., and Holmes, K. C. (1986). The Mechanism of Muscle Contraction. *Critical Reviews in Biochemistry*, *21*(1), 53–118.

Cope, M. J. T. V., Whisstock, J., Payment, I., and Kendrick-Jones, J. (1996). Conservation within the myosin motor domain: Implications for structure and function. *Structure*, *4*(8), 969–987.

Ĉopiĉ, A., Latham, C. F., Horlbeck, M. A., D'Arcangelo, J. G., and Miller, E. A. (2012). ER Cargo Properties Specify a Requirement for COPII Coat Rigidity Mediated by Sec13p. *Science*, *335*(6074), 1359–1362.

Cornell, R. B., and Taneva, S. G. (2006). Amphipathic Helices as Mediators of the Membrane Interaction of Amphitropic Proteins, and as Modulators of Bilayer Physical Properties. *Current Protein and Peptide Science, 7*(6), 539–552.

Cozier, G. E., Carlton, J., McGregor, A. H., Gleeson, P. A., Teasdale, R. D., Mellor, H., and Cullen, P. J. (2002). The phox homology (PX) domain-dependent, 3-phosphoinositide-mediated association of sorting nexin-1 with an early sorting endosomal compartment is required for its ability to regulate epidermal growth factor receptor degradation. *Journal of Biological Chemistry*, *277*(50), 48730–48736.

Cui, H., Lyman, E., and Voth, G. A. (2011). Mechanism of membrane curvature sensing by amphipathic helix containing proteins. *Biophysical Journal*, *100*(5), 1271–1279.

Daniel, C., Sohn, K. E., Mates, T. E., Kramer, E. J., Rädler, J. O., Sackmann, E., Nickel, B., and Andruzzi, L. (2007). Structural characterization of an elevated lipid bilayer obtained by stepwise functionalization of a self-assembled alkenyl silane film. *Biointerphases*, *2*(3), 109–118.

Danielli, J. F., and Davson, H. (1935). A contribution to the theory of permeability of thin films. *Journal of Cellular and Comparative Physiology*, *5*(4), 495–508.

Davidson, W. S., Jonas, A., Clayton, D. F., and George, J. M. (1998). Stabilization of alpha-synuclein secondary structure upon binding to synthetic membranes. *The Journal of Biological Chemistry*, *273*(16), 9443–9449.

Davies, S. M. A., Epand, R. M., Kraayenhof, R., and Cornell, R. B. (2001). Regulation of CTP: Phosphocholine cytidylyltransferase activity by the physical properties of lipid membranes: An important role for stored curvature strain energy. *Biochemistry*, *40*(35), 10522–10531.

De La Cruz, E. M., and Ostap, E. M. (2004). Relating biochemistry and function in the myosin superfamily. *Current Opinion in Cell Biology*, *16*(1), 61–67.

de La Serna, J. B., Perez-Gil, J., Simonsen, A. C., and Bagatolli, L. A. (2004). Cholesterol rules: Direct observation of the coexistence of two fluid phases in native pulmonary surfactant membranes at physiological temperatures. *Journal of Biological Chemistry*, *279*(39), 40715–40722.

DeRosier, D. J., and Edds, K. T. (1980). Evidence for fascin cross-links between the actin filaments in coelomocyte filopodia. *Experimental Cell Research*, *126*(2), 490–494.

Doherty, G. J., and McMahon, H. T. (2008). Mediation, Modulation, and Consequences of Membrane-Cytoskeleton Interactions. *Annual Review of Biophysics*, *37*(1), 65–95.

Doucet, C. M., Esmery, N., De Saint-Jean, M., and Antonny, B. (2015). Membrane curvature sensing by amphipathic helices is modulated by the surrounding protein backbone. *PLoS ONE*, *10*(9), 1–23.

Dowhan, W., Bogdanov, M., and Mileykovskaya, E. (2016). Chapter 1 - Functional Roles of Lipids in Membranes. In N. D. Ridgway and R. S. McLeod (Eds.), *Biochemistry of Lipids, Lipoproteins and Membranes* (Sixth Edition, pp. 1–40). Boston: Elsevier.

Drin, G., Casella, J.-F., Gautier, R., Boehmer, T., Schwartz, T. U., and Antonny, B. (2007). A general amphipathic alpha-helical motif for sensing membrane curvature. *Nature Structural & Molecular Biology*, *14*(2), 138–146.

Edidin, M. (1974). Rotational and Translational Diffusion in Membranes. *Annual Review of Biophysics and Bioengineering*, *3*(1), 179–201.

Eisenberg, E., and Greene, L. E. (1980). The relation of muscle biochemistry to muscle physiology. *Annual Review of Physiology*, *42*(1), 293–309.

El-Mezgueldi, M., and Bagshaw, C. R. (2008). Chapter 3 – The Myosin Family: Biochemical and Kinetic Properties. In L. M. Coluccio (Ed.), *Myosins: A Superfamily of Molecular Motors* (pp. 55–94). Dordrecht: Springer.

El-Sayed, N. M. , Myler, P. J., Bartholomeu, D. C., Nilsson, D., Aggarwal, G., Tran, A.-N., Ghedin, E., Worthey, E. A., Delcher, A. L., Blandin, G., Westenberger, S. J., Caler, E., Cerqueira, G. C., Branche, C., Haas, B., Anupama, A., Arner, E., Åslund, L., Attipoe, P., Bontempi, E., Bringaud, F., Burton, P., Cadag, E., Campbell, D. A., Carrington, M., Crabtree, J., Darban, H., da Silveira, J. F., de Jong, P., Edwards, K., Englund, P. T., Fazelina, G., Feldblyum, T., Ferella, M., Frasch, A. C., Gull, K., Horn, D., Hou, L., Huang, Y., Kindlund, E., Klingbeil, M., Kluge, S., Koo, H., Lacerda, D., Levin, M. J., Lorenzi, H., Louie, T., Machado, C. R., McCulloch, R., McKenna, A., Mizuno, Y., Mottram, J. C., Nelson, S., Ochaya, S., Osoegawa, K., Pai, G., Parsons, M., Pentony, M., Pettersson, U., Pop, M., Ramirez, J. L., Rinta, J., Robertson, L., Salzberg, S. L., Sanchez, D. O., Seyler, A., Sharma, R., Shetty, J., Simpson, A. J., Sisk, E., Tammi, M. T., Tarleton, R., Teixeira, S., Van Aken, S., Vogt, C., Ward, P. N., Wickstead, B., Wortman, J., White, O., Fraser, C. M., Stuart, K. D, Andersson, B. (2005). The Genome Sequence of *Trypanosoma cruzi*, Etiologic Agent of Chagas Disease. *Science*, *309*(5733), 409–415.

Emmer, B. T., Maric, D., and Engman, D. M. (2010). Molecular mechanisms of protein and lipid targeting to ciliary membranes. *Journal of Cell Science*, *123*, 529–536.

Engelman, D. M. (2005). Membranes are more mosaic than fluid. *Nature*, *438*(7068), 578–580.

Farsad, K., and De Camilli, P. (2003). Mechanisms of membrane deformation. *Current Opinion in Cell Biology*, *15*(4), 372–381.

Farsad, K., Ringstad, N., Takei, K., Floyd, S. R., Rose, K., and De Camilli, P. (2001). Generation of high curvature membranes mediated by direct endophilin bilayer interactions. *Journal of Cell Biology*, *155*(2), 193–200.

Fertuck, H. C., and Salpeter, M. M. (1974). Localization of Acetylcholine Receptor by ^{125}I-Labeled α-Bungarotoxin Binding at Mouse Motor Endplates. *Proceedings of the National Academy of Sciences of the United States of America*, *71*(4), 1376–1378.

Feuer, G., Molnar, F., Pettko, E., and Straub F. B. (1948). Studies on the composition and polymerisation of actin. *Acta Physiologica Hungarica, 1*(4–5), 150-163.

Field, M. C., and Carrington, M. (2009). The trypanosome flagellar pocket. *Nature Reviews Microbiology*, *7*(11), 775–786.

Fischer, S., Windshügel, B., Horak, D., Holmes, K. C., and Smith, J. C. (2005). Structural mechanism of the recovery stroke in the Myosin molecular motor. *Proceedings of the National Academy of Sciences of the United States of America, 102*(19), 6873–6878.

Ford, M. G. J., Pearse, B. M. F., Higgins, M. K., Vallis, Y., Owen, D. J., Gibson, A., Hopkins, C. R., Evans, P. R., and McMahon, H. T. (2001). Simultaneous Binding of PtdIns(4,5)P_2 and Clathrin by AP180 in the Nucleation of Clathrin Lattices on Membranes. *Science, 291*(5506), 1051–1056.

Forestier, C.-L., Machu, C., Loussert, C., Pescher, P., and Späth, G. F. (2011). Imaging Host Cell-*Leishmania* Interaction Dynamics Implicates Parasite Motility, Lysosome Recruitment, and Host Cell Wounding in the Infection Process. *Cell Host & Microbe*, *9*(4), 319–330.

Foth, B. J., Goedecke, M. C., and Soldati, D. (2006). New insights into myosin evolution and classification. *Proceedings of the National Academy of Sciences of the United States of America*, *103*(10), 3681–3686.

Fribourg, P. F., Chami, M., Sorzano, C. O. S., Gubellini, F., Marabini, R., Marco, S., Jault, J.-M., and Lévy, D. (2014). 3D Cryo-Electron Reconstruction of BmrA, a Bacterial Multidrug ABC Transporter in an Inward-Facing Conformation and in a Lipidic Environment. *Journal of Molecular Biology*, *426*(10), 2059–2069.

Fujita-Becker, S., Tsiavaliaris, G., Ohkura, R., Shimada, T., Manstein, D. J., and Sutoh, K. (2006). Functional Characterization of the N-terminal Region of Myosin-2. *Journal of Biological Chemistry, 281*(47), 36102–36109.

Gallardo, R., Ivarsson, Y., Schymkowitz, J., Rousseau, F., and Zimmermann, P. (2010). Structural Diversity of PDZ-Lipid Interactions. *ChemBioChem*, *11*(4), 456–467.

Geeves, M. A., and Holmes, K. C. (1999). Structural mechanism of muscle contraction. *Annual Review of Biochemistry*, *68*(1), 687–728.

Geli, M. I. (2000). An intact SH3 domain is required for myosin I-induced actin polymerization. *The EMBO Journal*, *19*(16), 4281–4291.

Gerlach, H., Laumann, V., Martens, S., Becker, C. F. W., Goody, R. S., and Geyer, M. (2010). HIV-1 Nef membrane association depends on charge, curvature, composition and sequence. *Nature Chemical Biology*, *6*(1), 46–53.

Gibellini, F., and Smith, T. K. (2010). The Kennedy pathway-De novo synthesis of phosphatidylethanolamine and phosphatidylcholine. *IUBMB Life*, *62*(6), 414–428.

Gluenz, E., Ginger, M. L., and McKean, P. G. (2010). Flagellum assembly and function during the *Leishmania* life cycle. *Current Opinion in Microbiology*, *13*(4), 473–479.

Goñi, F. M. (2014). The basic structure and dynamics of cell membranes: An update of the Singer–Nicolson model. *Biochimica et Biophysica Acta - Biomembranes*, *1838*(6), 1467–1476.

Graeve, L., and Müller, M. (2014). Chapter 13 - Cytoskelett. In P. C. Heinrich, M. Müller, and L. Graeve (Eds.), *Löffler/Petrides: Biochemie und Pathobiochemie* (Ninth Edition., pp. 174–180). Berlin: Springer.

Guilford, W. H., Dupuis, D. E., Kennedy, G., Wu, J., Patlak, J. B., and Warshaw, D. M. (1997). Smooth Muscle and Skeletal Muscle Myosins Produce Similar Unitary Forces and Displacements in the Laser Trap. *Biophysical Journal*, *72*(3), 1006–1021.

Gull, K. (1999). The cytoskeleton of trypanosomatid parasites. *Annual Review of Microbiology*, *53*, 629–655.

Gupta, C. M., Thiyagarajan, S., and Sahasrabuddhe, A. A. (2015). Unconventional actins and actin-binding proteins in human protozoan parasites. *International Journal for Parasitology*, *45*(7), 435–447.

Harris, H. E., and Weeds, A. G. (1984). Plasma gelsolin caps and severs actin filaments. *FEBS Letters*, *177*(2), 184–188.

Hatzakis, N. S., Bhatia, V. K., Larsen, J., Madsen, K. L., Bolinger, P.-Y., Kunding, A. H., Castillo, J., Gether, U., Hedegård, P., and Stamou, D. (2009). How curved membranes recruit amphipathic helices and protein anchoring motifs. *Nature Chemical Biology*, *5*(11), 835–841.

Herm-Götz A., Weiss, S., Stratmann, R., Fujita-Becker, S., Ruff, C., Meyhöfer, E., Soldati, T., Manstein, D. J., Geeves, M. A., and Soldati, D. (2002). *Toxoplasma gondii* myosin A and its light chain: a fast , single-headed , plus-end-directed motor. *The EMBO Journal*, *21*(9), 2149–2158.

Hill, T. L., and Kirschner, M. W. (1982). Bioenergetics and kinetics of microtubule and actin filament assembly-disassembly. *International Review of Cytology, 78*, 1–125.

Hilpelä, P., Vartiainen, M. K., & Lappalainen, P. (2004). Regulation of the Actin Cytoskeleton by PI(4,5)P2 and PI(3,4,5)P3. In H. Stenmark (Ed.), *Phosphoinositides in Subcellular Targeting and Enzyme Activation* (pp. 117–163). Berlin: Springer.

Hodge, T., and Cope, M. J. T. V. (2000). A myosin family tree. *Journal of Cell Science*, *113*(19), 3353–3354.

Hofmann, K., and Bucher, P. (1996). The UBA domain: a sequence motif present in multiple enzyme classes of the ubiquitination pathway. *Trends in Biochemical Sciences*, *21*(5), 172–173.

Holmes, K. C. (1997). The swinging lever-arm hypothesis of muscle contraction. *Current Biology*, *7*(2), R112–R118.

Holmes, K. C. (2008). Chapter 2 - Myosin Structure. In L. M. Coluccio (Ed.), *Proteins and Cell Regulation: Myosins: A Superfamily of Molecular Motors* (Vol. 7, pp. 35–54). Dordrecht: Springer.

Holmes, K. C. (2009). Structural biology: actin in a twist. *Nature*, *457*(7228), 389–390.

Holmes, K. C., Popp, D., Gebhard, W., and Kabsch, W. (1990). Atomic model of the actin filament. *Nature*, *347*(6288), 44–49.

Holst, O. (2008). Chapter 7.1 - Glycolipids: Occurrence, Significance, and Properties. In B. O. Fraser-Reid, K. Tatsuta, and J., Thiem (Eds.), *Glysoscience* (Second Edition, pp. 1603–1627). Berlin: Springer.

Holt, A., and Killian, J. A. (2010). Orientation and dynamics of transmembrane peptides: The power of simple models. *European Biophysics Journal*, *39*(4), 609–621.

Hristova, K., Wimley, W. C., Mishra, V. K., Anantharamiah, G. M., Segrest, J. P., and White, S. H. (1999). An amphipathic alpha-helix at a membrane interface: A structural study using a novel X-ray diffraction method. *Journal of Molecular Biology*, *290*(1), 99–117.

Huxley, A. F. (1957). Muscle structure and theories of contraction. *Progress in Biophysics and Biophysical Chemistry*, *7*(1), 255–318.

Huxley, A. F., and Simmons, R. M. (1971). Proposed Mechanism of Force Generation in Striated Muscle. *Nature*, *233*(5321), 533–538.

Huxley, H. E. (1969). The Mechanism of Muscular Contraction. *Science*, *164*(3886), 1356–1366.

Hwang, P. M., and Sykes, B. D. (2015). Targeting the sarcomere to correct muscle function. *Nature Reviews Drug Discovery*, *14*(5), 313–328.

Inoue, A., Saito, J., Ikebe, R., and Ikebe, M. (2002). Myosin IXb is a single-headed minus-end-directed processive motor. *Nature Cell Biology*, *4*(4), 302–306.

Itoh, T. (2001). Role of the ENTH Domain in Phosphatidylinositol-4,5-Bisphosphate Binding and Endocytosis. *Science*, *291*(5506), 1047–1051.

Itoh, T., and De Camilli, P. (2006). BAR, F-BAR (EFC) and ENTH/ANTH domains in the regulation of membrane-cytosol interfaces and membrane curvature. *Biochimica et Biophysica Acta - Molecular and Cell Biology of Lipids*, *1761*(8), 897–912.

Iwaki, M., Tanaka, H., Iwane, A. H., Katayama, E., Ikebe, M., and Yanagida, T. (2006). Cargo-binding makes a wild-type single-headed myosin-VI move processively. *Biophysical Journal*, *90*, 3643–3652.

Kabsch, W., Mannherz, H. G., Suck, D., Pai, E. F., and Holmes, K. C. (1990). Atomic structure of the actin: DNase I complex. *Nature*, *347*(6288), 37–44.

Kanai, F., Liu, H., Field, S. J., Akbary, H., Matsuo, T., Brown, G. E., Cantley, L. C., and Yaffe, M. B. (2001). The PX domains of p47phox and p40phox bind to lipid products of PI(3)K. *Nature Cell Biology*, *3*(7), 675–678.

Kaneshiro, E. S., Jayasimhulu, K., and Lester, R. L. (1986). Characterization of inositol lipids from *Leishmania donovani* promastigotes: identification of an inositol sphingophospholipid. *Journal of Lipid Research*, *27*, 1294–1303.

Kapoor, P., Sahasrabuddhe, A. A., Kumar, A., Mitra, K., Siddiqi, M. I., and Gupta, C. M. (2008). An unconventional form of actin in protozoan hemoflagellate, *Leishmania*. *Journal of Biological Chemistry*, *283*(33), 22760–22773.

Karp, G. (2005). *Molekulare Zellbiologie* (First Edition). Berlin: Springer.

Katta, S. S., Sahasrabuddhe, A. A., and Gupta, C. M. (2009). Flagellar localization of a novel isoform of myosin, myosin XXI, in *Leishmania*. *Molecular and Biochemical Parasitology*, *164*(2), 105–110.

Katta, S. S., Tammana, T. V. S., Sahasrabuddhe, A. A., Bajpai, V. K., and Gupta, C. M. (2010). Trafficking activity of myosin XXI is required in assembly of *Leishmania* flagellum. *Journal of Cell Science*, *123*, 2035–2044.

Kay, B. K., Yamabhai, M., Wendland, B., and Emr, S. D. (1999). Identification of a novel domain shared by putative components of the endocytic and cytoskeletal machinery. *Protein Science*, *8*, 435–438.

Kaye, P., and Scott, P. (2011). Leishmaniasis: complexity at the host-pathogen interface. *Nature Reviews Microbiology*, *9*(8), 604–615.

Kerber, M. L., Jacobs, D. T., Campagnola, L., Dunn, B. D., Yin, T., Sousa, A. D., Quintero, O. A., and Cheney, R. E. (2009). A Novel Form of Motility in Filopodia Revealed by Imaging Myosin-X at the Single-Molecule Level. *Current Biology*, *19*(11), 967–973.

Keren, K. (2011). Cell motility : the integrating role of the plasma membrane. *European Biophysics Journal, 40(9)*, 1013–1027.

Korn, E. D. (2000). Coevolution of head, neck, and tail domains of myosin heavy chains. *Proceedings of the National Academy of Sciences of the United States of America*, *97*(23), 12559–12564.

Kozlov, M. M., and Bershadsky, A. D. (2004). Processive capping by formin suggests a force-driven mechanism of actin polymerization. *Journal of Cell Biology*, *167*(6), 1011–1017.

Kozlov, M. M., Campelo, F., Liska, N., Chernomordik, L. V., Marrink, S. J., and McMahon, H. T. (2014). Mechanisms shaping cell membranes. *Current Opinion in Cell Biology*, *29*(1), 53–60.

Krause, M., Dent, E. W., Bear, J. E., Loureiro, J. J., and Gertler, F. B. (2003). ENA/VASP PROTEINS: Regulators of the Actin Cytoskeleton and Cell Migration. *Annual Review of Cell and Developmental Biology*, *19*(1), 541–564.

Krendel, M., and Mooseker, M. S. (2005). Myosins: Tails (and Heads) of Functional Diversity. *Physiology*, *20*(4), 239–251.

Kron, S. J., and Spudich, J. A. (1986). Fluorescent actin filaments move on myosin fixed to a glass surface. *Proceedings of the National Academy of Sciences of the United States of America*, *83*(17), 6272–6276.

Kumar, G., Srivastava, R., Mitra, K., Sahasrabuddhe, A. A., and Gupta, C. M. (2012). Overexpression of S4D mutant of *Leishmania donovani* ADF/cofilin impairs flagellum assembly by affecting actin dynamics. *Eukaryotic Cell*, *11*(6), 752–760.

Kunding, A. H., Mortensen, M. W., Christensen, S. M., and Stamou, D. (2008). A Fluorescence-Based Technique to Construct Size Distributions from Single-Object Measurements: Application to the Extrusion of Lipid Vesicles. *Biophysical Journal*, *95*(3), 1176–1188.

Kurten, R. C., Eddington, A. D., Chowdhury, P., Smith, R. D., Davidson, A. D., and Shank, B. B. (2001). Self-assembly and binding of a sorting nexin to sorting endosomes. *Journal of Cell Science*, *114*, 1743–1756.

Kutateladze, T. G. (2006). Phosphatidylinositol 3-phosphate recognition and membrane docking by the FYVE domain. *Biochimica et Biophysica Acta - Molecular and Cell Biology of Lipids*, *1761*(8), 868–877.

Laemmli, U. K. (1970). Cleavage of Structural Proteins during the Assembly of the Head of Bacteriophage T4. *Nature, 227*(5259), 680-685.

Landfear, S. M., and Ignatushchenko, M. (2001). The flagellum and flagellar pocket of trypanosomatids. *Molecular and Biochemical Parasitology*, *115*(1), 1–17.

Larsen, J. B., Jensen, M. B., Bhatia, V. K., Pedersen, S. L., Bjørnholm, T., Iversen, L., Uline, M. J., Szleifer, I., Jensen, K. J., Hatzakis, N. S., and Stamou, D. (2015). Membrane curvature enables N-Ras lipid anchor sorting to liquid-ordered membrane phases. *Nature Chemical Biology*, *11*(3), 192–194.

Larsen, J., Hatzakis, N. S., and Stamou, D. (2011). Observation of inhomogeneity in the lipid composition of individual nanoscale liposomes. *Journal of the American Chemical Society*, *133*(28), 10685–10687.

Leduc, C., Campàs, O., Joanny, J. F., Prost, J., and Bassereau, P. (2010). Mechanism of membrane nanotube formation by molecular motors. *Biochimica et Biophysica Acta - Biomembranes*, *1798*(7), 1418–1426.

Lee, K., Gallop, J. L., Rambani, K., and Kirschner, M. W. (2010). Self-Assembly of Filopodia-Like Structures on Supported Lipid Bilayers. *Science*, *329*(5997), 1341–1345.

Lee, S. A., Kovacs, J., Stahelin, R. V., Cheever, M. L., Overduin, M., Setty, T. G.,Burd, C. G., Cho, W., and Kutateladze, T. G. (2006). Molecular mechanism of membrane docking by the Vam7p PX domain. *Journal of Biological Chemistry*, *281*(48), 37091–37101.

Lemmon, M. A. (2003). Phosphoinositide recognition domains. *Traffic*, *4*(4), 201–213.

Lemmon, M. A. (2007). Pleckstrin homology (PH) domains and phosphoinositides. *Biochemical Society Symposium*, *93*(74), 81–93.

Lemmon, M. A. (2008). Membrane recognition by phospholipid-binding domains. *Nature Reviews Molecular Cell Biology*, *9*(2), 99–111.

Lemmon, M. A., and Ferguson, K. M. (2000). Signal-dependent membrane targeting by pleckstrin homology (PH) domains. *Biochemical Journal*, *350*(1), 1–18.

Lengsfeld, A. M., Löw, I., Wieland, T., Dancker, P., and Hasselbach, W. (1974). Interaction of phalloidin with actin. *Proceedings of the National Academy of Sciences of the United States of America*, *71*(7), 2803–2807.

Les Erickson, F. (2003). Localization of a Class III Myosin to Filopodia Tips in Transfected HeLa Cells Requires an Actin-binding Site in its Tail Domain. *Molecular Biology of the Cell*, *14*(10), 4173–4180.

Leventis, P. A., and Grinstein, S. (2010). The Distribution and Function of Phosphatidylserine in Cellular Membranes. *Annual Review of Biophysics, 39*, 407–427.

Lewis, A. K., and Bridgman, P. C. (1992). Nerve growth cone lamellipodia contain two populations of actin filaments that differ in organization and polarity. *Journal of Cell Biology*, *119*(5), 1219–1244.

Lin, C. H., Espreafico, E. M., and Mooseker, M. S. (1996). Myosin Drives Retrograde F-Actin Flow in Neuronal Growth Cones. *Neuron, 16*, 769–782.

Lin, T., Tang, N., and Ostap, E. M. (2005). Biochemical and motile properties of Myo1b splice isoform. *Journal of Biological Chemistry*, *280*(50), 41562–41567.

Linington, C., and Rumsby, M. G. (1977). Localization of cerebroside in central-nervous-system myelin lamellae: an initial approach. *Biochemical Society Transactions*, *5*(1), 196–198.

Lodish, H., Berk, A., Zipursky, S. L., Matsudaira, P., Baltimore, D., and Darnell, J. (2000). *Molecular Cell Biology* (Fourth Edition). New York: W. H. Freeman.

Lottspeich, F., and Engels, J. W. (2012). *Bioanalytik* (Third Edition). Berlin: Springer.

Low, M. G. (1990). Purification of phosphatidylinositol 4-phosphate and phosphatidylinositol 4,5-bisphosphate by column chromatography. In R. F. Irvine (Ed.), *Methods in Inositide Research* (pp. 145–152). New York: Raven Press.

Lymn, R. W., and Taylor, E. W. (1971). Mechanism of adenosine triphosphate hydrolysis by actomyosin. *Biochemistry*, *10*(25), 4617–4624.

Madsen, K. L., Bhatia, V. K., Gether, U., and Stamou, D. (2010). BAR domains, amphipathic helices and membrane-anchored proteins use the same mechanism to sense membrane curvature. *FEBS Letters*, *584*(9), 1848–1855.

Mallavarapu, A., and Mitchison, T. (1999). Regulated actin cytoskeleton assembly at filopodium tips controls their extension and retraction. *Journal of Cell Biology*, *146*(5), 1097–1106.

Margossian, S. S., and Lowey, S. (1982). Preparation of myosin and its subfragments from rabbit skeletal muscle. *Methods in Enzymology*, *85*, 55–71.

Maric, D., Epting, C. L., and Engman, D. M. (2010). Composition and sensory function of the trypanosome flagellar membrane. *Current Opinion in Microbiology*, *13*(4), 466–472.

Marsh, D. (1996). Intrinsic curvature in normal and inverted lipid structures and in membranes. *Biophysical Journal*, *70*(5), 2248–2255.

Mashanov, G. I., and Molloy, J. E. (2007). Automatic detection of single fluorophores in live cells. *Biophysical Journal*, *92*(6), 2199–2211.

Mattila, P. K., and Lappalainen, P. (2008). Filopodia: molecular architecture and cellular functions. *Nature Reviews Molecular Cell Biology*, *9*(6), 446–454.

Mazerik, J. N., and Tyska, M. J. (2012). Myosin-1A targets to microvilli using multiple membrane binding motifs in the tail homology 1 (TH1) domain. *Journal of Biological Chemistry*, *287*(16), 13104–13115.

McLaughlin, S., and Murray, D. (2005). Plasma membrane phosphoinositide organization by protein electrostatics. *Nature*, *438*(7068), 605–611.

McMahon, H. T., and Boucrot, E. (2015). Membrane curvature at a glance. *Journal of Cell Science*, *128*(6), 1065–1070.

Mehrotra, N., Nichols, J., and Ramachandran, R. (2014). Alternate pleckstrin homology domain orientations regulate dynamin-catalyzed membrane fission. *Molecular Biology of the Cell*, *25*(6), 879–890.

Mehta, A. D., Rock, R. S., Rief, M., Spudich, J. A., Mooseker, M. S., and Cheney, R. E. (1999). Myosin-V is a processive actin-based motor. *Nature*, *400*(6744), 590–593.

Mitchison, T. J. (1995). Evolution of a Dynamic Cytoskeleton. *Philosophical Transactions of the Royal Society B, 349*(1329), 299–304.

Mogilner, A., and Oster, G. (1996). Cell motility driven by actin polymerization. *Biophysical Journal*, *71*(6), 3030–3045.

Moleirinho, S., Tilston-Lunel, A., Angus, L., Gunn-Moore, F., and Reynolds, P. A. (2013). The expanding family of FERM proteins. *The Biochemical Journal*, *452*(2), 183–193.

Mooseker, M. S., and Foth, B. J. (2008). Chapter 1 - The Structural and Functional Diversity of the Myosin Family of Actin-Based Molecular Motors. In L. M. Coluccio (Ed.), *Proteins and Cell Regulation: Myosins: A Superfamily of Molecular Motors* (Vol. 7, pp. 1–34). Dordrecht: Springer.

Mooseker, M. S., and Tilney, L. G. (1975). Organization of an actin filament membrane complex. Filament polarity and membrane attachment in the microvilli of intestinal epithelial cells. *Journal of Cell Biology*, *67*(3), 725–743.

Murphy, E. J., Stiles, T., and Schroeder, F. (2000). Sterol carrier protein-2 expression alters phospholipid content and fatty acyl composition in L-cell fibroblasts. *Journal of Lipid Research*, *41*(5), 788–796.

Nambiar, R., McConnell, R. E., and Tyska, M. J. (2010). Myosin motor function: The ins and outs of actin-based membrane protrusions. *Cellular and Molecular Life Sciences*, *67*(8), 1239–1254.

Nicolson, G. (1976). Trans-membrane control of the receptors on normal and tumor cells I. Cytoplasmic influence over cell surface components. *Biochimica et Biophysica Acta - Reviews on Biomembranes*, *457*(1), 57–108.

Niggli, V., Andréoli, C., Roy, C., and Mangeat, P. (1995). Identification of a phosphatidylinositol-4,5-bisphosphate-binding domain in the N-terminal region of ezrin. *FEBS Letters*, *376*(3), 172–176.

Norberg, R., Thorstensson, R., Utter, G., and Fagraeus, A. (1979). F-Actin-Depolymerizing Activity of Human Serum. *European Journal of Biochemistry, 100*(2), 575–583.

O'Connell, C. B., Tyska, M. J., and Mooseker, M. S. (2007). Myosin at work: Motor adaptations for a variety of cellular functions. *Biochimica et Biophysica Acta*, *1773*(5), 615–630.

Odronitz, F., and Kollmar, M. (2007). Drawing the tree of eukaryotic life based on the analysis of 2,269 manually annotated myosins from 328 species. *Genome Biology*, *8*(9), R196.

Ohtsuka, T., Nishijima, M., and Akamatsu, Y. (1993). A somatic cell mutant defective in phosphatidylglycerophosphate synthase, with impaired phosphatidylglycerol and cardiolipin biosynthesis. *Journal of Biological Chemistry*, *268*(30), 22908–22913.

Okabe, S., and Hirokawa, N. (1991). Actin dynamics in growth cones. *Journal of Neuroscience*, *11*(7), 1918–1929.

Otto, J. J. (1994). Actin-bundling proteins. *Current Opinion in Cell Biology, 6*(1), 105–109.

Palmer, M. (2004). Cholesterol and the activity of bacterial toxins. *FEMS Microbiology Letters*, *238*(2), 281–289.

Pantaloni, D. (2001). Mechanism of Actin-Based Motility. *Science*, *292*(5521), 1502–1506.

Pardee, J. D., and Spudich, J. A. (1982). Purification of muscle actin. *Methods in Enzymology*, *85*, 164–181.

Pearson, M. A., Reczek, D., Bretscher, A., and Karplus, P. A. (2000). Structure of the ERM protein moesin reveals the FERM domain fold masked by an extended actin binding tail domain. *Cell*, *101*(3), 259–270.

Peskin, C. S., Odell, G. M., and Oster, G. F. (1993). Cellular motions and thermal fluctuations: the Brownian ratchet. *Biophysical Journal*, *65*(1), 316–324.

Peter, B. J. (2004). BAR Domains as Sensors of Membrane Curvature: The Amphiphysin BAR Structure. *Science*, *303*(5657), 495–499.

Pike, L. J. (2006). Rafts defined: a report on the Keystone Symposium on Lipid Rafts and Cell Function. *Journal of Lipid Research*, *47*(7), 1597–1598.

Pollard, T. D., and Cooper, J. A. (2009). Actin, a Central Player in Cell Shape and Movement. *Science*, *326*(5957), 1208–1212.

Prévost, C., Zhao, H., Manzi, J., Lemichez, E., Lappalainen, P., Callan-Jones, A., and Bassereau, P. (2015). IRSp53 senses negative membrane curvature and phase separates along membrane tubules. *Nature Communications*, *6*, 8529.

Price, W. H. (1946). The effect of adenosinetriphosphate (ATP) on the viscosity of actin solutions. *Journal of Cellular and Comparative Physiology*, *27*(2), 118–121.

Pyrpassopoulos, S., Feeser, E. A., Mazerik, J. N., Tyska, M. J., and Ostap, E. M. (2012). Membrane-bound Myo1c powers asymmetric motility of actin filaments. *Current Biology*, *22*(18), 1688–1692.

Ramesh, P., Baroji, Y. F., Reihani, S. N. S., Stamou, D., Oddershede, L. B., and Bendix, P. M. (2013). FBAR syndapin 1 recognizes and stabilizes highly curved tubular membranes in a concentration dependent manner. *Scientific Reports*, *3*, 1565.

Raucher, D., Stauffer, T., Chen, W., Shen, K., Guo, S., York, J. D., Sheetz, M. P., and Meyer, T. (2000). Phosphatidylinositol 4,5-Bisphosphate Functions as a Second Messenger that Regulates Cytoskeleton–Plasma Membrane Adhesion. *Cell*, *100*(2), 221–228.

Reggiani, C., and Bottinelli, R. (2008). Chapter 5 – Myosin II: Sarcomeric Myosins, the Motors of Contraction in Cardiac and Skeletal Muscles. In L. M. Coluccio (Ed.), *Proteins and Cell Regulation: Myosins: A Superfamily of Molecular Motors* (Vol. 7, pp. 155–170). Dordrecht: Springer.

Ren, G., Vajjhala, P., Lee, J. S., Winsor, B., and Munn, A. L. (2006). The BAR Domain Proteins: Molding Membranes in Fission, Fusion , and Phagy The BAR Domain Proteins : Molding Membranes in Fission , Fusion, and Phagy. *Microbiology and Molecular Biology Reviews*, *70*(1), 37–120.

Riedl, J., Crevenna, A. H., Kessenbrock, K., Yu, J. H., Neukirchen, D., Bista, M., Bradke, F., Jenne, D., Holak, T. A., Werb, Z., Sixt, M., and Wedlich-Soldner, R. (2008). Lifeact: a versatile marker to visualize F-actin. *Nature Methods*, *5*(7), 605–607.

Rodrigues, J. C. F., Godinho, J. L. P., and de Sousa, W. (2014). Chapter 1 - Biology of Human Pathogenic Trypanosomatids: Epidemiology, Lifecycle and Ultrastructure. In A. L. S. Santos, M. H. Branquinha, C. M. d'Avila-Levy, L. F. Kneipp, and C. L. Sodré (Eds.), *Proteins and Proteomics of Leishmania and Trypanosoma* (pp. 1–42). Dordrecht: Springer.

Sackmann, E. (1995). Chapter 1 - Biological Membranes Architecture and Function. In R. Lipowsky and E. Sackmann (Eds.), *Structure and Dynamics of Membranes* (First Edition, pp. 1–64). Amsterdam: Elsevier.

Sahasrabuddhe, A. A., Bajpai, V. K., and Gupta, C. M. (2004). A novel form of actin in *Leishmania*: Molecular characterisation, subcellular localisation and association with subpellicular microtubules. *Molecular and Biochemical Parasitology*, *134*(1), 105–114.

Sakamoto, T., Amitani, I., Yokota, E., and Ando, T. (2000). Direct observation of processive movement by individual myosin V molecules. *Biochemical and Biophysical Research Communications*, *272*(2), 586–590.

Santagata, S. (2001). G-Protein Signaling Through Tubby Proteins. *Science*, *292*(5524), 2041–2050.

Santrich, C., Moore, L., Sherwin, T., Bastin, P., Brokaw, C., Gull, K., and Lebowitz, J. H. (1997). A motility function for the paraflagellar rod of *Leishmania* parasites revealed by *PFR-2* gene knockouts. *Molecular and Biochemical Parasitology*, *90*(1), 95–109.

Sasaki, N., Ohkura, R., and Sutoh, K. (2003). *Dictyostelium* myosin II mutations that uncouple the converter swing and ATP hydrolysis cycle. *Biochemistry*, *42*(1), 90–95.

Schirenbeck, A., Arasada, R., Bretschneider, T., Stradal, T. E. B., Schleicher, M., and Faix, J. (2006). The bundling activity of vasodilator-stimulated phosphoprotein is required for filopodium formation. *Proceedings of the National Academy of Sciences of the United States of America*, *103*(20), 7694–7699.

Schirenbeck, A., Bretschneider, T., Arasada, R., Schleicher, M., and Faix, J. (2005). The Diaphanous-related formin dDia2 is required for the formation and maintenance of filopodia. *Nature Cell Biology*, *7*(6), 619–625.

Schliwa, M., and Woehlke, G. (2003). Molecular motors. *Nature*, *422*(6933), 759–765.

Schmidt, T., Schütz, G. J., Baumgartner, W., Gruber, H. J., and Schindler, H. (1996). Imaging of single molecule diffusion. *Proceedings of the National Academy of Sciences of the United States of America*, *93*(7), 2926–2929.

Scita, G., Confalonieri, S., Lappalainen, P., and Suetsugu, S. (2008). IRSp53: crossing the road of membrane and actin dynamics in the formation of membrane protrusions. *Trends in Cell Biology*, *18*(2), 52–60.

Scrimgeour, C. M., and Harwood, J. L. (2007). Chapter 1 - Fatty Acid and Lipid Structure. In F. D. Gunstone, J. L. Harwood, and A. J. Dijkstra (Eds.), *The Lipid Handbook* (Third Edition, pp. 1–16). Boca Raton: CRC Press.

Seaman, M. N. J. (2002). Identification of the Functional Domains of Yeast Sorting Nexins Vps5p and Vps17p. *Molecular Biology of the Cell*, *13*(8), 2826–2840.

Seet, L.-F., and Hong, W. (2006). The Phox (PX) domain proteins and membrane traffic. *Biochimica et Biophysica Acta*, *1761*(8), 878–896.

Segrest, J. P., De Loof, H., Dohlman, J. G., Brouillette, C. G., and Anantharamaiah, G. M. (1990). Amphipathic helix motif: Classes and properties. *Proteins: Structure, Function, and Genetics*, *8*(2), 103–117.

Sellers, J. R. (1999). *Myosins* (Second Edition). New York: Oxford University Press.

Sept, D., and McCammon, J. A. (2001). Thermodynamics and kinetics of actin filament nucleation. *Biophysical Journal*, *81*(2), 667–674.

Sheetz, M. P., and Spudich, J. A. (1983). Movement of myosin-coated fluorescent beads on actin cables *in vitro*. *Nature*, *303*(5912), 31–35.

Shin, Y. K., and Freed, J. H. (1989). Dynamic imaging of lateral diffusion by electron spin resonance and study of rotational dynamics in model membranes. Effect of cholesterol. *Biophysical Journal*, *55*(3), 537–550.

Singer, S. J., and Nicolson, G. L. (1972). The Fluid Mosaic Model of the Structure of Cell Membranes. *Science*, *175*(4023), 720–731.

Slater, S. J., Kelly, M. B., Taddeo, F. J., Ho, C., Rubin, E., and Stubbs, C. D. (1994). The modulation of protein kinase C activity by membrane lipid bilayer structure. *Journal of Biological Chemistry*, *269*(7), 4866–4871.

Slotte, J. P., and Ramstedt, B. (2007). The functional role of sphingomyelin in cell membranes. *European Journal of Lipid Science and Technology*, *109*(10), 977–981.

Snead, D., Wragg, R. T., Dittman, J. S., and Eliezer, D. (2014). Membrane curvature sensing by the C-terminal domain of complexin. *Nature Communications*, *5*, 4955.

Soldati, T., and Schliwa, M. (2006). Powering membrane traffic in endocytosis and recycling. *Nature Reviews Molecular Cell Biology*, *7*(12), 897–908.

Song, X., Xu, W., Zhang, A., Huang, G., Liang, X., Virbasius, J. V., Czech, M. P., and Wayne Zhou, G. (2001). Phox homology domains specifically bind phosphatidylinositol phosphates. *Biochemistry*, *40*(30), 8940–8944.

Soumpasis, D. M. (1983). Theoretical analysis of fluorescence photobleaching recovery experiments. *Biophysical Journal*, *41*(1), 95–97.

Sousa, A. D., and Cheney, R. E. (2005). Myosin-X: A molecular motor at the cell's fingertips. *Trends in Cell Biology*, *15*(10), 533–539.

Spudich, J. A. (1994). How molecular motors work. *Nature*, *372*(6506), 515–518.

Spudich, G., Chibalina, M. V., Au, J. S.-Y., Arden, S. D., Buss, F., and Kendrick-Jones, J. (2007). Myosin VI targeting to clathrin-coated structures and dimerization is mediated by binding to Disabled-2 and PtdIns(4,5)P_2. *Nature Cell Biology*, *9*(2), 176–183.

Squires, A. M., Conn, C. E., Seddon, J. M., and Templer, R. H. (2009). Quantitative model for the kinetics of lyotropic phase transitions involving changes in monolayer curvature. *Soft Matter*, *5*(23), 1–8.

Stachowiak, J. C., Schmid, E. M., Ryan, C. J., Ann, H. S., Sasaki, D. Y., Sherman, M. B., Geissler, P. L., Fletcher, D. A., and Hayden, C. C. (2012). Membrane bending by protein–protein crowding. *Nature Cell Biology*, *14*(9), 944–949.

Stahelin, R. V., Burian, A., Bruzik, K. S., Murray, D., and Cho, W. (2003). Membrane binding mechanisms of the PX domains of NADPH oxidase $p40^{phox}$ and $p47^{phox}$. *Journal of Biological Chemistry*, *278*(16), 14469–14479.

Stahelin, R. V., Karathanassis, D., Murray, D., Williams, R. L., and Cho, W. (2007). Structural and membrane binding analysis of the phox homology domain of Bem1p: Basis of phosphatidylinositol 4-phosphate specificity. *Journal of Biological Chemistry*, *282*(35), 25737–25747.

Stahelin, R. V. (2009). Lipid binding domains: more than simple lipid effectors. *Journal of Lipid Research*, *50*, S299–S304.

Stano, P., and Luisi, P. (2016). Chapter 7 - Theory and Construction of Semi-Synthetic Minimal Cells. In D. N. Nesbeth (Ed.), *Synthetic Biology Handbook* (Seventh Edition, pp. 209–258). Boca Raton: CRC Press.

Stoscheck, C. M. (1990). Quantitation of protein. *Methods in Enzymology*, *182*, 50–68.

Straub, F. B. (1943). The specificity of the adenosine-triphosphoric acid effect. In A. Szent-Györgyi (Ed.), *Studies from the Institute of Medical Chemistry, University of Szeged* (Vol. 3, pp. 38–39). Szeged: KFT.

Suter, D. M., and Forscher, P. (2000). Substrate-cytoskeletal coupling as a mechanism for the regulation of growth cone motility and guidance. *Journal of Neurobiology*, *44*(2), 97–113.

Sutton, R. B., Davletov, B. A., Berghuis, A. M., Sudhof, T. C., and Sprang, S. R. (1995). Structure of the First C2 Domain of Synaptotagmin 1: A Novel Ca^{2+}/Phospholidpid-Binding Fold. *Cell*, *80*(6), 929–938.

Sweeney, H. L., and Houdusse, A. (2010). Structural and functional insights into the Myosin motor mechanism. *Annual Review of Biophysics*, *39*, 539–557.

van Swaay, D. and deMello, A. (2013). Microfluidic methods for forming liposomes. *Lab on a Chip*, *13*(5), 752–767.

Tammana, T. V. S., Sahasrabuddhe, A. A., Mitra, K., Bajpai, V. K., and Gupta, C. M. (2008). Actin-depolymerizing factor, ADF/cofilin, is essentially required in assembly of *Leishmania* flagellum. *Molecular Microbiology*, *70*(4), 837–852.

Tanford, C. (1980). *The Hydrophobic Effect: Formation of Micelles and Biological Membranes* (Second Edition). New York: John Wiley & Sons, Inc.

Teasdale, R. D., and Collins, B. M. (2012). Insights into the PX (phox-homology) domain and SNX (sorting nexin) protein families: structures, functions and roles in disease. *Biochemical Journal*, *441*, 39–59.

The Cell Image Library (2016): http://www.cellimagelibrary.org/home, retrieved on September 2, 2016.

Tilney, L. G., Bonder, E. M., and DeRosier, D. J. (1981). Actin filaments elongate from their membrane-associated ends. *Journal of Cell Biology*, *90*(2), 485–494.

Tokuo, H., and Ikebe, M. (2004). Myosin X transports Mena/VASP to the tip of filopodia. *Biochemical and Biophysical Research Communications*, *319*(1), 214–220.

Tokuo, H., Mabuchi, K., and Ikebe, M. (2007). The motor activity of myosin-X promotes actin fiber convergence at the cell periphery to initiate filopodia formation. *Journal of Cell Biology*, *179*(2), 229–238.

Tsakraklides, V., Krogh, K., Wang, L., Bizario, J. C., Larson, R. E., Espreafico, E. M., and Wolenski, J. S. (1999). Subcellular localization of GFP-myosin-V in live mouse melanocytes. *Journal of Cell Science*, *112*(17), 2853–2865.

Tyska, M. J., Mackey, A. T., Huang, J.-D., Copeland, N. G., Jenkins, N. A., and Mooseker, M. S. (2005). Myosin-1a is critical for normal brush border structure and composition. *Molecular Biology of the Cell, 16*(5), 2443–2457.

Unwin, N. (2005). Refined structure of the nicotinic acetylcholine receptor at 4 Å resolution. *Journal of Molecular Biology*, *346*(4), 967–989.

Varkey, J., Isas, J. M., Mizuno, N., Jensen, M. B., Bhatia, V. K., Jao, C. C., Petrlova, J., Voss, J. C., Stamou, D. G., Steven, A. C., and Langen, R. (2010). Membrane curvature induction and tubulation are common features of synucleins and apolipoproteins. *Journal of Biological Chemistry*, *285*(42), 32486–32493.

von Delius, M., and Leigh, D. A. (2011). Walking molecules. *Chemical Society Reviews*, *40*(7), 3656–3676.

Wang, Q., Deloia, M. A., Kang, Y., Litchke, C., Zhang, N., Titus, M. A., and Walters, K. J. (2007). The SH3 domain of a M7 interacts with its C-terminal proline-rich region. *Protein Science, 16*(2), 189–196.

Wasserman, S. R., Tao, Y. T., and Whitesides, G. M. (1989). Structure and reactivity of alkylsiloxane monolayers formed by reaction of alkyltrichlorosilanes on silicon substrates. *Langmuir*, *5*(4), 1074–1087.

Watanabe, T. M., Tokuo, H., Gonda, K., Higuchi, H., and Ikebe, M. (2010). Myosin-X induces filopodia by multiple elongation mechanism. *Journal of Biological Chemistry*, *285*(25), 19605–19614.

Weber, A., Pring, M., Lin, S. L., and Bryan, J. (1991). Role of the N- and C-terminal actin-binding domains of gelsolin in barbed filament end capping. *Biochemistry*, *30*(38), 9327–9334.

Wei, H.-C., Rollins, J., Fabian, L., Hayes, M., Polevoy, G., Bazinet, C., and Brill, J. A. (2008). Depletion of plasma membrane PtdIns(4,5)P_2 reveals essential roles for phosphoinositides in flagellar biogenesis. *Journal of Cell Science*, *121*(7), 1076–1084.

Wells, A. L., Lin, A. W., Chen, L. Q., Safer, D., Cain, S. M., Hasson, T., Carragher, B. O., Milligan, R. A., and Sweeney, H. L. (1999). Myosin VI is an actin-based motor that moves backwards. *Nature*, *401*(6752), 505–508.

Wetterau, J. R., and Jonas, A. (1982). Effect of dipalmitoylphosphatidylcholine vesicle curvature on the reaction with human apolipoprotein A-I. *Journal of Biological Chemistry*, *257*(18), 10961–10966.

WHO (2010). Control of the Leishmaniases. *Technical Report Series*, *949*. World Health Organization, Geneva

WHO (2016): http://www.who.int/leishmaniasis/burden/magnitude/burden_magnitude/en, retrieved on September 4, 2016.

Yang, L., and Huang, H. W. (2003). A rhombohedral phase of lipid containing a membrane fusion intermediate structure. *Biophysical Journal*, *84*(3), 1808–1817.

Zhan, Y., Virbasius, J. V., Song, X., Pomerleau, D. P., and Wayne Zhou, G. (2002). The $p40^{phox}$ and $p47^{phox}$ PX domains of NADPH oxidase target cell membranes via direct and indirect recruitment by phosphoinositides. *Journal of Biological Chemistry*, *277*(6), 4512–4518.

Zhang, G., Kazanietz, M. G., Blumberg, P. M., and Hurley, J. H. (1995). Crystal structure of the cys2 activator-binding domain of protein kinase Cδ in complex with phorbol ester. *Cell*, *81*, 917–924.

Zhang, H., Berg, J. S., Li, Z., Wang, Y., Lång, P., Sousa, A. D., Bhaskar, A., Cheney, R. E., and Strömblad, S. (2004). Myosin-X provides a motor-based link between integrins and the cytoskeleton. *Nature Cell Biology*, *6*(6), 523–531.

Zhang, Y., Li, X., Becker, K. A., and Gulbins, E. (2009). Ceramide-enriched membrane domains-Structure and function. *Biochimica et Biophysica Acta - Biomembranes*, *1788*(1), 178–183.

Zimmerberg, J., and Kozlov, M. M. (2006). How proteins produce cellular membrane curvature. *Nature Reviews Molecular Cell Biology*, *7*(1), 9–19.

Zinser, E., Sperka-Gottlieb, C. D. M., Fasch, E. V., Kohlwein, S. D., Paltauf, F., and Daum, G. (1991). Phospholipid synthesis and lipid composition of subcellular membranes in the unicellular eukaryote *Saccharomyces cerevisiae*. *Journal of Bacteriology*, *173*(6), 2026–2034.

Zot, H. G., Doberstein, S. K., and Pollard, T. D. (1992). Myosin-I moves actin filaments on a phospholipid substrate: Implications for membrane targeting. *Journal of Cell Biology*, *116*(2), 367–376.

Appendix A – Molecular Cloning

In this appendix, an overview of the recombinant DNA constructs produced throughout the course of the present study is given. DNA templates encoding the respective proteins were amplified by polymerase chain reaction. In order to create recombinant DNA, templates and respective plasmid vectors were subjected to restriction enzyme digestion, and subsequently ligated. An overview of the utilized primers, DNA templates, plasmid vectors, and restriction enzymes is given in Table A.1 and Table A.2. Nucleic acid sequences of primers are summarized in Table A.3.

Table A.1 Recombinant plasmids for protein expression. The table below lists all recombinant plasmids created for the purpose of protein expression in the present study. DNA templates encoding the respective proteins were amplified by PCR utilizing the primers listed below. Templates denoted as XXI and VI contain the complete or partial sequences of *L. donovani* myosin-XXI and chicken myosin-VI respectively. CaMX refers to *Xenopus laevis* calmodulin. "FL" designates full-length DNA sequences. Ligation of DNA templates and plasmid vector was prepared by restriction enzyme digestion using the indicated enzymes. The table further summarizes the fluorophore and the antibiotic resistance encoded by each vector. 1: The pet28a(+)-eGFP vector is a modified version of the pet28a(+) vector additionally containing the DNA sequence of eGFP. EGFP DNA was amplified by PCR (primers: mGFP-HindIII-FP, mGFP-NotI-RP), and pet28a(+) and the eGFP sequence were subjected to restriction enzyme digestion with NotI and HindIII to enable ligation. 2: This myosin-XXI construct contains a double-amino acid substitution (Arg705Leu, Tyr706Ser). Site-directed mutagenesis of the original recombinant pet-28(a)-eGFP-XXI aa 600-758 plasmid was implemented in two subsequent steps of PCR (primers: XXI-SDM-FP1 and XXI-SDM-RP1 in the first reaction, XXI-SDM-FP2 and XXI-SDM-RP2 in the second reaction). After PCR was finished, original pet-28(a)-eGFP-XXI aa 600-758 plasmid was digested by DpnI restriction enzyme (New England Biolabs) according to manufacturer´s instructions. 3: Recombinant plasmids encoding fusion constructs of eGFP and FL-XXI (aa 1-1050) or Trunc-XXI (aa 1-800) respectively were created by insertion of the eGFP sequence at the BamHI restriction site of the recombinant pFastBac™HT B-XXI aa 1-1050 or pFastBac™HT B-XXI aa 1-800 plasmids. PCR of eGFP DNA was carried out applying XXInGFPTR1 and XXInGFPTR2 primers. 4: This readily prepared recombinant plasmid was kindly provided by James R. Sellers (National Institutes of Health, Bethesda, Maryland).

Vector			**DNA Template**		Restriction Enzymes
Name	Antibiotic Resistance	Fluorophore	Amino Acid Sequence	Primers (PCR)	
pet-28a(+)-eGFP[1] (modified from pet-28a(+) (Merck))	Kanamycin	eGFP	Endophilin aa 1-247	eNBAR-FP, eNBAR-RP	BamHI, HindIII
			XXI aa 809-1050	XXI-809tail-BamHI-FP, XXI-1050-HindIII-RP	BamHI, HindIII
			XXI aa 930-1050	XXI-930tail-BamHI-FP, XXI-1050-HindIII-RP	BamHI, HindIII
			XXI aa 830-1050	XXI-830tail-BamHI-FP, XXI-1050-HindIII-RP	BamHI, HindIII
			XXI aa 600-758	XXICON-Bam-FP, XXICON-Hind-RP	BamHI, HindIII
			XXI aa 600-758 (R705L/Y706S)[2]	-	-
pFastBac™HT B (Thermo Fisher Scientific)	Ampicillin	-	XXI aa 1-1050 (FL)	XXIFP6, XXIRP2	BamHI, NotI
			XXI aa 1-800	XXIFP6, XXITR3	BamHI, NotI
			VI aa 1-1277 (FL)	CVI-SalI-FP, CVI-XhoI-RP	SalI, XhoI
			eGFP-XXI aa 1-1050[3]	-	-
			eGFP-XXI aa 1-800[3]	-	-
pFastBac™1[4]	Ampicillin	none	CaMX aa 1-149[7] (FL)	-	-

Table A.2 Recombinant plasmids for mammalian cell transfections. In the table below, recombinant plasmids used in the present mammalian cell transfection experiments are summarized. In addition to the respective DNA templates and plasmid vectors, primers used for template amplification and restriction enzymes applied to enable ligation of templates and vectors are listed. Template sequences termed XXI refer to myosin-XXI DNA constructs. Amino acid sequences designated as "FL" encode a full-length protein. Fluorophore sequences already contained in the vectors and the antibiotic resistance encoded by each vector are also specified. Importantly, control transfection experiments were performed with plasmids solely containing fluorophore DNA. Respective plasmids are indicated as "Control". 1: Vectors pmEGFP-C3 and pmRFP-C3-MCS were created and kindly provided by former lab member Natali Fili. 2: The complete recombinant plasmid already containing the lifeact DNA sequence was kindly provided by Roland Wedlich-Söldner (Westfälische Wilhelms-Universität Münster).

Vector			**DNA Template**		Restriction Enzymes
Name	Antibiotic Resistance	Fluorophore	Amino Acid Sequence	Primers (PCR)	
pZsGreen1-N1 (Clontech)	Kanamycin	ZsGreen1	- (Control)	-	-
			XXI aa 1-1050 (FL)	XXI-ZsG-FP, XXI-Zs-RP	HindIII, BamHI
			XXI aa 1-800	XXI-ZsG-FP, XXITr-Zs-RP	HindIII, BamHI
pmEGFP-C3[1]	Kanamycin	eGFP	- (Control)	-	-
			XXI aa 1-753	XXI-MAM-FP, XXI-MAM+PX-RP	XhoI, BamHI
			XXI aa 1-704	XXI-MAM-FP, XXI-MAM-PX-RP	XhoI, BamHI
pEGFP-C3 (Clontech)	Kanamycin	eGFP	XXI aa 46-1050	XXI-SH3-FP, XXI-RP-FL	XhoI, BamHI
			XXI aa 46-800	XXI-SH3-FP, XXI-RP-800	XhoI, BamHI
			XXI aa 46-753	XXI-SH3-FP, XXI-MAM+PX-RP	XhoI, BamHI
			XXI aa 46-704	XXI-SH3-FP, XXI-MAM-PX-RP	XhoI, BamHI
pmRFP-C3-MCS[1]	Kanamycin	DsRed2	- (Control)	-	-
			XXI aa 730-1050	XXI730FP-MAM, XXI-ENDRP-MAM	HindIII, BamHI
			XXI aa 830-1050	XXI830FP-MAM, XXI-ENDRP-MAM	HindIII, BamHI
			XXI aa 930-1050	XXI930FP-MAM, XXI-ENDRP-MAM	HindIII, BamHI
			XXI aa 730-936	XXI730FP-MAM, XXI930RP-MAM	HindIII, BamHI
			XXI aa 830-936	XXI830FP-MAM, XXI930RP-MAM	HindIII, BamHI
			XXI aa 730-836	XXI730FP-MAM, XXI830RP-MAM	HindIII, BamHI
mRFPRuby-N1[2]	Kanamycin	RFP	Lifeact aa 1-17[3] (FL)	-	-

Table A.3 Nucleic acid sequences of primers utilized for the amplification of DNA templates. Sequences are listed in the 5' to 3' direction. Bold letters indicate sites of restriction enzyme digestion. If not indicated, no restriction sites are present. Colored letters designate amino acid substitutions.

Primer Name	Nucleic Acid Sequence	Restriction Site
CVI-SalI-FP	AAA **GTC GAC** AAT GGA GGA CGG GAA GCC CGT TTG	SalI
CVI-XhoI-RP	A**CT CGA G**CT ATT TCA ACA GGT TCT GCA GC	XhoI
eNBAR-FP	GGG **GGA TCC** ATG AGT GTT GCA GGC CTG AAA AAA	BamHI
eNBAR-RP	AAA **AAG CTT** AGC CTG GCG GAT ACG TTC TTC CAG	HindIII
mGFP-HindIII-FP	CC**A AGC TT**G CAT GGT GAG CAA GGG CGA GGA GC	HindIII
mGFP-NotI-RP	TCT T**GC GGC CGC** CTT GTA CAG CTC GTC CAT GCC	NotI
XXI-1050-HindIII-RP	AAA **AAG CTT** GCT CAC CTT GAA CAG CA	HindIII
XXI-809tail-BamHI-FP	GGG **GGA TCC** CTG CAG TGG GTG GAG GAG GCG	BamHI
XXI-830tail-BamHI-FP	GGG **GGA TCC** GCC GTC GAG GCG GAC ACG CGC G	BamHI
XXI-930tail-BamHI-FP	GGG **GGA TCC** GGC ACG GAC AGC GAA TAT GCC	BamHI
XXI-ENDRP-MAM	AAA AAA **GGA TCC** CTA GCT CAC CTT GAA CAG C	BamHI
XXI-MAM-FP	AAA A**CT CGA G**AT GCC GGA GCG TGT GTC TG	XhoI
XXI-MAM-PX-RP	TTT TTT **GGA TCC** TTA CCC TTG CTT GAA CAA GGA GG	BamHI
XXI-MAM+PX-RP	TTT TTT **GGA TCC** TTA CGC GCG GCG ACG AAG CAC C	BamHI
XXI-RP-800	TTT TTT **GGA TCC** TTA GTC GGC GGC CTT GGC CTC CC	BamHI
XXI-RP-FL	TTT TTT **GGA TCC** CTA GCT CAC CTT GAA CAG C	BamHI
XXI-SDM-FP1	CCT TGT TCA AGC AAG GGC **T**GT ACA GCG ACG CGT CCC	-
XXI-SDM-FP2	CCT TGT TCA AGC AAG GGC **T**GT **C**CA GCG ACG CGT CCC AGG	-
XXI-SDM-RP1	GGG ACG CGT CGC TGT AC**A** GCC CTT GCT TGA ACA AGG	-
XXI-SDM-RP2	CCT GGG ACG CGT CGC TG**G** AC**A** GCC CTT GCT TGA ACA AGG	-
XXI-SH3-FP	AAA A**CT CGA G**GC GGC CGA TAA TGT GCA CGG	XhoI
XXI-ZsG-FP	GTG **AAG CTT** ATG CCG GAG CGT GTG TCT GTG	HindIII
XXI-Zs-RP	G**GG ATC C**GC CGC TCA CCT TGA ACA GC	BamHI
XXI730FP-MAM	GGG **AAG CTT** GGC AAG ACG AAG GTG TTC CTC C	HindIII
XXI830FP-MAM	GGG **AAG CTT** GCC GTC GAG GCG GAC ACG CGC G	HindIII
XXI830RP-MAM	AAA AAA **GGA TCC** CTA GCG CGT GTC CGC CTC GAC GGC	BamHI
XXI930FP-MAM	GGG **AAG CTT** GGC ACG GAC AGC GAA TAT GCC	HindIII
XXI930RP-MAM	AAA AAA **GGA TCC** CTA GGC ATA TTC GCT GTC CGT GCC	BamHI
XXICON-Bam-FP	TCT TCT **GGA TCC** TCG CAG CTT GAG TCC GCT GG	BamHI
XXICON-Hind-RP	TCT TCT **AAG CTT** ACC ACC TCC GCA GCG GTG CAG CAG CTG CG	HindIII
XXIFP6	A**GG ATC C**AT GCC GGA GCG TGT GTC TGT G	BamHI
XXInGFPTR1	G**GG ATC C**AT TGG CGG CGT CGG CGG CCT TGG C	BamHI
XXInGFPTR2	G**GG ATC C**TT TCT CCG CCG GCA CCA TTG GC	BamHI
XXIRP2	AAA A**GC GGC CGC** CTA GCT CAC CTT GAA CAG C	NotI
XXITr-Zs-RP	G**GG ATC C**AT TGG CGG CGT CGG CGG CCT TGG C	BamHI
XXITR3	AAA A**GC GGC CGC** CTA ATT GGC GGC GTC GGC GGC	NotI

Appendix B – Myosin-XXI Sequence

The following nucleic acid sequence encodes *L. donovani* myosin-XXI. The sequence is given in the 5’ to 3’ direction:

ATGCCGGAGCGTGTGTCTGTGAATCAGGAGGTGTACTACTTCGACACCAAGAGCGGGTGGCTGCGTGGCACCGTGAAGGAGG
TCGATGGCGCCAAGGTGACGGTAGAGGACAATGCCTCGCAGAGTGCCGTGAAAGTGGCGGCCGATAATGTGCACGGCTACAT
GTCGGAGAGCTACGATATCGAGGACGCGGACCTCTTCCACGTGAGCGATCTGCACGTGGCCACTCTCTTGCACTGCGTCAAG
GACCGTTTTGAGAAGCTGCACAAGCAGTACTCGCTCATGGGGGAGATGGTGCTCTCCGTCAACCCATTTCGCCTCATGCCCT
TCAACAGCGAAGAGGAGCGTAAAGAGTATCTGGCCCTGCCGGACCCCCGCATGCTGCCCCCGCACATCTGGCAGGTGGCGCA
CAAGGCCTTCAACGCGGTCTTCGTTCAGGGTCAGGGCAACCAGTCCATCGTCATCTCCGGCGAGTCCGGTTCCGGAAAAACC
GAGAACGCCAAGATGCTCATCGCGTACCTGGGCCAACTCAGCTACATGCACAGCAAGAACACCTCGCAGCGCAGCATCGCGG
ACAAGATCGACGAGAACCTAACCTGGAGCAACCCCGTCATGGAGTCGTTCGGCAACGCCCGCACCGTGCGCAACGACAACTC
TTCGCGCTTCGGCAAGTACATCAAGCTCTACTTTGATCCTGTATCTGGCGTCATGGTGGGGGGCCAGACCGTCACCTACTTG
CTGGAGAGGAGCCGCATCATCATGCAGTCTCCTGGCGAGCGCAACTACCACATCTTCTACGAGATGCTGGCGGGCCTGTCGC
CGACAGAGAAGCAGCAGCTTGGCGGGCTCAAGACTGCCCAGGACTACAAGTGCCTGAACGGCGGTAACACCTTCATCCGCCG
CGGCGTGGATGGCAAGCCGCTCGACGACGCGCACGAGTTTCAGATGGTGCGCCGCGCGCTTTCCATGATCGGTGTGCCGCTG
GAGACGCAGAACTGCATGTTGCGCGTGCTGGCGGCCATCCTGCACCTGATGGAGGTCGAGTTCGAGCCCGACAACAACGACA
AGGCACAGATCGCAAACGGGACACCGCTCGCGACGGCCTGCGCGCTGCTCTGCCTGGATGAGGCCAAGGTGCGCGAGTGCTT
TCTCGTGAGGAGCAAGACGTCGCTTGTCACGATCCTCGCCTCCAAGACGGAGGCGGAGGGCCTGCGCAACGCCTTCTGCAAG
GGACTTTACGTTGGCATGTTCGACCGGCTGGTCGAGTTTGTGAACGCCGCCATTCAGCCCCGGGTGGACTGCAGCGACTGCA
AGTACGTCGGCCTGCTCGATATTTTCGGCTTTGAAAACTTCACGCGCAACAGCTTCGAGCAGATCTGCATCAATTACGCGAA
CGAGTCGCTGCAAAACCACTACAACAAGTACACGTTCATCAACGACGAAGAGGAGTGCCGCCGCGAGGGTATCCAGACCCCG
AATATCGAGTTCCCAGACAACTCCGAGTGCGTCAACATGCTCGATGCGAAGCGCGTCGGCATCTTCTCGATGCTGGATGAGG
AGTGCAACTTCAAGGGCGGCAACACAGACCGCTTCACCACGAACCTTTGGGAGGAGTGGGCTGGCAGGAACCCGTACTTTGT
GAAGCCGAAGAGCACGATCCCGAACCAGTTCGGCGTGAACCACTACGCTGCCTTCGTCAACTACAACACGGCGGACTGGTTG
GAGAAGAACACGGACGCACTCAAGGAAGACATGTATGAGTGCGTGAGTGAGTCCACCGACGAGTTCATTCGGACCCTTCTCT
CGACGGAGAAGAGCGAGGCACGCCGCAAGCAGACCGTTGCCATCCGCTTCCAGCGCCAGCTCACGGACCTGCGCTCCGAGCT
GGAGTCCACCGAGACACGGTTCATTCGCTGCATCAAGCCAAATATGGAGGCAAGCCCCTCGTTCCTCGAAAACCTTCTCGTC
GGCTCGCAGCTTGAGTCCGCTGGTGTGCTGCAGACCATCTCCCTCAAGCGTCAGGGCTACCCGGTGCGCCGTCCGCTGGAGC
AGTTTTGCAGGTACTTCTACCTTGTCATGTCCCGCACCACCGCCTCCTTGTTCAAGCAAGGGCGGTACAGCGACGCGTCCCA
GGACTTTCTGCAGCGACACCAGCGCCTCTACAGCTGGGCGGAGCCCAACTACGCCGTTGGCAAGACGAAGGTGTTCCTCCGG
GCTGAGGTGTGGTCGGCGCTGGAGCGGCTGGTGCTTCGTCGCCGCGCGCAGCTGCTGCACCGCTGCAAGCCCTACCTGCGCC
GCTGGATCGACGAGCTCCGCGAGCGCAGGCGTATCGAGGAGCAGAAGCGGCTGGAGGCAGCGCGCAAGCTGCGCGAGGCGCG
GGAGGCCAAGGCCGCCGACGCCGCCAATGGTGTGCCGGCGGAGAAACTGCAGTGGGTGGAGGAGGCGTCGAACATGTTCCCA
GACTTCGACACGGACACGCTGCTCGACGTTGCCGTCGAGGCGGACACGCGCGAGGAGGCTCTCAGCGCCATCCTTGCCATCC
AGGCTGACCGCCTTGACAAGCAGACAGCCTCTGGATTCATGGAAGTGATGGCGGCTGCGAACGTGCGCCGTGGCGTCATCAA
CAACTTTATCTCGGCGGACATCAAGACGGTGTCGGCGCTGTCGAGGCTGCAGCCGGAGGATATGAAGAGCCTCGGCGCCAGT
GAGATGGAGGTGGTGGCGATCACGAAGAAGCTGGCGGAGCAGCAGGGGCAGCGCGTCAAGTACCAGCGCCTCGCCGAGGCCA
TCGGCACGGACAGCGAATATGCCGCCGCTGGCGCCGTCCAACGCGCCGAGGTGGCTCGCCACCAGGAAGACTTCGACGCCAA
AGTGCAGACCCTTGCCAGCATGGGCTTTGATGAGCCCACCGGCCGCCTCGTGCTGGCGCACTACAACGGCGACGTGCAGCGC
ACGGCGGCGCGCCTGCTTTATGGCGTGGACAGCCGGAAGATGAGGAACAACGCGCGCAAGCACAAGAACTTCAACACAACGG
ACCCCAACGTGCAGCAGCTCATCTCTCTCGGTGCGACGAAGCAGGATGCAAAGATGGCACTACGTCGCAACAACGGAGACGC
GAACGCCGCCGTTAAGATGCTGTTCAAGGTGAGCTAG

Appendix C – Structural Motifs of Myosin-XXI

In this appendix, the types and intramolecular positions of the structural motifs so far identified within *L. donovani* myosin-XXI are summarized.

Table C.1 Structural motifs of *L. donovani* myosin-XXI. This table lists the myosin-XXI structural motifs known at present and states their position within the aa sequence of the motor protein. Full-length myosin-XXI comprises 1050 aa. Data have partially been reported in a previous publication of our research group (Batters *et al.*, 2014). In the respective study, BHB domains were predicted by basic and hydrophobic score calculation (1) and sequence analysis (2).

Structural Motif	Start at aa	End at aa
SH3-like domain	11	37
motor domain	65	747
• ATP/ADP binding pocket	103	166
• switch I	219	222
• switch II	445	451
• relay Loop	473	496
• converter	662	747
IQ motif	754	769
predicted coiled coils	744	809
	828	856
	878	961
	1016	1046
PX domain	705	752
predicted BHB domains (1)	765	776
	781	793
	796	808
	897	912
	996	1006
	1033	1044
predicted BHB domains (2)	752	770
	999	1006
UBA Domains	950	992
	1013	1046

Appendix D – Lateral Diffusion Coefficients of Planar Lipid Bilayers

In Fluorescence Recovery after Photobleaching experiments, planar lipid bilayers were tested for their fluidity. Analysis of FRAP measurements resulted in the determination of lateral diffusion constants. By comparison of the respective diffusion constants with published data, quality of the prepared bilayer samples could be verified. Here, the diffusion coefficients obtained from each individual measurement are listed.

Table D.1 Lateral diffusion coefficients determined by FRAP measurements. In FRAP experiments, tethered and supported planar bilayers of different lipid composition were investigated. From each individual measurement, a diffusion coefficient D_i was determined. Subsequently, average lateral diffusion constants D were calculated, which are stated as mean ± standard deviation. The tethered bilayer sample is labeled as "TB", and the number of evaluated samples of each bilayer type is stated.

D_i [10^{-12} $m^2 \cdot s^{-1}$] for bilayers composed of		
97.3 mol% POP 1.5 mol% Biotin DHPE 1.2 mol% Rhodamine DHPE (6 samples)	73.0 mol% POPC 26.0 mol% cholesterol 1.0 mol% Rhodamine DHPE (5 samples)	94.0 mol% POPC 4.8 mol% $PI(3,5)P_2$ 1.2 mol% Rhodamine DHPE (TB, 1 sample)
0.74	0.81	1.18
0.99	0.85	1.39
1.00	0.89	1.48
1.03	0.97	1.49
1.08	0.97	1.70
1.13	0.99	
1.14	1.01	
1.18	1.02	
1.23	1.07	
1.25	1.09	
1.26	1.10	
1.35	1.12	
1.39	1.14	
1.41	1.16	
1.46	1.16	
1.55	1.19	
1.60	1.23	
1.76	1.27	
1.98	1.31	
2.05	1.35	
2.18	1.49	
2.20	1.60	
2.47	2.03	
2.59	2.16	
average lateral diffusion constant D [10^{-12} $m^2 \cdot s^{-1}$]		
1.50±0.50	1.21±0.33	1.45±0.19

Appendix E – Protein-Vesicle Co-Sedimentation

Co-sedimentation assays were carried out prior to the investigation of the bilayer binding behavior of proteins in Single Liposome Curvature assays. In order to test the respective proteins for their capability to bind to bovine brain extract vesicles, protein-vesicle mixtures were prepared and subjected to ultracentrifugation. Sedimentation of protein indicated vesicle binding. To rule out significant vesicle-independent precipitation of protein, negative control sedimentation assays with solutions solely containing protein were performed. In this appendix, results of all co-sedimentation experiments and negative control assays are stated.

Table E.1 Results of negative control sedimentation assays. For each protein, 3 negative control assays, i.e. sedimentation assays in the absence of vesicles, were performed. Below, the fraction of sedimented protein detected in each individual assay is listed. The resulting average values are given as mean ± standard deviation.

Protein	Fraction of Protein in the Precipitate			
	Assay 1	Assay 2	Assay 3	Average
eNBAR	0.0	0.0	0.0	0.0±0.0
FL-XXI	2.9	0.0	2.2	1.6±1.5
Trunc-XXI	0.0	0.0	4.1	1.3±2.4
XXI-930 Tail	0.0	0.0	0.0	0.0±0.0
XXI-830 Tail	0.0	0.0	0.0	0.0±0.0
XXI-809 Tail	0.0	0.0	0.0	0.0±0.0
XXI-Conv. WT	0.0	0.0	0.0	0.0±0.0
XXI-Conv. M	0.0	0.0	0.0	0.0±0.0

Table E.2 Results of co-sedimentation assays with bovine brain extract vesicles. For each protein, 5 co-sedimentation assays were carried out. In the table below, the fraction of precipitated protein detected in each assay is given. The resulting average values are stated as mean ± standard deviation.

Protein	Fraction of Protein in the Precipitate					
	Assay 1	Assay 2	Assay 3	Assay 4	Assay 5	Average
eNBAR	79.3	82.7	85.3	88.3	79.1	82.9±4.0
FL-XXI	29.5	15.7	22.5	23.8	20.9	22.4±5.0
Trunc-XXI	9.6	16.5	11.7	17.6	11.1	13.3±3.6
XXI-930 Tail	80.4	53.6	35.7	100.0	100.0	75.8±28.6
XXI-830 Tail	71.4	63.7	66.1	62.8	73.1	67.0±4.6
XXI-809 Tail	0.0	0.0	0.0	0.0	0.0	0.0±0.0
XXI-Conv. WT	0.0	0.0	0.0	0.0	0.0	0.0±0.0
XXI-Conv. M	0.0	0.0	0.0	0.0	0.0	0.0±0.0

Publications

Parts of the results described in this thesis have already been published:

Journal articles:

Batters, C., Ellrich, H., Helbig, C., Woodall, K. A., Hundschell, C., Brack, D., and Veigel, C. (2014). Calmodulin regulates dimerization, motility, and lipid binding of *Leishmania* myosin XXI. *Proceedings of the National Academy of Science of the United States of America*, *111*(2), E227–E236.

Meeting abstracts:

Helbig, C., Batters, C., Averbeck, B., and Veigel, C. (2015). *In vivo* and *in vitro* Studies of Myosin-XXI Dynamics. *Biophysical Journal*, *108*(2), 303a.

Batters, C., Ellrich, H., Helbig, C., Woodall, K., Hundschell, C., Brack, D., and Veigel, C. (2014). Calmodulin and Lipid Binding Regulate Dimerisation and Motility of Myosin-XXI in Leishmania. *Biophysical Journal*, *106*(2), 180a.

Helbig, C., Ellrich, H., Hundschell, C., Batters, C., and Veigel, C. (2013). Myosin-XXI, a Motor with many Missions. *Biophysical Journal*, *104*(2), 644a.

Poster presentations:

Helbig, C., Saczko-Brack, D., Ellrich, H., Werner, C., Averbeck, B., Batters, C., and Veigel, C. Structure and Binding Behavior of Myosin-VI and Myosin-XXI. Workshop of SFB 863 “Forces in Biomolecular Systems”, Hohenkammer, Germany, October 2014.

Helbig, C., Ellrich, H., Hundschell, C., Batters, C., and Veigel, C. Myosin XXI - a myosin with many missions. Center for NanoScience Workshop “Nanosciences: Soft, Solid, Alive and Kicking”, Venice, Italy, September 2012.

Danksagung

An dieser Stelle möchte ich mich bei all jenen Menschen bedanken, die mich während der spannenden, lehrreichen, aber auch herausfordernden Zeit meiner Promotion unterstützt haben.

Zunächst gilt mein Dank Frau Prof. Dr. C. Veigel, die mir durch die Promotion an ihrem Lehrstuhl die Möglichkeit gegeben hat, sowohl mein biophysikalisches Wissen anzuwenden und zu erweitern als auch neue molekularbiologische und biochemische Techniken und Methoden zu erlernen.

Außerdem möchte ich ein großes Dankeschön an meine Betreuerin Frau Dr. Beate Averbeck richten. Durch zahlreiche hilfreiche Gespräche, wertvolle Ratschläge, aufmunternde Worte und mit viel Humor hat sie einen wesentlichen Beitrag zum Gelingen dieser Arbeit geleistet.

Nicht zu vergessen sind auch Christopher Toseland, Christopher Batters, und besonders Natali Fili, von denen ich viele wichtige Methoden der Laborarbeit gelernt habe und die mir stets mit fachlichem Rat zur Seite standen. Für ihre Hilfsbereitschaft, die gute Zusammenarbeit und die tolle Arbeitsatmosphäre möchte ich mich außerdem bei Irene Schneider, Roswitha Maul, Sascha Blumentritt und Susanne Schickle bedanken. Wichtige Unterstützung während meiner Promotion habe ich auch von Heike Ellrich erhalten, bei der ich mich für den gelungenen fachlichen Austausch, die erfolgreiche Zusammenarbeit im Labor und ein freundschaftliches und erinnernswertes Miteinander am Lehrstuhl bedanke. Erwähnen möchte ich ebenfalls Christian Hundschell und Benoît Rogez, die mich mit ihren IT-Kenntnissen unterstützt haben, und Robert Waberer und Günther Zitzelsberger, die stets engagierte Arbeit bei der Herstellung von Bauteilen und Hilfsmitteln geleistet haben.

Meinen Eltern, Petra und Frank, und meiner Schwester Elisa gilt an dieser Stelle ebenfalls mein Dank. Ohne eure stets offenen Ohren, eure Ermunterung und euren Rat und Beistand hätte ich diese Promotion nicht so erfolgreich gemeistert.

Abschließend möchte ich mich bei meinem Freund, Christoph Pellinger, bedanken. Du warst in dieser ganzen Zeit mein Fels in der Brandung.

Eidesstattliche Versicherung

Ich, Constanze Helbig, erkläre hiermit an Eides statt, dass ich die vorliegende Dissertation mit dem Thema

„Functional Characterization of Leishmania donovani Myosin-XXI in Transfection and Lipid Binding Studies"

selbständig verfasst, mich außer der angegebenen keiner weiteren Hilfsmittel bedient und alle Erkenntnisse, die aus dem Schrifttum ganz oder annähernd übernommen sind, als solche kenntlich gemacht und nach ihrer Herkunft unter Bezeichnung der Fundstelle einzeln nachgewiesen habe.

Ich erkläre des Weiteren, dass die hier vorgelegte Dissertation nicht in gleicher oder in ähnlicher Form bei einer anderen Stelle zur Erlangung eines akademischen Grades eingereicht wurde.

München, 28.08.2017	
Ort, Datum	Unterschrift